NYU WIRELESS TR 2014-002

Technical Report

Antenna Diversity Combining and Beamforming at Millimeter Wave Frequencies

Shu Sun, Theodore S. Rappaport

ss7152@nyu.edu, tsr@nyu.edu

NYU WIRELESS

NYU Polytechnic School of Engineering

2 MetroTech Center
Brooklyn, NY 11201

June 10, 2014

ABSTRACT

Antenna Diversity Combining and Beamforming at Millimeter Wave Frequencies

Shu Sun, Theodore S. Rappaport
New York University, 2014

This thesis focuses on antenna diversity combining and beamforming at millimeter wave (mmWave) frequencies. Extensive outdoor channel propagation measurement campaigns have been conducted in downtown dense urban environments of New York City at 28 GHz and 73 GHz, from which huge amount of data were acquired and post-processed to obtain various channel parameters and statistics for the next generation wireless communications. Using the measured data, theoretical analysis of antenna diversity combining has been performed to investigate its effect on improving the received signal quality and extending coverage range. Various broadband mmWave beamforming algorithms and hardware architectures have also been reviewed and investigated in this thesis, with an emphasis on the design and characterization of optically addressed phased array antennas.

Table of Contents

List of Tables

List of Figures

CHAPTER 1 INTRODUCTION

1.1 Project Purpose

Since the first demonstration of radio's ability to provide continuous contact with ships sailing the English channel by Guglielmo Marconi in the year 1897, various wireless communications technologies and services have been evolving and spreading rapidly throughout the world, and wireless communications has become an indispensable part of our everyday life. Up to now, four generations of wireless communication systems have been developed in the USA with each new generation emerging every ten years or so since around 1980: first generation analog FM cellular systems in 1981; second generation digital technology in 1992; third generation (3G) in 2001, and fourth generation (4G) Long Term Evolution–Advanced (LTE-A) in 2011. First generation cellular networks were basic analog systems designed for voice communications. A move to early data services and improved spectral ef_ciency was realized in 2G systems through the use of digital modulations and time division or code division multiple access.3G introduced high-speed Internet access, highly improved video and audio streaming capabilities by using technologies such as Wideband Code Division Multiple Access (W-CDMA) and High Speed Packet Access (HSPA). HSPA is an amalgamation of two mobile telephony protocols, High Speed Downlink Packet Access (HSDPA) and High Speed Uplink Packet Access (HSUPA), which extends and improves the performance of existing 3G mobile telecommunication networks utilizing WCDMA protocols. An improved 3GPP (3rd Generation Partnership Project) standard, Evolved HSPA (also known as HSPAC), was released in late 2008 with subsequent worldwide utilization beginning in 2010. HSPA has been deployed in over 150 countries by more than 350 communications service providers (CSP) on multiple frequency

bands and is now the most extensively sold radio technology worldwide, though LTE is bridging the gap.

The rapid increase of mobile data growth and the use of smartphones are creating unprecedented challenges for wireless service providers to overcome a global bandwidth shortage. As the demand for capacity in mobile broadband communications increases dramatically every year, wireless carriers must be prepared to support up to a thousand-fold increase in total mobile traffic by 2020, requiring researchers to seek greater capacity and to find new wireless spectra beyond the 4G standard. Recent studies suggest that millimeter wave (mmWave) frequencies could be used to augment the currently saturated 700 MHz to 2.6 GHz radio spectrum bands for wireless communications. The combination of cost-effective CMOS technology that can now operate well into the mmWave frequency bands, and high-gain, steerable antennas at the mobile and base station, strengthens the viability of mmWave wireless communications. Further, mmWave carrier frequencies allow for larger bandwidth allocations, which translate directly to higher data transfer rates. Mm-wave spectrum would allow service providers to significantly expand the channel bandwidths far beyond the present 20 MHz channels used by 4G customers. By increasing the RF channel bandwidth for mobile radio channels, the data capacity is greatly increased, while the latency for digital traffic is greatly decreased, thus supporting much better internet-based access and applications that require minimal latency. MmWave frequencies, due to the much smaller wavelength, may exploit polarization and new spatial processing techniques, such as massive MIMO and adaptive beamforming. Given this significant jump in bandwidth and new capabilities offered by mmWaves, the base station-to-device links, as well as backhaul links between base stations, will be able to handle much greater capacity than today's 4G networks in highly populated areas.

Also, as operators continue to reduce cell coverage areas to exploit spatial reuse, and implement new cooperative architectures such as cooperative MIMO, relays, and interference mitigation between base stations, the cost per base station will drop as they become more plentiful and more densely distributed in urban areas, making wireless backhaul essential for flexibility, quick deployment, and reduced ongoing operating costs. Finally, as opposed to the disjointed spectrum employed by many cellular operators today, where the coverage distances of cell sites vary widely over three octaves of frequency between 700 MHz and 2.6 GHz, the mmWave spectrum will have spectral allocations that are relatively much closer together, making the propagation characteristics of different mmWave bands much more comparable and homogenous.

This research project funded by Samsung, Nokia Solutions and Networks (NSN), and other NYU WIRELESS industrial affiliates is aimed at investigate the outdoor channel propagation characteristics at mmWave frequencies of 28 GHz and 73 GHz to provide information for the beamforming (BF) algorithms and hardware architectures. Important channel propagation parameters at 28 GHz and 73 GHz carrier frequencies, such as path loss, RMS delay spread, angles of arrival (AOAs), angles of departure (AODs), and their relationships with each other, have been extensively explored. In addition, fundamental knowledge on multiple-input-multiple-output (MIMO) wireless systems have been introduced, high-resolution direction of arrival (DOA) estimation algorithms have been studied, and a series of BF algorithms and architecture have been reviewed.

1.2 Project Goals

The mmWave outdoor channel sounding campaign at 28 GHz concentrates on investigating the propagation channel characteristics in the scenario of base station-to-mobile downlink communications, where the base station transmitter (TX) height is either 7 m or 17 m from

ground, and the mobile receiver (RX) height is 1.5 m from ground (to emulate the average hand-held mobile device height). The measurement campaign at 73 GHz focuses on two scenarios: (1) base station-to-mobile downlink communications, where the base station TX height is either 7 m or 17 m from ground, and the mobile RX height is 2 m from ground; (2) backhaul-to-backhaul communications, where the TX height is either 7 m or 17 m from ground, and the RX height is 4.06 m from ground. Key propagation parameters including path loss, RMS delay spread, angles of arrival (AOAs), angles of departure (AODs), and their relationships with each other are investigated by post-processing the huge amount of data obtained from the measurement campaigns. By analyzing these parameters, statistical spatial channel models can be built for next generation mmWave wireless communications.

MIMO technology shows great potential to increase channel capacity, increase received signal reliability, and/or increase link budget. There are three main functions of MIMO systems: antenna diversity, spatial multiplexing, and BF. Equal-gain combining (EGC) is one of the antenna diversity techniques that can be utilized to improve SNR and to extend the link budget. Hybrid-selection equal-gain beam combining is performed theoretically using the measured data to investigate its effect on path loss exponents (PLEs) and coverage range. Spatial multiplexing and beamforming are intended for different purposes, but they can be combined to improve channel performance. Different BF algorithms and hardware architectures abound, in order to be suitable for mmWave broadband communications, one major issue is how to implement phase shifting or time delaying in phased array antennas for BF. Various approaches are reviewed in this thesis, among which the optically controlled phased array antennas are of special interest due to the inherent broadband, lightweight, small-size features of optical waves.

1.3 Literature Review of MIMO Systems

1.3.1 Antenna Diversity

Multiple-input-multiple-output (MIMO) wireless systems, first investigated by computer simulations in the 1980s [1], are those with multiple antenna elements at both the transmitter and receiver [2]. There are two ways to exploit the multiple antennas in MIMO systems: antenna diversity and spatial multiplexing.

The principle of diversity is to make sure that the same information is obtained at the receiver (RX) through statistically independent channels. The most common form of diversity is microdiversity. Microdiversity refers to the diversity schemes that can combat small-scale fading [3]. There are five most common microdiversity techniques: 1) Spatial diversity: several antenna elements separated in space; 2) Temporal diversity: transmission of the signal at different times; 3) Frequency diversity: transmission of the signal on different frequencies; 4) Pattern diversity: multiple antennas (with or without spatial separation) with different antenna patterns; 5) Polarization diversity: multiple antennas with different polarizations (e.g., vertical and horizontal). Among them, spatial diversity, pattern diversity, and polarization diversity can be classified as antenna diversity. This chapter will focus on antenna diversity methods.

Antenna diversity is aimed at counteracting the effect of fading. Each antenna will experience a different interference environment, if one antenna is experiencing a deep fade, it is likely that another has a sufficient signal. If numerous independent copies of the same signal are available, they can be combined into a total signal with high quality even if the signal quality of some of the copies is low. Antenna diversity can be implemented at both the transmitter (transmit diversity) and receiver (receive diversity). The research on transmit diversity started in the 1990s. If the channel is known to the transmitter, multiple transmitted signal copies can be matched to

the channel, leading to the same gains as for receive diversity. If the channel is unknown to the transmitter, other techniques such as delay diversity and space-time coding have to be utilized. It is then natural to consider the combination of transmit diversity and receive diversity. As demonstrated in [4], when there are N_t transmit antennas and N_r receive antennas, a diversity order of $N_t N_r$ can be realized. Receive diversity has been studied for over 60 years. For receive diversity, multiple received signal copies are weighted and added, and the resultant signal at the combiner output can be demodulated and decoded.

1.3.1.1 Spatial diversity

Spatial diversity is the most conventional and simplest form of diversity and is thus also the most widely used. It is noteworthy that signals received by different antenna elements may be correlated with each other, and a large correlation between signals is undesirable as it reduces the effectiveness of diversity [3]. Hence an important procedure in designing diversity antennas is to establish a relationship between antenna spacing and the correlation coefficient. Again, only mobile receiver antennas are considered here.

As a standard assumption for mobile receivers, the incident waves come from all directions at the receiver. Therefore, points of constructive and destructive interference of multipath components (MPCs) are separated by approximately$\lambda/4$, which is thus the minimum distance required for decorrelation of received signals. For the millimeter wave (mmWave) spectrum, this minimum distance is several millimeters or less.

1.3.1.2 Pattern Diversity

The principle of pattern diversity is that MPCs interfere differently for the antennas with different patterns. Pattern diversity is often employed together with spatial diversity as it enhances the decorrelation of signals at closely spaced antenna elements. Different antenna

patterns can be achieved easily: different types of antennas have different patterns; identical antennas can also have different patterns when mounted close to each other due to mutual coupling, or when located on different parts of the equipment [3].

1.3.1.3 Polarization diversity

Since the reflection and diffraction in a wireless channel rely on polarization of the electromagnetic waves, MPCs with different polarization states experience different propagation processes. The fading of signals with different polarizations is statistically independent thus providing diversity, which does not require a minimum distance between antenna elements.

1.3.1.4 Processing Techniques of Receive Diversity

Diversity can be used to improve the total quality of the received signal via selecting or combining the signals at different antenna elements. There are mainly three types of processing techniques of receive diversity: selection diversity, scanning diversity, maximal ratio combining (MRC), and equal gain combining (EGC).

A. Selection Diversity

Selection diversity is the simplest diversity technique. In selection combining, the strongest signal is selected out of the N received signals, when the N signals are independent and Rayleigh distributed, the expected diversity gain has been shown to be $\sum_{k=1}^{N} \frac{1}{k}$ [5]. There are two major criteria on choosing the best antenna elements, which are introduced below.

(1) Received-Signal-Strength-Indication-Driven Selection Diversity

In general, two types of selection diversity criteria can be exploited: received-signal-strength-indication (RSSI)-driven selection diversity and bit-error-rate (BER)-driven selection diversity [3]. In the former mechanism, the RX chooses the signal with

the largest instantaneous power (or RSSI), and then processes it. N_r antenna elements, N_r RSSI sensors, a N_r-to-1 multiplexer (switch), and only one RF chain are required for this selection diversity scheme. If the BER is determined by noise, then RSSI-driven diversity is the optimum of all the selection diversity approaches since maximization of the RSSI maximizes the SNR as well. On the other hand, if the BER is determined by co-channel interference, then RSSI is no longer a good selection criterion. Since high received power might be caused by a strong interference, leading the RSSI criterion to select branches with a low signal-to-interference (SIR) ratio.

(2) Bit-Error-Rate-Driven Selection Diversity

In this method, a training sequence is first transmitted, then the RX demodulates the signal from each receive antenna element and compares it with the transmit signal. The antenna whose received signal gives the lowest BER is considered to be the best and thus utilized for the subsequent reception of payload signals. If the channel is time variant, the training sequence needs to be sent repeatedly at regular time intervals and the selection of the best antenna element has to be performed afresh. The repetition rate depends on the coherence time of the channel. Several disadvantages exist in BER-driven diversity: 1) In order to evaluate the signal at all antenna elements, either the RX requires N_r RF chains and demodulators thus complicating the RX structure, or the training sequence needs to be repeated N_r times hence decreasing spectral efficiency. 2) If the RX has just one demodulator, then monitoring the BER of all diversity branches continuously is impossible. 3) Since the duration of the training sequence is finite, the selection criterion cannot be determined exactly. The variance of the BER around its true mean value decreases with the increase of the duration of the training sequence, there is therefore a tradeoff between the performance loss due to the erroneous judgment of the BER and spectral

efficiency loss owing to longer training sequences.

B. Scanning or Feedback Diversity

Scanning diversity is very similar to selection diversity with the difference that all the antenna signals are scanned in a fixed sequence until one is found to be above a predetermined threshold, rather than always using the best of all antenna signals [6]. The selected signal is then received until it falls below threshold after which the scanning process is initiated anew. The resulting fading statistics are often inferior to those obtained through the other schemes, but the benefit with this method is that it is very simple to implement: only one RF chain is required and the switching rate is more relaxing than that of selection diversity.

C. Maximal Ratio Combining

In maximal ratio combining (MRC), first proposed by Kahn [7], the signals from all the antenna elements are weighted with respect to their signal-to-noise ratios (SNRs) and then summed, the optimum weights are matched to the wireless channel. Different from selection or scanning diversity, the individual signals must be co-phased before being summed, thus requiring an individual RF chain and phasing circuit for each antenna element. MRC provides an output SNR equal to the sum of the individual SNRs, which produces the best statistical reduction of fading of any known linear diversity combiner.

D. Equal Gain Combining

In equal gain combining (EGC), all the received signals are summed with equal weights. The possibility of providing an acceptable signal from a few unacceptable inputs is still retained, and the performance is merely marginally inferior to MRC and superior to selection diversity and scanning diversity. The performance assessment of EGC with equal power co-channel

interference is reported in [8], [9] analyzed the error probability of EGC with quantized channel phase compensation in Rayleigh fading channels, the performance of EGC receivers in generalized fading channels has also been explored [10], and recently an approximate expression for BER using EGC in multicarrier code-division multiple-access (MC-CDMA) systems was achieved [43]. While research works on EGC abound, most of them are focused on the theoretical error and SNR analysis without thorough experimental data, and selected well-known conventional channel models.

1.3.2 Spatial Multiplexing and Antenna Selection

Spatial multiplexing is another approach to exploiting the multiple antenna elements, whose principle is illustrated in Fig. 1. Different data streams are transmitted in parallel from the different transmit antennas. The multiple receive antenna elements are used for separating the different data streams at the receiver. We have N_r combinations of the N_t transmit signals. If the channel is well-behaved, so that the N_r received signals represent linearly independent combinations, we can recover the transmit signals as long as $N_t \leq N_r$ [12]. The merit of this method is that the data rate can be increased by a factor N_t without requiring more spectrum.

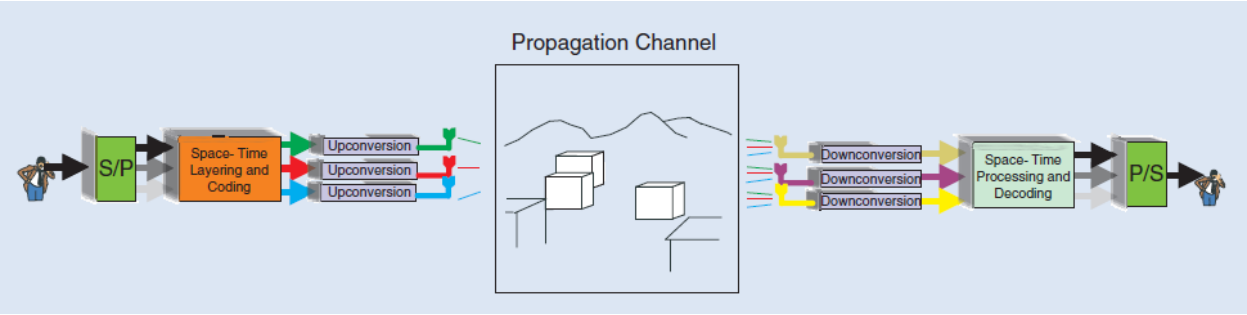

Fig. 1. Principle of spatial multiplexing [12].

If the channel state information is known to the TX, the Nt different beams formed at the transmit antennas can be pointed at different interacting objects (IOs), and different data streams can be transmitted over them [3]. Similarly, at the RX, Nr beams can be formed and pointed at different IOs. If all the beams can be kept orthogonal to each other, then there is no interference between the data streams and thus parallel channels are established. The IOs combined with the beams pointing in their direction act like wires in the transmission of multiple data streams on multiple wires. The number of possible data streams is limited by min(Nt, Nr, Ns), with Ns denoting the number of major IOs. As a result, not only the number of transmit/receive antennas but also the amount of IOs pose upper limits on the number of data streams, since the RX cannot sort two data streams out by forming different beams if the two data streams are pointed to the same IO.

The major blemish of any MIMO system is the increased complexity and hence cost. For example, MIMO systems with N_t transmit antennas and N_r receive antennas require N_t and N_r complete RF chains at the transmitter and receiver respectively, including low-noise amplifiers (LNAs), downconverters, and analog-to-digital converters (ADCs). Owing to this fact, a technique named hybrid-selection (H-S) scheme has been proposed. In the H-S scheme, the strongest L out of N antenna signals are selected (either at one or both links), downconverted, and processed, which reduces the amount of necessary RF chains from N to L thus resulting in substantial savings. This advantage comes at the price of a performance loss compared to the full-complexity MIMO system. When the H-S scheme is used in multiple antennas for diversity purposes with MRC, the method is called hybrid selection/maximal ratio combining (H-S/MRC), or generalized selection combining [13]; in the case that it is employed for spatial multiplexing, the scheme is called hybrid selection/MIMO (H-S/MIMO) [43].

In an H-S wireless system, a bit stream is sent via a vector encoder and modulator. This encoder converts a single bit stream into L_t parallel streams of complex symbols. These streams can have all the same information (e.g., for a simple transmit diversity system with channel knowledge), can all have independent symbol streams (e.g., in spatial multiplexing), or have partially correlated data streams. Subsequently, a multiplexer switches the modulated signals to the best L_t out of N_t available antenna branches. For each selected branch, the signal is multiplied by a complex weight *u* whose actual value depends on the current channel realization. If the channel is unknown at the transmitter, all weights are set to unity. Fig. 2 sketches the structure of the system described above. A few assumptions listed below are made here: 1) The fading at the different antenna elements is independent identically distributed (i.i.d.) Rayleigh fading and is frequency flat; 2) The receiver has full knowledge of the propagation channel; 3) The channel is quasistatic, i.e., the coherence time of the channel is long enough for almost infinitely number of bits to be transmitted within this time.

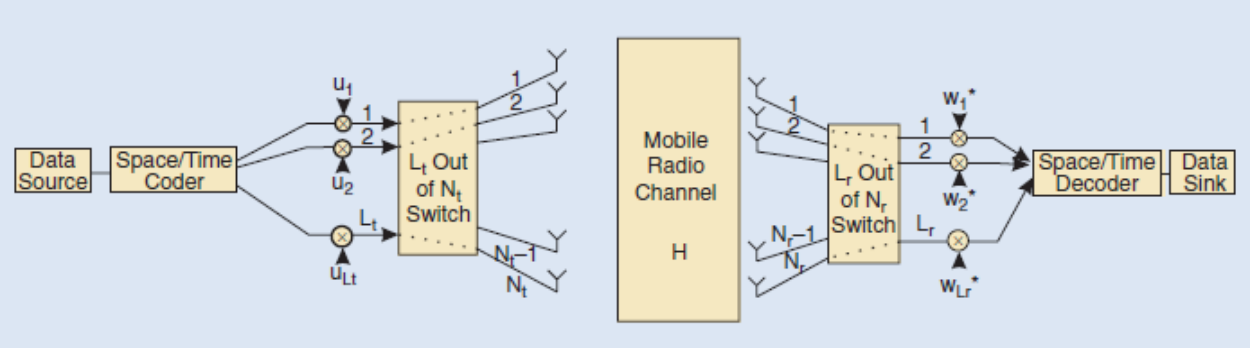

Fig. 2. Block diagram of the H-S system [12].

The channel can be denoted by an $N_r \times N_t$ matrix *H* whose entry $h_{k,m}$ represents the complex attenuation between the *m*th transmit antenna and the *k*th receive antenna. The output of the

channel is smeared by independent additive white Gaussian noise (AWGN). The received signals at the best L_r out of N_r antenna elements are selected and downconverted, thus only L_r complete RF chains are needed. The input-output relationship can be expressed as follows:

$$\vec{\boldsymbol{y}} = \boldsymbol{H}\vec{\boldsymbol{s}} + \vec{\boldsymbol{n}} = \vec{\boldsymbol{x}} + \vec{\boldsymbol{n}} \quad (1)$$

where *H* is the channel matrix, $\vec{s}$ is the transmit signal vector, and $\vec{n}$ is the noise vector [12].

1.3.2.1 Single Input Multiple Output (SIMO) Systems

SIMO systems are those with a single transmit antenna and multiple receive antennas, and the antenna selection is exploited at the receiver so that only H-S/MRC diversity can be considered. It is optimum to select the L out of N antennas that provide the largest SNR at each instant. These antennas can then be combined using MRC. Similar to MRC, the instantaneous output SNR of H-S/MRC is:

$$\boldsymbol{\gamma_{H-S/MRC}} = \sum_{\boldsymbol{i=1}}^{\boldsymbol{L}} \boldsymbol{\gamma_i} \quad (2)$$

where $\gamma_{H-S/MRC}$ denotes the instantaneous output SNR of a H-S/MRC system, and γ_i is the instantaneous SNR of the *i*th best antenna element. It is worth mentioning that selection diversity and MRC are two special cases of H-S/MRC with L=1 and L=N, respectively.

Two kinds of gains can be achieved by multiple antennas: diversity gain and beamforming gain. The diversity gain stems from the fact that the probability for very low SNRs is

significantly reduced since it is almost impossible that multiple antenna elements are in a fading dip simultaneously. The beamforming gain is originated from the fact that the combiner output SNR using MRC is the sum of the individual antenna SNRs, thereby the combiner output SNR is greater by a factor of L than the SNR at one antenna element even if the SNRs at all antenna elements are the same. Antenna selection techniques exhibit desirable diversity gain but not full beamforming gain.

The analysis of H-S/MRC is demonstrated in [15], where a novel concept of virtual branch was proposed. The correlated ordered-branch variables are transformed into a new set of i.i.d. virtual branches, and the ordered-branch SNR variables can be expressed by a linear function of i.i.d. virtual branch SNR variables. The main advantage of this transformation is that it allows the combiner output SNR to be expressed in terms of i.i.d. virtual branch SNR variables and creates greater flexibility in the selection process of the ordered instantaneous SNR values. Generally, the evaluation of the mean SNR of ordered branches involves nested integrals since the statistics of the ordered branches are no longer independent. This complicated calculation can be alleviated by transforming the instantaneous SNR of the ordered diversity branches into a new set of virtual branch instantaneous SNR's, V_i, using the following relation [15]:

$$\boldsymbol{\gamma_i} = \sum_{\boldsymbol{n=i}}^{\boldsymbol{N}} \frac{\boldsymbol{\Gamma}}{\boldsymbol{n}} \boldsymbol{V_n} \tag{3}$$

where γ_i denotes the instantaneous SNR of the *i*th diversity branch, Γ is the average SNR at each branch which is the same for all branches. It can be verifies that the instantaneous SNR's of the virtual branches are i.i.d. normalized exponential random variables. The instantaneous SNR

of the combiner output can now be expressed with respect to the instantaneous SNR of the virtual branches as [15]:

$$\boldsymbol{\gamma_{GDC}} = \sum_{\boldsymbol{n=1}}^{\boldsymbol{N}} \boldsymbol{b_n V_n} \tag{4}$$

where γ_{GDC} represents the instantaneous SNR of general diversity-combiner (GDC) output, and

$$\boldsymbol{b_n} = \frac{\boldsymbol{\Gamma}}{\boldsymbol{n}} \sum_{\boldsymbol{i=1}}^{\boldsymbol{n}} \boldsymbol{a_i} \tag{5}$$

where $a_i \in \{0, 1\}$. Based on the property that normalized exponential random variables have unity mean, the mean of the combiner output SNR can be computed as [15]:

$$\boldsymbol{\Gamma_{GDC}} = \mathbb{E}\left\{\sum_{\boldsymbol{n=1}}^{\boldsymbol{N}} \boldsymbol{b_n V_n}\right\} = \sum_{\boldsymbol{n=1}}^{\boldsymbol{N}} \boldsymbol{b_n} \tag{6}$$

Similarly, the variance of the combiner output SNR is [15]:

$$\boldsymbol{\sigma^2{}_{GDC}} = \boldsymbol{Var}\left\{\sum_{\boldsymbol{n=1}}^{\boldsymbol{N}} \boldsymbol{b_n V_n}\right\} = \sum_{\boldsymbol{n=1}}^{\boldsymbol{N}} \boldsymbol{b_n}^{\boldsymbol{2}} \tag{7}$$

since the variance of the normalized exponential random variable is unity. Note that the independence of the virtual branch variables plays a crucial role in simplifying the derivation of (6) and (7). Using Eqs. (6) and (7), the average SNR gain of the diversity combining compared with a single branch system and the normalized standard deviation of the combiner output SNR can be obtained as follows [15]:

$$G_{GDC} = 10log_{10}\left\{\frac{\Gamma_{GDC}}{\Gamma}\right\} = 10log_{10}\left\{\frac{\sum_{n=1}^{N} b_n}{\Gamma}\right\} \tag{8}$$

$$\sigma_{n,GDC} = 10log_{10}\left\{\frac{\sqrt{\sigma^2{}_{GDC}}}{\Gamma_{GDC}}\right\} = 10log_{10}\left\{\frac{\sqrt{\sum_{n=1}^{N} b_n{}^2}}{\sum_{n=1}^{N} b_n}\right\} \tag{9}$$

Now we can apply the general theory derived above to the H-S/MRC. For the instantaneous SNR defined in Eq. (2), we have:

$$a_i = \begin{cases} 1, & i = 1, \ldots, L \\ 0, & otherwise \end{cases} \tag{10}$$

Therefore,

$$b_n = \begin{cases} \Gamma, & n \leq L \\ \Gamma\dfrac{L}{n}, & otherwise \end{cases} \tag{11}$$

Substituting (11) into (6) and (7), the mean and the variance of the combiner output SNR for H-S/MRC can be easily obtained [15]:

$$\gamma_{H-S/MRC} = L\left(1 + \sum_{n=L+1}^{N} \frac{1}{n}\right)\bar{\gamma} \tag{12}$$

and

$$\sigma^2{}_{H-S/MRC} = L\left(1 + L\sum_{n=L+1}^{N} \frac{1}{n^2}\right)\bar{\gamma}^2 \tag{13}$$

where $\bar{\gamma}$ is the mean SNR at each antenna element.

The fact that the combiner output SNR can be expressed in terms of i.i.d. virtual branch variables enormously simplifies the performance analysis of the system. For example, the derivation of the symbol error probability (SEP) for uncoded H-S/MRC systems, which normally would require the evaluation of nested N-fold integrals, essentially reduces to the evaluation of a single integral with finite limits.

It is noteworthy that the identical principles can also be used for multiple-input-single-output (MISO) systems [12], i.e., where there are multiple antenna elements at the transmitter and only one antenna at the receiver. If the transmitter has complete channel state information (CSI), it can select transmit weights that are matched to the channel. If the transmitter uses all antenna elements, this is known as "maximum ratio transmission" (MRT) [16]; if antenna selection is applied, the system is called "hybrid-selection/maximum ratio transmission.

1.3.2.2 Spatial Multiplexing

For spatial multiplexing, different data streams are transmitted from the different antenna elements; in the following, we consider the case where the transmitter, which has no channel knowledge, uses all antennas, while the receiver uses antenna selection [17]. In the block

diagram of Figure 1, this means that the transmit switch is omitted. For a practical H-S/MIMO system, the number of parallel data streams is upper-limited by the number of transmit antennas. On the other hand, the number of receive antennas should be equal to or larger than that of the data streams in order to separate the various data streams and allow demodulation. Therefore, the capacity is linearly proportional to min (N_r, N_t) [18].

The capacity of a MIMO system using all antenna elements is given by [18]:

$$\boldsymbol{C_{full} = log_2\left[det\left(I_{N_t} + \frac{\bar{\Gamma}}{N_t} HH^{\dagger}\right)\right]} \tag{14}$$

where I_{N_t} is the $N_t \times N_t$ identity matrix, $\bar{\Gamma}$ is the mean SNR per receiver branch. The receiver now chooses the antennas that maximize the capacity, thereby [17]:

$$\boldsymbol{C_{select} = max_{S(\tilde{H})}\left(log_2\left[det\left(I_{N_t} + \frac{\bar{\Gamma}}{N_t} HH^{\dagger}\right)\right]\right)} \tag{15}$$

where $\tilde{H}$ is created by eliminating N_r - L_r columns from H, and $S(\tilde{H})$ denotes the set of all possible $\tilde{H}$, whose cardinality is $\binom{N_r}{L_r}$.

An upper bound for the capacity for i.i.d. fading channels was derived in [17]. For $L_r \leq N_t$, this bound is:

$$\mathbf{C_{H-S/MIMO}} \leq \sum_{\mathbf{i=1}}^{\mathbf{L_r}} \mathbf{log_2}\left(\mathbf{1} + \frac{\bar{\boldsymbol{\gamma}}}{\mathbf{N_t}}\boldsymbol{\gamma}_\mathbf{i}\right) \tag{16}$$

For $L_r > N_t$, the upper bound is:

$$\mathbf{C_{H-S/MIMO}} \leq \sum_{\mathbf{j=1}}^{\mathbf{N_t}} \mathbf{log_2}\left(\mathbf{1} + \frac{\bar{\boldsymbol{\gamma}}}{\mathbf{N_t}} \sum_{\mathbf{i=1}}^{\mathbf{L_r}} \boldsymbol{\gamma_i}\right) \tag{17}$$

The cumulative distribution functions (CDFs) of the capacity obtained by Monte Carlo simulations for $N_r = 8$, $N_t = 3$, and $L_r = 2, 3, \ldots, 8$ are displayed in Fig. 3. With full exploitation of all available elements, a mean capacity of 23 b/s/Hz can be transmitted over the channel. This number decreases gradually as the number of selected elements L_r decreases, reaching 19 b/s/Hz at $L_r = 3$, which is comparable to 23 b/s/Hz. Thus when $L_r \geq N_t$, selecting the best L_r antennas provides almost the same capacity as the full-complexity system. For $L_r < N_t$, the capacity decreases drastically, since a sufficient number of antennas to spatially multiplex N_t independent transmission channels is no longer available. For $L_r \geq N_t$, the slight performance loss is justified by a significant reduction in hardware costs. Instead of a full N_r transceiver chains, only L_r transceiver chains along with an RF switch are required.

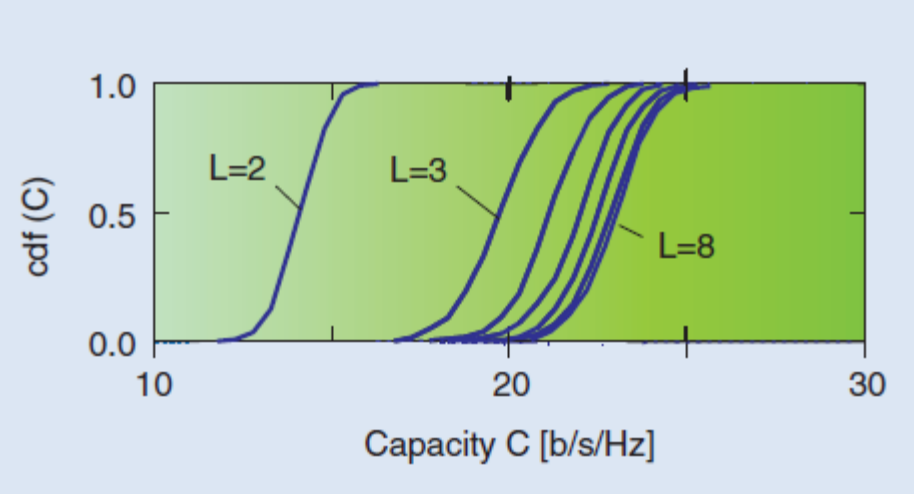

Fig. 3. Capacity for a spatial multiplexing system with SNR = 20 dB, Nr = 8, Nt = 3, and Lr = 2, 3, …, 8 [12].

1.3.2.3 Antenna Selection Algorithms

For a truly optimum selection of the antenna elements, the only mechanism is an exhaustive search of all possible combinations for the one that provides the best SNR (for diversity) or capacity (for spatial multiplexing). However, this requires some $\binom{N_t}{L_t}\binom{N_r}{L_r}$ computations of determinants for each channel realizations, which quickly becomes impractical. For this reason, various simplified selection algorithms have been proposed. Most of them are intended for systems where the selection is done at only one link end.

The simplest selection algorithm is the one based on the power of the received signals. For the diversity case, this algorithm is quite effective. However, for spatial multiplexing, this approach breaks down. Only in around half of all channel realizations does the power-based selection give the same result as the capacity-based selection, and the resulting loss in capacity can be significant. This behavior can be interpreted physically: the goal of the receiver is to separate the different data streams. Thus, it is not good to use the signals from two antennas that

are highly correlated, even if both have high SNR. Fig. 4 shows the capacities that are obtained through antenna selection using the power criterion compared to the optimum selection.

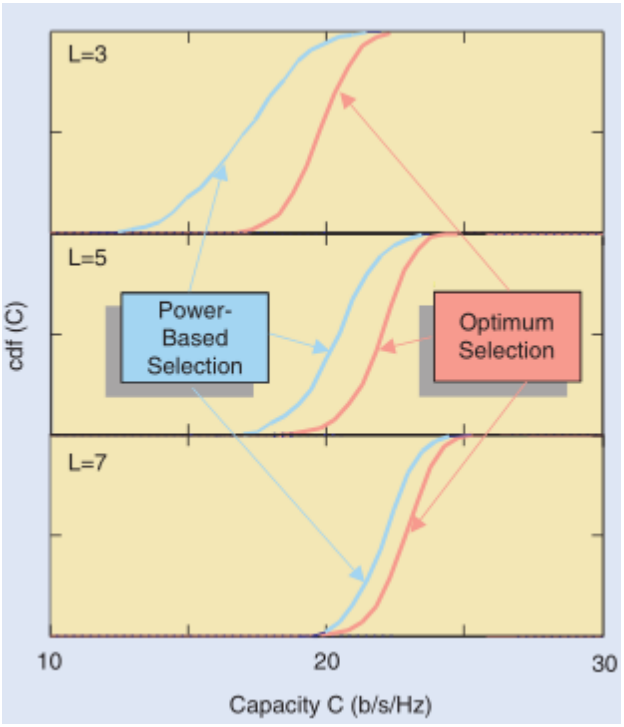

Fig. 4. CDF of the capacity of a system with $N_r = 8$, $N_t = 3$. Selection of antenna by capacity criterion (solid) and by power criterion (dashed).

Based on these considerations, an alternative class of algorithms has been suggested by [19]. Suppose there are two rows of the H that are identical. Since these two rows carry the same information, we can eliminate either of these two rows. When there are no identical rows, we search for the two rows with highest correlation and then delete the row with the lower power. In this manner, we can have the channel matrix $\tilde{H}$ whose rows have minimum correlation and have maximum powers. This method achieves capacities within a few b/s/Hz.

1.3.3 Beamforming

1.3.3.1 Beamforming Algorithms

An antenna can be regarded as a device converting spatiotemporal signals into strictly temporal signals, thus making them available to a broad variety of signal processing techniques [20]. Beamforming or spatial filtering, is the method of creating the radiation pattern of the antenna array by constructively adding the phase of the signals in the direction of the targets/mobiles desired, and nulling the pattern of the targets/mobiles that are undesired. Specifically, beamforming is achieved by adapting the amplitude and phase of the signal from each antenna element by using the product of each user's signal and weight vectors. Using this technique, the transceivers can modify the direction that their cumulative antenna is pointing. More significantly, when an obstruction appears between the transmitter and receiver (e.g. automobile, crowd of people, tree branches, or buildings), the beam steering technique can be applied to produce a link by rotating the beam towards a non-line-of-sight (NLOS) reflector.
Smart antennas is a system of antenna arrays which employs beamforming algorithms to identify spatial signal and is utilized to calculate beamforming vectors to track the antenna beam on the receiver. The overall radiation pattern of an antenna array is determined by the radiation pattern of the individual elements, their positions, orientations in space, and the relative phase and amplitudes of the feeding currents to the elements.

Considering the case where isotropic antennas are used at both TX and RX, Friis' equation shows that the path loss is proportional to the frequency squared [21]:

$$P_{RX} = P_{TX}G_{TX}G_{RX}\left(\frac{\lambda}{4\pi R}\right)^2$$

$$= P_{TX} \cdot 1 \cdot 1 \cdot \left(\frac{\lambda^2}{4\pi}\right)\left(\frac{1}{4\pi R^2}\right)$$

$$= \boldsymbol{P_{TX} \cdot 1 \cdot 1 \cdot \left(\frac{c^2}{4\pi f^2}\right)\left(\frac{1}{4\pi R^2}\right)} \quad (18)$$

where P_{RX} and P_{TX} represent the received power and transmitted power respectively, R denotes the distance between the TX and RX. When the TX antenna is isotropic but the RX employs array antennas, the received power is:

$$P_{RX} = P_{TX}G_{TX}G_{RX}\left(\frac{\lambda}{4\pi R}\right)^2$$

$$= P_{TX} \cdot 1 \cdot G_{RX}\left(\frac{\lambda^2}{4\pi}\right)\left(\frac{1}{4\pi R^2}\right)$$

$$= P_{TX} \cdot 1 \cdot A_{e,RX}\left(\frac{4\pi}{\lambda^2}\right)\left(\frac{\lambda^2}{4\pi}\right)\left(\frac{1}{4\pi R^2}\right)$$

$$= \boldsymbol{P_{TX} \cdot 1 \cdot A_{e,RX}\left(\frac{1}{4\pi R^2}\right)} \quad (19)$$

in which $A_{e,RX}$ is the aperture of the RX antenna. Eq. (19) indicates that the same size of RX antenna aperture captures the same received power regardless of the frequency. Further, if array antennas are utilized at both TX and RX, we obtain:

$$P_{RX} = P_{TX}G_{TX}G_{RX}\left(\frac{\lambda}{4\pi R}\right)^2$$

$$= P_{TX}G_{TX}G_{RX}\left(\frac{\lambda^2}{4\pi}\right)\left(\frac{1}{4\pi R^2}\right)$$

$$= P_{TX}A_{e,TX}A_{e,RX}\left(\frac{4\pi}{\lambda^2}\right)\left(\frac{4\pi}{\lambda^2}\right)\left(\frac{\lambda^2}{4\pi}\right)\left(\frac{1}{4\pi R^2}\right)$$

$$= P_{TX}A_{e,TX}A_{e,RX}\left(\frac{4\pi}{\lambda^2}\right)\left(\frac{1}{4\pi R^2}\right)$$

$$= \boldsymbol{P_{TX}A_{e,TX}A_{e,RX}\left(\frac{4\pi f^2}{c^2}\right)\left(\frac{1}{4\pi R^2}\right)} \quad (20)$$

where $A_{e,TX}$ is the aperture of the TX antenna. As shown by Eq. (20), the received power is even stronger with a higher carrier frequency when array antennas are implemented at both TX and RX, implying the merits of using array antenna at mmWave frequencies.

There are mainly two types of smart antennas: switched beam systems and adaptive array systems. The former presents a predetermined set of beams which can be selected as appropriate. The problem of this approach is that the user of interest may not be in the center of the main beam. Adaptive arrays allow the antenna to steer the beam to any direction of interest while simultaneously nulling interfering signals. Beam direction can be estimated using the so-called direction-of-arrival (DOA) estimation methods. Fig. 13 shows the comparison of radiation patterns between switched beam system and adaptive array system. It can be observed that in the switched beam system, the user of interest does not lie directly in the middle of the main beam. At the same time, interferers are not located in a radiation null. However, with the adaptive beamformer we can adapt to the specific conditions of the environments (position of user of interest and of interferers) and generate the required radiation pattern, with a main lobe focusing towards the user of interest and nulls in the direction of the interferers.

A. Adaptive Arrays

In a mobile communication system, the mobile is generally moving, therefore the DOAs of the received signals in the base station are time-varying [22]. Also, due to the time-varying wireless channel between the mobile and the base station, and the existence of the cochannel interference, multipath, and noise, the parameters of each impinging signal are varied with time. For a beamformer with constant weights, the resulting beampattern cannot track these time-varying factors. However, an adaptive array [43] may change its patterns automatically in response to the signal environment. An adaptive array is an antenna system that can modify its

beampattern or other parameters, by means of internal feedback control while the antenna system is operating. Adaptive arrays are also known as adaptive beamformers, or adaptive antennas. A simple narrowband adaptive array is shown in Fig. 6.

In Fig. 6, the complex weights $w_1,\ldots, w_M$ are adjusted by the adaptive control processor. The method used by the adaptive control processor to change the weights is called the adaptive algorithm. Most adaptive algorithms are derived by first creating a performance criterion, and then generating a set of iterative equations to adjust the weights such that the performance criterion is met [22]. Some of the most frequently used performance criteria include minimum mean squared error (MSE), maximum signal-to-interference and noise ratio (SINR), maximum likelihood (ML), minimum noise variance, minimum output power, maximum gain, etc. [23]. These criteria are often expressed as cost functions which are typically inversely associated with the quality of the signal at the array output. As the weights are iteratively adjusted, the cost function becomes

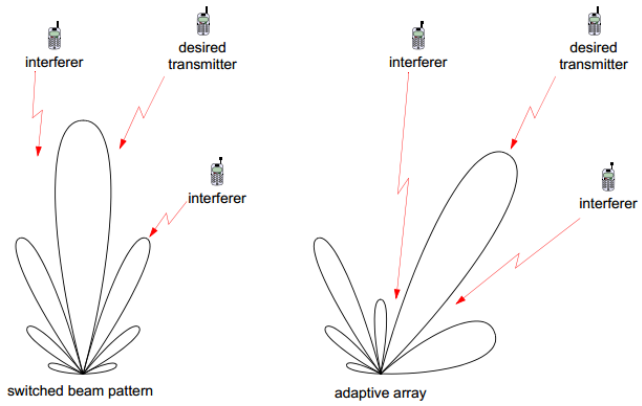

Fig. 5. Radiation patterns of switched beam system and adaptive array system [3].

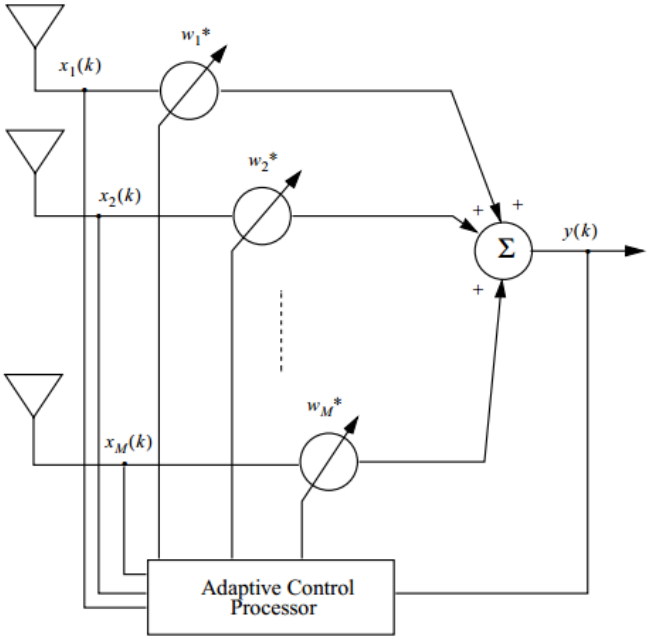

Fig. 6. A simple narrowband adaptive array [22].

smaller and smaller. When the cost function is minimized, the performance criterion is met and the algorithm is considered to have converged [22].

B. Adaptive Beamforming Algorithms

According to previous literature, a diversity of adaptive array algorithms has been utilized for beamforming. Different algorithms may lead to different accuracy, computational complexity, error level, rate of convergence, robustness, etc. In order to select proper algorithms for various adaptive systems as well as to explore novel algorithms based on practical requirements, we need to have a good knowledge of the merits and/or defects of existing algorithms. In general, adaptive beamforming algorithms can be classified into two groups: non-blind adaptive algorithms and blind adaptive algorithms [23].

In a non-blind adaptive algorithm, a training signal, d(t), which is known to both the transmitter and receiver, is sent from the transmitter to the receiver during the training period.

The beamformer in the receiver uses the information of the training signal to compute the optimal weight vector, w_{opt}. After the training period, data is sent and the beamformer uses the weight vector computed previously to process the received signal. If the radio channel and the interference characteristics remain constant from one training period until the next, the weight vector w_{opt} will contain the information of the channel and the interference, and their effect on the received signal will be compensated in the output of the array. However, since the desired data cannot be transmitted over the radio channel during the training period, the spectral efficiency is reduced.

Blind adaptive algorithms do not require a training sequence. The use of a blind algorithm can potentially eliminate the necessity for training sequences, thus increasing the available data rate. Nevertheless, blind algorithms cannot be guaranteed to converge to the desired solution generally, unlike the non-blind algorithms where a known training sequence is adopted. Besides, blind algorithms usually converge more slowly.

C. Non-blind Adaptive Algorithms

The most basic non-blind adaptive algorithm is Wiener solution, which aims to minimize the mean-squared error between the desired signal and the array output. The error signal is given by [22]:

$$\boldsymbol{e(k) = d(k) - y(k)} \tag{21}$$

with

$$\boldsymbol{y(k) = w^H x(k)} \tag{22}$$

and the mean-square error is defined as:

$$\boldsymbol{J = E[|e(k)|^2]} \tag{23}$$

where d(k) and y(k) are the desired signal and sampled signal at time instant t_k, respectively, w is the weight vector, x(k) is the input signal at t_k, and $E[\cdot]$ denotes the ensemble expectation operator. The gradient vector of J is expressed as:

$$\boldsymbol{\nabla(J) = 2\frac{\partial J}{\partial w^*}} \tag{24}$$

In order to minimize J, let

$$\boldsymbol{\nabla(J)|_{w_{opt}} = 0} \tag{25}$$

from which we obtain

$$\boldsymbol{w_{opt} = R^{-1}p} \tag{26}$$

where R is the M×M correlation matrix of the input data vector x(k), and p is the M×1 cross-correlation vector between x(k) and d(k).

As shown by Eq. (26), Wiener solution needs to calculate the inverse of the correlation matrix, which results in a high computational complexity. An alternative approach, the method of steepest-descent (SD) can be employed. The key observation of the SD method is given by

$$\boldsymbol{w}(\boldsymbol{k}+\mathbf{1}) = \boldsymbol{w}(\boldsymbol{k}) + \boldsymbol{\mu}\boldsymbol{E}[\boldsymbol{x}(\boldsymbol{k})\boldsymbol{e}^{*}(\boldsymbol{k})] \tag{27}$$

in which μ is a positive real-valued constant that controls the size of the incremental correction applied to the weight vector, thus is referred to as step-size parameter or weighting constant.

Since exact measurements of the gradient vector are often not possible in reality, it is necessary to estimate the gradient vector based on the available data. A viable approach is the least-mean-squares (LMS) algorithm, whose outcome is expressed as:

$$\boldsymbol{w}(\boldsymbol{k}+\mathbf{1}) = \boldsymbol{w}(\boldsymbol{k}) + \boldsymbol{\mu}\boldsymbol{x}(\boldsymbol{k})\boldsymbol{e}^{*}(\boldsymbol{k}) \tag{28}$$

where the expected value in Eqn. (13) is replaced by the instantaneous estimate.

D. Blind Adaptive Algorithms

There are three main categories of blind adaptive algorithms: (1) algorithms based on estimation of the DOAs of the received signals; (2) algorithms based on property-restoral techniques; (3) algorithms based on the demodulated signals at the receiver. Among the first kind of algorithms, MUSIC and ESPRIT are the most well-known techniques. The drawbacks of DOA-estimation-based algorithms are obvious: the reliability of the prior spatial information is usually unavailable or inaccurate, the computational complexity is very high, and the number of

DOAs that can be estimated is limited by the number of array elements.

One example of property-restoral-based algorithms is the constant modulus algorithm (CMA), which makes use of the constant envelop of communication signals such as frequency-shift keying (FSK), phase-shift keying (PSK), and analog FM signals. The initial goal of CMA is to minimize the cost function

$$\boldsymbol{J(k) = E[||y(k)|^p - 1|^q]} \tag{29}$$

Assuming p = 1 and q = 2 and utilizing the method of SD-CMA, the results are described by Eq. (28), but with

$$\boldsymbol{e(k) = \frac{y(k)}{|y(k)|} - y(k)} \tag{30}$$

Notice that the error signal equals zero if y(k) has a unity magnitude. Comparing Eqs. (21) and (30), it is seen that the term $\frac{y(k)}{|y(k)|}$ in CMA is equivalent to the desired signal d(k) in LMS, whereas a reference signal is not required to generate the error signal in CMA.

Another type of blind adaptive algorithms is the decision directive (DD) algorithm where the demodulated signal is employed as a reference signal in the adaptation of a weight vector in a low bit error rate (BER) system. The steepest-descent DD (SD-DD) algorithm can be realized by using Eq. (28) and substituting $\frac{y(k)}{|y(k)|}$ in the SD-CMA with the decision term sgn[Re(y(k))], where sgn[·] represents the signum function, i.e.

$$\mathbf{e(k)} = \mathbf{sgn}\left[\mathbf{Re}\left(\mathbf{y(k)}\right)\right] - \mathbf{y(k)} \tag{31}$$

Table 1 contains a list and comparison of various adaptive array beamforming algorithms.

Table 1. List and comparison among different adaptive array algorithms for beamforming.

			Advantages	Disadvantages
Adaptive Beamforming Algorithms	Non-blind Adaptive Algorithm	Wiener Solution	Directly getting results by multiplication	High computational complexity
		Steepest-Descent (SD) Method	No need to calculate the inverse of the correlation matrix	Require measurements of the pertinent correlation functions or matrix inversion
		Least-Mean-Squares (LMS) Algorithm (Using steepest-descent to update the weight vector)	Require no measurements of the pertinent correlation functions or matrix inversion	Require the information of the eigen-value of the correlation matrix of the input data vector
	Blind Adaptive Algorithms	Algorithms based on estimation of DOAs of received signals (MUSIC, ESPRIT)	High resolution	1 Depend on array manifold, which is unavailable 0r high-cost; 2 The number of DOAs is limited by the number of array elements; 3 Fail to exploit the temporal structure of incoming signals.
		Constant Modulus Algorithm (CMA) (including Steepest-Descent CMA and Least-Squares CMA)	LS-CMA converges faster than SD-CMA	1. Phase of the array output is indeterminate 2. The desired signal may be nulled by the array
		Decision Directed (DD) Algorithm	High precision near the convergence position	1.Only applicable in low BER systems 2. The weight vector may lose acquisition of the channel

1.3.3.2 Beamforming Architectures

A. Switched Beamforming Architectures

Electronic beamforming has long been commonplace in military systems such as direction-finding radars. It is also becoming practical for commercial communications especially newer cellular systems incorporating adaptive antenna technologies such as multiple-input, multiple-output (MIMO) antenna arrays to minimize the effects of interference and distortion. Numerous investigations have been focused on switched beam antenna systems as it is easy to implement and requires lower cost as compared to a fully adaptive antenna array. In a communication setting, fixed beamforming has been exploited in two ways: either switched beamforming or sectored beamforming [24]. Fig. 7 presents the general scheme of a switched beam system. The signals from the N antenna elements are the input to a beamforming network with P beams. In general, $P \geq N$. The Butler matrix is a beamforming network that forms $P = N$ beams. For each user, the signal-to- noise ratio (SNR) of each beam is measured and the maximum is determined. The beam associated with the largest SNR is chosen for further processing. At any given time, all channels assigned to the cell that this array is serving are available to all users. Therefore, a particular beam, at certain times, may serve several users.

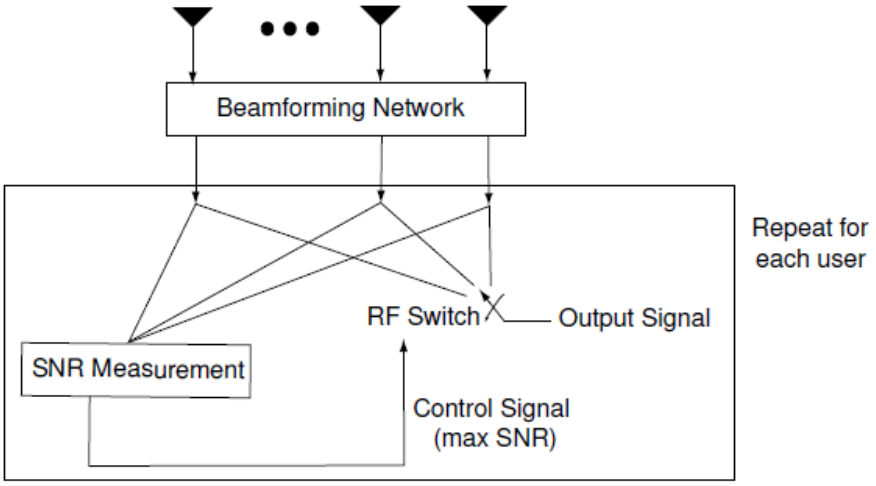

Fig. 7. The general scheme of a switched beam system [24].

(1) Butler Matrix

A mainstay of many switched beam systems is the Butler matrix. The Butler matrix was first described by Jesse Butler and Ralph Lowe in [25] in the year 1961. It is an N x N matrix, where N equals the number of input and output ports, such as a 4 x 4 or an 8 x 8 Butler matrix. A passive Butler matrix can be fabricated by a combination of components, including power dividers/combiners, hybrid couplers, and phase shifters. A quadrature hybrid, for example, will yield two outputs that are in phase and in quadrature (90-deg. offset) relative to the phase of an input signal. Hybrid couplers can provide a 180-deg. phase shift; this enables different components to be combined, achieving (to give one example) outputs with 0, 90, 180, and 270 deg. phase states relative to an input signal for beamforming. The block diagram of a 4×4 Butler matrix is shown in Fig. 8.

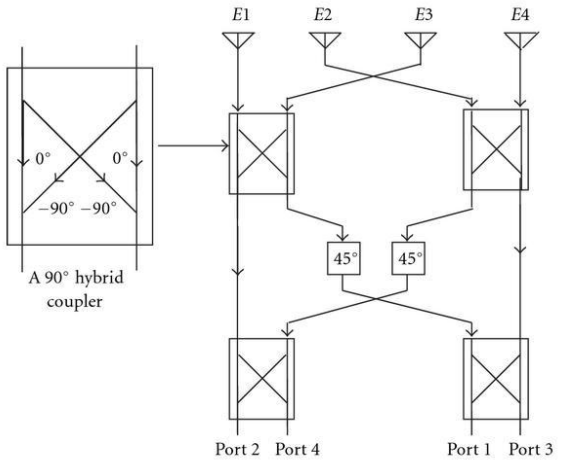

Fig. 8. Block diagram of a 4×4 Butler matrix [24].

A wideband 4×4 Butler matrix was proposed in [26]. Fig. 9 shows the photograph of the proposed matrix. A wider bandwidth can be obtained by using a widened cross junction as demonstrated in [27]. Coupler performances under -20dB for the isolation and the return loss can be achieved over the frequency range 10.75-14.2GHz in this case study (easily up-scalable to mmWave range). This frequency range represents a 28% bandwidth for wideband applications.

Fig. 9. Photograph of the proposed 4×4 wideband Butler matrix [26].

In addition, a novel design of Butler matrix was proposed using substrate integrated

waveguide (SIW) technology in double layer topology for 24 GHz multibeam antenna in automotive radar systems [28]. The proposed doubled layer structure is constructed using a combination of hybrids with broad-wall slot coupling and couplers [43]. Measured return loss and isolation of the proposed E-plane coupler are better than 20 dB over a bandwidth of 28.6%. The image of this Butler matrix is shown in Fig. 10.

Fig. 10. Images of the developed four antenna array fed by 4×4 Butler matrix with two different antenna configurations of ALTSA and slot arrays [26].

(2) Rotman lens

The Rotman lens is another type of beam-forming network. Phase shifters are costly to fabricate and introduce considerable RF losses, while a Rotman lens allows multiple antenna beams to be formed without the need for switches or phase shifters [30][43], which is useful for linear antennas providing the advantage of broadband performance and frequency invariant beam pointing. A Rotman lens comprises a parallel plate region (body) with beam ports and array ports distributed along opposite contours. The central beam port provides equal path lengths to each array element. An offset beam port produces a path length difference and hence a phase gradient along an array, giving a steered beam [31]. A schematic representation of a Rotman lens is given in Fig. 11. The functional principle of beamforming using a Rotman lens is sketched in Fig. 12.

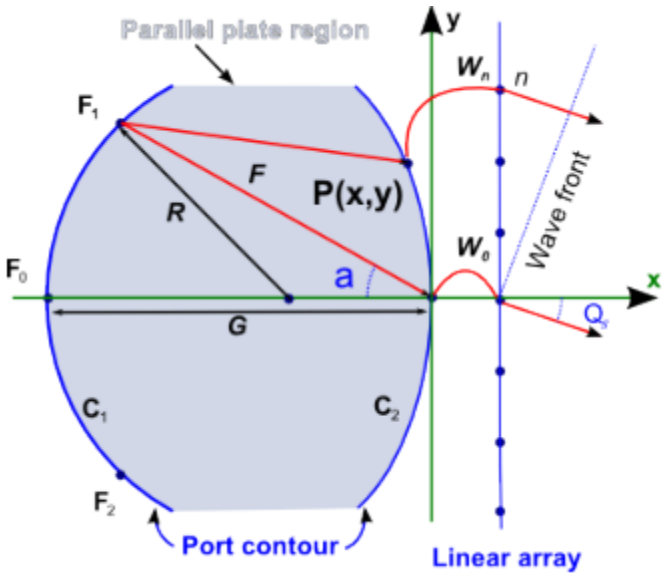

Fig. 11. Schematic layout of a Rotman lens [32].

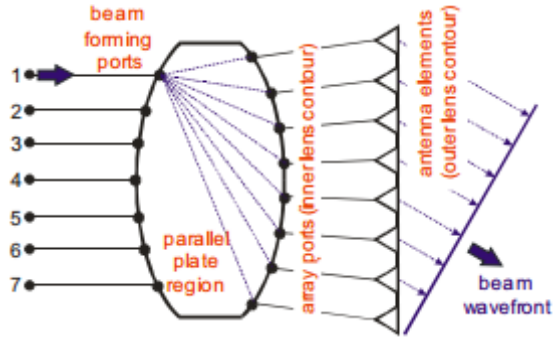

Fig. 12. Sketch of the functional principal of a Rotman lens [30].

The design and development of a compact Rotman lens at 94 GHz feeding an antenna array for beam steering applications was realized using conventional waveguide technology [33]. The construction includes the Rotman lens with connecting lines between the antenna ports and open ended waveguides as radiating elements. The photograph of the proposed Rotman lens is shown in Fig. 13.

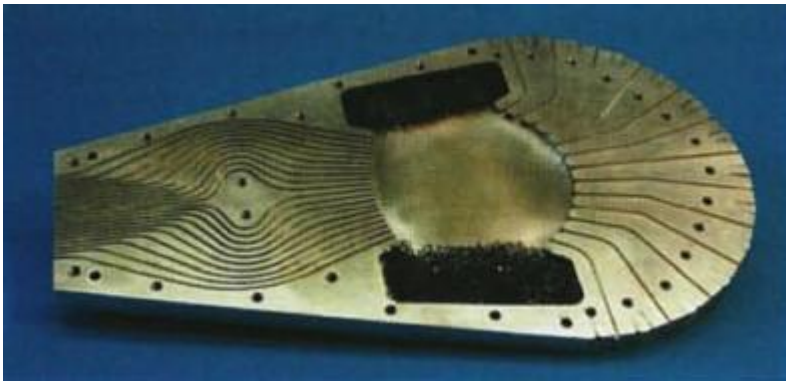

Fig. 13. Photograph of the W-band Rotman lens [33].

A two-layer Rotman lens for millimeter-wave (mmWave) system-in-package (SiP) applications has been designed in [34]. A new design of constrained lines is proposed to reduce the delay lines at 24 GHz. In addition to the size reduction, the proposed two-layer Rotman lens can improve the performances such as efficiency and beam pattern. The Geometry of the proposed two-layer Rotman lens-fed antenna array is shown in Fig. 14.

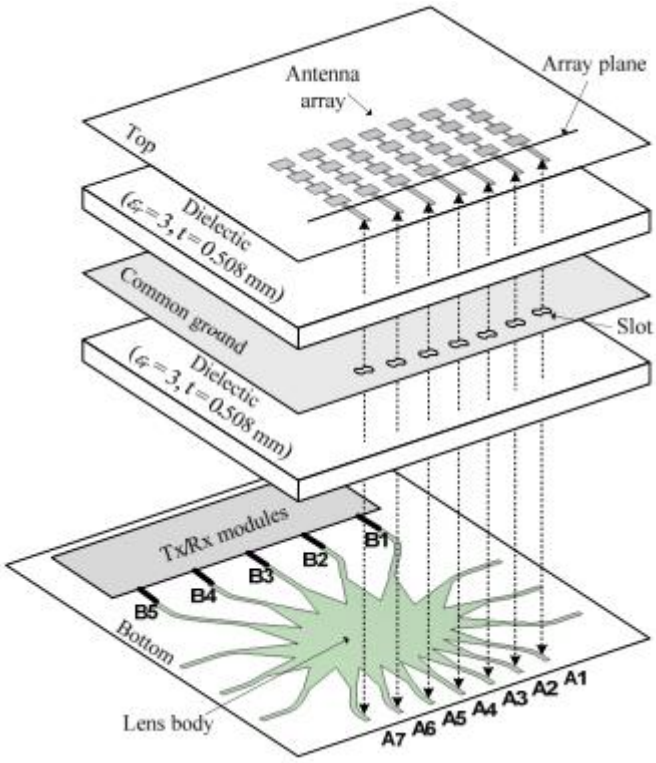

Fig. 14. Geometry of the proposed two-layer Rotman lens-fed antenna array [34].

(3) Other Switched Beam Systems

An intelligent three-beam one-trunk (a trunk is a set of channels shared by one set of subscribers) was proposed in [35] (See Fig. 15). The antenna switch incorporated signal processing capability to locate the subscriber within a beam and controlled the switching to connect the subscriber beam to the assigned radio channel unit. An intelligent antenna system was defined as one where the number of trunks, n, was less than the number of beams, m, while n=m in a conventional antenna system. The relationship between number of subscribers per unit and the number of antenna beams in different antenna systems was shown in Fig. 15. It is conspicuous from Fig. 15 that the capacity can be substantially improved with the increase in the number of antenna beams. As much as 100% capacity increase is possible for a 12-beam system.

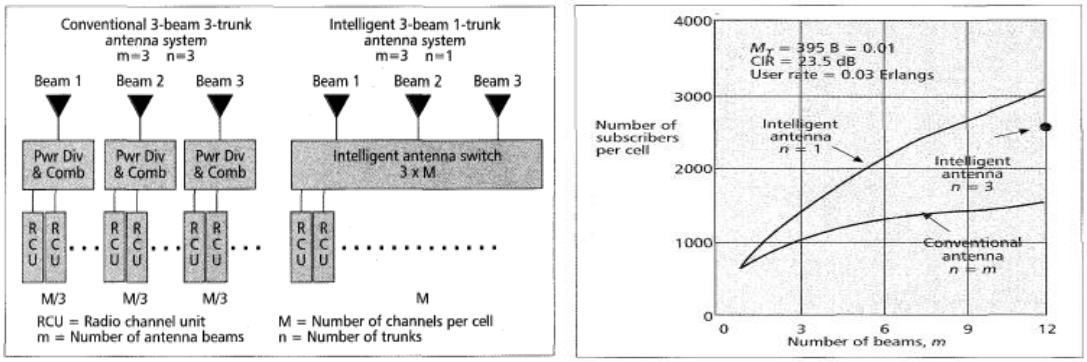

Fig. 15. (Left) Block diagram of three-beam system architectures. (Right) Relationship between number of subscribers per unit and the number of antenna beams in different antenna systems [35].

Preston *et al* investigated the use of switched parasitic elements in electronic beam steering applications [36]. A linear five element steerable patch antenna array with one driven element surrounded by a number of parasitic elements operating at 1.55 GHz was constructed. The architecture of the antenna array was shown in Fig. 16.

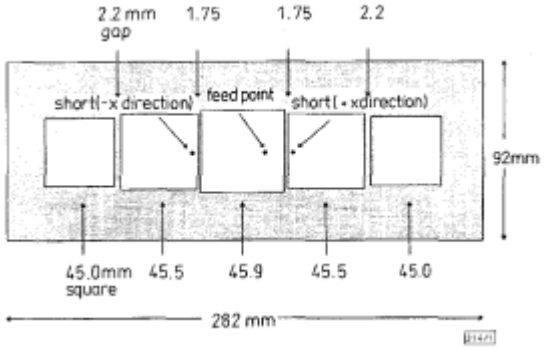

Fig. 16. Physical dimensions of switched five element switched parasitic array. The active element was 45.9mm square, the first parasitics 45.5mm square and second parasitics 45mm square. The feed was chosen to be offset by 12.5mm to give an input impedance close to 50Ω and both shorts were offset by 2.25mm [36].

The advantages of this parasitic switching approach are that only one element is active at any one time and the insertion loss results only from the RF switch in the first structure and nothing in the second structure. Besides, the control system is very simple as there are a limited number of directions in which to steer the beam. By using shorted parasitic elements, they steered the

beam in two directions for tracking polar orbiting satellites. Fig. 17 displays the computed and measured radiation patterns for beams oriented in the forward and backward directions. It can be concluded from the figure that the technique is valid for a two direction linearly polarized array. It is seen that by shorting only one point on two of the parasitic elements of the array, the beam can be steered in two directions. The maximum beam elevation angles measured were -34.8^0 and 39.6^0, compared with the simulated elevation angles of -38.4^0 and 38.4^0. The computed gain was 2.4dBi in the forward direction and 2.6dBi in the backward direction. The minimum gain over the range of elevation angles $+70^0$ was -1.5dBi in the forward direction and -0.08dBi in the backward direction.

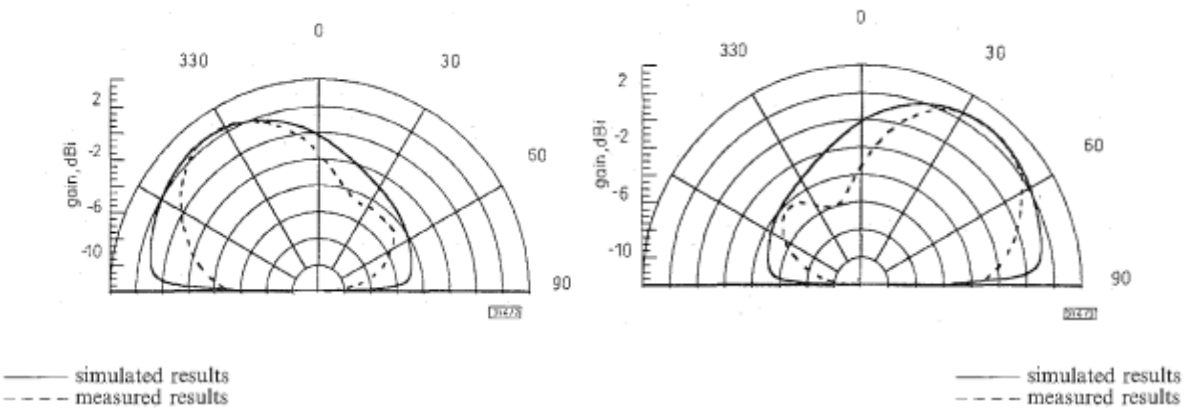

Fig. 17. E-theta radiation pattern measured in dBi for forward (+x) direction (left) and backward (-x) direction (right) [36].

B. Sectored Beamforming

Different from switched beam systems, in a sectored approach, the channels available in the cell are equally divided between the *P* beams [24]. A mobile that transmits within that beam is assigned a channel (if available) from that beam only. If the mobile moves into the area covered by a different beam, a handoff must occur. A sectored approach, therefore, inherently suffers

from greater numbers of handoffs.

Clearly a switched approach is more efficient. All channels are available to all beams. A particular beam would be able to cover a hot spot, an area with many users. A switched beamformer could serve up to N_k users (where N_k is the number of channels available to the base station) [24]. However, the trade-off is that a switched beam approach is significantly more complex to implement such a system requires the ability to measure the SNR, determine the maximum and a RF switch selecting the appropriate beam. This process must be repeated for each user.

C. Adaptive Beamforming Architectures

Switched or sectored beamforming can only steer beams to several fixed directions, thus may not be able to form the beam to the desired target or suppress interference effectively. On the other hand, adaptive array antennas can steer the main beam autonomously into the desired direction and steer nulls into the directions from which interference or jamming waves come. Therefore, adaptive beamforming is much more flexible. There are five possible architectures via which adaptive beamforming can be carried out: digital beamforming (DBF), local beamforming (LBF), microwave beamforming (MBF), aerial beamforming (ABF), and optical beamforming (OBF) [37]. Their pros and cons are also discussed here. The block diagrams of the five beamforming architectures are shown in Fig. 18. Table 2 shows signal processing stages for the five adaptive beamforming structures.

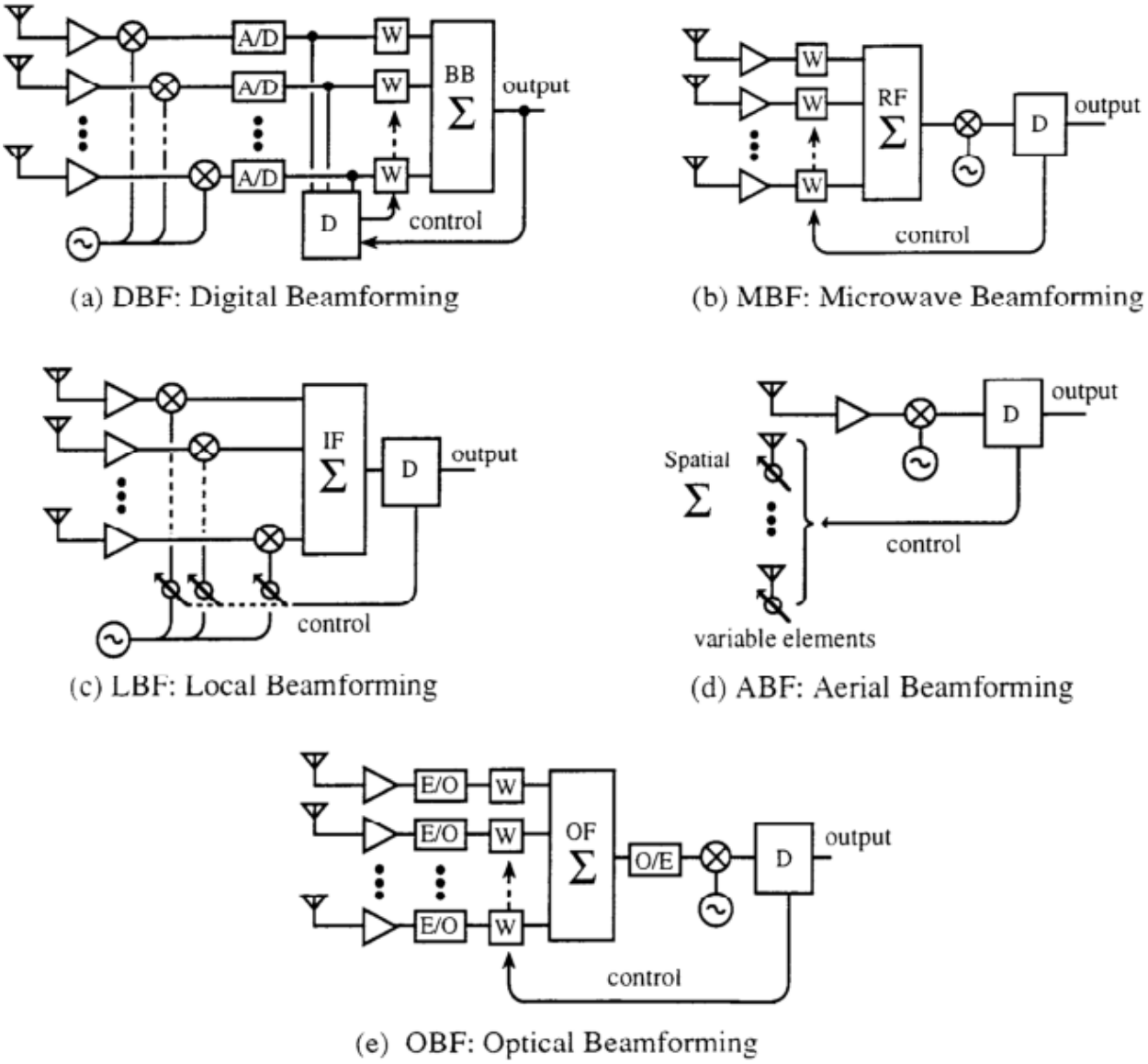

Fig. 18. Adaptive beamforming architectures [37].

(1) Digital Beamforming

For DBF, beamforming is done in the digital stage, and each branch has a low-noise amplifier (LNA), a frequency converter, and an analog-to-digital (A/D) converter prior to the beamformer. Since DBF needs the same number of A/D converters and frequency converters as the number of antenna elements, the fabrication cost increases with the number of antenna

elements. In addition, high-resolution sampling and quantization in the A/D conversion process dissipates high dc power. For the above reasons, DBF has mainly been employed in military applications.

Table 2. Sigma1 processing stages for the five adaptive beamforming architectures (reproduced from [37]).

Signal Process	DBF	MBF	LBF	ABF	OBF
Complex Weighting	Digital	RF Stage	LO Stage	Aerial	Optical
Vector Combining	Digital	RF Stage	IF Stage	Spatial	Optical
Decision + Control	Digital	Digital	Digital	Digital	Digital

(2) Microwave Beamforming

MBF is carried out in the microwave stage, namely, before frequency conversion. Obviously, MBF is superior to DBF in terms of the necessary number of frequency converters and A/D converters. Besides, the dynamic range of MBF is n times wider than DBF because the signals from all n branches are coherently combined before detection, whereas the signals in DBF suffer from quantization errors before they are combined. However, MBF needs weighting devices operative at radio frequencies rather than baseband digital circuits. One approach to large-scale RF circuits is using the recently maturing GaAs monolithic microwave integrated circuit (MMIC)

technology that allows beamformers to be integrated into a single chip.

A prototype of the GaAs MMIC microwave signal processing (MSP) chip for MBF is illustrated by Fig. 19. The archetype is a microwave BFN with 32-element active phased arrays [38]. A large-scale network consisting of 63 power dividers, 63 combiners, 64 weight control dc terminals, 32 RF input ports, 32 pairs of vector-synthetic phase/amplitude controllers, and an RF output port has been successfully developed and integrated into an 11 mm × 13 mm GaAs MMIC. It accommodates 1000 integrated circuit elements, i.e., 128 metal-semiconductor field effect transmitters (MES-FET's), 448 spiral inductors, 527 metal-insulator-metal (MIM) capacitors, and 357 ion-implanted resistors. Full 360^0 phase was observed at the 2.5 GHz. Unlike DSP or DBF that need multiple high-speed DAC's, this structure can perform adaptive beamforming functions with very low dc-power consumption.

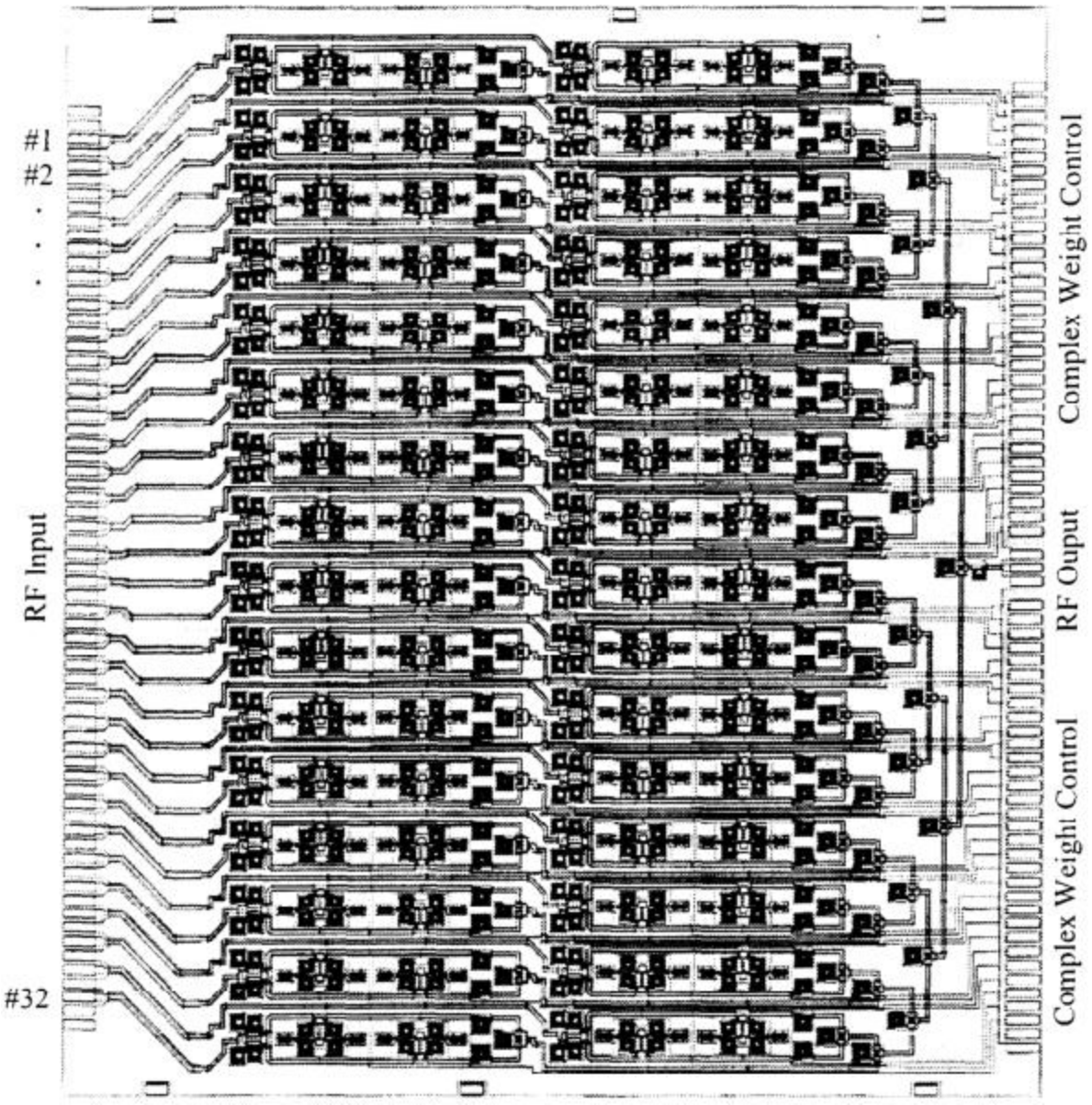

Fig. 19. View of the developed prototype GaAs megalithic beamforming network (BFN) [37].

(3) Local Beamforming

LBF was first reported as an optical signal processing phased array [39], and has been attempted to apply to base stations in wireless-local-loop systems [43]. LBF has a series of distinct features compared with MBF. Weighting is achieved through phase control only without

any gain control operation. As shown in Fig. 18(c), to obtain the same beamforming performance as MBF, the number of branches needs to be doubled. The phase shifters in LBF are on local paths instead of on RF paths, since the LO signal is merely a single-tone, LBF phase shifters have no nonlinearity effect, while RF phase shifters usually exhibit nonlinear phase-vs-frequency effect. Therefore, LBF is especially advantageous when the RF signal spectrum is broadband. As to the disadvantages, LBF requires *n* frequency converters and a high LO power to compensate for the *n* phase shifters' insertion loss.

(4) Aerial Beamforming

ABF is aimed at accomplishing ultimate reduction in the weight, size, power dissipation, and fabrication cost of adaptive antennas. It is called "aerial beamforming" because signal combining is performed in space rather than in circuits, its operation relies on electromagnetic coupling among array elements. The RF circuit scale is substantially reduced compared with other architectures since only one RF port needs to be fed.

A practical hardware implementation of ABF is an electronically steerable passive array radiator (ESPAR) antenna [41], which is displayed in Fig. 20 [37]. In the architecture, a single quarter-wavelength vertical monopole radiator on a ground plane is excited from the bottom in a coaxial fashion, which exhibits an omnidirectional radiation pattern itself. Directivity is realized via electromagnetic coupling by placing passive radiators in equal intervals around the active radiator and loaded with variable reactors in the bottom. To control the directivity through electronic approaches, each reactor is implemented with a varactor diode and two fixed inductors in series and parallel that can carry out any positive and negative value of variable reactance. The series inductor may be omitted by extending the element length instead. The ESPAR antenna has much higher gain than omni-directional antennas, owns a simple structure, consumes low dc

power, and can be fabricated cost-effectively, thus it is prospective in systems such as portable wireless user terminals with built-in smart antennas.

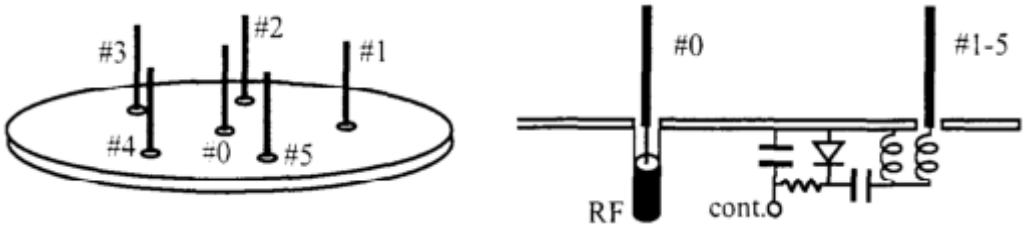

Fig. 20. Electronically steerable passive array radiator (ESPAR) antenna [37].

(5) Optical Beamforming

In OBF, the RF signal is once converted into a light wave signal, proceeds in an optical frequency region, and then converted back down to the original RF frequency. It requires *n* electric-to-optical (E/O) devices and one optical-to-electric (O/E) devices as well as photonic circuits. Since the OBF architecture is extremely low loss, lightweight, and interference-free, it owns special merits in applications where the beamforming network has to be situated far from the radiating elements. As drawbacks, the fabrication cost is relatively high compared to the other beamforming structures.

1.3.4 Broadband Beamforming

Broadband, or ultrawideband (UWB) communication systems are defined as having a relative bandwidth larger than 20% of the carrier frequency or an absolute bandwidth greater than 500 MHz [42]. UWB systems have some distinguishing properties compared with narrowband systems, thus deserves special investigation. Delay dispersion is a notable characteristic in UWB systems. The impulse response of a UWB propagation channel can be

expressed as a sum of discrete MPCs:

$$\boldsymbol{h(t,\tau)} = \sum_{\boldsymbol{i=1}}^{\boldsymbol{N}} \boldsymbol{a_i(t)\chi_i(t,\tau)\otimes\delta(\tau-\tau_i)} \tag{32}$$

where N denotes the number of MPCs and $a_i(t)$ is the complex amplitude of the ith MPC. The phase of $a_i(t)$ varies quickly with time (or location of the mobile station), whereas $|a_i(t)|$ and τ_i vary slowly. $\chi_i(t,\tau)$ represents the time-varying distortion of the ith MPC due to the frequency selectivity of the channel. It is noteworthy that the presence of $\chi_i(t,\tau)$ is the distinct feature of UWB channels; the traditional narrowband model applies when $\chi_i(t,\tau) = \text{const}$.
As has been observed in many measurements, MPCs arrive in clusters. The most popular model reflecting this feature is the Saleh-Valenzuela model [43]. Another approach is based on the $\Delta - K$ model [44].

Steering of broadband signals is performed by introducing time delays at the array elements and selecting these delays such that the desired signal components impinging the array elements are time-aligned. Since the processing of array signals is usually performed digitally, demodulators followed by ADC circuitries are inserted at the antennas' output. The sampled signals are passed through a bank of shift-registers from which the delayed signals are tapped out. Interpolation may also be performed over the samples from the shift-registers to achieve the desired delays with a sufficient accuracy.

Direct extensions of null-steering and beam-space beamformers to broadband signals are not possible. However, they may be implemented if a broadband signal is partitioned into a sufficient number of narrowband signals, and each narrowband signal is treated as a phasor. For narrowband signals, the conventional beamforming was established by the conjugate of the element of the steering vector. This is equivalent to time-aligning the signals received by the

array elements for the desired look direction. Applying the same concept to broadband signals, one will find that a conventional beamformer is implemented simply by adding a scaling factor at the output.

1.3.4.1 Frost Beamformer

One of the conventional broadband beamformers is the Frost beamformer [45], whose structure is shown in Fig. 21. In this structure, there are L sensors and J taps per sensor, $T_1,\ldots, T_L$ are the presteering delays to align the signals to the look direction. Transversal filters are implemented using Tapped Delay Lines (TDLs) in each channel, T_S is the time delay between any two adjacent taps, $x_{i,j}(n)$ is the sampled data variable, which satisfies:

$$\boldsymbol{x_{i,j}(n) = x_i[n-(j-1)], i = 1,\ldots,L; j = 1,\ldots,J} \tag{33}$$

where $x_i(n)$ is the presteered data from the ith sensor.

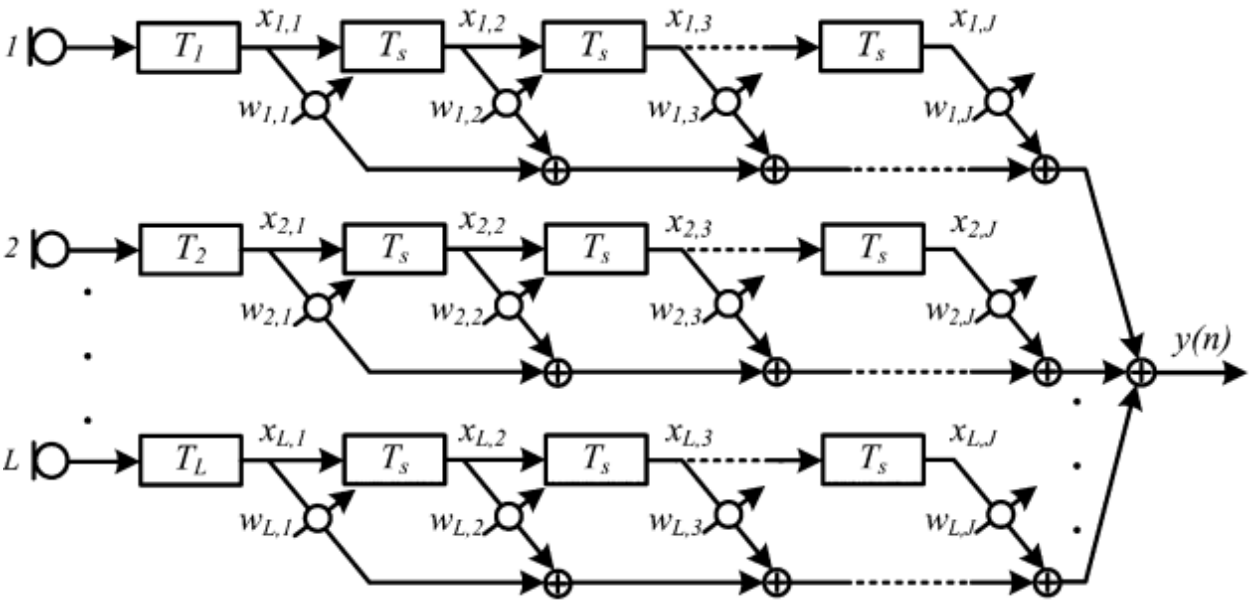

Fig. 21. Frost beamforming structure [46].

1.3.4.2 Time-Shift Operator Based on Matrices

For narrowband signals time delays are effectively approximated by shifting the phase of the signal. Broadband signals, however, require time-shift operators to perform the beamforming function. The time-shift operators are matrices while phase shifts are scalars, thus the computational costs will be different. The time-shift operator Δ can be functionally expressed as [47]:

$$\Delta(\boldsymbol{\tau})\mathbf{s}(\mathbf{t}) = \mathbf{s}(\mathbf{t}+\boldsymbol{\tau}) \tag{34}$$

The simplest time-shift operator is the identity matrix that shifts the time-series signal by a zero amount. Using matrices with ones along other diagonals leads to time shifts by a discrete number of time samples. It is worth considering the unit time-shift operator $\Delta(1)$, which may be written

in a Toeplitz matrix form as [47]:

$$\Delta(1) = \begin{pmatrix} 0 & 1 & 0 & 0 & \cdots \\ 0 & 0 & 1 & 0 & \ldots \\ 0 & 0 & 0 & 1 & \cdots \\ 0 & 0 & 0 & 0 & \cdots \\ \vdots & \vdots & \vdots & \vdots & \ddots \end{pmatrix}$$

Construction of the fractional time-shift operator, $\Delta(\tau)$, for an arbitrary time shift τ is best done in the frequency domain where the fractional time shift can be effected by a phase shift. This operation can be realized by multiplying three matrices: the Fourier matrix *F*, the phase shift matrix $\Delta(\theta)$, and the inverse Fourier matrix F^{-1}. Thus the resultant time-shift operator can be expressed as:

$$\Delta(\boldsymbol{\tau}) = \boldsymbol{\mathcal{F}^{-1}}\Delta(\boldsymbol{\theta})\boldsymbol{\mathcal{F}} \tag{35}$$

1.3.4.3 Frequency Band Decomposition

In most of frequency invariant beamforming methods the frequency dependent weights of the antenna array is implemented by using TDL filters at each branch. Many methods such as two-dimensional inverse Fourier transform [48], least squares error [49], and the minimax method [50] have been proposed to design TDL filters of frequency invariant beamformers. Since the length of TDLs is proportional to the signal bandwidth, the computational load of designing such filters makes these methods inefficient for large bandwidth-signals [51]. To solve this problem beamforming processing in frequency domain has been proposed [52]. However, the FFT processing used in such methods is computationally intensive which makes it not

suitable for real time applications [51].

The author in [53] proposed a new frequency invariant beamforming method based on decomposing of the frequency band of the desired source and implementing the weight functions of each branch based on this decomposition. These weight functions compensate the frequency-dependent response of the array. The typical structure of a broadband beamformer with frequency dependent weight functions is illustrated in Fig. 22.

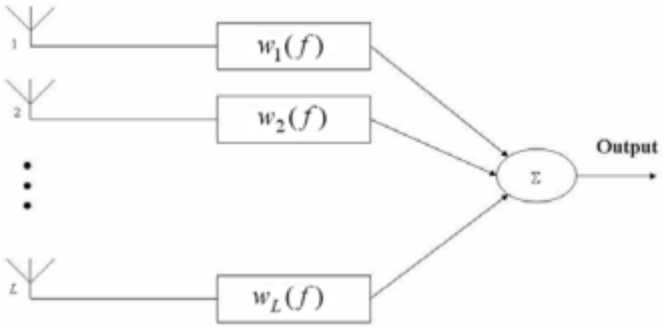

Fig. 22. Typical structure of a broadband beamformer with frequency dependent weights [53].

The array response can be expressed as:

$$\boldsymbol{H(f,\theta) = W^H(f)S(f,\theta)} \tag{36}$$

where f is the single frequency, θ is the arrival angle, the superscript H denotes the transpose conjugate operator, W is the weight vector, and $S(f,\theta)$ is the $L\times1$ steering vector of the broadband source at θ which for a linear broadband array defined as [53]

$$\boldsymbol{S(f,\theta) = [1, \exp\left(-j2\pi f \frac{d}{c}\cos\theta\right), \dots, \exp\left(-j2\pi f \frac{d}{c}(L-1)\cos\theta\right)]^T} \tag{37}$$

To have a frequency invariant beamformer, one should first fix the main lobe width for all uniformly sampled frequencies in frequency design band. From now on, we name these frequencies as selected frequencies. Some beam pattern parameters such as null-to-null beam width are a function of frequency, inter-element spacing, and the number of antennas and the role of weight functions on each branch is only array steering [45]. So to determine the main lobe width of a broad band array at a selected frequency we derive the formula of a uniformly weighted linear broad band array at selected frequency of f_i as [53]:

$$\boldsymbol{H(f_i,\theta)=\frac{\sin(\frac{\pi f_i}{2f_h}Lcos\theta)}{\sin(\frac{\pi f_i}{2f_h}cos\theta)}} \tag{38}$$

The peak response of beam pattern shown in Eq. (38) occurs at $\theta = 90^o$ and the first null of beam pattern with respect to broadside occurs at θ_0 where [53]

$$\boldsymbol{cos(\theta_0)=\frac{2f_h}{Lf_i}} \tag{39}$$

It can be obtained from Eq. (39) that the null-to-null main beam width at selected frequency f_i is a function of maximum frequency of desired signal f_h and the number of antennas. Further, the maximum number of antennas required to guarantee a predefined null-to-null main beam width in typical frequency band of $[f_l, f_h]$ can be determined from Eq. (39):

$$\boldsymbol{L_{max}=\left\lfloor\frac{2f_h}{f_l cos(\theta_0)}\right\rfloor} \tag{40}$$

where L_{max} is the total number of antennas and $\lfloor \ \rfloor$ represents the nearest integer. It is obvious from Eq. (39) that in order to have the same main lobe width at selected frequency of f_i as the main lobe width at minimum frequency, the number of antennas at the selected frequency f_i must be set to:

$$\boldsymbol{L_i = \left\lfloor \frac{2f_h}{f_i cos(\theta_0)} \right\rfloor} \tag{41}$$

In the proposed approach, the decomposition of frequency band into some number of side bands by means of Sinc functions, makes it possible to reduce easily the total number of active antennas at each selected frequency f_i by setting the weights of $(L_{max} - L_i)$ antennas to zero. Using proposed method, the beam pattern at selected frequency f_i can be written as [53]:

$$\boldsymbol{H(f,\theta) = \sum_{m=1}^{L_i} w_m(f_i) \exp\left(-j2\pi f \frac{d}{c}(\mathrm{m}-1)\cos\theta\right)} \tag{42}$$

Eq. (42) clearly shows that the number of antennas at each selected frequency is variable, making the main lobe width becomes frequency invariant at all selected frequencies.

To shape and steer the beam pattern at each selected frequency by proper weight functions, the least squares method is used. A frequency independent desired pattern $\beta_d(u)$ for all frequencies is defined by substituting $\cos\theta$ with u and is shown in Fig. 23.

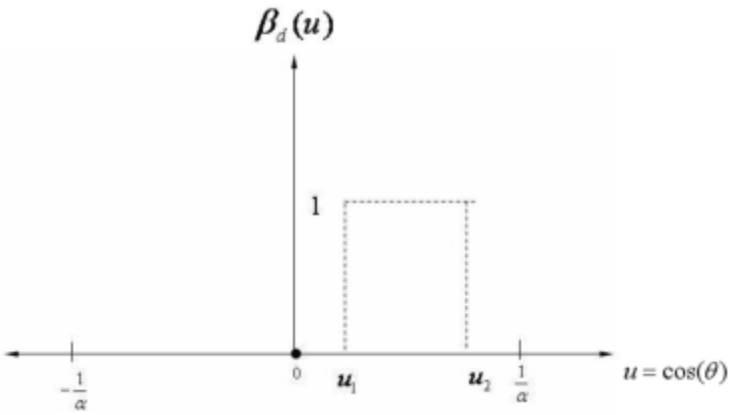

Fig. 23. Desired pattern in the proposed approach [53].

By solving the quadratic error function using the least squares criterion, the weight of the *m*th antenna at the selected frequency f_i is expressed as:

$$\boldsymbol{w_m(f_i) = \frac{\alpha}{2\mu}[\exp(\mu u_2) - \exp(\mu u_2)]} \tag{43}$$

in which $\alpha = \frac{f_i}{f_h}$, $\mu = -j\pi\alpha(m-1)$.

The next step is to estimate the complete function of frequency dependent weights of each antenna by weighted linear combination of basis functions. One of the best basis functions is the set of shifted Sinc functions since they are orthogonal and easily span the desired band of frequency. The Sinc function is given by [53]:

$$\boldsymbol{Sinc\left(\frac{f - f_i}{\sigma}\right) = \frac{\sin\left(2\pi\left(\frac{f - f_i}{\sigma}\right)\right)}{2\pi(f - f_i)}} \tag{44}$$

where σ is a scaling factor defined as [53]:

$$\boldsymbol{\sigma = \frac{f_h - f_l}{N - 1}} \tag{45}$$

with *N* denoting the number of sampled frequencies at the desired band. Using the Sinc functions, the frequency dependent weight function of the *m*th antenna can be expressed as [53]:

$$\boldsymbol{w_m(f) = \sum_{i=1}^{N} w_m(f_i) Sinc\left(\frac{f - f_i}{\sigma}\right)} \tag{46}$$

The architecture of the proposed frequency invariant beamforming antenna array is displayed in Fig. 24.

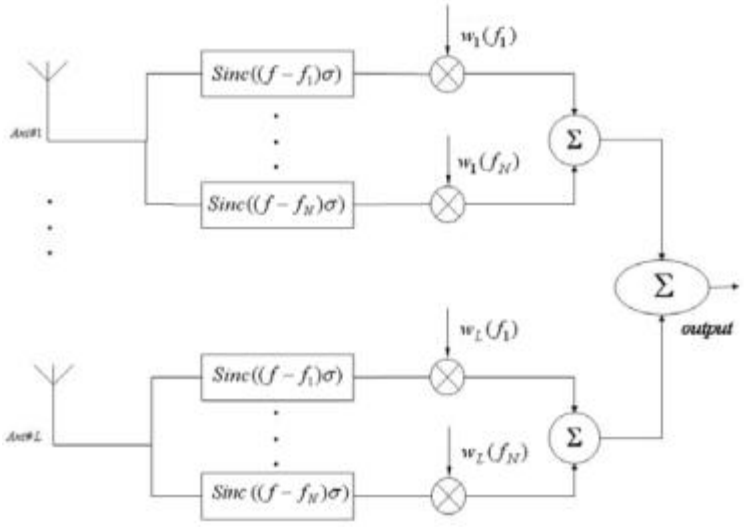

Fig. 24. Detailed architecture of the proposed frequency invariant beamforming antenna array [53].

1.3.4.4 Frequency-Domain Equalization (FDE)

The complexity of conventional equalization approaches generally grows linearly or even exponentially with the number of symbols of dispersion. Broadband channels may hence call for low complexity solutions. Methods to allow the receiver to find burst and symbol timing and a modified decision-feedback equalizer structure are proposed.

Frequency-domain equalization (FDE) is a technique that exhibits relatively low complexity growth with increasing channel memory. A feasible alternative is hence to use an adaptive equalizer that operates in the spatial-frequency domain and uses either least mean square (LMS) or recursive least squares (RLS) adaptive processing [54]. A prefix of length greater than the channel memory is inserted before each block of data transmitted to ensure that the block appears to have cyclic properties at the receiver. Block diagrams of the transmitted block and the receiver are shown in Fig. 25. The received signals are sampled such that aliasing distortion is avoided and transformed using a fast Fourier transform (FFT) algorithm. The discrete frequency components of each diversity branch are then weighted suitably and combined. Computational complexity of this technique is considerably lesser than time-domain equalization.

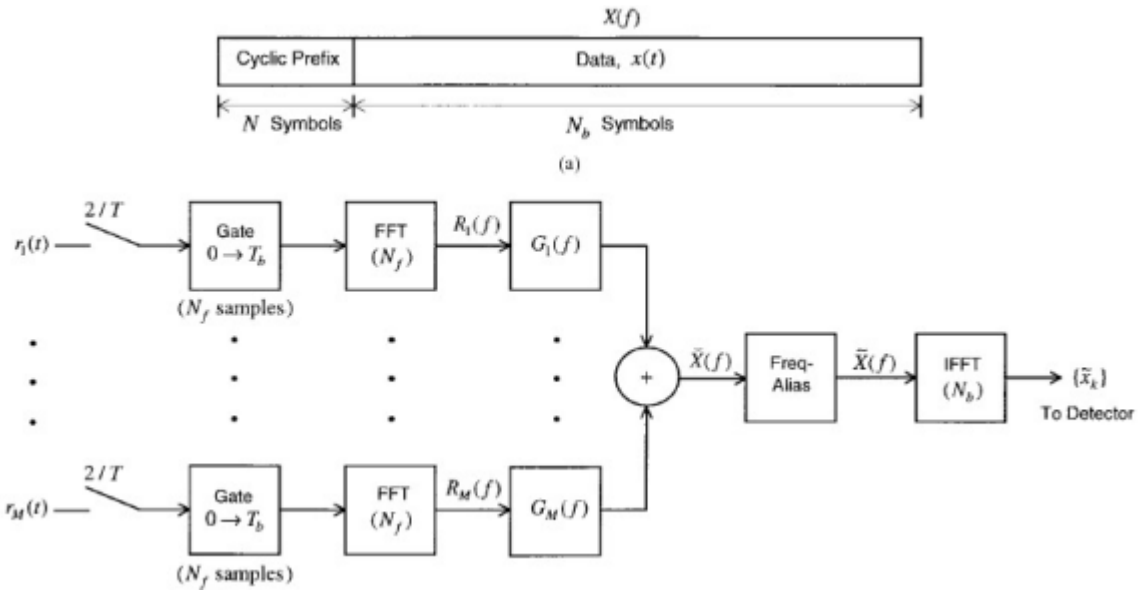

Fig. 25. Transmitted block and Receiver of a Frequency-Domain Equalizer [54].

CHAPTER 2 CHANNEL SOUNDING SYSTEM

2.1 Channel Sounding Methods

2.1.1 Narrowband Method

Channel measurements (or channel sounding) are split between narrowband and wideband characterizations of the channel. The most common and simplest way of characterizing a channel is at a single frequency, also known as continuous wave (CW) channel sounding [55]. A low phase noise oscillator generates a single frequency that is sent with no modulation through the channel. A simple power detector is present at the receiver to record the received signal strength, which may vary in time as the channel changes or as the receiver moves. The narrowband method is primarily used for attenuation in LOS, penetration attenuation, and short distance reflection experiments. When a single frequency is being received, a reflection of the signal may arrive at the receiver out-of-phase with the desired signal which results in a deep fading signal. The deepest fades occur when the reflected signal goes through a path that is near an odd multiple of $\lambda/2$. This effect may be exaggerated by the short wavelengths at mmWave frequencies, where the signal fade occur more often. Since a communication system possesses a non-zero bandwidth and a rather large one in high data rate systems, a narrowband technique does not yield all the information needed about the channel, yet it provides a simple and highly controlled way for performing channel attenuation experiments. Using wideband channel sounding, narrowband fading can be demonstrated by observing the frequency domain representation of a received wideband signal.

2.1.2 Wideband Methods

2.1.2.1 Periodic Pulse Technique

A full characterization of the channel is provided by wideband channel sounding techniques, where “wideband” is defined as a probed channel bandwidth that is sufficiently greater than the system bandwidth used in the intended application [56]. The most intuitive method to characterize the system is the periodic pulse technique. The impulse response of the channel can be found by sending an impulse and receiving the resulting signal. However, an impulse requires infinite bandwidth from both the transmitting and receiving hardware. Fortunately, wireless applications demand bandlimited signals for accommodating many users and networks. Thus, a pulse is generated with a first null bandwidth that is several times the symbol rate of the application of interest. The pulse is used to modulate a carrier. The receiver captures the pulse after a path delay and any replicas of the pulse that originate from multipath. The periodicity of the transmitted pulse is present for characterization of the time varying response of the channel to extract Doppler frequency shifts in a time-variant response. The hardware for a periodic pulse channel sounder uses few components and so is relatively simple to implement. A common implementation has a digital circuit or comparator-based latch for generating a short duration pulse which controls a RF (ON/OFF) switch. The switch is connected to a signal generator (which produces the carrier frequency) and the second terminal is connected to the antenna. An isolator (i.e. terminated circulator) may be used between the antenna and the switch to ensure a good match and remove any system induced reflections. This is especially critical when the antenna is connected to the hardware through a long cable, where a reflection may induce a signal at several nanoseconds after the original signal was sent causing artificial measured multipath. The main disadvantage in the pulse method for millimeter wave systems is the need for very short duration pulses, which are both difficult to generate and capture (or digitize). In addition, the system dynamic range is set by the transmitted signal power, thermal noise which

increases with signal bandwidth, and limitation in the circuit component dynamic range. Thus, a wideband periodic pulse system may have unacceptably low dynamic range.

2.1.2.2 Swept Frequency Technique

The alternative to a time-domain channel sounding technique (i.e. pulse-based) is a frequency-based technique known as swept frequency [56]. A time-invariant impulse response can be exactly represented by the steady state frequency spectrum of the channel. A continuous wave at a single frequency is sent through the channel in the same way a narrowband channel sounder operates. In order to develop the channel response for the full spectrum of interest, the frequencies are swept for the full bandwidth in what is known as a chirp signal (i.e. a ramp in frequency of the signal). This technique is very common for short range indoor channels, especially at high frequencies, such as millimeter wave. The basic structure only requires a vector network analyzer (VNA), which is commercially built with very high dynamic range and large range of frequency generation capabilities. Since the VNA is commercially built and verified, it requires very low implementation time since all the complexity is dealt with by the VNA designer. Since millimeter wave VNAs are expensive, most researchers use a VNA with a lower frequency range which they mix with a CW signal to reach higher frequencies. A significant drawback to the system is the requirement that both receiver and transmitter be connected through a cable to the VNA, which physically limits the transmitter to receiver separation possible. The loss of the received signal through the cable (which is likely to have about 1-3dB of loss per meter at 5 GHz) can be quite large and so limit the dynamic range of the system. Thus, a swept frequency system is rarely used in outdoor measurement, and quite less so for cellular type measurements.

2.2 Spread Spectrum Modulation

Spread spectrum modulation techniques utilize a transmission bandwidth several orders of magnitude greater than the minimum required signal bandwidth. The advantage of this technique is that many users can share the same bandwidth simultaneously without significantly interfering with one another. Spread spectrum signals are pseudorandom and noise-like when compared with the digital information data. The spreading waveform is controlled by a pseudo-noise (PN) sequence or PN code, which is a binary sequence that appears random but can be reproduced in a deterministic way by the intended receivers. Spread spectrum signals can be demodulated at the receiver by cross-correlation with a locally-generated identical version of the PN sequence. Cross-correlating the same PN sequence dispreads the spread spectrum signal and recovers the modulated message in the same narrow band as the original data, while cross-correlation with the signal from a non-targeted user leads to a tiny amount of wideband noise at the output of the receiver.

The most prominent merit of spread spectrum is its inherent interference rejection capability. Even though multiple users use the same spectrum at all times, the receiver can still separate each user according to their PN code since each user is assigned a unique code that is approximately orthogonal to the codes of other users. Secondly, a particular spread spectrum signal can also be completely restored even when it is jammed by a narrowband interferer, since narrowband interference influences only a small part of the spread spectrum signal, the interference can be easily removed via notch filtering without losing much information. Another advantage of using spread spectrum modulation technique is its resistance to multipath fading. Since spread spectrum signals have uniform energy over a very large bandwidth, merely a small part of the spectrum will experience fading caused by frequency selectivity of the channel.

2.3 Pseudo-Noise Sequences

A pseudo-noise (PN) or pseudorandom sequence is a binary sequence with an autocorrelation that resembles the autocorrelation of a random binary sequence and the autocorrelation of bandlimited white noise. In spite of being deterministic, a PN sequence possesses many features which are similar to those of random binary sequences, such as having very low cross-correlation between any two different sequences, very low correlation between shifted versions of the same sequence, and a nearly equal number of 1s and 0s.

2.4 Sliding Correlator Description

2.4.1 Characteristics of Sliding Correlator

Our channel sounding system uses a spread spectrum sliding correlator method introduced by Donald Cox for use in early cellular channels. The fundamental concept is to correlate two pseudo-random noise (PN) sequences at slightly different clock speeds at the transmitter and receiver, which results in a time dilation allowing a high effective digitization rate of the received signal. The sliding correlator channel sounding system deployed in this measurement campaign can provide 2.5 nanoseconds multipath time resolution. In the future mmWave communication regime, propagation delays will be measured on the order of tens of nanoseconds due to the greater bandwidths involved in order to have sufficient time resolution in a multipath-rich environment.

The PN sequence used in our channel sounding system is a maximal sequence, or m-sequence for short. The period of an m-sequence is expressed as:

$$\boldsymbol{L = 2^N - 1} \qquad (\mathbf{47})$$

where N is the number of bits in one sequence. The linear feedback shift register can generate

m-sequences. An N-bit shift register holds the previous N terms of the m-sequence, the terms in the ith registers are weighted based on their individual feedback coefficients c_i and summed modulus 2 using exclusive OR (XOR) gates. At each clock cycle, the summation is input to the shift register and the (n-N)th term is shifted out. If the shift register is clocked at a frequency of f_c, then each term of the m-sequence is generated every $1/ f_c$ seconds and each term can be represented as a rectangular pulse with duration $T_c = 1/ f_c$. Hence the PN sequence is an infinite train of rectangular pulses where the value of the ith pulse is decided by the ith term of the m-sequence, and each pulse is usually referred to as a chip. Assuming a bi-phase output with amplitudes $\pm V_0$ where $a_i = 1$corresponds to $+ V_0$ and $a_i = 0$ corresponds to $-V_0$, which provides an analog waveform x(t) representing the PN sequence. In our channel sounding system, N = 11, L = 2047, f_c = 400Mcps (Mega-chip-per-second), T_c = 2.5 ns. The autocorrelation of the PN sequence results in a train of triangular pulses with a base width of 2 T_c, a maximum amplitude of V_0^2, a period of LT_c, and a DC offset of $-V_0^2/L$.

A fixed, static channel can be modeled as a tapped-delay line in which individual multipath components (MPCs) are delayed and complex-scaled copies of the transmitted signal. The convolution between the tapped-delay line representation of the wireless channel and the autocorrelation of the transmitted signal is equivalently a scaled copy of the band-limited channel impulse response (CIR). At the receiver side, the received signal would be sampled by an analog-to-digital converter (ADC). To properly sample the received signal, the ADC's sampling rate should be equal to or larger than twice the baseband bandwidth. For wideband wireless channel measurements, a high-speed ADC is required associated with high cost.

A true autocorrelation involves two identical sequences driven by a same frequency, whereas the autocorrelation in a slide correlator uses two identical sequences but one sequence is clocked

at a slightly slower rate than the other. Sliding correlation of two identical PN sequences would result in a time-dilated autocorrelation of the PN sequence and the distortion to the time-dilated autocorrelation. A key parameter related to sliding correlator is the slide factor, γ, which is defined as [56]:

$$\boldsymbol{\gamma = \frac{f_c}{f_c - f_c'}} \qquad (\mathbf{48})$$

where f_c' is the clock frequency of the PN sequence at the receiver.

In frequency domain, the time-dilated autocorrelation spectrum is centered at DC and has a $sinc^2(\frac{f\gamma}{f_c})$ envelope, hence most of its power lies within the main lobe region $(-\frac{f_c}{\gamma}, \frac{f_c}{\gamma})$. While the undesired distortion is centered at a higher frequency, thus the distortion can be removed by low-pass filtering the sliding correlator product. After low-pass filtering, the majority of the time-dilated autocorrelation will remain whereas a large portion of the undesired distortion will be removed.

In our channel sounder equipment, The PN sequence is generated using an 11-bit shift register and the length of the PN sequence is 2^11-1=2047. The clock rate of the TX PN sequence and RX PN sequence is 400 Mcps (Mega-chip-per-second) and 399.95 Mcps, respectively, and the difference between the two clock rates is 50 Kcps. Thus the slide factor is sf = 400/(400-399.95)=8000. the actual time it takes for a period of the PN sequence to occur is 2.5ns*2047*8000 which is approximately 40ms, where 2.5ns (=1/400Mcps) is the time duration of one chip, 2047 is the length of the PN sequence, and 8000 is the slide factor.

There are a few important parameters that determine the channel sounder capabilities and thus the fidelity of the band-limited CIR obtained by the sliding correlator channel sounder. Three most fundamental system parameters are: the length of the PN sequence L, the transmitter

PN chip rate f_c, and the slide factor γ. Some other parameters are as follows:

A. Multipath Time Resolution

Multipath time resolution is defined as the minimum time required to distinguish two adjacent MPCs. For a sliding correlator channel sounder with a transmitter PN chip rate of f_c, the multipath time resolution is $1/f_c$, which is 2.5 ns in our system.

B. Maximum Resolvable Multipath Delay

The maximum resolvable multipath delay is L/f_c, which is the period of transmitted PN sequence. Accordingly, the maximum resolvable path length can be obtained by multiplying the free space propagation velocity of the electromagnetic (EM) wave *c*:

$$\boldsymbol{d_{max} = \frac{cL}{f_c}} \quad (\mathbf{49})$$

C. Processing Gain

The processing gain (PG) is defined as the ratio of the SNR after a process to the SNR before the process [57], i.e.,

$$\boldsymbol{PG = 10log_{10}\left(\frac{SNR_{out}}{SNR_{in}}\right)\ (dB)} \quad (\mathbf{50})$$

The function of the PG is to spread the power spectrum of the undesired noise and interferents. Multiplying the complex-baseband equivalent of a continuous wave interferent at the system's RF carrier with the receiver PN sequence will spread the interferent's power spectral density across a complex-baseband bandwidth of approximately f_c'. The interferent's spread spectrum at frequencies greater than $f_c - f_c'$ will be blocked by low-pass filtering the correlation output, hence only $100 \times (f_c - f_c')/f_c'\%$ of the interferent's power is maintained. Since $f_c' \approx f_c$, the interferent's power will be decreased by a factor of γ. In a word, the signal's power remains the

same while the power of the noise and interferents is significantly reduced, thus the SNR is equivalently increased. Therefore, the linear PG for a sliding correlator system is γ, which in dB is:

$$\boldsymbol{PG = 10log_{10}(\gamma)\ (dB)} \tag{51}$$

It is noteworthy that the PG for a direct sequence spread spectrum system is approximately $10log_{10}(L)$, which is different from the PG described above because of the sliding correlating operation.

Table **2** provides the main advantages and disadvantages of various channel sounding techniques.

Table 2 Comparison of various channel sounding techniques.

	Advantages	Disadvantages
CW (Narrowband Method)	Simplicity of implementation (Requires a low phase noise oscillator; No modulation)	Signal fade occurs very often; Does not yield all the information needed about the channel; Easy to be interfered or jammed
Periodic Pulse Technique (Wideband Method)	Relatively simple implementation, requiring only an RF switch, signal generator, and pulse generator; Provides multipath resolution equal to the width of the pulse; The received signal can be coherently demodulated to provide Doppler Spectra	High resolution of multipath signals requires a high-speed RF switch and pulse generator; The system requires a high peak-to-average power ratio to detect weak multipath, however, most transmitters are peak power limited, thus limiting the dynamic range of the system; The bandpass filter at the receiver must have a very wide bandwidth, making it susceptible to noise and interference

Swept Frequency Technique (Wideband Method)	Simplicity of implementation (Requires a VNA, a signal generator, and antennas); High resolution of multipath, proportional to the frequency step size;	TX and RX need to be connected through a cable to the VNA; Low dynamic range due to cable loss; Useful only for either time-invariant channels, or channels which vary slowly with respect to the step time; No Doppler shift or spectra can be obtained from the system due to the frequency stepping technique
Spread Spectrum Sliding Correlation (Wideband Method)	Large dynamic range; PN sequence is easy to generate; Interference robust; Superior multipath time resolution; Small 1st null-to-null bandwidth; Controllable processing gain;	Complex structure; Reduced real time behavior due to correlation;

2.4.2 Noise in a Sliding Correlator

2.4.2.1 Thermal Noise

Thermal noise is a significant noise process when a weak signal is received, and so sets the sensitivity of a receiver. The thermal noise power is known to be equal to kTB, where B is the frequency limitation imposed by filters in the system. Considering the first null-to-null bandwidth of 800 MHz, at room temperature of 300 K, a thermal noise of 1.38e-23*300*800e6 = 3.312*10-12 W is produced at the input of the receiver antenna, which may be expressed as -114.8 dBm over the 800 MHz bandwidth. As thermal noise passes through a downconverter (or any other amplifier chain), its amplitude is multiplied by the amplifiers' gains since the amplifier cannot distinguish between in-band noise and signal. Additional noise is added to the signal from

each component in the downconverter and is expressed by the noise factor (F) of the component, or alternatively by the noise figure (NF) which is 10log(F) [58]. The noise figure of the downconverters is given to be 5.22 dB.

2.4.2.2 PN Sequence Correlation Self-Noise

The first source of self-noise (i.e. noise generated by the correlation process) encountered in performing a PN sequence correlation is due to the non-zero DC value of the time waveform when the PN sequences do not overlap [59]. It is desired that the output of a channel sounder is exactly zero when a pulse isn't received. For a direct sequence spread spectrum system, this means that a zero output is provided when PN sequences are non-overlapping. However, spread spectrum theory says that correlation of non-overlapping PN sequences results in a DC value of 1/L, where L is the length of the sequence [59]. Fortunately, this DC offset can be easily removed from a measured waveform by AC coupling.

The second source of self-noise is unique to the sliding correlator. The output of a multiplication of two identical PN sequences with different chip rates contains the desired sinc squared frequency response centered at DC and replica distortion terms centered at integer multiplies of Rc/L. The distortion terms are of the same magnitude and shape as the desired output. The presence of these distortion terms is unavoidable since they are fundamental to the sliding correlator operation. However, in order to ensure that minimal power from the distortion terms enters the band of interest, which is defined as the 1st null bandwidth of the pulse (Rc-Rc'), the distortion terms must be sufficiently separated from the DC-centered pulse.

The important parameter for improving the distortion term rejection can be derived by setting an upper limit on the amount of in-band distortion allowed. The separation of the 1st null frequency of the desired output to the peak of the adjacent distortion term is used to express the

dependence of the in-band distortion on system parameters since this separation should be maximized for reducing the self-noise.

$$\boldsymbol{f_{sep} = \frac{R_c}{L} - (R_c - R_c') = (R_c - R_c')\left(\frac{\gamma}{L} - 1\right)} \quad (52)$$

where γ is the slide factor.

2.4.2.3 Quantization Noise

An important limitation for nearly all mixed signal systems is the analog to digital converter (ADC) resolution. $\sigma^2_{n,quant}$ represents the RMS quantization noise power, where the quantization noise is assumed to be uniformly distributed between -1/2LSB and +1/2LSB, and is spectrally white [51].

$$\sigma^2_{n,quant} = \frac{\Delta^2}{12} \quad (53)$$

where Δ is the voltage difference between adjacent ADC levels and is equal to VFS/2N (VFS = full scale voltage, N = number of ADC bits).

Using the above equation, and assuming an input sinusoid signal of peak-to-peak swing equal to the full scale ADC voltage, a signal-to-quantization noise (SQNR) ratio can be found (Johns & Martin, 1997).

$$\boldsymbol{SQNR = \frac{P_{sig}}{\sigma^2_{n,quant}} = \frac{0.5\left(\frac{V_{FS}}{2}\right)^2}{\frac{\Delta^2}{12}} = 1.5 \times 2^{2N} = 6.02N + 1.76\ (dB)} \quad (54)$$

The current data acquisition board uses an 8-bit ADC. According to Expression (54), the maximum SQNR achieved by the system is 49.9 dB. Although the sliding correlator does not deal with a sinusoidal input, its waveform is quite similar to half a sinusoid during the time of the correlation peak. The NI USB-5133 data acquisition card sets the ADC voltage range as [-Vref/2,

+Vref/2]. The energy (area under voltage squared curve) of a triangular peak which rises from zero to Vref/2 during the time at which the peak is occurring can be expressed by,

$$E_{peak} = \frac{1}{2}\left(\frac{V_{ref}}{2}\right)^2 T_{width} \tag{55}$$

where T_{width} is the duration of the triangular peak.

Eq. (9) can be utilized for the case of a finite time triangular peak by assuming an approximately constant quantization noise with time since the quantized waveform changes quickly and has a large swing.

$$SQNR_{triangle} = \frac{E_{peak}}{T_{width}\sigma_{n,quant}^2} = \frac{\frac{1}{2}\left(\frac{V_{ref}}{2}\right)^2 T_{width}}{\frac{\Delta^2}{12} T_{width}} = 1.5 \times 2^{2N} \tag{56}$$

$$= 6.02N + 1.76\ (dB)$$

Eq. (56) predicts an identical SQNR for the sliding correlator situation of a triangular peak.

The noise sources described above and the associated mitigating methods are summarized in Table 3.

Table 3 Noise sources and the corresponding methods of mitigating them.

Noise Source	Method of Mitigating the Noise Source
Thermal noise	Use components with low noise figures
Self-noise (due to distortion terms of sliding correlation)	Increase $\frac{\gamma}{L}$ ratio
Quantization noise	Increase the resolution of the ADC used in data quantization

2.5 Channel Sounding System for 28 GHz Outdoor Propagation Measurements

In the summer of 2012and 2013, outdoor millimeter wave (mmWave) propagation measurements were performed on NYU main campus in downtown Manhattan at 28 GHz and 73 GHz, respectively. The channel sounder used in the 73 GHz measurements will be described in detail below. The channel sounder for the 28 GHz measurements is similar to that for the 73 GHz measurements, and the detailed description to it can be found in [60][61][62].

2.6 Channel Sounding System for 73 GHz Outdoor Propagation Measurements

2.6.1 Transmitter Hardware / Specifications

This section describes the technical specifications of the channel sounder transmitter. Fig. 26 is a block diagram of the transmitter system. The baseband signal is a PN sequence with a chip rate of 400 Megachip-per-second (Mcps). The PN sequence is generated by a custom printed circuit board (PCB) using an 11-bit maximal length code with the shift register tapped at the 9th and 11th flip-flop outputs. The PN signal is generated and upconverted to an intermediate frequency (IF) of 5.625 GHz generated by a QuickSyn signal generator and then passed through a variable attenuator to adjust the transmitted power. The local oscillator (LO) with a frequency of 22.625 GHz, which is generated by doubling the 11.3125 GHz signal, is fed into the upconverter and is further tripled and mixed with the IF inside the upconverter to generate a 73.5 GHz RF signal. A 27 dBi (70 half-power beamwidth in both azimuth and elevation) steerable horn antenna is connected to the output of the upconverter via a waveguide flange. The other components used at the transmitter are shown in Fig. 27 ~ Fig. 33.

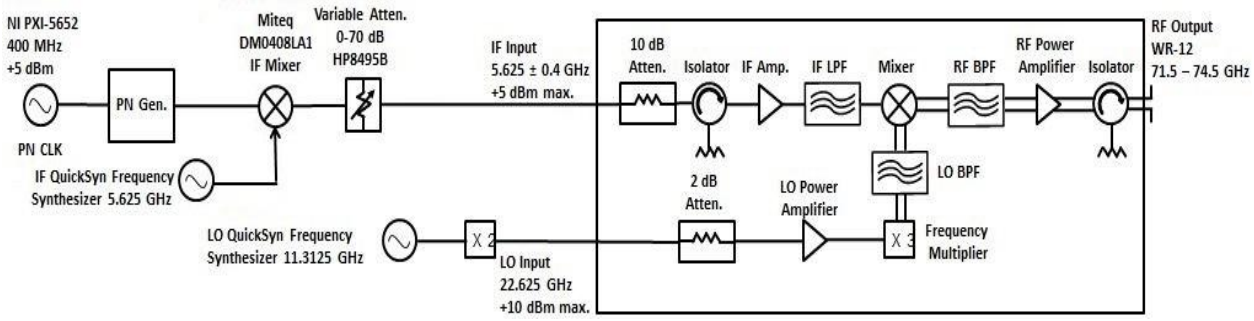

Fig. 26. Block diagram of the transmitter used to characterize the 72 GHz cellular channel in New York City. The TX PN Generator produces a 400-750 Mcps pseudo-random sequence which is upconverted to the 72 GHz RF, modulated by the 5.5 GHz Intermediate Frequency (IF) and multiplied by the tripled 22 GHz Local Oscillator (LO). The HP8495B variable attenuator may be manually changed from 0 to 70 dB in steps of 10 dB in order to adjust the transmit power.

A. ON Semiconductor NBC12439 Chip and Evaluation Board – used as a baseband oscillator to produce a clock signal of 400 MHz at 5 dBm, which drives the PN Code Generator.

Fig. 27. ON Semiconductor NBC12439 Chip and Evaluation Board

- *NI PXI-5652 6.6 GHz RF Signal Generator and CW Source* – used as a baseband oscillator to produce a clock signal of 400-750 MHz at +5 dBm, which drives the PN Code Generator.

Fig. 28. NI PXI-5652 6.6 GHz RF Signal Generator and CW Source

- *Marki M10408HA Mixer* – upconverts the baseband PN code to a 5.5 GHz IF. The output of the Marki mixer produces an IF signal modulated with the 400-750 Mcps PN code at a maximum power level of 0 dBm. The output of the mixer connects to the "IF" input on the Samsung RF upconverter. The mixer specifications are as follows:
    - Frequency Range: 4.0 GHz – 8.0 GHz
    - Conversion Loss: 5.5 dB
    - LO to RF Isolation: 35 dB

Fig. 29. Marki M10408HA Mixer

- *HP 8495B Variable Attenuator* – used to calibrate and verify the linearity of the channel sounding system by providing accurate attenuation in steps of 10 dB from 0 to 70 dB through all frequencies of interest.

Fig. 30. HP 8495B Attenuator

- *PN Generator* – 11-bit sequence code that has a length of 2047. The rate of the PN Code is 400-750 Mcps and the output power is -1.5 dBm. The PN Generator can operate up to 800 Mcps with selectable code chip rates.

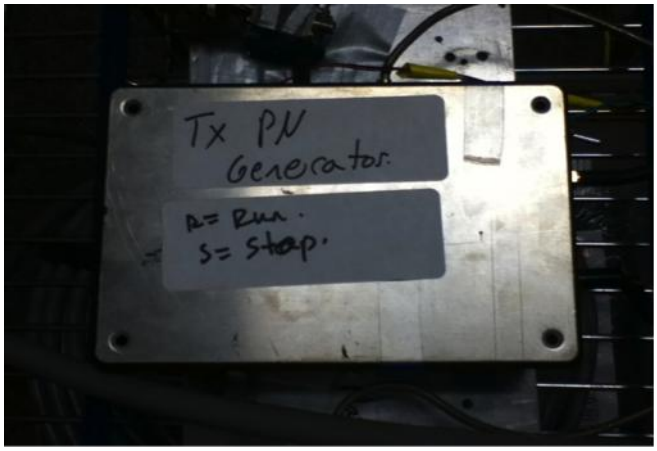

Fig. 31. Transmitter Pseudorandom Noise Generator (PN Gen.).

- *QuickSyn Frequency Synthesizer* – provides a 5.5 GHz signal for the IF LO input of the 72 GHz SpaceK upconverter. This LO drives a Marki mixer which upconverts the baseband Pseudorandom Noise (PN) Code to the IF.

Fig. 32. QuickSyn Frequency Synthesizer (0.5-10 GHz).

- *QuickSyn Frequency Synthesizer with Frequency Doubler* – provides a 22 GHz signal for the RF LO input of the 72 GHz SpaceK upconverter, which is tripled to 66 GHz in the upconverter.

Fig. 33. QuickSyn Frequency Synthesizer (0.5-20 GHz) with Frequency Doubler.

This section describes the specifications of the measurement receiver used in this campaign.

At the 73.5 GHz receiver, an RF downconverter with the aforementioned antenna connected to receive the RF signal. The received signal is downconverted to a 5.625 GHz IF when mixed with a 67.875 GHz (22.625 GHz tripled LO) signal. The received IF signal is attenuated and amplified by a controllable attenuator and a low noise amplifier. After amplification, the IF signal is demodulated to in-phase *I* and quadrature *Q* baseband signal components. A National Instruments (NI) USB-5133 digitizer samples the time-dilated *I* and *Q* signal components and the corresponding received power is recovered using National Instruments LabVIEW software, implemented to square and add the two voltage components $I^2 + Q^2$ to collect a power delay profile (PDP). The correlation is performed by a reference PN sequence at a slightly lower chip rate (399.95 Mcps) to create a slide factor of 8000.

The highly directional horn antennas ensure a large overall system dynamic range of over 170 dB. Cable connection is not required between the TX and RX. The raw correlator output I and Q data are averaged over 20 instantaneous successive PDPs. Multipath channel parameters such as path loss and RMS delay spread can be extracted from the measured data through post-processing.

The block diagram of the receiver is shown in Fig. 34, and Fig. 35 ~ Fig. 44 are pictures of the individual equipment used.

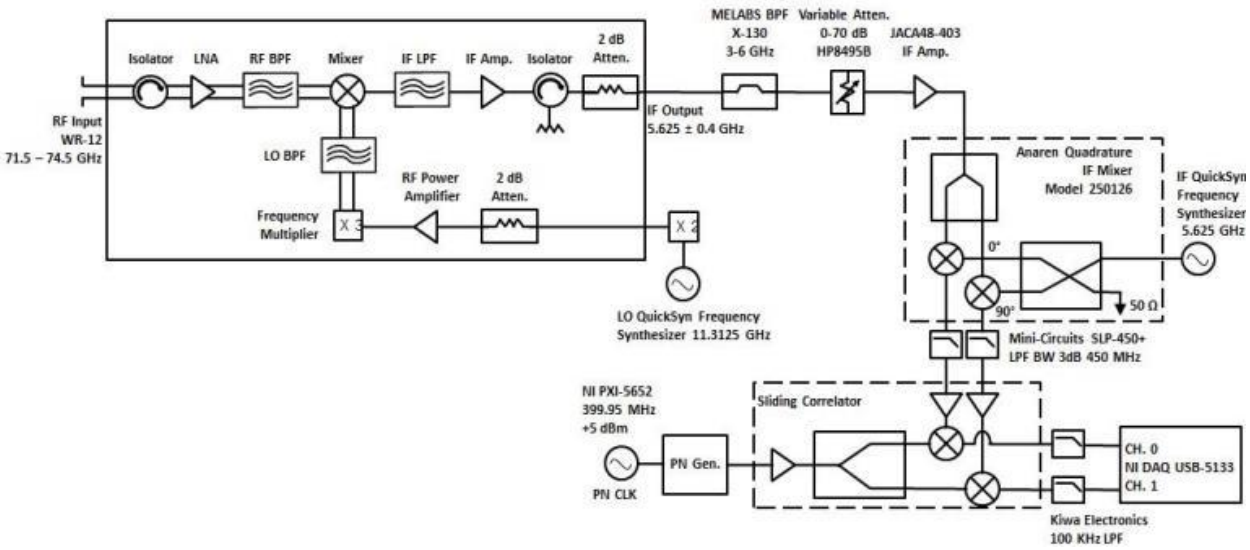

Fig. 34. Block diagram of the receiver used to characterize the 72 GHz cellular channel in New York City. The 750 Mcps baseband signal is downconverted from the 72 GHz RF via the 5.5 GHz Intermediate Frequency (IF). The RX PN Generator produces a 399.95-749.9625 Mcps pseudo-random sequence, and is multiplied with the 400-750 Mcps baseband signal in the sliding correlator, yielding the impulse response of the measured channel. The HP8495B variable attenuator may be manually changed from 0 to 70 dB in steps of 10 dB.

- *NI PXI-5652 6.6 GHz RF Signal Generator and CW Source* – supplies a 5 dBm 749.9625 MHz clock signal to the RX PN Generator. The RX PN Generator operates at a slightly slower frequency than the TX PN Generator (750 Mcps) to allow the sliding correlator operation and to produce Power Delay Profiles (PDPs).

Fig. 35. NI PXI-5652 6.6 GHz RF Signal Generator and CW Source,

- *QuickSyn Frequency Synthesizer* – provides the RX IF LO of 5.5 GHz to the Anaren Quadrature IF Mixer to downconvert the received signal from IF to baseband.

Fig. 36. QuickSyn Frequency Synthesizer (0.5-10 GHz).

- *QuickSyn Frequency Synthesizer with Frequency Doubler* – provides a 22 GHz signal to the RF LO input of the 72 GHz SpaceK downconverter.

Fig. 37. QuickSyn Frequency Synthesizer (0.5-20 GHz) with Frequency Doubler.

- *MELABS X-1300 Band Pass Filter* – is a band pass filter at the IF output of the SpaceK downconverter. The 3 dB bandwidth is 3 GHz – 6 GHz which attenuates any frequencies greater or lower than the IF bandwidth.

Fig. 38. MELABS X-1300 Band Pass Filter.

- *HP 8495B Variable Attenuator* – Variable Attenuator is used to calibrate and verify the linearity of the channel sounding system by providing accurate attenuation in steps of 10 dB from 0 to 70 dB.

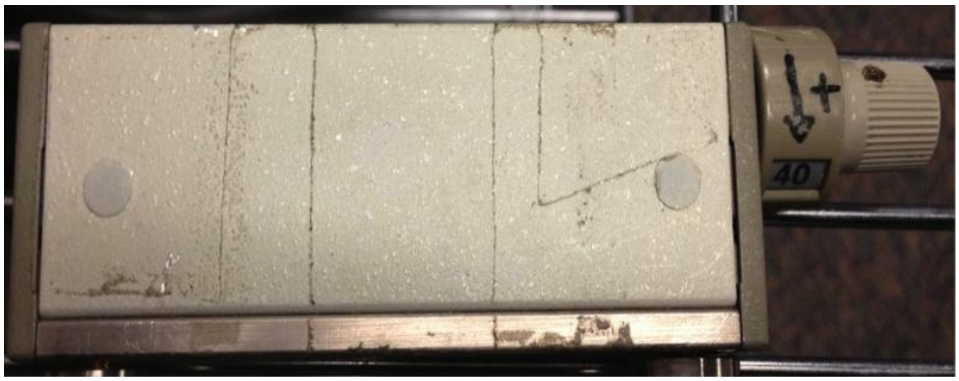

Fig. 39. HP 8495B Attenuator.

- *Anaren Quadrature IF Mixer* – downconverts the received signal from 5.5 GHz IF to baseband. The mixer also separates the signal into its In-phase (I) and Quadrature (Q) components, which are inputted into the correlator. The specifications are as follows.
    - Frequency Range: 4.0 GHz – 8.0 GHz
    - Conversion Loss: 10 dB
    - LO to RF Isolation: 20 dB

Fig. 40. Anaren Quadrature IF Mixer Model 250127

- *Mini-Circuits SLP-450+ Low Pass Filter* – attenuates high frequency components after the received signal is downconverted from IF to baseband.

Fig. 41. Mini-Circuits SLP-450+ Low Pass Filter (LPF).

- *Correlator* – generates a Power Delay Profile (PDP) of the measurement channel by correlating the transmitted TX PN code with the RX PN code. Since the codes operate at slightly different frequencies, the correlator "slides" the two codes and produces a wideband pulse when the codes align, and pseudo noise when the codes are misaligned. This sliding process creates a time-dilation which allows adequate sampling by a low-speed off-the-shelf analog-to-digital converter (ADC). The correlator contains an amplifier, splitter, and mixer to correlate the two 400-750 Mcps PN codes offset by 5 MHz and creates a slide factor of 8,000-20,000.

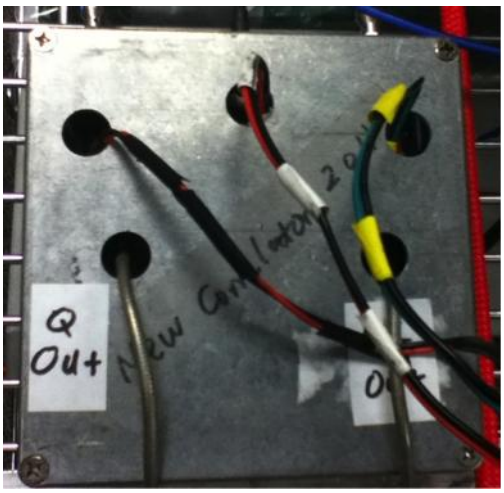

Fig. 42. . Correlator

- *Kiwa Electronics 100 kHz Low Pass Filter* – used at the output of the correlator. The LPFs perform integration for the correlation process and also attenuate any undesirable higher frequencies from the output of the mixer in the correlator.

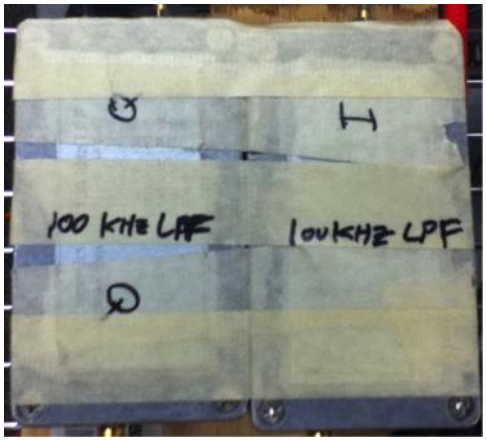

Fig. 43. Kiwa Electronics 100 kHz Low Pass Filter (LPF).

- *National Instruments Data Acquisition USB 5133* – digitizer to sample the PDP and contains two input BNC channels for the correlated I and Q signals. The output is a USB port, which connects to a laptop installed with NI LabVIEW software for control and data logging. The input impedance of the digitizer is 1 MΩ and the maximum sampling rate is 100 MHz.

Fig. 44. National Instruments Data Acquisition USB 5133.

The spread spectrum channel sounder specifications at 28 GHz and 73 GHz are shown in Table 4. Fig. 45 shows the LabVIEW user interface for data acquisition in the channel sounding measurements.

Table 4 Spread spectrum channel sounder specifications at 28 GHz and 73 GHz.

Description	73 GHz Campaign	28 GHz Campaign
Carrier Frequency	73.5 GHz	28 GHz
Sequence	11^{th} order PN Code (Length = 2047)	
Transmitter Chip Rate	400 Mcps	
Receiver Chip Rate	399.95 Mcps	
First null-to-null RF Bandwidth	800 MHz	
Slide Factor	8000	
Multipath Time Resolution	2.5 nanoseconds	
Maximum Measurable Path Loss (5 dB SNR)	181 dB	178 dB
Maximum TX output	14.6 dBm	30 dBm
TX/RX Antenna	27 dBi Horn Antenna	24.5 dBi Horn Antenna
TX/RX Antenna Azimuth and Elevation HPBW	7°	10.9°/8.6°
Antenna Polarization	Vertical Polarization	Vertical Polarization
TX-RX Synchronization	Unsupported	Unsupported

Fig. 45. LabVIEW user interface for data acquisition in the channel sounding measurements.

CHAPTER 3 MEASUREMENT PROCEDURE AND RESULTS AT 28 GHZ AND 73 GHZ

3.1 28 GHz Measurement Procedure

3.1.1 Calibration Procedure

5-meter free space calibrations were performed before and after field measurements each day to provide a day-to-day characterization of the receiver (RX) system. The transmitter (TX) and RX were separated by 5 meters in an open area with no obstructions between them to create a free space line-of-sight (LOS) environment. A variable attenuator was employed in the RX system, which was tuned from 0 dB to 70 dB in 10 dB increments to effectively emulate the increase in path loss induced by the increase in TX-RX distance. At each attenuation setting, one PDP was acquired, and the corresponding trigger level and attenuation value were recorded. In the post-processing, the received powers contained in the PDPs were calculated, plotted as a function of the RX attenuation, and linearly fitted to obtain the linear range of the RX system. A typical calibration plot is shown in Fig. 46, where the blue line is the original plot of RX power versus RX attenuation, the red line is the linear-fitted line, “Pcal” is the theoretical received power using 5 m free space path loss, “Scal” is the slope of the fitted line, and “Int” denotes the intercept with the y-axis of the fitted line. “RxGain”, a key parameter, represents the RX system gain and is the difference between Int and Pcal.

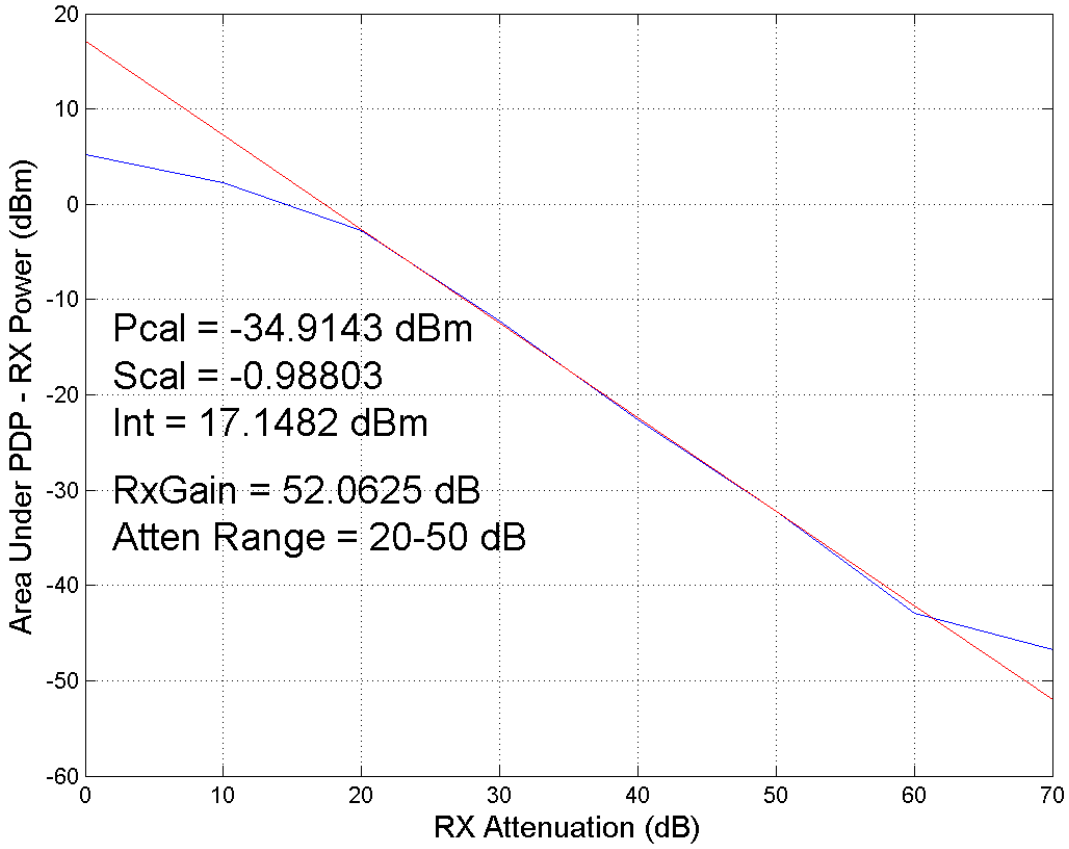

Fig. 46. Example calibration plot obtained in the post-processing for the 28 GHz measurements.

3.1.2 Field Measurement Procedure

The 28 GHz channel propagation measurements were performed at the NYU campus in downtown Manhattan, New York City, using a pair of vertically polarized 24.5 dBi (10.9^0 beamwidth) steerable horn antennas at both the TX and RX. Measurement sites included a wide range of urban environments, including parks, commercial districts, and general university areas with high rise buildings and dense pedestrian and vehicular traffic. To simulate future cellular base stations with relatively low heights, two TX sites were located on the Coles Sports Center building rooftop (7 m above ground level, with the TX located on the northwest and northeast corners of the roof), and one TX site was on the five-story balcony of Kaufman Business School

(17 m above ground level). All three TX sites used the same set of 25 RX sites, which were 1.5m high and were chosen randomly based on the availability of AC power, thus yielding 75 unique TX-RX location combinations.

At each RX measurement location, for measurements 1 through 10, the TX and RX directional antennas were pointed in several different directions in elevation and the RX antenna was rotated exhaustively in the azimuth plane to find the strongest received power. The strongest link was usually made when the TX and RX antennas were directly pointed at each other. The 0^0 azimuth angle of the TX was set at the angle with the strongest link with 10^0 downtilt. Measurements were then taken for three different TX azimuth angles, -5^0, 0^0, and $+5^0$ (with respect to the 0^0 azimuth angle), and for three different RX elevations, -20^0, 0^0, and $+20^0$, with all possible combinations between the two (i.e. 9 total TX-RX antenna configurations). For each of the nine TX-RX antenna configurations, the RX antenna was rotated 360^0 in the azimuth plane and a power delay profile (PDP) measurement was recorded at every 100 where a link was made (Path Loss < 168 dB). In all locations, both the TX and RX used 24.5 dBi vertically polarized horn antennas with 100 3-dB half-power beamwidth (HPBW). The angle combinations used for the Manhattan measurements can be found in Table **5**. Besides the ten measurements described above, additional measurements from measurement 11 to 13 were performed with 15 dBi (30° 3-dB beamwidth) directional horn antennas at both the TX and RX at a few RX locations. The rotation steps for measurements 11 through 13 were 30^0. The angle combinations used for the 15 dBi horn antenna measurements are also given in Table **5**.

Table 5 The different antenna pointing angle combinations used for all outdoor Manhattan measurements at 28 GHz. "Narrow" and "Wide" mean 24.5 dBi horn antenna (with 10.9° beamwidth) and 15 dBi horn antenna (with 28.8° beamwidth), respectively. The Elevation column represents the number of beam widths above or below horizon. The TX Azimuth column represents the number of beam widths left or right from boresight where boresight is the angle with the strongest multipath link found during the initial cursory sweep. Positive beamwidths correspond to a counterclockwise increasing direction about the antenna boresight.

Measurement #	TX Antenna Beam width	TX Elevation (# of Beam Widths)	TX Azimuth (# of BeamWidths from Strongest)	RX Polarization	RX Antenna Beam width	RX Elevation (# of Beam Widths)
1	Narrow	-1	-1/2	Vertical	Narrow	0
2	Narrow	-1	-1/2	Vertical	Narrow	-2
3	Narrow	-1	-1/2	Vertical	Narrow	+2
4	Narrow	-1	0	Vertical	Narrow	0
5	Narrow	-1	0	Vertical	Narrow	-2
6	Narrow	-1	0	Vertical	Narrow	+2
7	Narrow	-1	+1/2	Vertical	Narrow	0
8	Narrow	-1	+1/2	Vertical	Narrow	-2
9	Narrow	-1	+1/2	Vertical	Narrow	+2
10	Narrow	-1	360°	Vertical	Narrow	Strongest
11	Wide	-1/3	0	Vertical	Wide	1/2
12	Wide	-1/3	0	Vertical	Wide	0
13	Wide	-1/3	0	Vertical	Wide	+1/2

In addition to the Manhattan measurements, outdoor propagation measurements were also conducted in downtown Brooklyn around NYU-Poly campus. The measurement procedure differs from that in Manhattan. The Brooklyn TX was located on the rooftop of Rogers Hall (eight-story high, 40 m above ground level) with eight RX locations. For all the Brooklyn measurements, the RX rotated 360° with angular steps of 10° which was the identical procedure to the Manhattan sites. Note that the TX antenna in configurations #7-9 was a wide beam 15 dBi horn antenna with 28.8° (≈ 30°)beamwidth, thus a TX elevation of -1/2 would be -15° below horizon. The angle combinations for the Brooklyn measurements are displayed in Table **6**.

Small-scale linear track measurements were conducted at three of the RX locations (RX1, RX2, and RX3), with a step increment of 5.35 mm (λ/2) along a 107 mm (10λ) length linear track. The experimental setup for the small-scale linear track measurements is sketched in Fig. **47**.

Note that at RX3, small-scale linear track measurements were performed for only 8 out of 12 measurements (antenna pointing configurations) due to time limit. The RX azimuth angle was set to 0° when the RX antenna pointed directly at the TX, for LOS and NLOS conditions. At each λ/2 track position, measurements were recorded at 10° counterclockwise azimuth increments at the RX to perform a 360° sweep with the TX azimuth held constant. Thus, 36 PDP measurements were completed at each λ/2 position for small-scale fading analysis. Small-scale linear track measurements were not conducted in Manhattan.

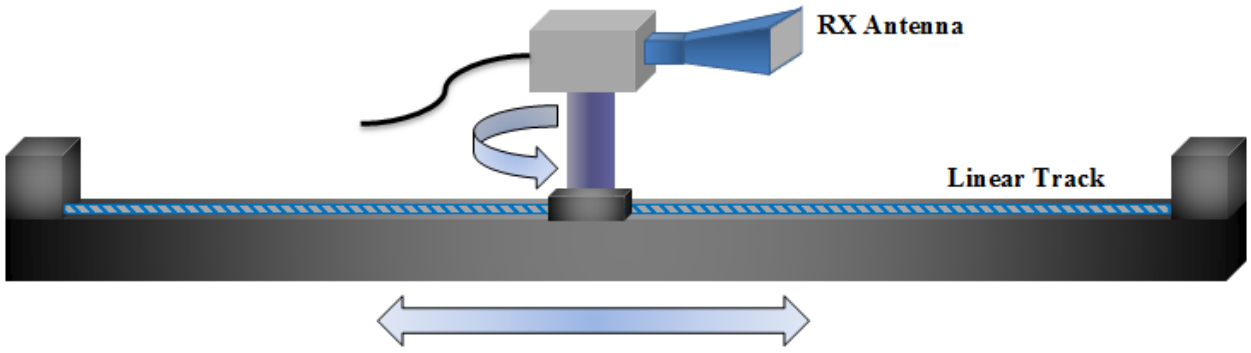

Fig. 47. Schematic diagram of the experimental setup for the small-scale linear track measurements in Brooklyn at 28 GHz.

Table 6 The different antenna pointing angle combinations used for all outdoor Brooklyn measurements at 28 GHz. "Narrow" means 24.5 dBi horn antenna with 10.9° beamwidth and "Wide" means 15 dBi with 28.8° beamwidth. The Elevation column represents the number of beam widths above or below horizon.

Measurement #	TX Polarization	TX Antenna Beam Width	RX Polarization (# of Beam Widths)	RX Antenna Beam width	TX Elevation (# of Beam Widths)	RX Elevation (# of Beam Widths)
1	Vertical	Narrow	Vertical	Narrow	0	0
2	Vertical	Narrow	Vertical	Narrow	0	-1
3	Vertical	Narrow	Vertical	Narrow	0	-2
4	Vertical	Narrow	Vertical	Narrow	0	+1
5	Vertical	Narrow	Vertical	Narrow	0	+2
6	Vertical	Narrow	Vertical	Narrow	0	+3
7	Vertical	Wide	Vertical	Narrow	-1/2	0
8	Vertical	Wide	Vertical	Narrow	-1/2	-1
9	Vertical	Wide	Vertical	Narrow	-1/2	+1

10	Vertical	Narrow	Horizontal	Narrow	0	0
11	Vertical	Narrow	Horizontal	Narrow	-1	0

3.2 73 GHz Measurement Procedure

3.2.1 Calibration Procedure

Before and after each measurement day the transmitter and receiver carts are brought adjacent to each other to perform the calibration. The general calibration procedure involves transmitting the upconverted PN signal from transmitter to receiver at a known transmitted power level.4-meter free space calibrations were performed before and after field measurements each day to provide a day-to-day characterization of the receiver (RX) system. The transmitter (TX) and RX were separated by 4 meters in an open area with no obstructions between them to create a free space LOS environment. A variable attenuator was employed in the RX system to manually vary the signal power through the receiver IF components, which was tuned from 0 dB to 70 dB in 10 dB increments to effectively emulate the increase in path loss induced by the increase in TX-RX distance. A measurement is done at each attenuation level and the area under the PDP is saved to form a plot (in dB). The resulting plot is investigated by the experimenter to determine the linear range of the plot, which matches the linear range of the receiver IF components. The voltage values in the linear range should be noted, so that channel measurements can be taken only when the channel sounder is operating at its linear operating range.

3.2.2 Field Measurement Procedure

The 73 GHz outdoor propagation measurement campaign was conducted in downtown Manhattan around the NYU campus, New York City. Measurements were conducted at five TX

locations and 27 RX locations. Two TX sites were located on the Coles Sports Center building rooftop (7 m above ground level, with the TX located on the northwest and northeast corners of the roof), another two TX sites were on the 2nd-floor balcony of the Kimmel center of NYU (7 m above ground level, with the TX situated on the northwest and southeast corners of the balcony), and one TX site was on the five-story balcony of Kaufman Business School (17 m above ground level). For each TX location, a number of RX locations which were separated from the TX within 200 meters were chosen, yielding a total of 39 unique TX-RX location combinations. Two types of measurements were carried out at almost all the RX locations: 1) base station-to-mobile scenario where the RX height is 2 m, and 2) backhaul-to-backhaul scenario where the RX height is 4.06 m. A mast was employed to adjust the height of the receiver antenna. Fig. **48** ~ Fig. **50** show the five TX locations and the corresponding RX locations. For each TX-RX location combination and scenario, the TX and RX antennas were mechanically steered in both the azimuth and elevation planes to exhaustively search for the strongest receive power angle combinations. For the strongest receive power angle combination identified, the RX antenna was swept in 10° increments in the azimuth plane with the TX antenna fixed in both the azimuth and elevation plane. At each increment in the azimuth plane a PDP was recorded at the RX where a signal could be acquired. Then the RX elevation was fixed to +/- one beamwidth in the elevation plane for two RX sweeps and the TX elevation was fixed to +/- one beamwidth in the elevation plane for two RX sweeps, resulted in five RX sweeps. Afterwards, TX sweeps were conducted with the RX antenna fixed in the two strongest azimuth and elevation angle combinations determined during the first five RX sweeps. Following the two TX sweeps, another main angle of departure at the TX was selected to perform five more similar RX sweeps, resulting in 12 possible measurement sweeps per TX-RX scenario combination.

Measurements were conducted in both line-of-sight (LOS) and non-line-of-sight (NLOS) environments. In the LOS environment, there was a clear optical path between the TX and RX, but the TX and RX antennas were not always on boresight (i.e. directly pointing at each other). Fig. **51** shows the TX and RX equipment setup in the field measurements. A pneumatic mast was employed to adjust the RX antenna height.

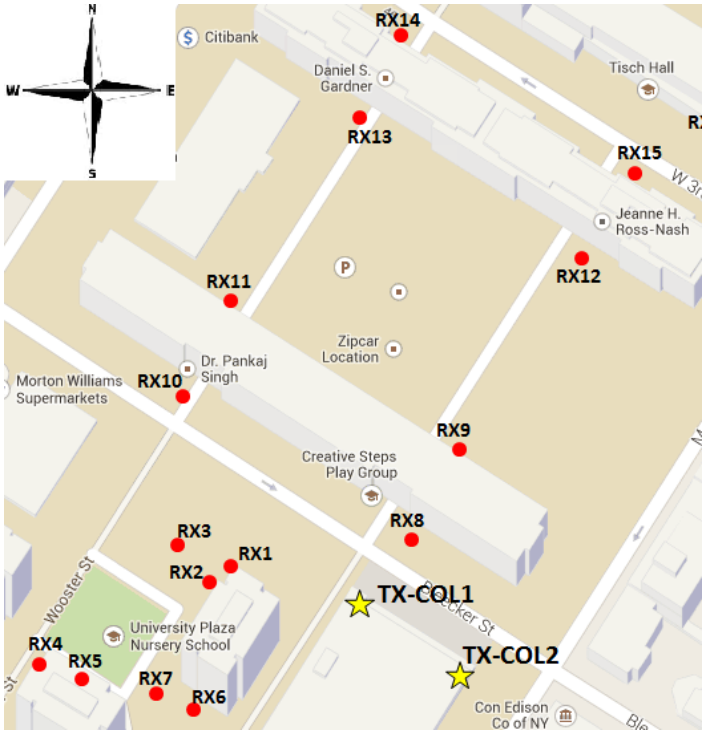

Fig. 48. 73 GHz propagation measurement locations around Coles Sport Center of NYU in Manhattan. The two yellow stars denote the TX locations of the roof of Coles Sport Center, and the red dots represent the RX locations.

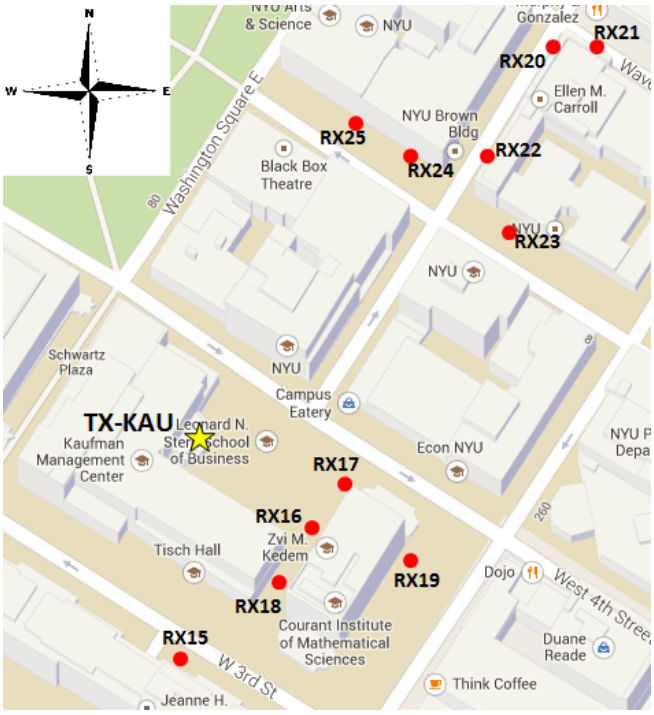

Fig. 49. 73 GHz propagation measurement locations around Kaufman Building of NYU in Manhattan. The two yellow stars denote the TX locations of the roof of Coles Sport Center, and the red dots represent the RX locations.

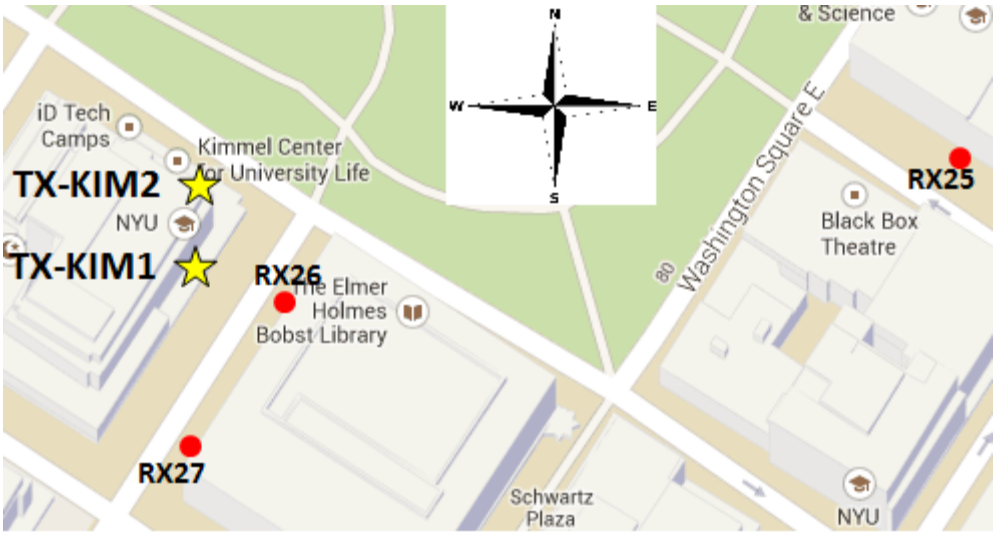

Fig. 50. 73 GHz propagation measurement locations around Kimmel Center of NYU in Manhattan. The two yellow stars denote the TX locations of the roof of Coles Sport Center, and the red dots represent the RX locations.

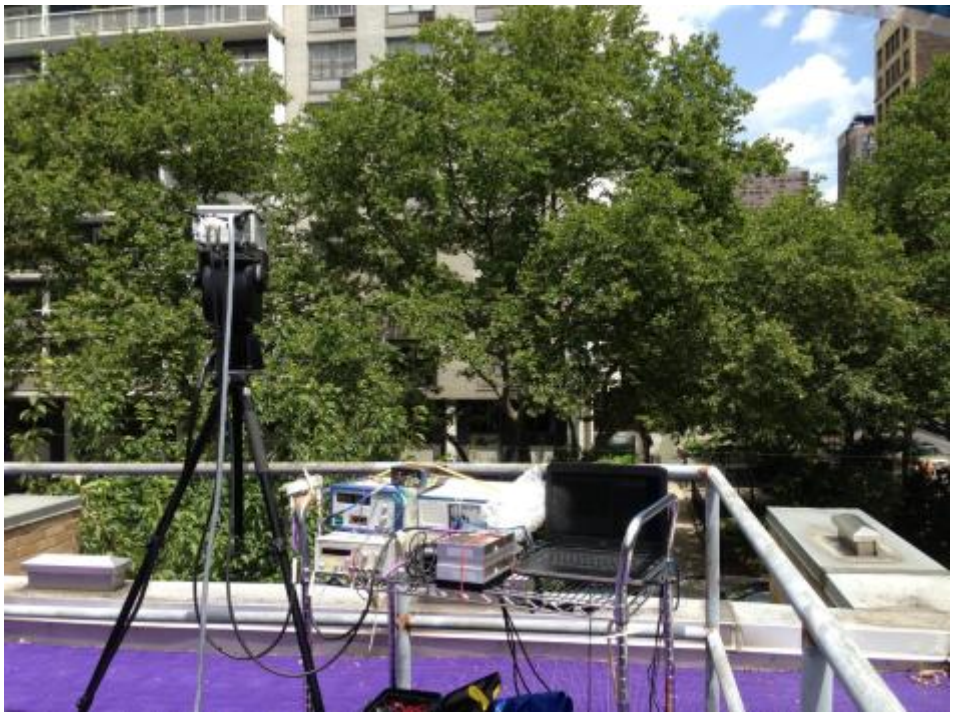

(a)

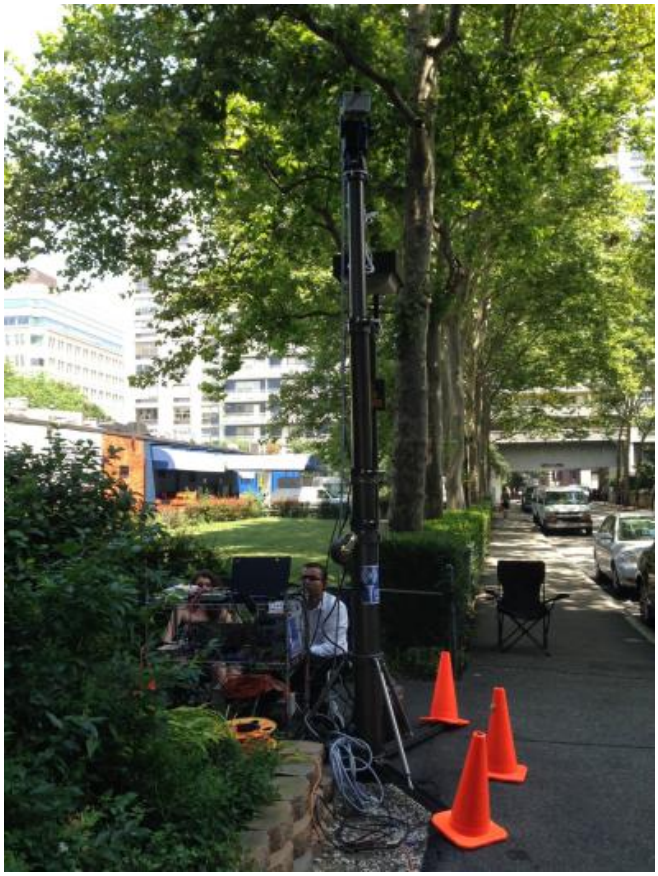

(b)

Fig. 51. (a) Transmitter and (b) receiver setup in the 73 GHz outdoor measurements in New York City.

3.2.3 Filing Naming and Organization

The filing naming convention and directory hierarchy for 73 GHz measurement data are similar to those for 28 GHz in general with some distinctions. The highest level of the hierarchy directory denotes the macro measurement area, i.e. Manhattan. The second level of the hierarchy indicates the measurement scenario. Two scenarios were deployed in the 73 GHz measurement campaign: mobile and backhaul, based on the receiver antenna height. One level down in the hierarchy is directories for the TX locations. In this project, five TX locations were chosen: COL1, COL2 (on the northwest and northeast corners of the roof of the Coles Sports Center building, respectively, 7 m above ground level), KAU (on the five-story balcony of Kaufman Business School, 17 m above ground level), and KIM1 and KIM2 (on the northwest and southeast corners of the 2^{nd}-floor balcony of the Kimmel center of NYU respectively, 7 m above ground level). The next level in the hierarchy exhibits RX locations. These are numbered, rather than named, since their positions are not as unique as the TX locations. Inside each RX location directory lays the individual measurement directories. The measurement numbers refer to the order at which measurements were taken. This is done for record keeping reasons. Following the measurement folders in the hierarchy is the track position, where "Track 1" represents RX antenna azimuth sweeps and "Track 2" stands for TX antenna azimuth sweeps. The rotation (Rot) number folders are at the lowest level of the hierarchy. Positive rotation numbers imply counterclockwise azimuth rotations from the RX azimuth angle offset (which can be obtained from the manual log sheets), and negative rotation numbers means clockwise azimuth rotations from the RX azimuth angle offset. For example, if the RX azimuth angle offset for a measurement is 122^0E, the rotation number is 9 and the rotation step is 10^0, then the actual

azimuth angle is 122^0E - 9×10^0 = 32^0E. Each of the rotation folders contains the raw ASCII text file data as well as the electronic log text file containing important measurement information. The hierarchy directory is illustrated in Fig. 52. The TX-RX separations are not accurate in the electronic log sheets, Tables 7 and 8 list the correct TX-RX separations and the associated propagation environments for mobile and backhaul scenarios respectively.

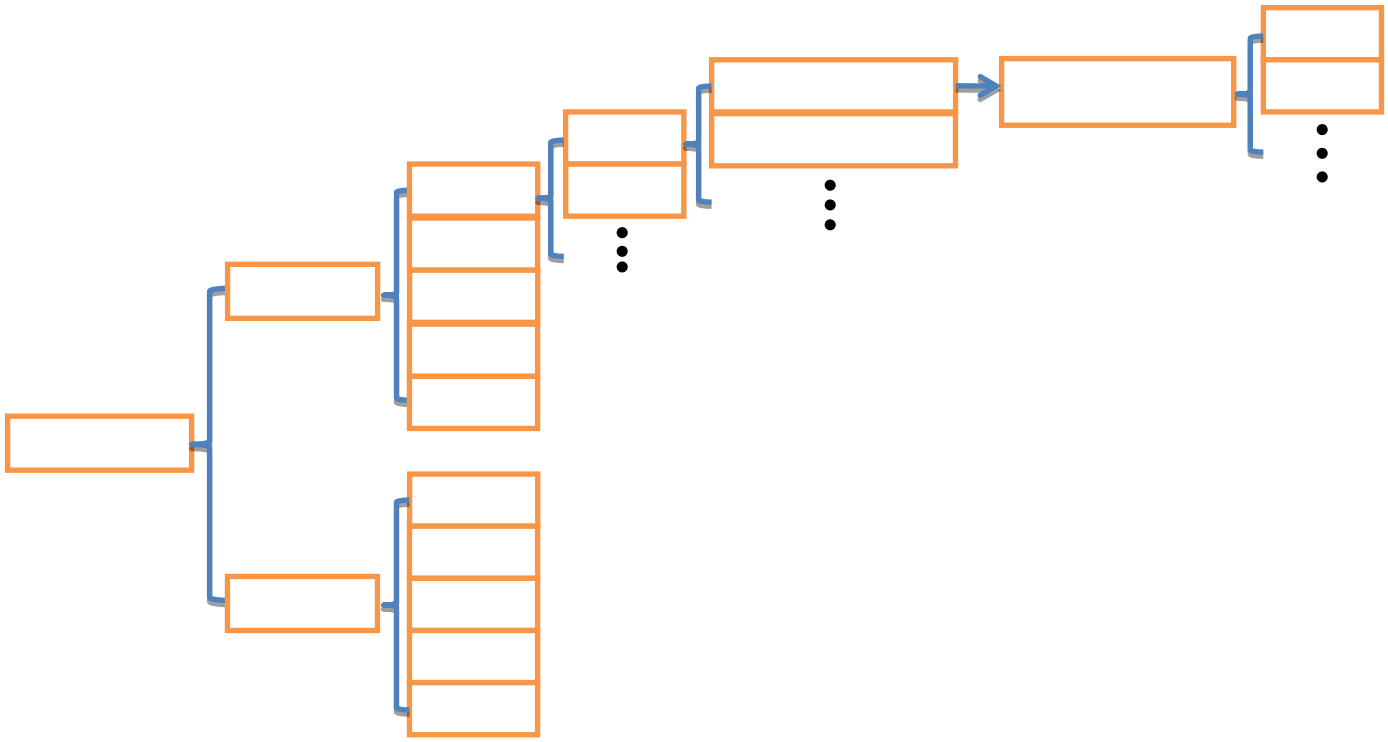

Fig. 52. Directory hierarchy for organizing measurement data at 73 GHz.

Table 7 TX and RX locations and the corresponding TX-RX distances for the mobile scenario.

TX ID	RX ID	TX-RX Separation (m)	Propagation Environment
COL1	RX1	48	LOS-Foliage
COL1	RX2	53	NLOS
COL1	RX3	64	LOS-Foliage

COL1	RX4	104	NLOS
COL1	RX5	95	NLOS
COL1	RX6	71	NLOS
COL1	RX7	76	NLOS
COL1	RX8	30	LOS
COL2	RX2	91	NLOS
COL2	RX3	106	NLOS
COL2	RX4	139	NLOS
COL2	RX5	128	NLOS
COL2	RX6	99	NLOS
COL2	RX8	50	LOS
KAU	RX15	80	NLOS
KAU	RX16	53	LOS
KAU	RX17	49	LOS
KAU	RX18	59	NLOS
KAU	RX19	79	NLOS
KAU	RX20	167	NLOS
KAU	RX21	180	NLOS
KAU	RX22	129	NLOS
KAU	RX23	127	NLOS
KAU	RX24	118	NLOS
KAU	RX25	116	NLOS
KIM1	RX25	190	NLOS

KIM1	RX26	50	NLOS
KIM1	RX27	74	NLOS
KIM2	RX25	182	NLOS
KIM2	RX27	40	LOS

Table 8 TX and RX locations and the corresponding TX-RX distances for the backhaul scenario.

TX ID	RX ID	TX-RX Separation (m)	Propagation Environment
COL1	RX9	58	NLOS
COL1	RX10	95	LOS-Foliage
COL1	RX11	109	NLOS
COL1	RX12	140	NLOS
COL2	RX1	88	NLOS
COL2	RX2	91	NLOS
COL2	RX3	106	NLOS
COL2	RX4	139	NLOS
COL2	RX5	128	NLOS
COL2	RX6	99	NLOS
COL2	RX7	107	NLOS
COL2	RX9	70	NLOS
COL2	RX10	137	LOS-Foliage
COL2	RX11	148	NLOS
COL2	RX12	140	NLOS
KAU	RX15	80	NLOS
KAU	RX16	53	LOS

KAU	RX17	49	LOS
KAU	RX18	59	NLOS
KAU	RX19	79	NLOS
KAU	RX20	167	NLOS
KAU	RX21	180	NLOS
KAU	RX22	129	NLOS
KAU	RX23	127	NLOS
KAU	RX24	118	NLOS
KAU	RX25	116	NLOS
KIM1	RX25	190	NLOS
KIM1	RX26	50	NLOS
KIM1	RX27	74	NLOS
KIM2	RX25	182	NLOS
KIM2	RX26	27	LOS
KIM2	RX27	40	LOS

The same as 28 GHz measurement data, inside some of the RX location directories, there is one or two folders named “Folder Number ##”, which contain the free space calibration files, and a folder called “Calibration Data FS (free space)” is included one level down. Following are the attenuation directories, which are labeled by the attenuation values from 0 dB to 70 dB in steps of 10 dB. Every attenuation folder involves the raw ASCII text file data as well as the electronic log text file containing key calibration information.

3.2.4 Manual Log Sheets

In addition to the electronic log sheets contained in the raw data folders, there is another type of log sheets recorded by measurement conductors during each measurement (manual log sheets), which is crucial in understanding and processing the raw data.

Both calibration and field measurement information is recorded in each manual log sheet. Key information such as TX ID, RX ID, TX-RX distance and RX attenuation settings is included in the calibration log sheets. What's worth special attention is the field measurement log sheets, in which measurement number, track number, TX ID and initial angle offsets, RX ID and initial angle offsets, rotation steps as well as rotation numbers are minuted. As mentioned in the measurement procedure section, before the first measurement for each TX-RX location combination and scenario, the TX and RX antennas were mechanically steered in both the azimuth and elevation planes to exhaustively search for the strongest receive power angle combinations, through which the best antenna pointing angle at both TX and RX was determined and logged down as the initial azimuth and elevation angle offsets. Then the actual angle in each rotation step can be calculated using the angle offset, rotation number and rotation increment, as exemplified in the preceding section. Notice that there is an item called "Zero Position of Gimbal", this was aimed to track the RX azimuth angle offset in the first measurement for the convenience of the measurement conductors and need not be considered in data processing.

3.3 Outdoor Cellular Propagation Measurements Results at 28 GHz

3.3.1 Power Delay Profile (PDP)

A typical measured power delay profile (PDP) at a particular pointing angle in a non-line-of-sight (NLOS) environment using 24.5 dBi 10.9◦half-power beamwidth (HPBW) antennas at both the TX and RX is illustrated in Fig. **53.** A total of 9 distinguishable multipath components are seen with an RMS delay spread of 12.3 ns. Different pointing angles yielded different PDPs at all locations. The rich multipath provides great opportunity to implement beam combining and beamforming in dense urban environments.

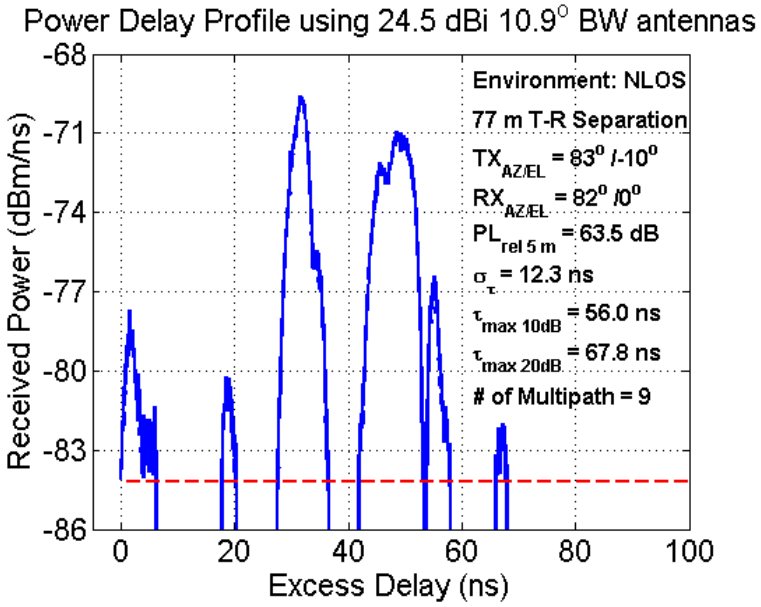

Fig. 53. Measured 28 GHz power delay profile (PDP) in a NLOS urban environment in New York City. PDPs were measured over a wide range of pointing angles at many locations. The red dashed line depicts the noise threshold for this PDP.

3.3.2 Multipath Components

Our measurements used two antenna cases: (1) Narrowbeam antenna case: the 24.5 dBi narrow (10.9^0 HPBW) beamwidth horn antennas were used at both the TX and RX, and, (2)

Wide-beam antenna case: a 15 dBi wide (28.8^0 HPBW) beamwidth horn antenna was employed at either the TX or the RX with the other transceiver side using the narrow (10.9^0) beamwidth horn antenna. Fig. **54** displays the average number of resolvable multipath components measured in a PDP at all azimuth and elevation angles considered at each T-R separation distance. As can be observed, the average number of resolvable multipath components first ascends with increasing the distance, then generally descends as the distance further increases. This trend is likely due to the fact that the transmitted signal is more scattered and reflected as the T-R distance increases, but after the signal reaches a certain distance, the power contained in some paths is too weak to be detected, thus reducing the number of distinct multipath components at the RX. For both narrow-beam antenna and wide-beam antenna cases, an ensemble average of 4.6 distinguishable multipath components was found over all measured PDPs at all azimuth and elevation pointing angles.

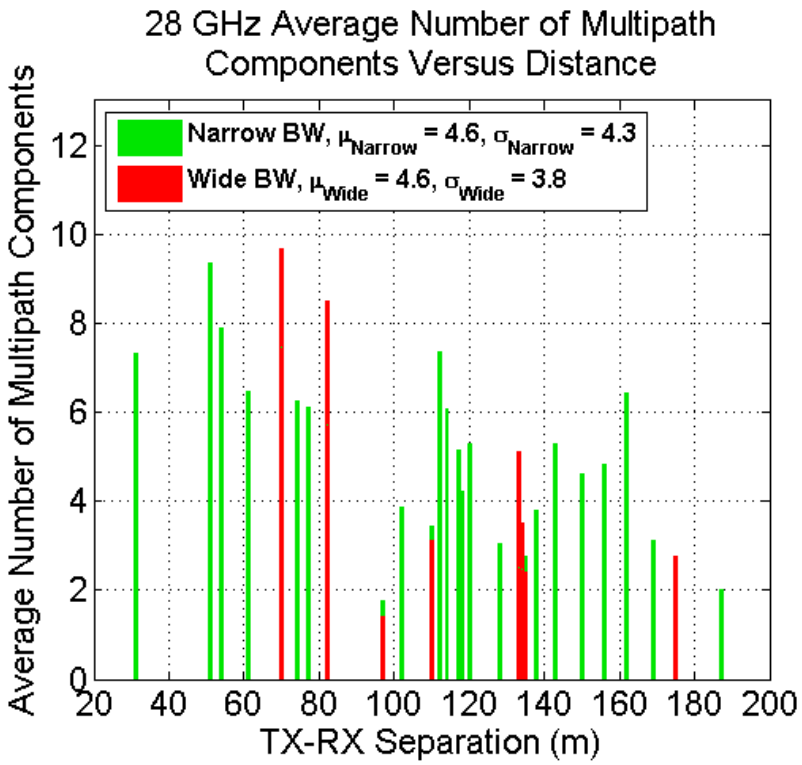

Fig. 54. Average number of resolvable multipath components (where a link was made) for arbitrary pointing angles versus T-R separation in NLOS environments for the narrow beamwidth and wide beamwidth antennas at 28 GHz in New York City (Manhattan and Brooklyn). The statistics of multipath components are measured at all pointing angles using 360◦azimuthal sweeps at various elevation angles over all locations, and by using only PDPs where signals were detected [64].

3.3.3 RMS Delay Spread

The relationship between RMS delay spread and T-R separation, and the CDF of RMS delay spread are shown in **Fig. 55**. The average and maximum values of RMS delay spread using narrow-beam antennas are 17.1 ns and 751.3 ns, respectively, where the largest propagation excess delay is around 1.77 us for a particular TX-RX pointing angle combination, whereas the RMS delay spread values decreased to 16.2 ns and 566.0 ns respectively for the wide-beam antenna.

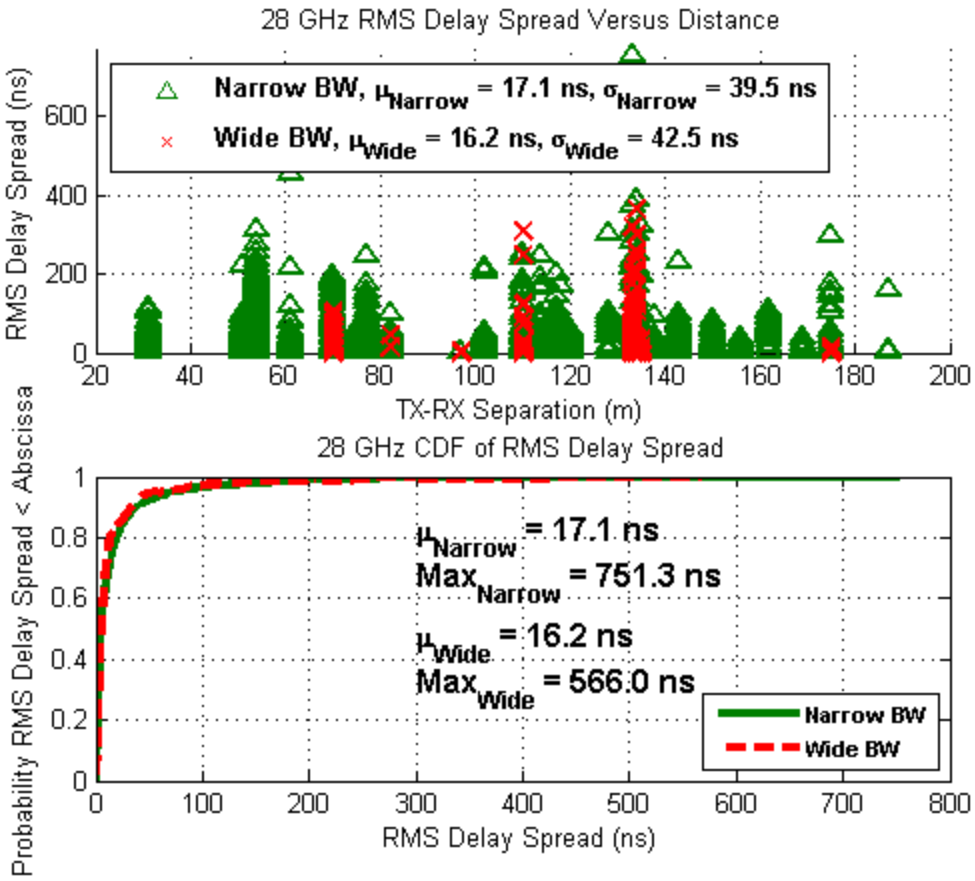

Fig. 55. 28 GHz RMS delay spread versus T-R separation (upper) and CDF of RMS delay spread (lower) using 24.5 dBi 10.9◦beamwidth and 15 dBi 28.8◦beamwidth receiver antennas [64].

3.3.4 Angle of Arrival (AOA) and Angle of Departure (AOD)

AOA and AOD statistics are crucial to implementing beamforming techniques. The distributions of AOA and AOD along with the associated received power level for one TX location are shown in Fig. **56**, where the angles on the axes are relative to a true north bearing with positive values representing clockwise rotating angles and negative for counterclockwise. AODs are concentrated between -80^0 and -10^0 with AOAs distributed uniformly from -180^0 to 180^0 over this AOD range. Strongest signals are received when the TX antenna points in a narrow span of $-20^0 \sim -10^0$. This figure indicates that beamforming at the TX should focus in a

narrow sector of space. This was also shown in [65].

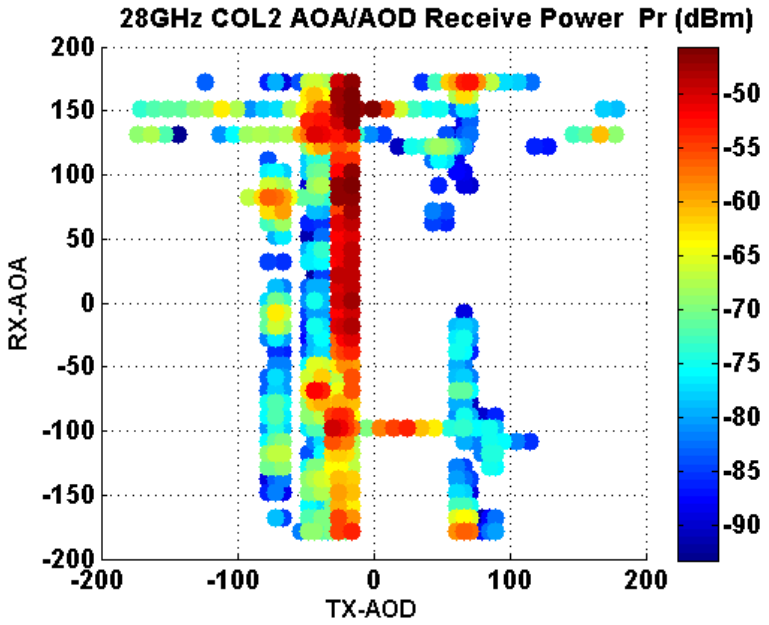

Fig. 56. Distributions of AOA/AOD and received power for the transmitter at COL2 at 28 GHz. Each dot in the graph stands for a TX-RX link and the color of each dot indicates the corresponding received power with red representing high power [64].

The measured received power distribution with the varying RX antenna elevation angles and TX-RX separation distances for the 7 m-high TX antenna height and 1.5 m-high RX antenna is shown in Fig. 57, where the colored points represent the strongest received power at a particular distance-angle combination, the values under the colorbar denote the received power level in dBm, and the white solid curve and the yellow solid curve represent the theoretical projected elevation angles and the ground bouncing angles at the RX, respectively. As can be observed, the measured received power generally decreases as the TX-RX separation distance increases for $\pm\mathbf{20^0}$ RX antenna elevation angles, which can be explained intuitively by the increasing path loss with propagation distance. While for the 0^0 RX elevation angle, strong power can still be received at some large TX-RX separation distances, which may be explained by scattering effects around the receivers. Since the measurements were conducted only at three different RX

elevation angles for 7 m-high TX and four different RX elevation angles for 17 m-high TX, and did not search for the best antenna pointing angles at all locations, the data is not sufficient to provide an accurate statistical result. Similar phenomena are observed for the 17 m-high TX antenna, as shown in Fig. 58.

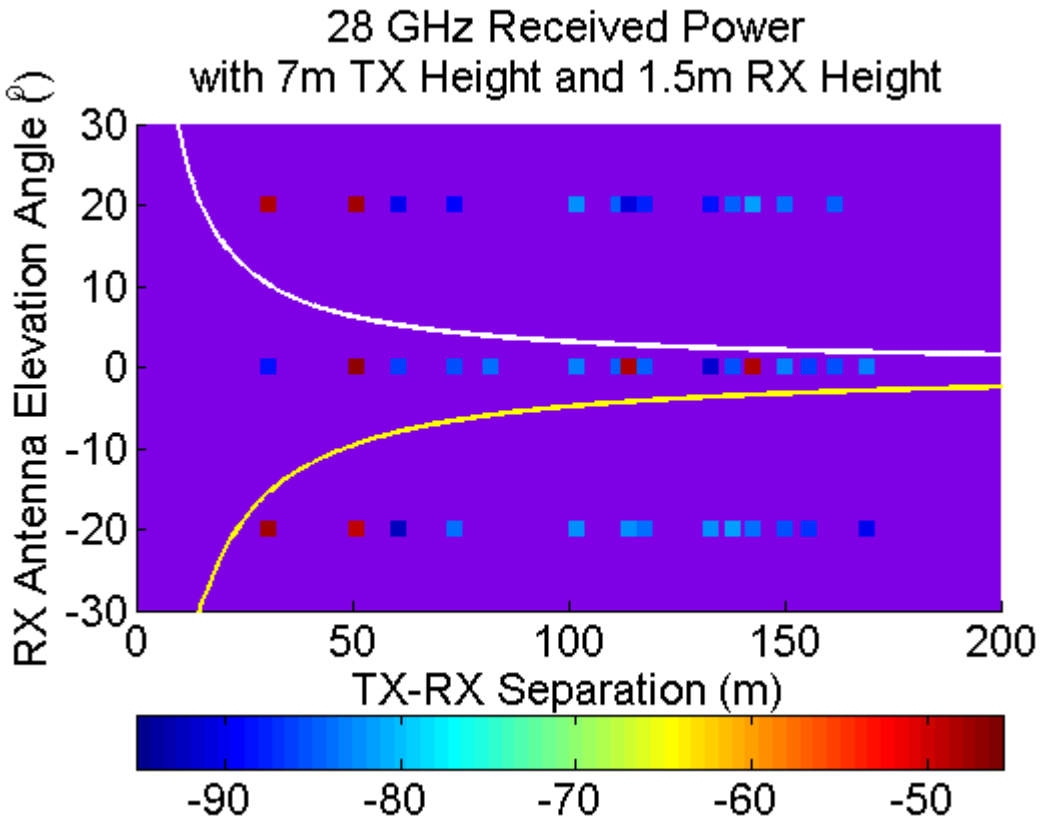

Fig. 57. Received power distribution as a function of RX antenna elevation angle and TX-RX separation distance for 7 m-high TX antenna and 1.5 m-high RX antenna at 28 GHz. The values under the colorbar denote the received power level in dBm. The white solid curve and the yellow solid curve represent the theoretical projected elevation angles and the ground bouncing angles at the RX, respectively.

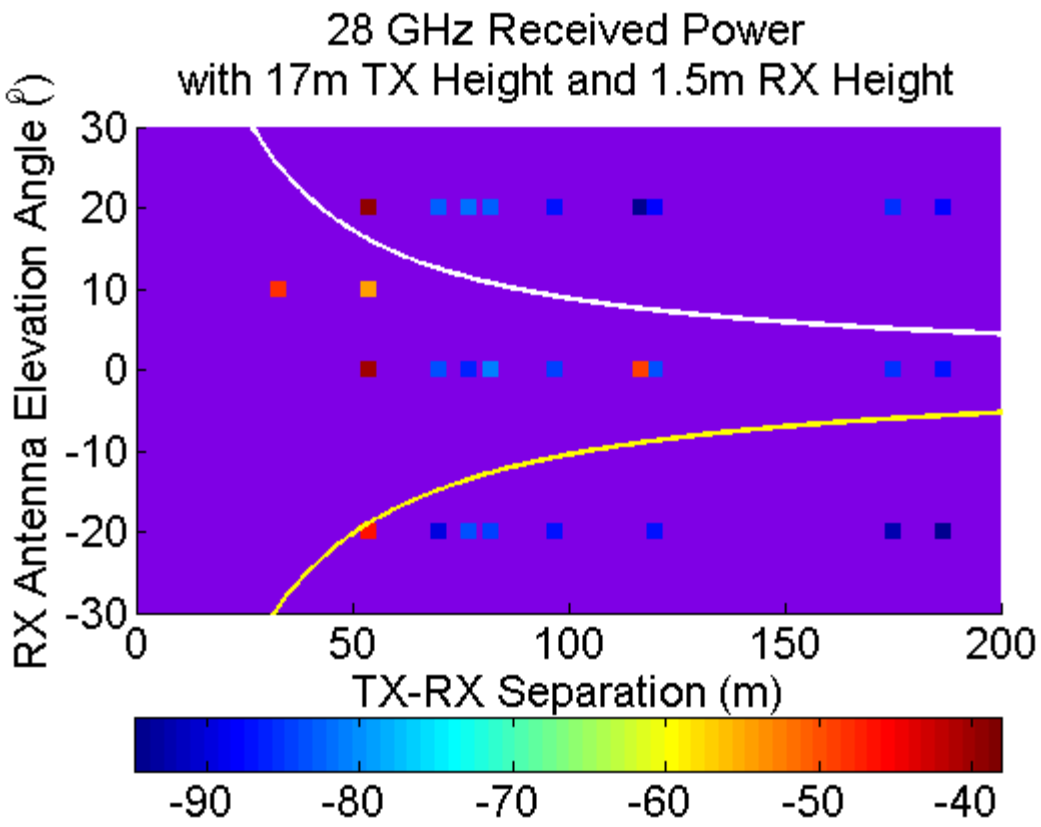

Fig. 58. Received power distribution as a function of RX antenna elevation angle and TX-RX separation distance for 17 m-high TX antenna and 1.5 m-high RX antenna at 28 GHz. The values under the colorbar denote the received power level in dBm. The white solid curve and the yellow solid curve represent the theoretical projected elevation angles and the ground bouncing angles at the RX, respectively.

3.3.5 Large-scale Path Loss

The path loss exponent (PLE) is a parameter commonly used to describe the attenuation of a signal as it propagates in the channel. Path loss at a close-in reference distance d_0 is calculated as the free space path loss by Eq. (57)

$$PL(d_0) = 20log_{10}\left(\frac{4\pi d_0}{\lambda}\right) \tag{57}$$

where λ is the wavelength of the carrier frequency, which equals 10.71 mm at 28 GHz and 4.1 mm at 73.5 GHz. In our measurements, d_0 = 4 m. Path loss at a TX-RX separation d, beyond d_0, is given by the following equation [55]:

$$PL(d) = PL(d_0) + 10nlog_{10}\left(\frac{d}{d_0}\right) + X_\sigma \quad (58)$$

where $\mathrm{PL(d)}$ is the path loss in dB for a TX-RX separation of *d*, n is the path loss exponent, and X_σ, also called shadowing factor (SF), represents a log-normal random variable in dB with a standard deviation of σ dB.

Fig. **59** is a scatter plot of path loss versus T-R distance in NLOS environments. Path loss at a T-R separation d in meters, beyond a close-in free space reference distance d0, is given by Eq. (1), where PL(d) is the path loss in dB for a T-R separation of d in meters, PL(d0) is the free space path loss in dB at d0, n is the path loss exponent (PLE), and χσ is a Gaussian random variable with a mean of 0 dB and standard deviation of σ in dB, also known as the shadow factor. The PLEs for the 15 dBi antenna are lower than the 24.5 dBi antenna, because the wide-beam antenna captures more multipath energy, despite having a smaller gain, yet is unable to cover greater distances. By selecting the best TX- RX pointing angle combinations at any location, the PLEs are significantly reduced.

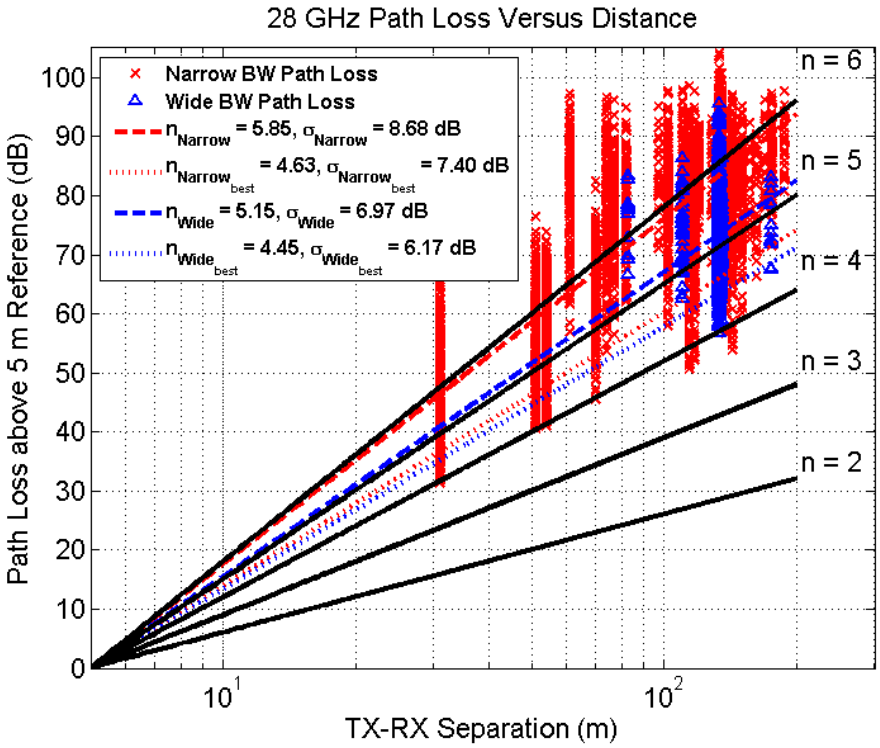

Fig. 59. 28 GHz scatter plot of path loss as a function of T-R separation using 10.9◦beamwidth TX antenna, and 10.9◦beamwidth and 28.8◦beamwidth antennas [64].

3.3.6 Outage Analysis

An outage study was conducted in Manhattan, New York, to find the locations and distances where energy could not be detected Fig. **59**. As seen in Fig. 7, the map is sectioned into sectors corresponding to TX locations. Signal acquired by the RX for all cases was within 200 meters. While all RX locations within the range of 200 meters from the TX detected a signal, in some instances, signal-to-noise ratio (SNR) was not high enough for a signal to be acquired by the hardware. Of the measurements taken in Manhattan, it was found that 14% of locations were outages due to the obstructive nature of the channel within 200 m from the TX [66].

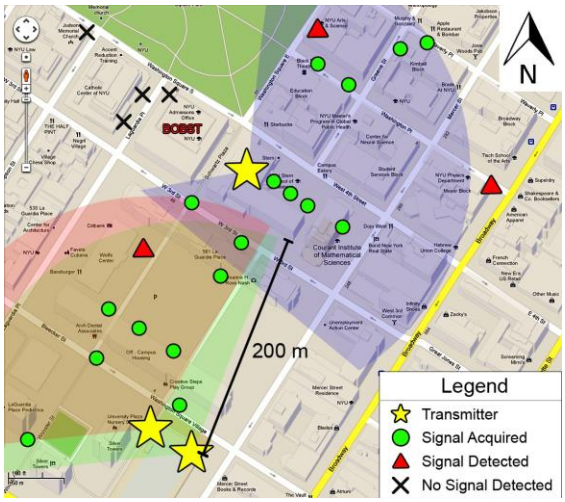

Fig. 60. Map showing all Manhattan coverage cells with radii of 200 m and their different sectors. Measurements were recorded for each of the 25 RX sites from each of the three TX sites (yellow stars). Signal Acquired means that signal was detected and acquired. Signal Detected means that signal was detected, but low SNR prevented data acquisition by the system [62].

The outage probability is greatly affected by the transmitted power, antenna gains as well as the propagation environment. Fig. **61** displays the relationship between the maximum coverage distance of the base station and the combined TX-RX antenna gain. To calculate the maximum coverage distance, we subtracted the 49 dBi combined antenna gain from the total measurable path loss of 178 dB (which was obtained using the two 24.5 dBi antennas), resulting in the dynamic range without the antenna gain. Since our system requires approximately 10 dB SNR for a comfortable detecting level, the actual maximum measureable path loss is 119 dB, and was then used to compute the coverage distances corresponding to various antenna gains were computed. The four blue curves denote the cases for PLEs equal to 3, 4, 5 and 5.76. The red squares Fig. 8 highlight the distance corresponding to the two 15 dBi horn antennas and 24.5 dBi horn antennas at the TX and RX. Obviously, the maximum coverage distance rises with increasing of antenna gains and a decrease of the PLE. For example, the radio waves can propagate about 200 m in a highly obstructed environment with a PLE of 5.76 when the

combined TX-RX antenna gain is 49 dBi, which agrees with the measured value (200 m) very well. This suggests that we can enlarge the coverage region of a base station by increasing antenna gains, and may use less antenna gain (or TX power) when in LOS conditions.

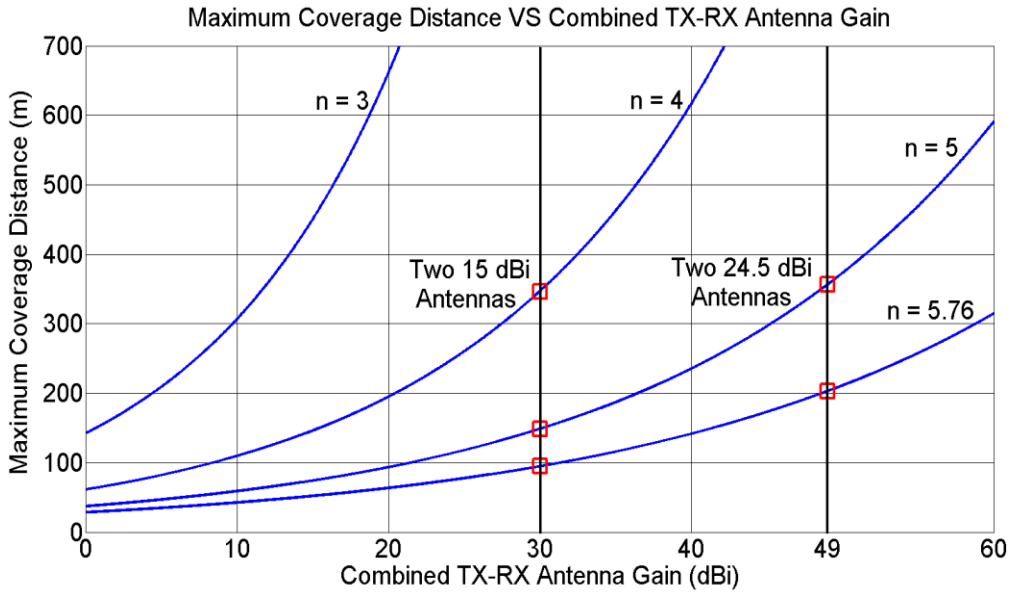

Fig. 61. Maximum coverage distance at 28 GHz for 800 MHz null-to-null RF bandwidth (400 Mcps) with 178 dB maximum path loss dynamic range and 10 dB SNR [62].

3.4 Outdoor Cellular Propagation Measurements Results at 73 GHz

3.4.1 Power Delay Profile

A typical PDP in a NLOS environment in the 73 GHz outdoor measurements is shown in Fig. 62. The heights of the TX and RX are 7 m and 2 m respectively with a TX-RX distance of 95 m. The path loss is 72.9 dB with an RMS delay spread of 20.3 ns, and the maximum excess delay (20 dB down with respect to the highest peak) is 91.3 ns.

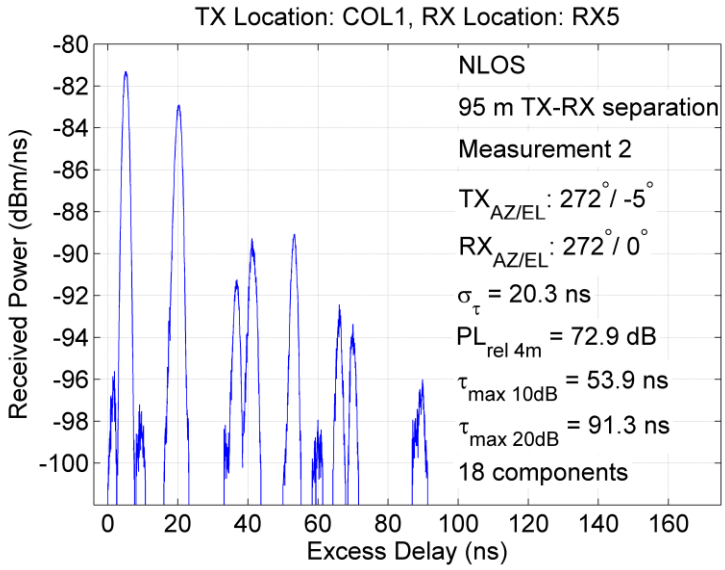

Fig. 62. PDP recorded in a NLOS environment at 73 GHz for the 7 m-high TX on the roof of Coles Sport Center and the RX located 95 m away from the TX. The path loss relative to 4 m reference, maximum excess delay (10 dB and 20 dB), RMS delay spread (στ), number of distinguishable multipath components, and TX and RX azimuth and elevation angles are shown on the right of the PDP.

3.4.2 AOA and AOD

Fig. 63 shows the measured angle-of-arrival (AoA) power profile at a typical RX location in the 73 GHz measurements, which displays the received power in dBm as a function of azimuth AoAs in a NLOS environment. The 0^0 azimuth pointing angle refers to true north. The rotation step between adjacent PDP measurements was 8^0. As is observed, signals were received at 31 out of 45 RX azimuth angles, implying that the downtown Manhattan area is a multipath-rich environment with numerous reflective objects and that signals come from a myriad of beams which can be combined to enhance the received signal level. Moreover, the received power at different angles vary significantly with strong power contained in two main directions, indicating the necessity of beamforming in order to obtain the desired signal with a high SNR.

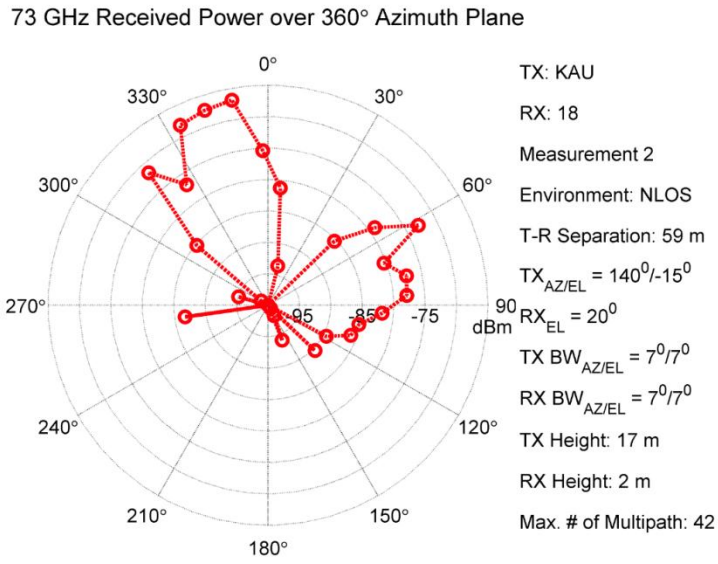

Fig. 63. Polar plot showing the received powers at a NLOS location at 73 GHz with 17 m-high TX, 2 m-high RX and 59 m TX-RX separation. The red dots represent total received powers in dBm at different RX azimuth angles.

The distribution of TX and RX azimuth angles for all mobile-height receivers corresponding to the TX at COL1 is plotted in Fig. **64**. In the figure, 0^o denotes the boresight-to-boresight direction between TX and RX, negative angles imply clockwise rotations with respect to 0^o, while positive angles represent counterclockwise rotations. As indicated by Fig. **64**, the majority of angles of departure (AoDs) concentrate on the right-hand (clockwise) region of the TX, and most AoAs appear in the left-hand (counterclockwise) area of the RXs, the reason for this asymmetry is the location of the TX antenna and surrounding reflectors and scatterers, which is evidenced by Fig. 3. Take RX3 for example, the long building in the middle of the map, which is right to TX-COL1 and left to RX3, serves as a good reflector for transmitted signals, thus considerable links can be made when both TX and RX antennas point at the building. Fig. **65** shows the AODs and AOAs for mobile-height receivers corresponding to the TX at KAU. In contrast to Fig. **64**, AODs are distributed in a narrow angle range, i.e. $-35^o \sim 35^o$, with minor exceptions, while AOAs are nearly uniformly distributed from $-180^o \sim 180^o$. These figures

indicate the site-specific effect on the AOD and AOA distributions.

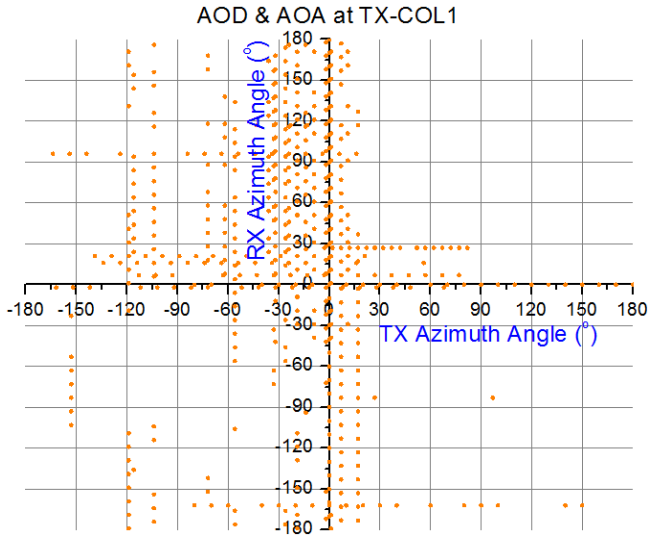

Fig. 64. Scatter plot of TX and RX azimuth angles for the links made at the TX of COL1 in the base station-to-mobile scenario. Each dot corresponds to successfully established link between TX and RX.

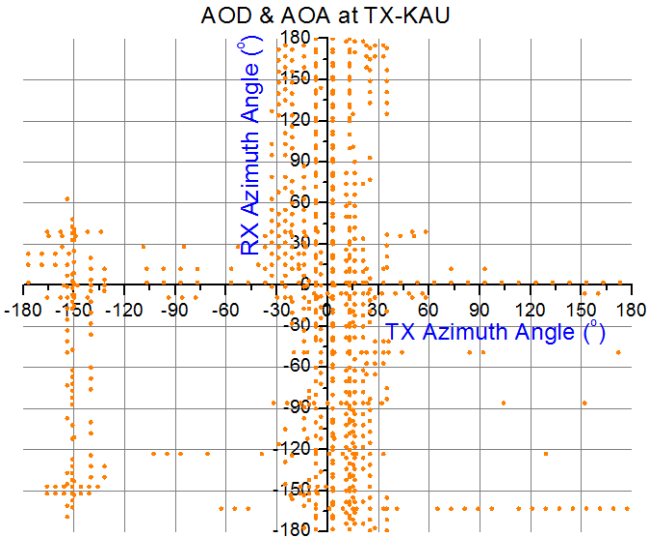

Fig. 65. Scatter plot of TX and RX azimuth angles for the links made at the TX of KAU in the base station-to-mobile scenario. Each dot corresponds to successfully established link between TX and RX.

The measured received power distribution with the varying RX antenna elevation angles and TX-RX separation distances for the 7 m-high TX antenna height and all RX antenna heights (2

m and 4.06 m) are shown in Fig. 66, where the points represent the strongest received power at a particular distance-angle combination, and the values under the colorbar denote the received power level in dBm. As can be observed, the measured received power generally decreases as the TX-RX separation distance increases for various RX antenna elevation angles, which can be explained intuitively by the increasing path loss with propagation distance. Relatively strong power is received when the RX antenna elevation angle ranges from -5^0 to 15^0. Further, the Elevation angles corresponding to strong received powers agree well with the theoretical projected elevation angles (the white solid curve) and ground bouncing angles (the yellow solid curve) for 7 m-high TX locations. Since ground bouncing elevation angles were not investigated for the 17 m-high TX, there are no measured data associated with the yellow curve, but it can be predicted that the data will fit the curve very well, as in the 7 m-high TX case, if measurements were conducted at ground reflection angles.

Comparing Fig. 66 and Fig. 67, it is obvious that for the same TX-RX separation distance, the RX antenna elevation angles need to be larger in order to receive strong power, which is the natural consequence of the elevated TX antenna height.

The power distribution for the 2 m-high RX antenna and 4.06 m-high RX antenna are displayed in Fig. 68 and Fig. 69, respectively, which exhibit similar trends as Fig. 66 and Fig. 67.

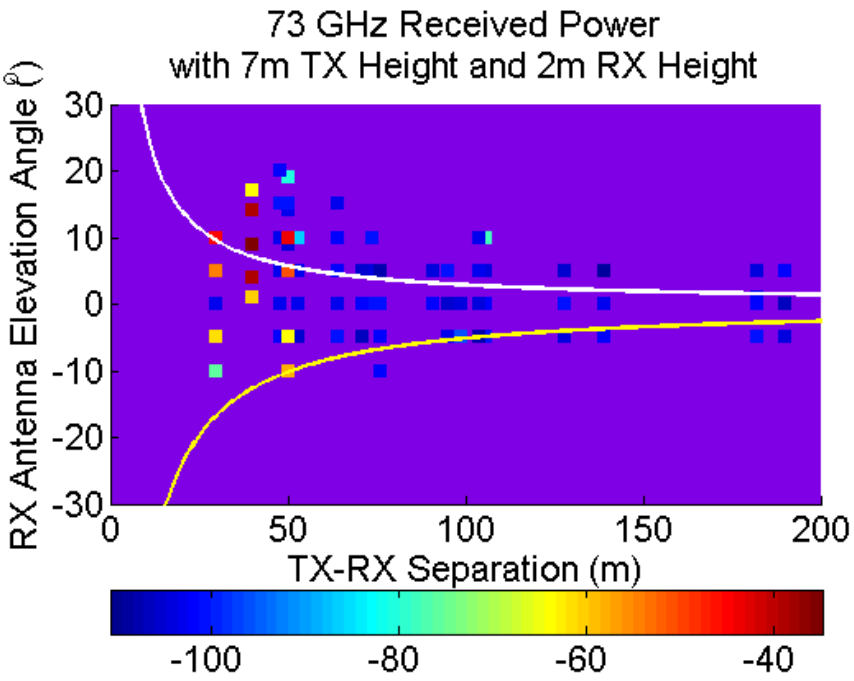

Fig. 66. Received power distribution as a function of RX antenna elevation angle and TX-RX separation distance for 7 m-high TX antenna at 73 GHz. The points in the figure represent the strongest received power at a particular distance-angle combination. The values under the colorbar denote the received power level in dBm. The white solid curve and the yellow solid curve represent the theoretical projected elevation angles and the ground bouncing angles at the RX, respectively.

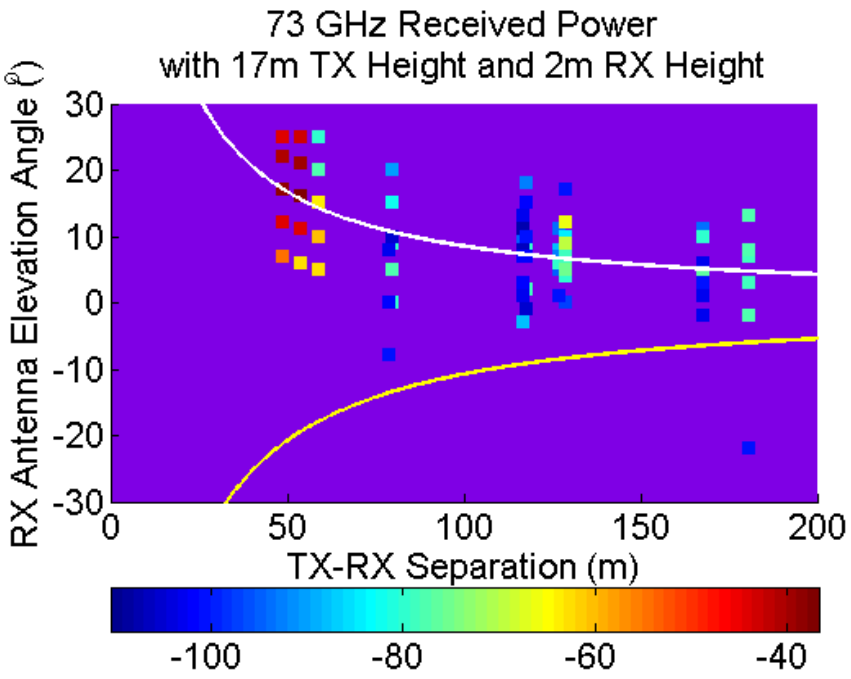

Fig. 67. Received power distribution as a function of RX antenna elevation angle and TX-RX separation distance for 17 m-high TX antenna at 73 GHz. The points in the figure represent the strongest received power at a particular distance-angle combination. The values under the colorbar denote the received power level in dBm. The white solid curve and the yellow solid curve represent the theoretical projected elevation angles and the ground bouncing angles at the RX, respectively.

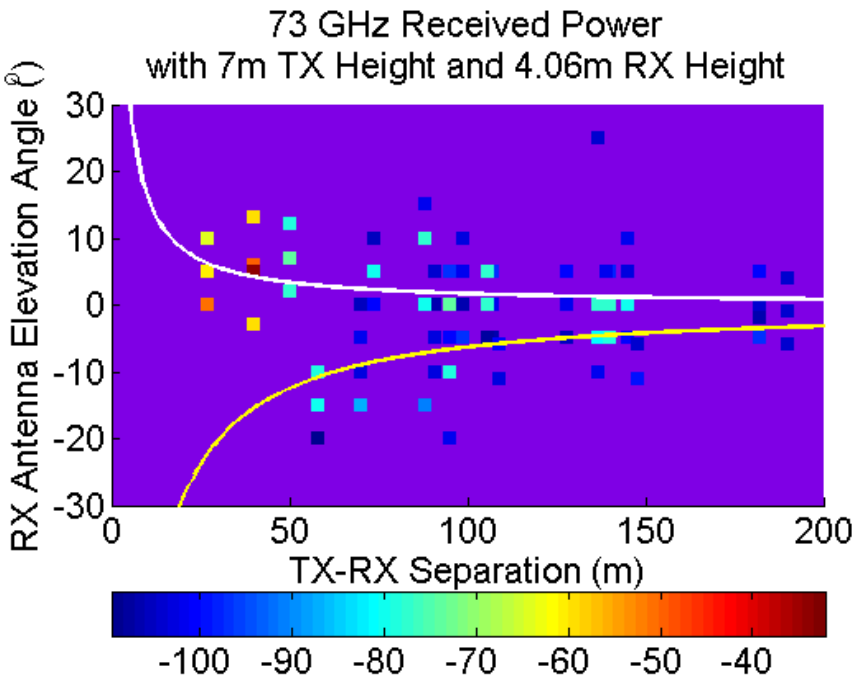

Fig. 68. Received power distribution as a function of RX antenna elevation angle and TX-RX separation distance for 2 m-high RX antenna at 73 GHz. The points in the figure represent the strongest received power at a particular distance-angle combination. The values under the colorbar denote the received power level in dBm. The white solid curve and the yellow solid curve represent the theoretical projected elevation angles and the ground bouncing angles at the RX, respectively.

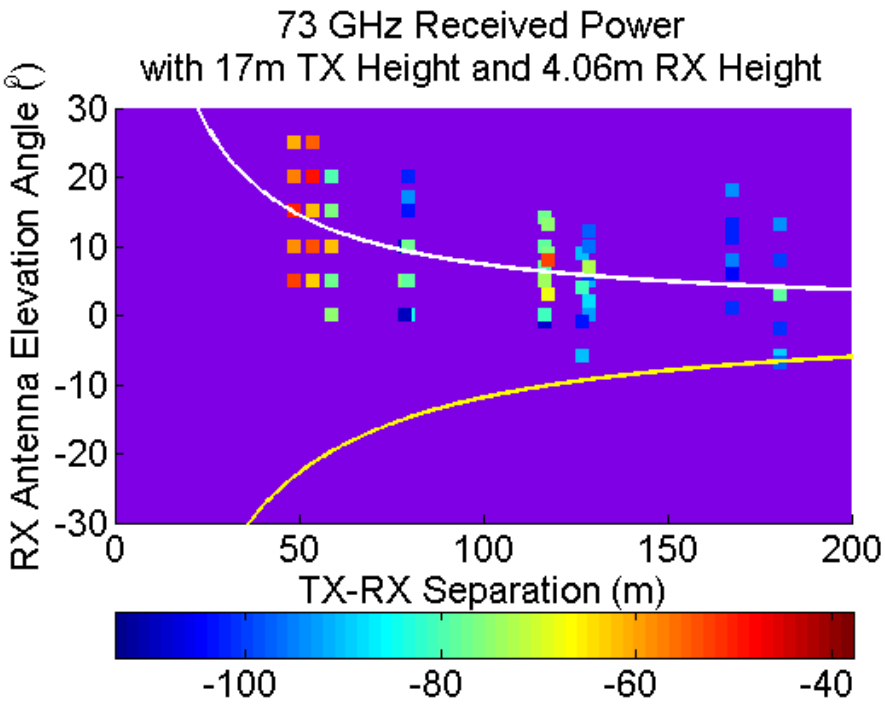

Fig. 69. Received power distribution as a function of RX antenna elevation angle and TX-RX separation distance for 4 m-high RX antenna at 73 GHz. The points in the figure represent the strongest received power at a particular distance-angle combination. The values under the colorbar denote the received power level in dBm. The white solid curve and the yellow solid curve represent the theoretical projected elevation angles and the ground bouncing angles at the RX, respectively.

3.4.3 Large-scale Path Loss

Aiming at creating 3GPP-like models for large-scale path loss, floating intercept omnidirectional path loss models [67] with respect to a 1 m free space reference are investigated here.

Fig. **70** shows the path loss values obtained from all mobile-scenario measurements at the 7 m-high TX on the rooftop of Coles Sport Center at 73 GHz. The PLEs for the entire NLOS environment is 4.91, which reduces to 3.81 when considering just the single strongest signal at each RX location. The PLE for LOS is 2.49, which is higher than the theoretical value 2, the reason lies in that in our LOS definition, the TX and RX antennas are facing each other boresight-to-boresight, but it is difficult to perfectly align the antennas boresight-to-boresight at

such large distances, thus the PLE increases. The floating intercept omnidirectional path loss model is also shown in the figure, where the path loss values are obtained by summing all received powers at all azimuth and elevation angles and removing TX and RX antenna gains for each individual measurement (12 different azimuth and elevation antenna orientations, where 10 antenna orientations had the RX antenna moving across all azimuth angles in 8^0 steps for NLOS environments and 10^0 steps for LOS environments with a fixed RX elevation and a fixed TX azimuth and elevation. The 11th and 12th antenna orientations had the RX fixed at a particular azimuth and elevation angle and the TX antenna swept in the azimuth plane in 8^0 or 10^0 steps based on the environment) for each T-R separation distance, that is, summing all received contributions from both AOA and AOD (TX sweep) measurements, and recovering the corresponding path loss. Fig. **71** is the path loss scatter plot with the TX located on the 5^{th}-floor balcony of Kaufman Building (17 m above ground) and RX antennas elevated to 2 m height. In general, the PLEs for LOS, NLOS and NLOS-best are better (lower) than those in Fig. 70. The path loss scatter plots for the backhaul scenario (where the RX antenna height is 4.06 m) with TX antenna heights 7 m and 17 m are illustrated in Fig. **72** and Fig. **73**, respectively. Comparing Fig. **70** and Fig. **71**, as well as Fig. **72** and Fig. **73**, it can be observed that the PLEs for NLOS, NLOS-best, and LOS become lower when the TX antenna is elevated, this is likely due to the fact that the transmitted signals would encounter fewer obstructions (especially obstructions lower than the TX antenna height) when the TX antenna height is increased from 7 m to 17 m, which indicates that received signal power may be increased by lifting the TX antenna in a proper range depending on the topography.

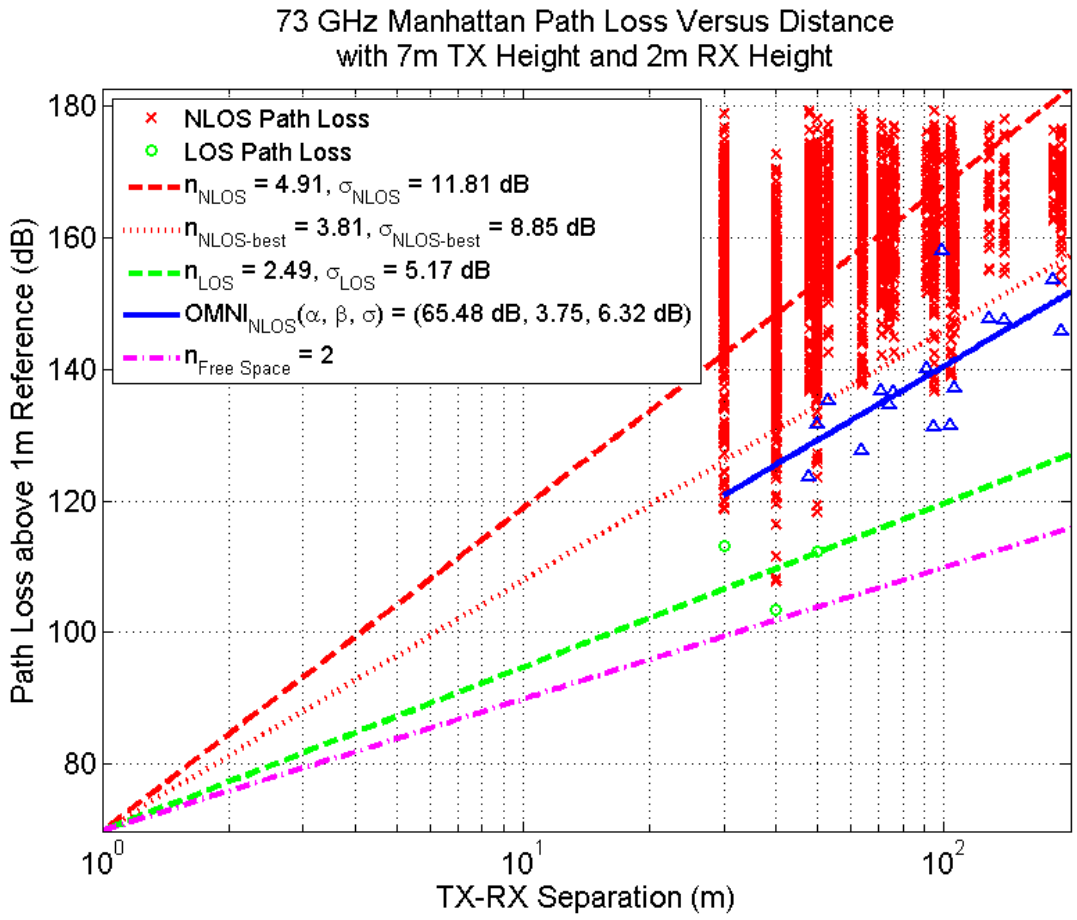

Fig. 70. New York City path losses at 73 GHz as a function of T-R separation distance for 7 m-high TX and 2 m-high RX using vertically polarized 27 dBi, 7°half-power beamwidth TX & RX antennas. All data points represent path loss values calculated from recorded PDP measurements. Red crosses indicate all NLOS pointing angle data points, green circles indicate LOS data points, and blue triangles represent omnidirectional pure NLOS data points. The measured path loss values are relative to a 1 m free space close-in reference distance. NLOS PLEs are calculated for the entire data set and also for the best recorded link. LOS PLEs are calculated for strictly boresight-to-boresight scenarios. n values are PLEs and σ values are shadow factors. The solid blue line is the omnidirectional (α, β) model.

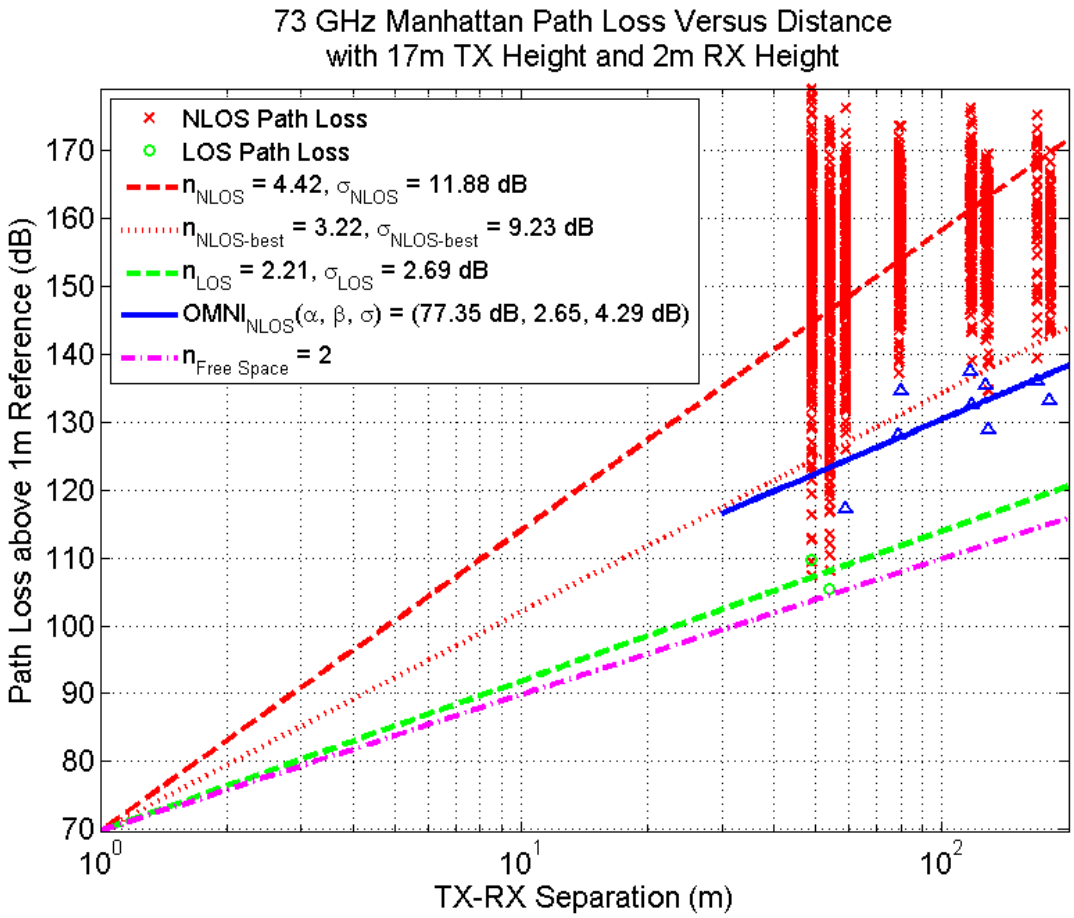

Fig. 71. New York City path losses at 73 GHz as a function of T-R separation distance for 17 m-high TX and 2 m-high RX using vertically polarized 27 dBi, 7◦half-power beamwidth TX & RX antennas. All data points represent path loss values calculated from recorded PDP measurements. Red crosses indicate all NLOS pointing angle data points, green circles indicate LOS data points, and blue triangles represent omnidirectional pure NLOS data points. The measured path loss values are relative to a 1 m free space close-in reference distance. NLOS PLEs are calculated for the entire data set and also for the best recorded link. LOS PLEs are calculated for strictly boresight-to-boresight scenarios. n values are PLEs and σ values are shadow factors. The solid blue line is the omnidirectional (α, β) model.

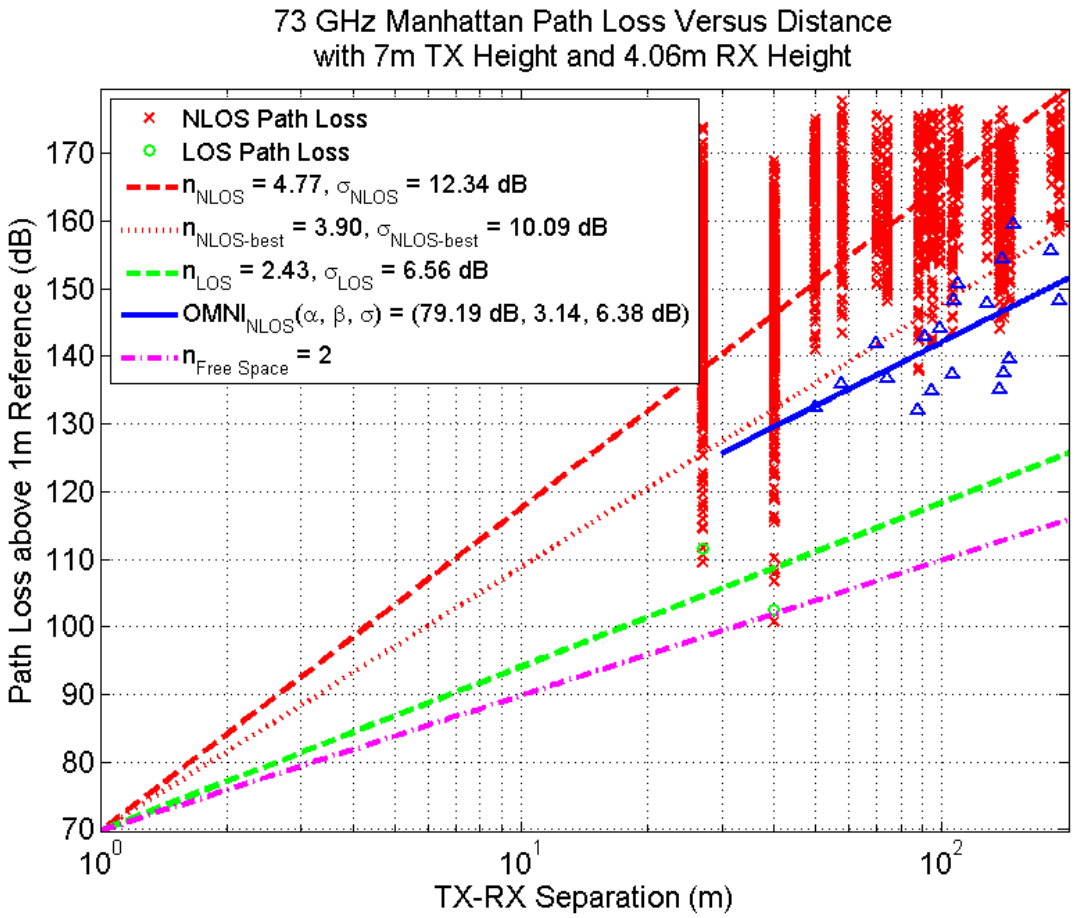

Fig. 72. New York City path losses at 73 GHz as a function of T-R separation distance for 7 m-high TX and 4.06 m-high RX using vertically polarized 27 dBi, 7°half-power beamwidth TX & RX antennas. All data points represent path loss values calculated from recorded PDP measurements. Red crosses indicate all NLOS pointing angle data points, green circles indicate LOS data points, and blue triangles represent omnidirectional pure NLOS data points. The measured path loss values are relative to a 1 m free space close-in reference distance. NLOS PLEs are calculated for the entire data set and also for the best recorded link. LOS PLEs are calculated for strictly boresight-to-boresight scenarios. n values are PLEs and σ values are shadow factors. The solid blue line is the omnidirectional (α, β) model.

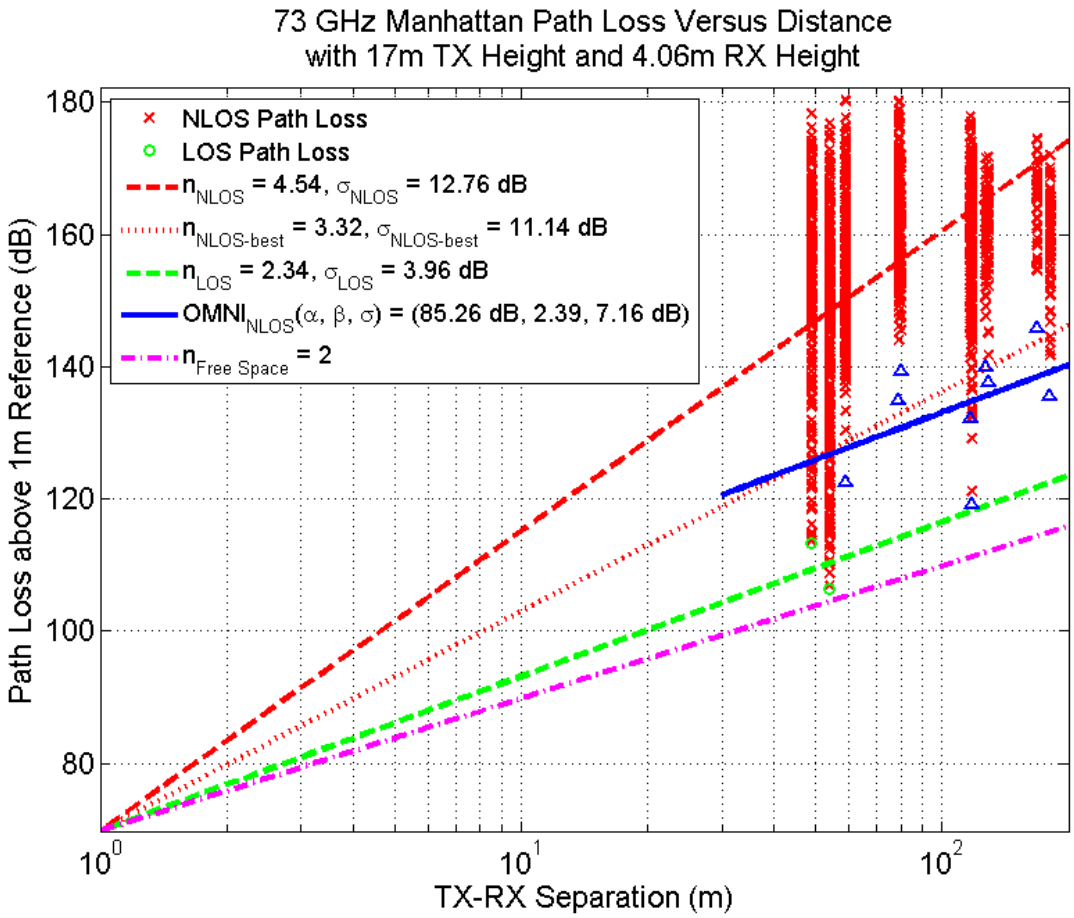

Fig. 73. New York City path losses at 73 GHz as a function of T-R separation distance for 17 m-high TX and 4.06 m-high RX using vertically polarized 27 dBi, 7°half-power beamwidth TX & RX antennas. All data points represent path loss values calculated from recorded PDP measurements. Red crosses indicate all NLOS pointing angle data points, green circles indicate LOS data points, and blue triangles represent omnidirectional pure NLOS data points. The measured path loss values are relative to a 1 m free space close-in reference distance. NLOS PLEs are calculated for the entire data set and also for the best recorded link. LOS PLEs are calculated for strictly boresight-to-boresight scenarios. n values are PLEs and σ values are shadow factors. The solid blue line is the omnidirectional (α, β) model.

CHAPTER 4 BEAM COMBINING AT 28 GHZ AND 73 GHZ

4.1 Concept of Beam Combining

Diversity is a powerful communication technique which can reduce the detrimental effects of signal fading on wireless communication system performance, for instance, signal outage and average bit error rate (BER), and improve signal-to-noise ratio (SNR) by using two or more communication channels with different characteristics. There exist a variety of diversity schemes, such as time diversity, frequency diversity, space diversity and polarization diversity, which provide significant link budget and signal quality improvement. Space diversity, also known as antenna diversity, is one of the most effective implementations of diversity utilized in wireless communication systems. A wide range of space diversity reception techniques can be distinguished: selection diversity (SD), feedback diversity (FD), maximal ratio combining (MRC) and equal gain combining (EGC).

Beamforming at the base station significantly increases the signal-to-interference ratio (SIR) at the target mobile receiver. On the other hand, the received signal quality will be further enhanced if the signal power at the receiver can be combined using a phased array capable of combining energy from multiple beams simultaneously. To date, cellular beam combining has been investigated primarily for cellular CDMA systems, where RAKE receivers align the received signal in multiple beams and combine the signal energy for signal-to-noise ratio (SNR) enhancement, where capacity evaluations are often performed by computer simulation, without the benefit of experimental results from real world channels.

The 28 GHz propagation measurements provided AOA and AOD data for multipath angular spread analysis. By completing a 360° exhaustive sweep of the TX and RX antennas in 10° steps, the angles with the highest received power were determined by observing PDPs. **Fig. 74** shows an

example of the PDPs with the four strongest received signals contained in different beams at an arbitrary measurement location. The diverse multipath beams can be utilized for beam combining. **Fig. 75** illustrates a typical measured polar plot displaying the azimuth angles of arrival (AOAs) at one RX in a NLOS environment at 28 GHz. The 0^0 azimuth pointing angle refers to the north direction. The rotation step was 80. As is observed, power was received at 26 out of 45 RX azimuth angles, implying that downtown Manhattan is a multipath-rich environment with numerous reflective objects and that signals coming from a myriad of beams can be combined to enhance the received signal level. At all 26 TX-RX location combinations in the 28 GHz measurements and 41 TX-RX location combinations for 73 GHz, at least four distinct signals coming from different directions were obtained at each single location combination by measuring various azimuth and elevation angles. A typical measured polar plot at 73 GHz is shown in Fig. **76.**

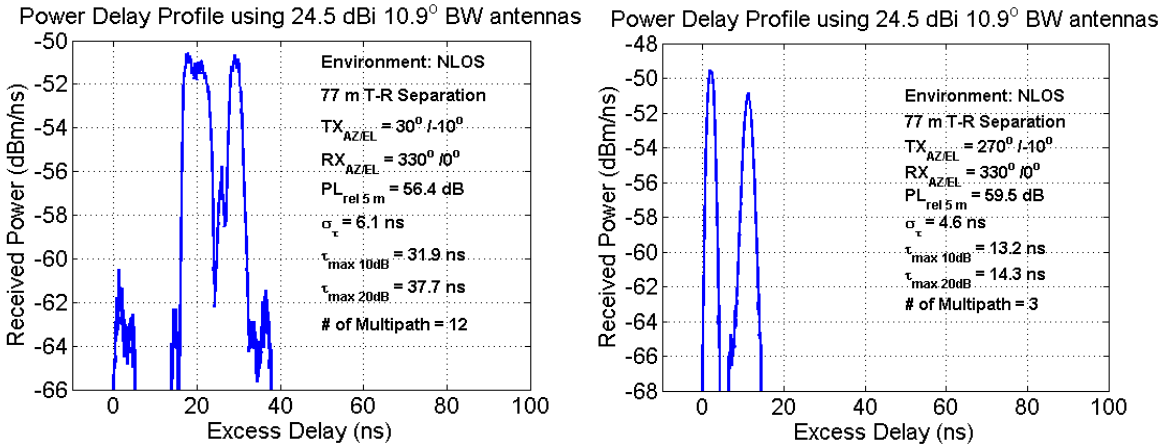

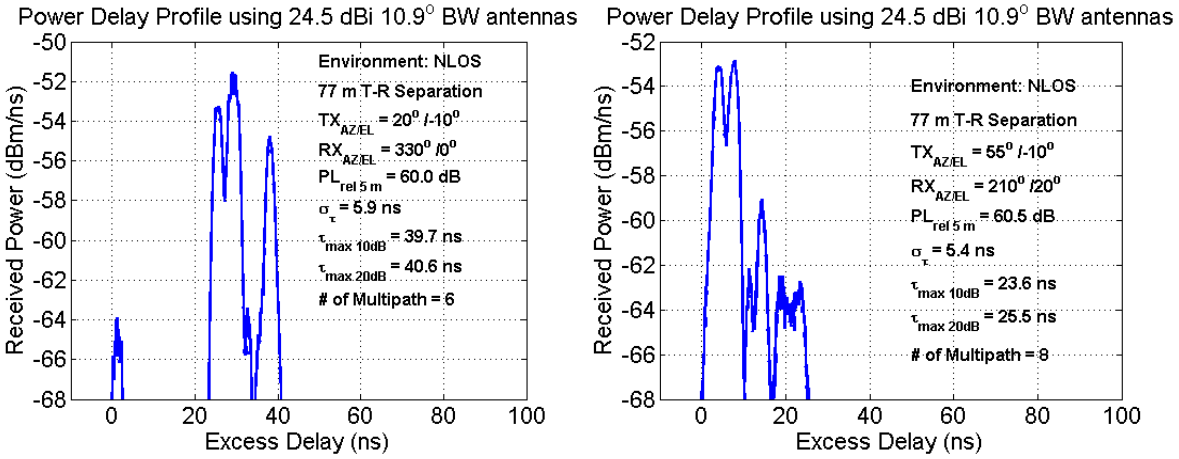

Fig. 74. PDPs of incident beams containing the three strongest received powers at 28 GHz in a NLOS environment in Manhattan using 24.5 dBi horn antennas at both TX and RX.

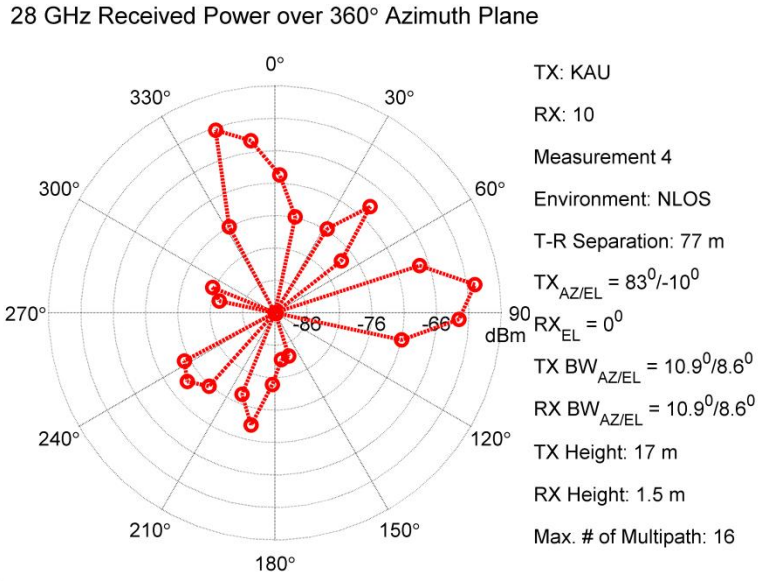

Fig. 75. Polar plot showing the received powers at a NLOS location at 28 GHz with 17 m-high TX, 1.5 m-high RX and 77 m TX-RX separation. The red dots represent total received powers in dBm at different RX azimuth angles.

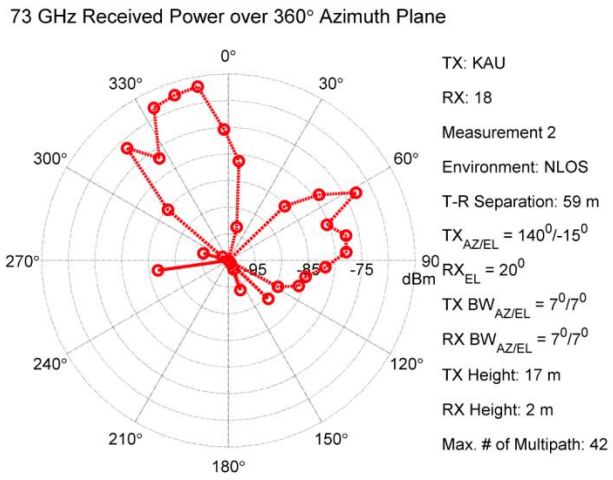

Fig. 76. Polar plot showing the received powers at a NLOS location at 73 GHz with 17 m-high TX, 2 m-high RX and 59 m TX-RX separation. The red dots represent total received powers in dBm at different RX azimuth angles.

4.2 Beam Combining Procedure

Beam combining considers combining the received powers that were recorded from different 10° angular segments measured at a particular RX location. Future work will use the data to create statistical models for arbitrary antenna arrays, but for this paper, we focus on measured results using 10° beamwidth antennas. Using the measured data, we then consider the potential improvement resulting from both coherent and noncoherent reception at the RX. For coherent reception, we assume that the received powers from each of the best beam headings of interest are combined using known carrier phase information (this results in optimal/maximum power from each of the combined beams), while noncoherent reception is considered by simply adding (linearly) the powers received from each beam heading without considering phase information. This non-coherent approach is based on the reasonable assumption that the incoming phases of each received signal in each beam is uniformly and identically, independently distributed (iid) so that the powers can simply be added [69][70]. Note that we do not assume alignment or equalization of individual multipath delays from each of the individual beams, but simply compute received power at each location as the area under the PDP, as current OFDM and very wideband modulation

methods equalize out multipath. Thereby, focusing on the powers from different beams provides good first order insight into the potential improvement in link coverage that might be obtained from beam combining.

The measured NYC data occupies over 100 Gigabytes, hence computer (and not manual) inspection of all PDP measurements for all antenna pointing angle combinations at each of the individual RX locations was needed to find the PDPs and their corresponding antenna pointing angles that provided the strongest (i.e. smallest path loss), second strongest, third strongest, and the fourth strongest received signals at each RX location. For each RX location, all ten antenna configurations were considered, which is reasonable since adaptive antennas will be employed at both the TX and RX in mmWave cellular systems. The single strongest, the first and second strongest, the first three strongest, and the first four strongest power levels from the measured PDPs over all of the different pointing angles at each RX location were then combined either coherently or noncoherently, and the results for path loss over all RX locations were observed. For the case of coherent beam combining, the square root of the absolute (i.e. linear) received power levels in Watts were computed, and the voltages obtained at the strongest few 3D (three dimensional) angular segments were summed, thus the total coherent voltage was found at each RX location, and then this value was squared to obtain received power in units of Watts, which was then converted into dBm. To compute noncoherent power, each of the strongest received powers was converted from dBm to its linear value in Watts, and summed directly. The total noncoherent power value was then converted back to dBm. Eqs. (59) and (60) illustrate the approaches of calculating the total received coherent (PC) and noncoherent (PNC) powers at each RX using the combination of the N strongest beams, respectively:

$$P_C = \left(\sum_{i=1}^{N} \sqrt{P_i}\right)^2 \tag{59}$$

$$P_{NC} = \sum_{i=1}^{N} P_i \tag{60}$$

where P_C and P_{NC} denote the coherently and noncoherently combined powers in Watts, respectively. P_i (i=1,2,…, N) represents the ith strongest received power (in Watts). By employing the resulting obtained received power from beam combining, the corresponding path loss was calculated. Finally, scatter plots of path loss (PL) versus TX-RX separation were generated.

Since the measurements provided no absolute phase information, the assumption of absolute phase must be made, which is a reasonable assumption for coherent modulation that would be implemented in commercial mm-wave cellular systems. Coherent combining is expected to provide superior improvement in SNR as compared to noncoherent methods, and 3dB improvement is a general rule of thumb.

4.3 Path Loss Models

4.3.1 Floating Intercept Model

Path loss (in dB) usually has a linear relationship with logarithmic distance. In the floating intercept model, path loss can be expressed by the following equation:

$$\overline{PL(d)}[dB] = \beta \cdot 10\log_{10}(d) + \alpha \tag{61}$$

where $\overline{PL(d)}$ (in dB) denotes the average path loss taken over all antenna pointing angles at a TX-RX separation of d (in meters), β is the linear slope, and α is the floating intercept in dB. Path loss is essential in studying link budget and system capacity, as the higher the path loss, the greater the attenuation of the propagating signal (i.e. this sets the limit on range from a base station, determines interference from neighboring cells, and plays a major role in determining infrastructure investment).

In Eq. (61), $\overline{PL(d)}$ (in dB) is obtained by the least-square linear regression fit, in which the

linear slope β can be derived as below:

$$\beta = \frac{\sum_i^n (d_i - \bar{d}) \cdot (PL_i - \overline{PL})}{\sum_i^n (d_i - \bar{d})^2} \tag{62}$$

where n denotes the total number of measurement snapshots, d_i is the distance of the i^{th} measurement snapshot in logarithmic scale, $\bar{d}$ indicates the average distance of all measurement snapshots in logarithmic scale, which is obtained by converting all d_i's from linear scale (in meters) to logarithmic scale and then finding the average distance in logarithmic scale. PL_i (in dB) is the path loss value of the i^{th} measurement snapshot, and $\overline{PL}$ (in dB) is the average path loss value over all measurement snapshots.

The floating intercept α can be derived by:

$$\alpha(dB) = \overline{PL[dB]} - \beta \cdot \overline{10 \log_{10} d} \tag{63}$$

where α is denoted over a specific range of distances (30 m – 200 m in our case) based on measured locations and resulting path losses. The regression fit is performed for all 26 NLOS TX-RX location combinations where a signal was recorded.

Shadow fading (SF, or shadowing) is another factor influencing path loss, which is caused by the surrounding environmental clutter [55] and thus expected to be larger in dense urban environment such as NYC. SF is generally expressed as a zero-mean Gaussian random variable $X_{\sigma SF}$ with standard deviation σ_{SF} (in log scale) about $\overline{PL(d)}$ in Eq. (61). Therefore, the total path loss due to attenuation and SF in the channel can be described as follows:

$$PL(d)\,[dB] = \overline{PL(d)}[dB] + X_{\Sigma SF}[dB] \tag{64}$$

where PL(d) represents the total path loss (a random variable), $\overline{PL(d)}$ is the path loss due to attenuation, and $X_{\Sigma SF}$ is due to shadowing.

As shown in [68], the model and parameters in Eq. (63) are very sensitive to perturbations in

measurements.

4.3.2 Close-in Free Space Reference Model

Path loss at a close-in reference distance d_0 is calculated as the free space path loss by Eq. (65):

$$\mathrm{PL}(\mathrm{d}_0) = 20\log_{10}\left(\frac{4\pi \mathrm{d}_0}{\lambda}\right) \tag{65}$$

where λ is the wavelength of the carrier frequency, which equals 10.71 mm at 28 GHz and 4.08 mm at 73.5 GHz. Without loss of generality, in our measurements d_0 is set to 4 m, which is much larger than the Fraunhofer distances for our antennas at both frequencies. Path loss at a TX-RX separation d, beyond d_0, is given by the equation below [55]:

$$\mathrm{PL}(\mathrm{d}) = \mathrm{PL}(\mathrm{d}_0) + 10\mathrm{n}\log_{10}\left(\frac{\mathrm{d}}{\mathrm{d}_0}\right) + X_\sigma \tag{66}$$

where $\mathrm{PL}(\mathrm{d})$ is the path loss in dB for a TX-RX separation of d, n is the path loss exponent, and X_σ, usually called shadowing factor (SF), represents a normal random variable in dB having a standard deviation of σ dB.

4.4 Beam Combining Results at 28 GHz

4.4.1 Beam Combining Results Using the Floating Intercept Model

Five scatter plots of path loss versus distance (TX-RX separation) were produced from our measured data in Manhattan. Among the 28 TX-RX location combinations where signals were acquired, 2 were LOS Boresight (LOS_B) cases, 4 LOS Non Boresight (LOS_NB) cases, and the remaining 22 were NLOS case. Since the LOS_B case provides very close to free space path loss, which is often the best case for urban propagation channels, only the more challenging LOS_NB and NLOS measurements are considered here, and both LOS_NB and NLOS are classified as NLOS environments in this section (Note that this classification will be altered in next section). The

relationship between path loss and TX-RX separation, as well as regression fit path loss results corresponding to all uncombined received signals, the best (i.e. strongest) received signal over all angular segments in 3D at each RX, the best two combined signals, the best three combined signals, and the best four combined signals are displayed in Fig. **77** to Fig. **81.** Table **9** shows the received power and improvement in path loss from various beam combining combinations over all NLOS locations, and the overall average improvement.

It can be summarized from Fig. **78** to Fig. **81** that the average path loss at a certain distance drops monotonically as the number of combined signals increases from one to four for both noncoherent and coherent combinations of beams. For instance, the path loss at 30 m TX-RX separation corresponding to four coherently combined signals improved by about 10 dB compared to that of using the single best beam. It is also worth noting that for a fixed number of combined beams, the path loss for coherent combining is always at least ~ 3 dB better (i.e. smaller) than for the noncoherent case, showing the dramatic improvement that can be achieved using coherent power combining over the best few received beams in 3D. For example, in the case of combining four signals coherently, the path loss decreases by 5.9 dB, on average, with respect to that of noncoherent combining of four beams, as can be observed from the last row of Table **9**. This is not surprising, as coherent combination of in-phase signals gives rise to the strongest power compared with noncoherent combination and non in-phase coherent combination, yet this is the first known data of this type for mm-wave cellular. The results are important, since an improvement of 5.9 dB in average path loss results in a cell radius coverage range increase of 41% compared to a single beam RX in a n=4 propagation environment. Furthermore, the improvement in path loss when combining the best two beams *coherently* (15.7 dB above arbitrary single beam pointing) is even more conspicuous than that of combining the best four beams *noncoherently* (15.0 dB), thus

showing *coherent* combining of fewer antennas easily justifies the receiver complexity. Comparing the improvement in path loss for the case of coherent combining for the four strongest beams, and that of just a single strongest beam, it can be observed that the average improvement in link budget goes from 10.1 dB up to 20.9 dB, yielding 10.8 dB improvement, which is remarkably significant to carriers (86% range extension for n=4).

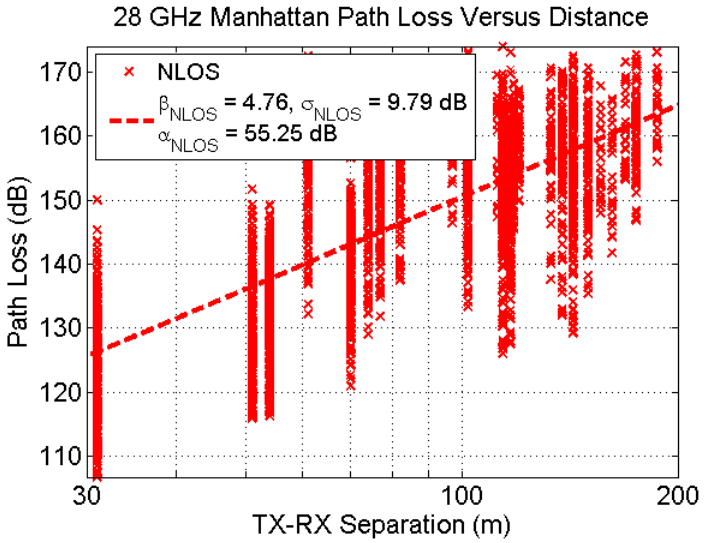

Fig. 77. Measured path loss versus TX-RX separation for 28 GHz outdoor cellular channels in NYC. The red crosses represent measured path loss values obtained from PDPs, and the red line denotes least-square fit through the path losses. The slope of the red line is 4.76, the intercept is 55.25 dB, and the shadow fading factor is 9.79 dB.

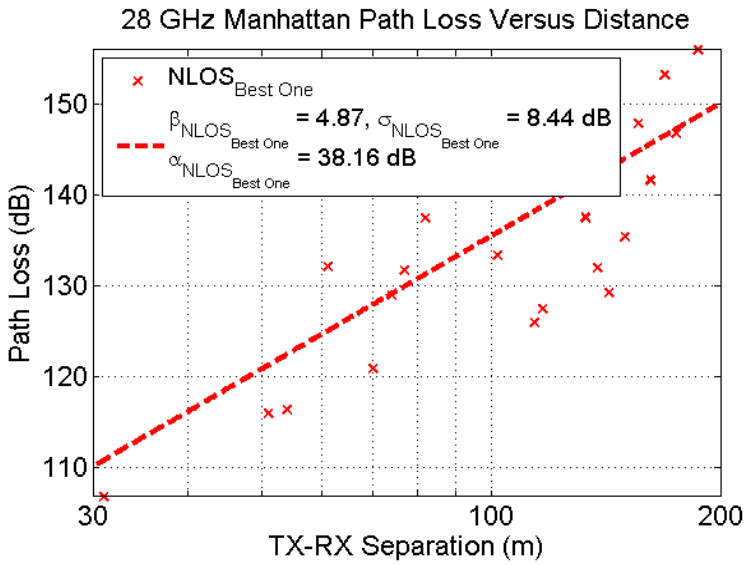

Fig. 78. Path loss versus TX-RX separation at 28 GHz in NYC for the best (i.e. strongest) signal at each RX location. The red crosses represent path loss values, and the red line denotes least-square fit through the path losses. The slope of the red line is 4.87, the intercept is 38.16 dB, and the shadow fading factor is 8.44 dB.

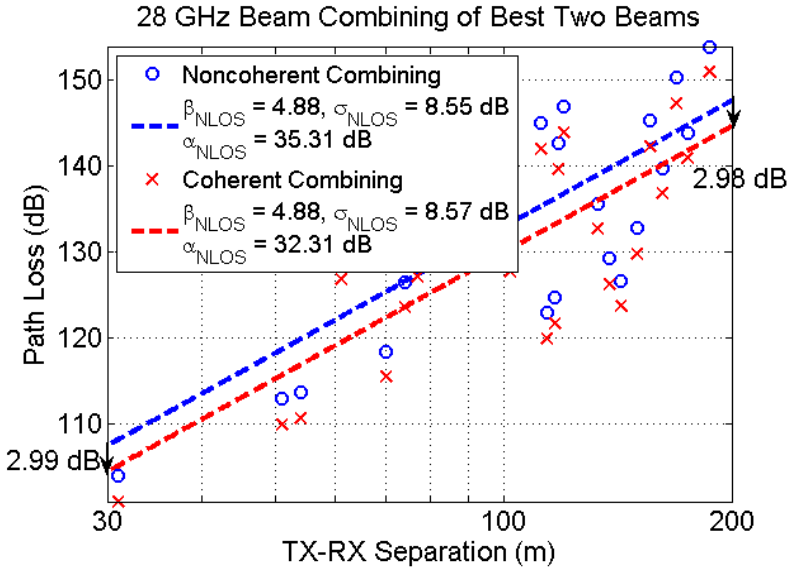

Fig. 79. Path loss versus TX-RX separation at 28 GHz in NYC for the best (i.e. strongest) two signals combined noncoherently and coherently at each RX location. The blue circles and red crosses represent path loss values for noncoherent combination and coherent combination, respectively. The blue and red lines denote least-square fit through the path losses.

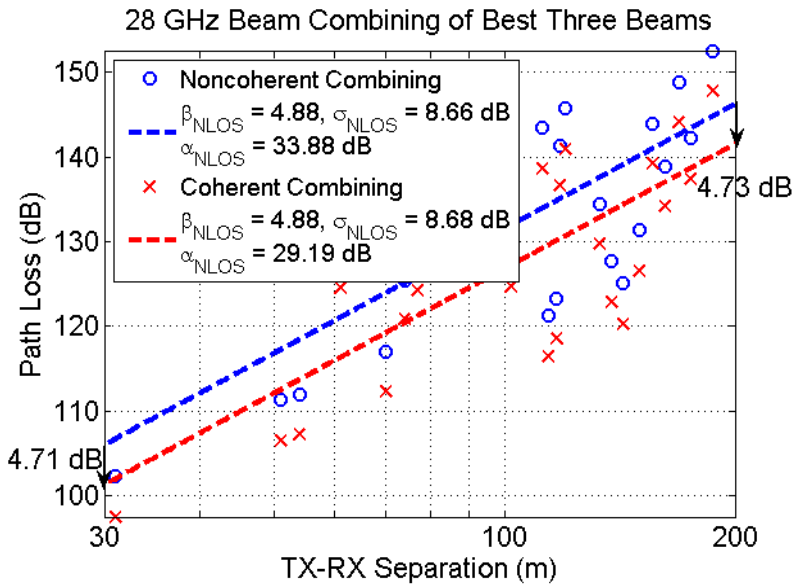

Fig. 80. Path loss versus TX-RX separation at 28 GHz in NYC for the best (i.e. strongest) three signals combined noncoherently and coherently at each RX location. The blue circles and red crosses represent path loss values for noncoherent combination and coherent combination, respectively. The blue and red lines denote least-square fit through the path losses.

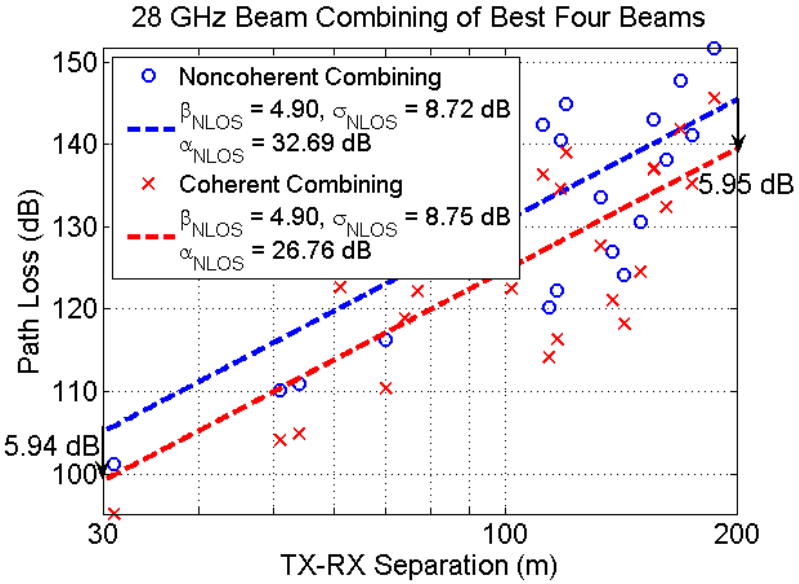

Fig. 81. Path loss versus TX-RX separation at 28 GHz in NYC for the best (i.e. strongest) four signals combined noncoherently and coherently at each RX location. The blue circles and red crosses represent path loss values for noncoherent combination and coherent combination, respectively. The blue and red lines denote least-square fit through the path losses.

Table 9. TX-RX separation, average received power (Pav), received power of the best single signal – i.e. from the single best antenna pointing angle (PC1 or PNC1), received power of the best two, three, and four signals combined noncoherently (denoted by PNC2, PNC3, PNC4 respectively), received power of the best two, three, and four signals combined coherently (denoted by PC2, PC3, PC4 respectively), and the corresponding improvement in path

loss compared to the average received power at each RX location. The red circles highlight the values corresponding to non-coherent combining of four beams and coherent combining of two beams.

RX	TX-RX Separation (m)	Pav (dBm)	P_{C1} (or P_{NC1}) (dBm)	Improvement in Path Loss (dB)	Noncoherent Combining						Coherent Combining					
					P_{NC2} (dBm)	Improvement in Path Loss (dB)	P_{NC3} (dBm)	Improvement in Path Loss (dB)	P_{NC4} (dBm)	Improvement in Path Loss (dB)	P_{C2} (dBm)	Improvement in Path Loss (dB)	P_{C3} (dBm)	Improvement in Path Loss (dB)	P_{C4} (dBm)	Improvement in Path Loss (dB)
1	91	-57.5	-46.1	11.4	-43.3	14.2	-41.7	15.8	-40.5	17.0	-40.3	17.2	-36.9	20.6	-34.5	23.0
2	61	-67.0	-55.1	14.0	-50.8	16.3	-50.0	17.0	-49.4	17.7	-47.8	19.3	-45.4	21.6	-43.6	23.4
3	102	-68.4	-54.3	14.1	-51.6	16.8	-50.3	18.1	-49.4	19.1	-48.6	19.8	-45.6	22.9	-43.4	25.0
4	118	-73.6	-66.5	7.1	-63.6	10.0	-62.3	11.3	-61.4	12.2	-60.6	13.0	-57.6	16.0	-55.4	18.2
5	114	-60.5	-46.9	13.6	-43.9	16.6	-42.2	18.3	-41.1	19.4	-40.9	19.6	-37.4	23.1	-35.1	25.4
6	133	-70.4	-58.5	12.0	-56.5	13.9	-55.3	15.1	-54.5	15.9	-53.6	16.8	-50.6	19.8	-48.6	21.8
7	162	-71.0	-62.6	8.5	-60.7	10.4	-59.7	11.3	-59.1	12.0	-57.8	13.3	-55.1	15.9	-53.3	17.8
8	82	-77.7	-71.9	5.8	-70.1	7.6	-69.0	8.7	-68.5	9.2	-67.2	10.5	-64.4	13.3	-62.8	15.0
9	51	-54.1	-45.6	8.5	-42.6	11.5	-40.9	13.1	-39.8	14.3	-39.6	14.5	-36.2	17.9	-33.8	20.3
10	74	-63.7	-49.9	13.8	-47.5	16.3	-46.4	17.3	-45.6	18.1	-44.5	19.3	-41.7	22.0	-39.7	24.0
11	143	-65.1	-50.2	14.9	-47.6	17.5	-46.0	19.1	-45.1	20.1	-44.6	20.5	-41.3	23.9	-39.1	26.1
12	156	-73.7	-68.8	4.9	-66.2	7.5	-64.8	8.9	-63.9	9.8	-63.2	10.4	-60.1	13.6	-57.9	15.8
13	150	-69.0	-56.3	12.7	-53.7	15.3	-52.3	16.7	-51.4	17.6	-50.7	18.3	-47.5	21.5	-45.5	23.6
14	138	-66.3	-52.9	13.4	-50.1	16.2	-48.6	17.7	-47.9	18.4	-47.1	19.2	-43.8	22.5	-42.0	24.3
15	169	-78.9	-74.2	4.7	-71.2	7.6	-69.7	9.2	-68.7	10.2	-68.2	10.6	-65.0	13.9	-62.7	16.2
16	112	-74.8	-68.3	6.5	-65.9	8.9	-64.3	10.4	-63.3	11.5	-62.9	11.9	-59.6	15.2	-57.3	17.5
17	77	-65.8	-52.7	13.1	-50.9	14.9	-49.8	16.0	-49.0	16.8	-48.0	17.8	-45.2	20.6	-43.1	22.7
18	54	-47.8	-37.3	10.5	-34.5	13.3	-32.9	14.9	-31.8	16.0	-31.5	16.3	-28.1	19.7	-25.8	22.1
19	120	-77.8	-70.7	7.1	-67.8	10.0	-66.6	11.2	-65.8	12.0	-64.8	13.0	-61.9	15.9	-59.9	17.9
20	82	-67.0	-58.4	8.6	-55.4	11.5	-53.9	13.1	-52.8	14.2	-52.4	14.5	-49.1	17.8	-46.7	20.2
21	97	-74.3	-67.2	7.0	-64.7	9.6	-63.2	11.0	-62.5	11.8	-61.7	12.6	-58.5	15.8	-56.5	17.8
22	187	-82.8	-76.9	5.9	-74.8	8.0	-73.5	9.3	-72.5	10.3	-71.9	10.9	-68.8	14.1	-66.5	16.3
23	175	-76.8	-67.7	9.1	-64.8	12.0	-63.1	13.7	-62.1	14.7	-61.8	15.0	-58.4	18.5	-56.1	20.7
24	117	-61.6	-48.4	13.1	-45.6	15.9	-44.2	17.4	-43.2	18.4	-42.6	18.9	-39.4	22.1	-37.2	24.4
25	70	-64.7	-52.2	12.5	-49.7	15.0	-48.3	16.4	-47.6	17.2	-46.8	18.0	-43.6	21.1	-41.6	23.1
Average Improvement in Path Loss (dB)			10.1		12.7		14.1		15.0		15.7		18.8		20.9	

4.4.2 Beam Combining Results Using the Close-in Free Space Reference Model

The path loss measured with a 7m-high TX antenna on the roof of Coles Sports Center for the NLOS environment is displayed in Fig. **82**. The overall PLE for NLOS is 4.47 with a SF of 10.20 dB. But when only considering the best beam at each RX site, the PLE is reduced to 3.68 with a SF of 8.76 dB. The noncoherent and coherent beam combining results for NLOS are given by Fig. **83**. Note that the PLE becomes lower after beam combining and keeps decreasing with the increasing number of combined beams, e.g., the PLE drops from 3.68 (using the single best beam) to 3.41 when the best two signals are combined coherently, and becomes 3.15 when combining the strongest four signals coherently. It is also worth mentioning that the shadowing factors are always lower after

beam combining compared to the one for all path loss values. Similar path loss scatter plot and coherent beam combining results for the 17 m-tall TX on the five-story balcony of Kaufman Business School at 28 GHz are given in Fig. **84** and Fig. **85.**

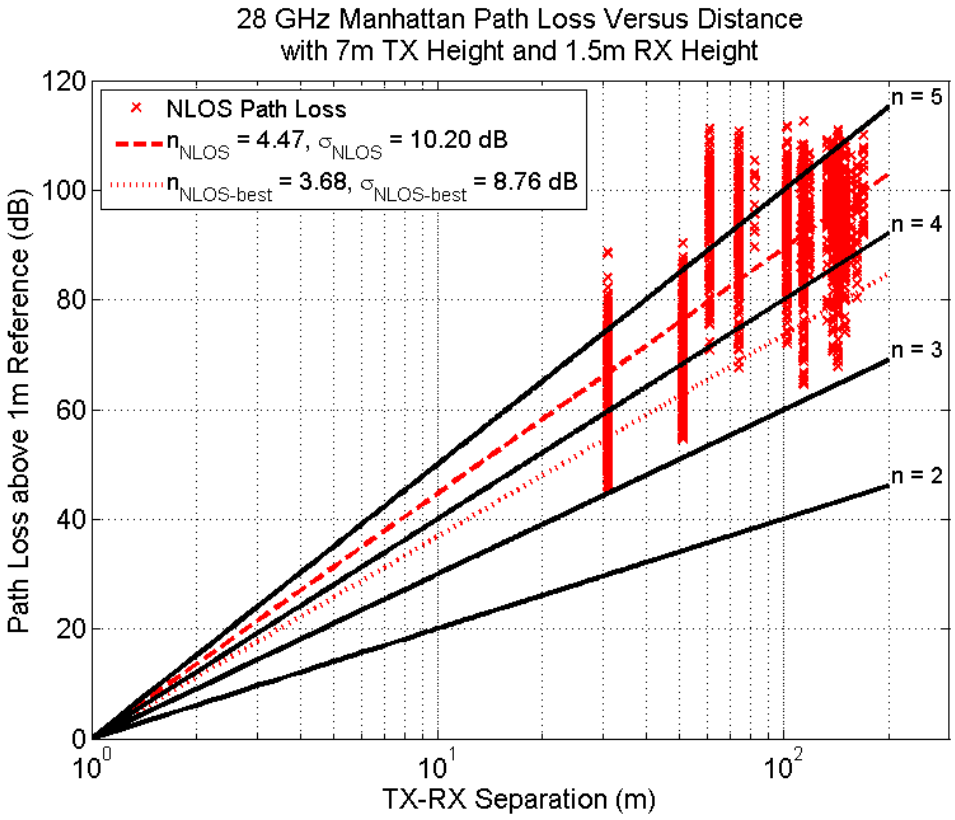

Fig. 82. Measured path loss values relative to 1 m free space path loss for 28 GHz outdoor cellular channels. These path loss values were measured using the 24.5 dBi narrow beam antennas with 7m TX height and 1.5m RX height. The values in the legend represent the PLEs and shadowing factors.

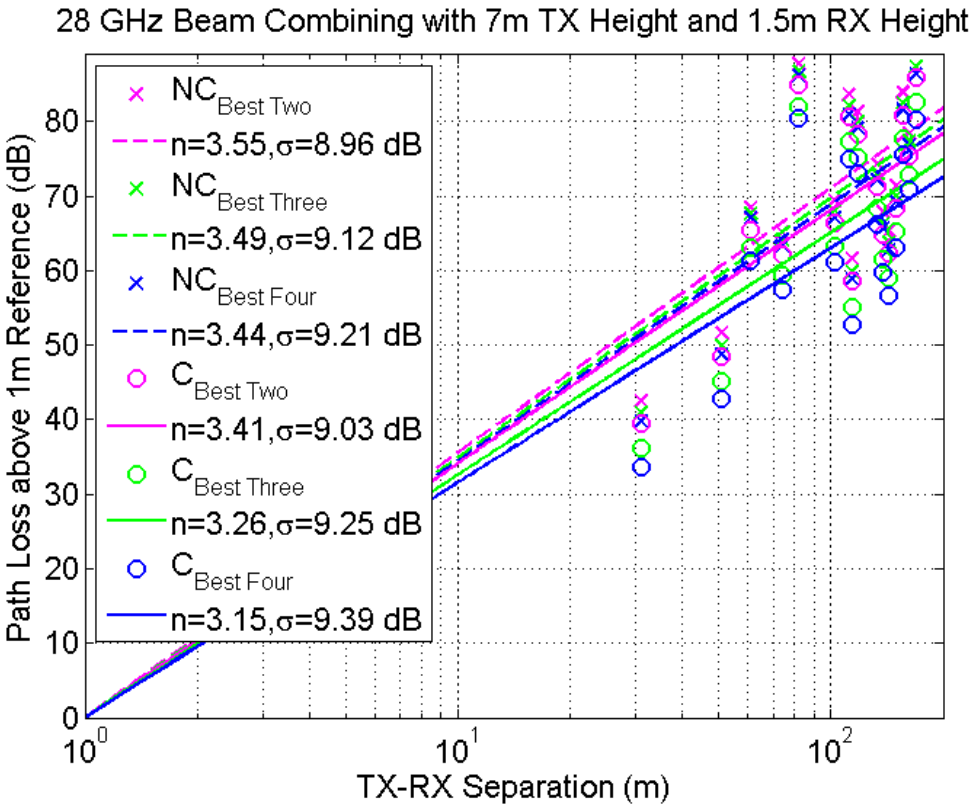

Fig. 83. Path loss versus TX-RX separation at 28 GHz in NYC for the best (i.e. strongest) two, three and four signals combined coherently at each RX location with the 7m-high TX and 1.5m-high RX. The values in the legend represent the PLEs and shadowing factors for each kind of beam combination.

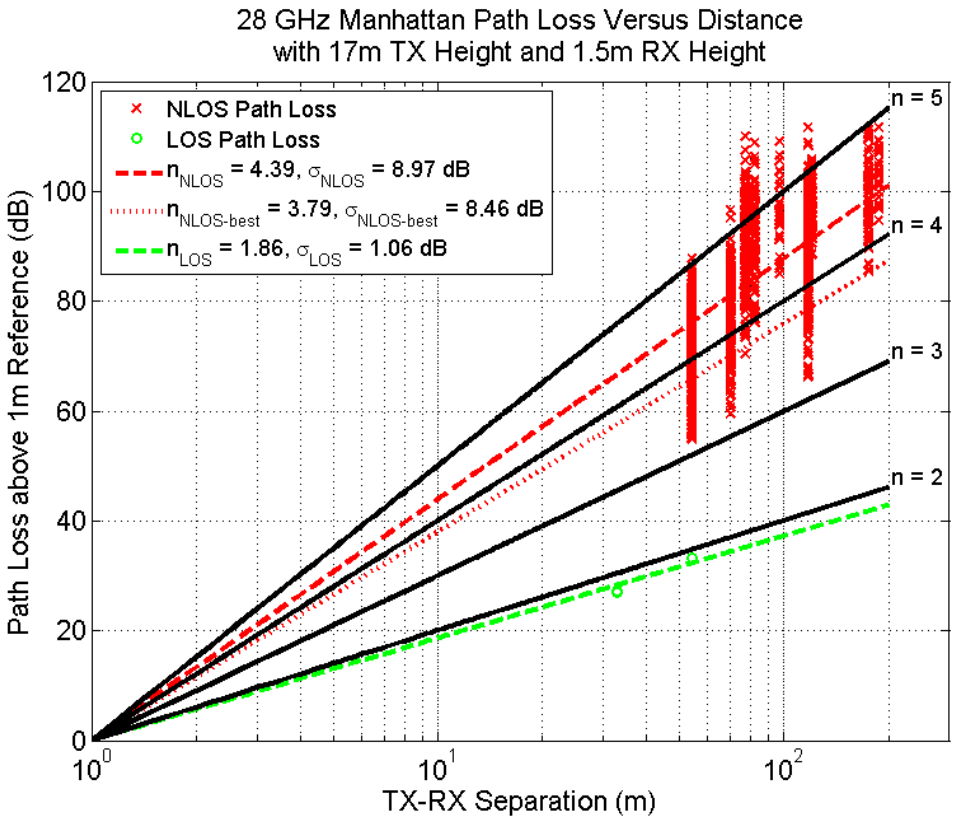

Fig. 84. Measured path loss values relative to 1 m free space path loss for 28 GHz outdoor cellular channels. These path loss values were measured using the 24.5 dBi narrow beam antennas with 17m TX height and 1.5m RX height. The values in the legend represent the PLEs and shadowing factors. The values in the legend represent the PLEs and shadowing factors.

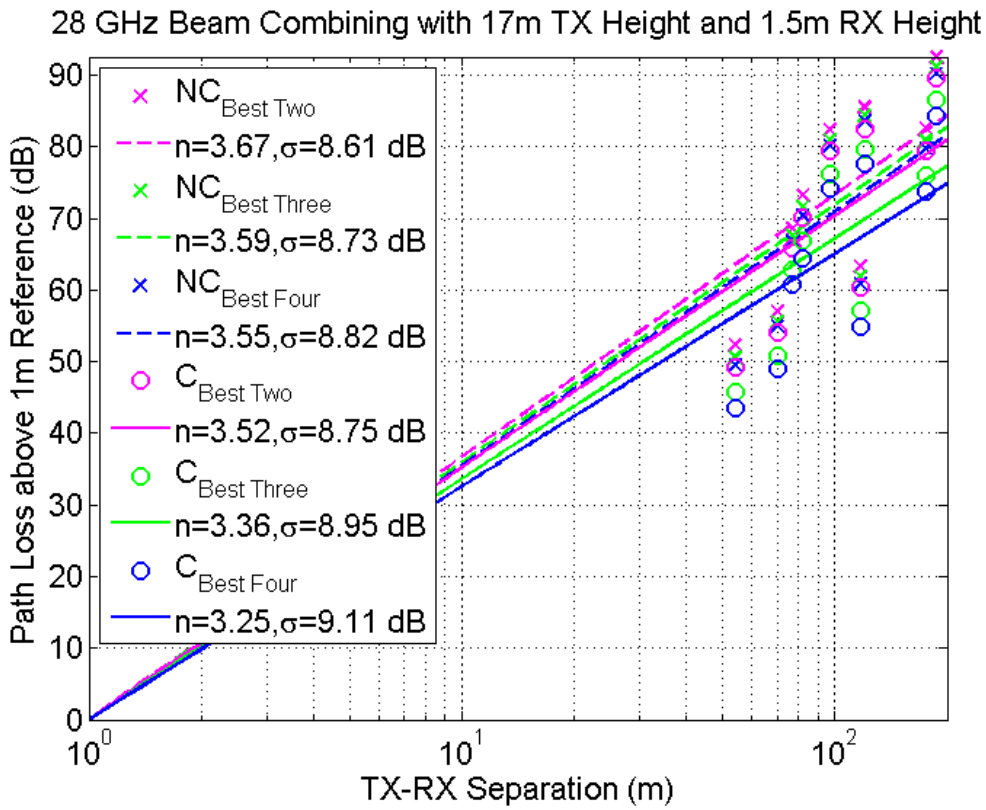

Fig. 85. Path loss versus TX-RX separation at 28 GHz in NYC for the best (i.e. strongest) two, three and four signals combined coherently at each RX location with the 17m-high TX and 1.5m-high RX. The values in the legend represent the PLEs and shadowing factors for each kind of beam combination.

4.5 Beam Combining Results at 73 GHz

Fig. **86** shows the path loss values obtained from all measurements at a 7 m-high TX and 2 m-high RXs at 73 GHz. The PLEs for the entire NLOS environment is 4.91, which reduces to 3.81 concerning just the single strongest signal at each RX location. The PLE for LOS is 2.49, which is higher than the theoretical value 2, the reason lies in that in our LOS definition, the TX and RX antennas are facing each other boresight-to-boresight, but it is difficult to perfectly align the antennas boresight-to-boresight at such large distances, thus the PLE increases. Fig. **87** displays the corresponding beam combining outcomes. After implementing four-beam combining, as is shown in Fig. **87**, the PLE descends to 3.26, much more favorable for propagation. Similar path loss scatter

plot and coherent beam combining results for the 7 m-high TX and 4.06 m-high RXs at 73 GHz are given in Fig. **88** and Fig. **89.**

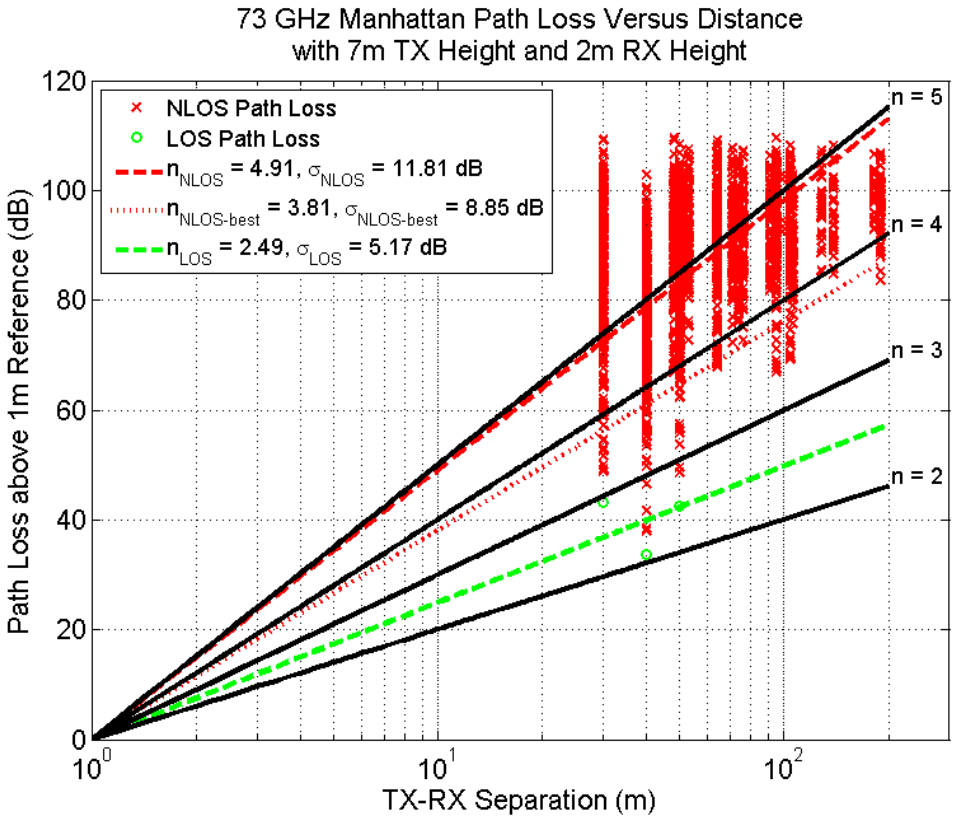

Fig. 86. Measured path loss values relative to 1 m free space path loss for 73 GHz outdoor cellular channels. These path loss values were measured using the 27 dBi narrow beam antennas for 19 TX-RX location combinations with 7m TX height and 2m RX height. The values in the legend represent the PLEs and shadowing factors.

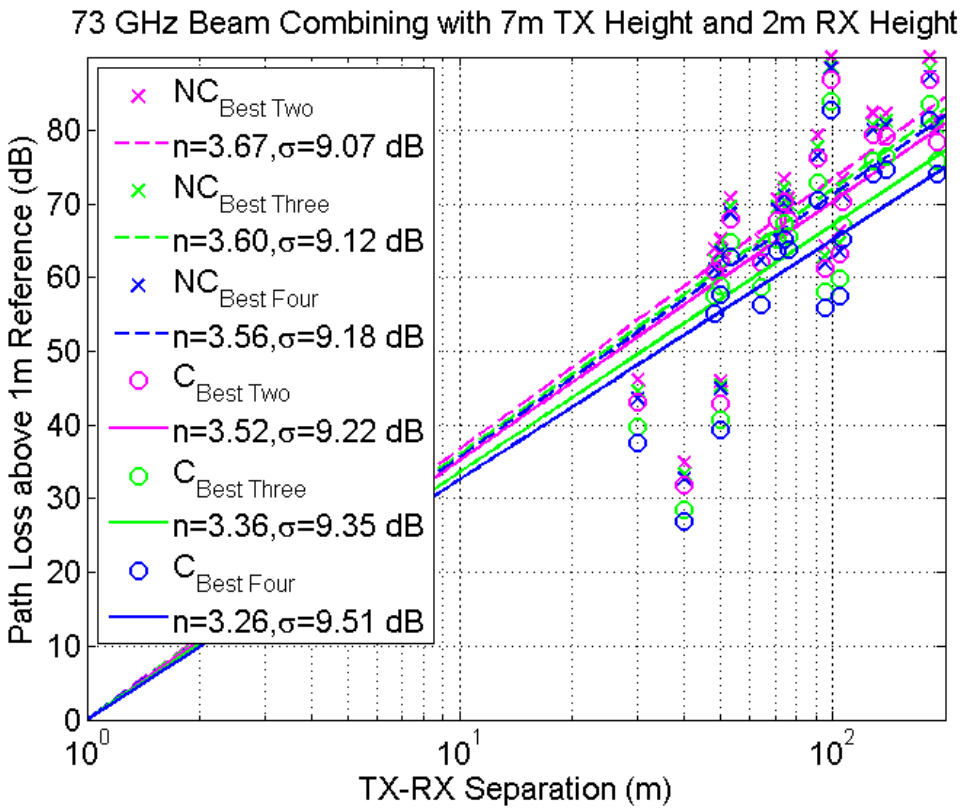

Fig. 87. Path loss versus TX-RX separation at 73 GHz in NYC for the best (i.e. strongest) two, three and four signals combined noncoherently and coherently at each RX location for 19 NLOS TX-RX location combinations with the 7m-high TX and 2m-high RX. The values in the legend represent the PLEs and shadowing factors for each kind of beam combination, "NC" denotes non-coherent combining, and "C" means coherent combining.

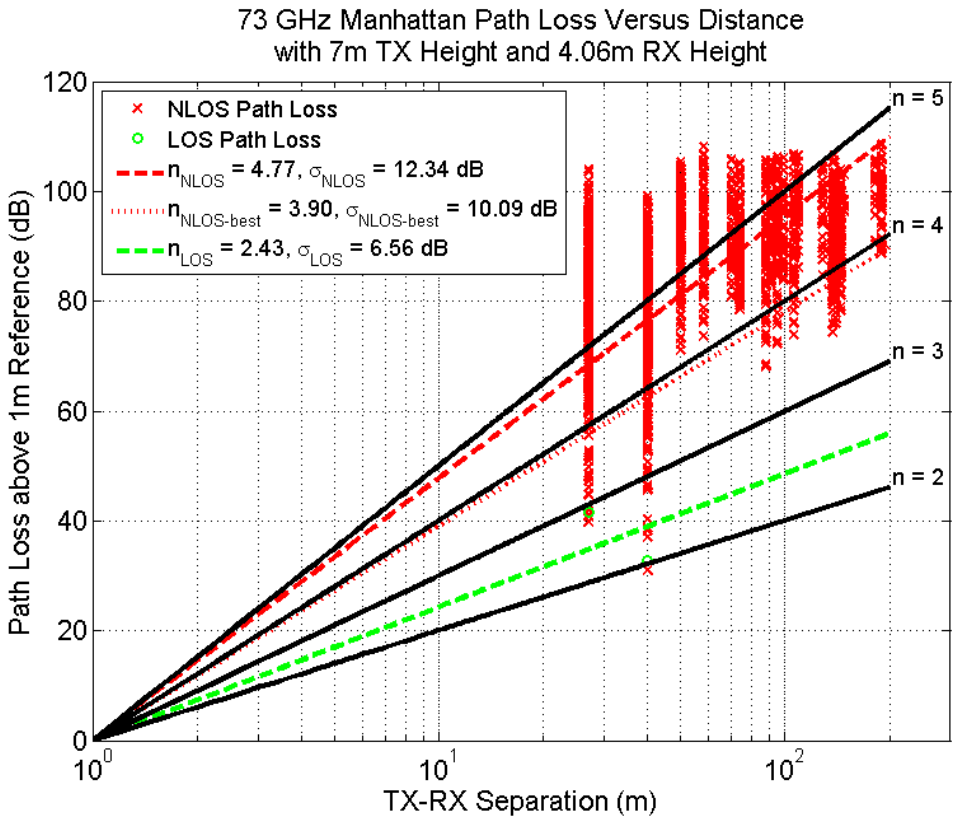

Fig. 88. Measured path loss values relative to 1 m free space path loss for 73 GHz outdoor cellular channels. These path loss values were measured using the 27 dBi narrow beam antennas for 21 TX-RX location combinations with 7m TX height and 4.06m RX height. The values in the legend represent the PLEs and shadowing factors.

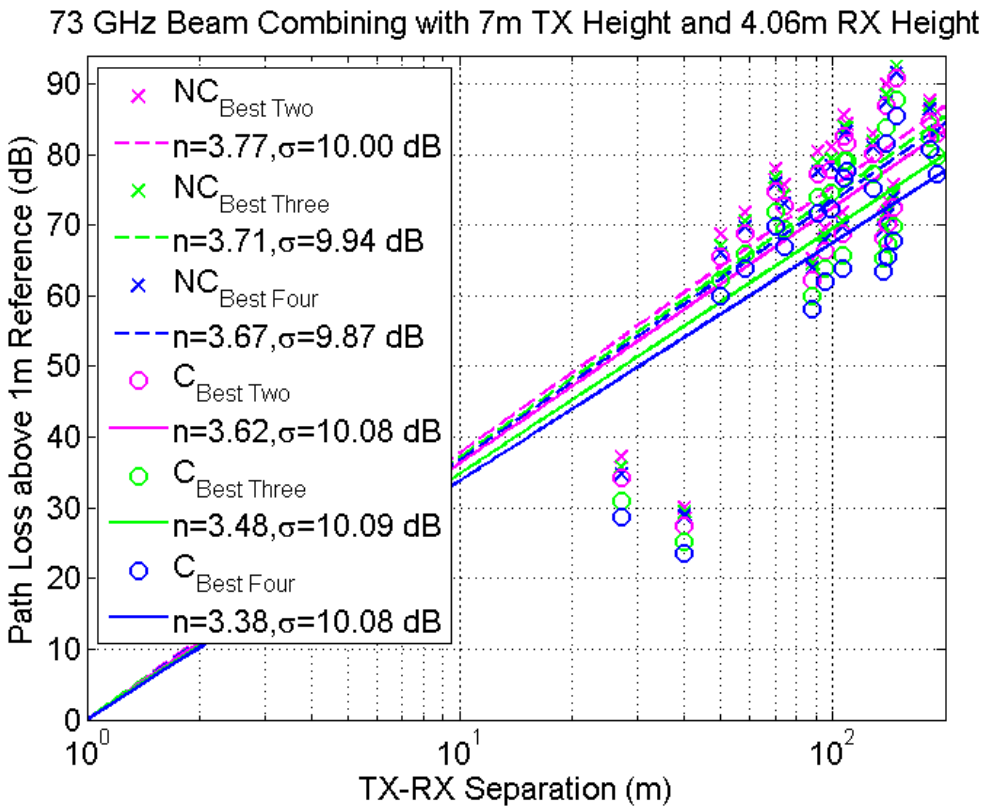

Fig. 89. Path loss versus TX-RX separation at 73 GHz in NYC for the best (i.e. strongest) two, three and four signals combined noncoherently and coherently at each RX location for 21 NLOS TX-RX location combinations with the 7m-high TX and 4.06m-high RX. The values in the legend represent the PLEs and shadowing factors for each kind of beam combination, "NC" denotes non-coherent combining, and "C" means coherent combining.

Fig. **90** and Fig. **91** demonstrate the behavior of PLEs and shadowing factors before and after coherent multi-beam combining for the backhaul-to-backhaul scenario with the 17m-high TX and 2 m-high RX antennas. It is conspicuous from these figures that combining the few strongest signals can tremendously raise signal quality and reduce the PLEs, thus equivalently improving the link budget and extending the transmitter's coverage area. Similar path loss scatter plot and coherent beam combining results for the 17 m-high TX and 4.06 m-high RXs at 73 GHz are given in Fig. **92** and Fig. **93.**

The PLEs and shadowing factors without and with multi-beam combining for all TX and RX heights at 73 GHz are provided in Table **10.** It can be summarized from the table that the PLEs are generally lower when the height of TX antenna is raised while the RX antennas are of the same

height at 73 GHz. This is because when the TX antenna is raised, the emitted signal usually encounters fewer obstructions which may block the path or absorb its energy as it propagates in the channel, thus would be less attenuated. This implies the possibility of obtaining better signal quality by increasing the TX antenna height at 73 GHz.

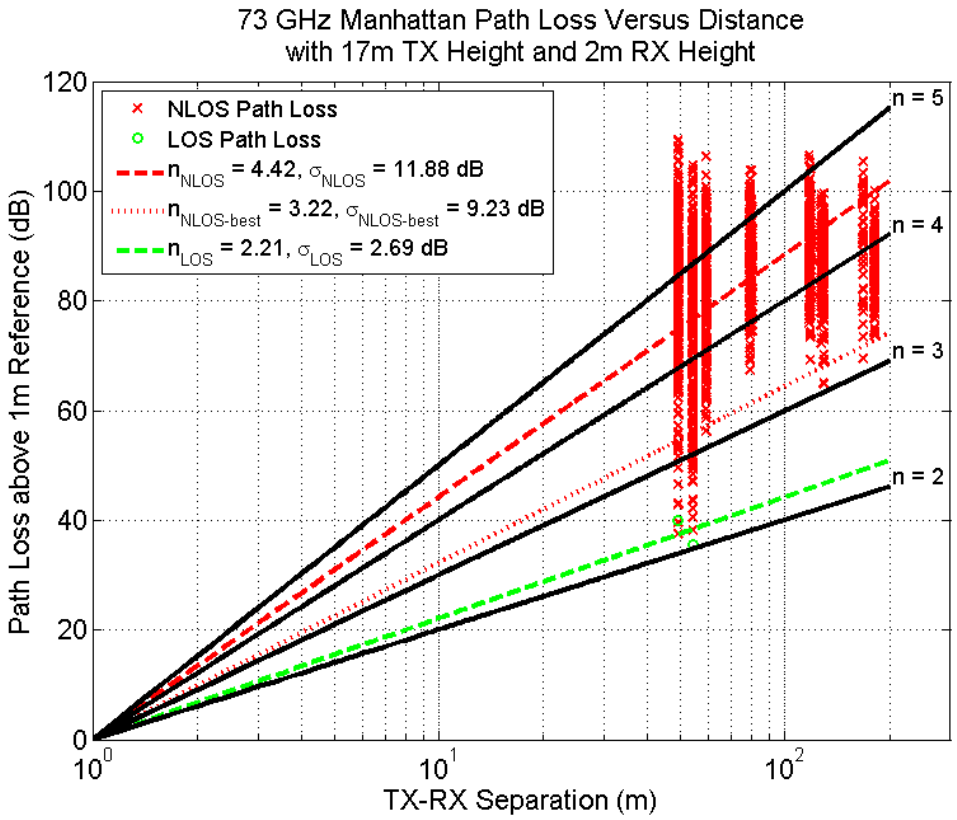

Fig. 90. Measured path loss values relative to 1 m free space path loss for 73 GHz outdoor cellular channels. These path loss values were measured using the 27 dBi narrow beam antennas for 11 TX-RX location combinations with 17m TX height and 2m RX height. The values in the legend represent the PLEs and shadowing factors.

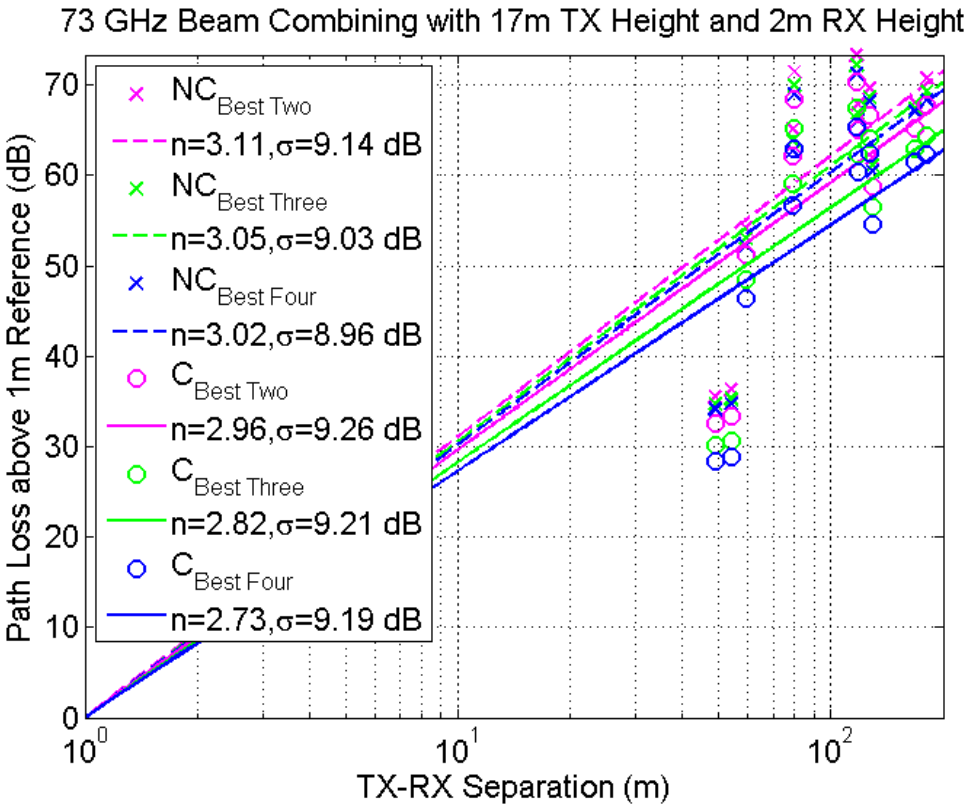

Fig. 91. Path loss versus TX-RX separation at 73 GHz in NYC for the best (i.e. strongest) two, three and four signals combined noncoherently and coherently at each RX location for 11 NLOS TX-RX location combinations with the 17m-high TX and 2m-high RX. The values in the legend represent the PLEs and shadowing factors for each kind of beam combination, "NC" denotes non-coherent combining, and "C" means coherent combining.

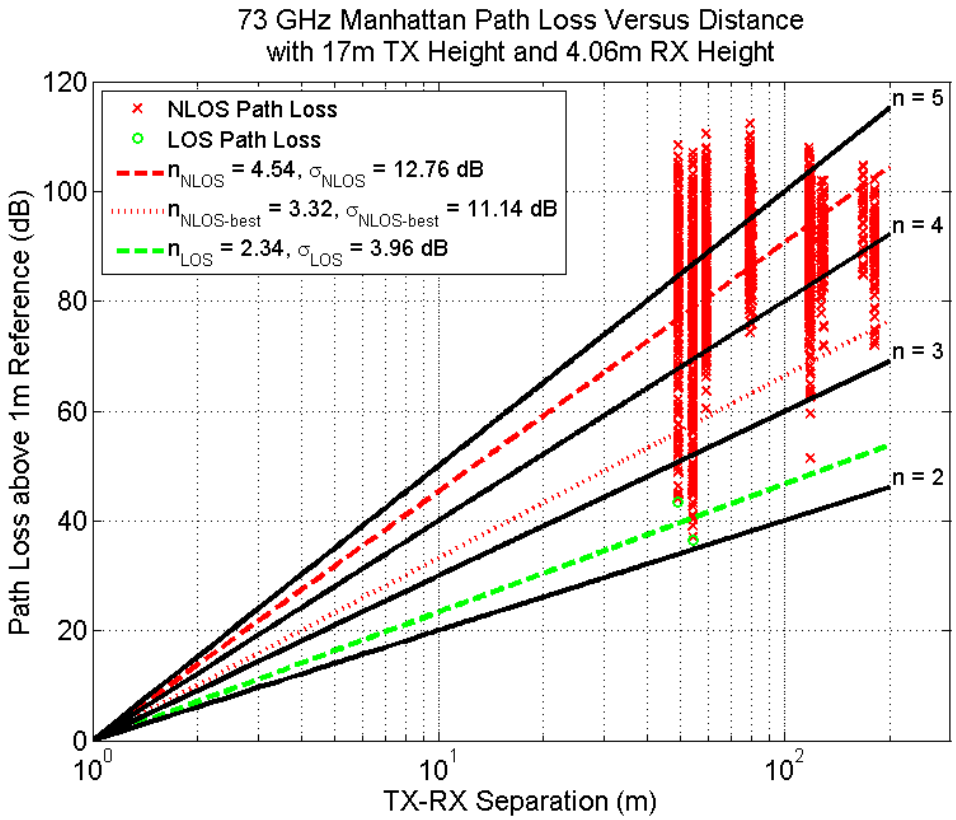

Fig. 92. Measured path loss values relative to 1 m free space path loss for 73 GHz outdoor cellular channels. These path loss values were measured using the 27 dBi narrow beam antennas for 11 TX-RX location combinations with 17m TX height and 4.06m RX height. The values in the legend represent the PLEs and shadowing factors.

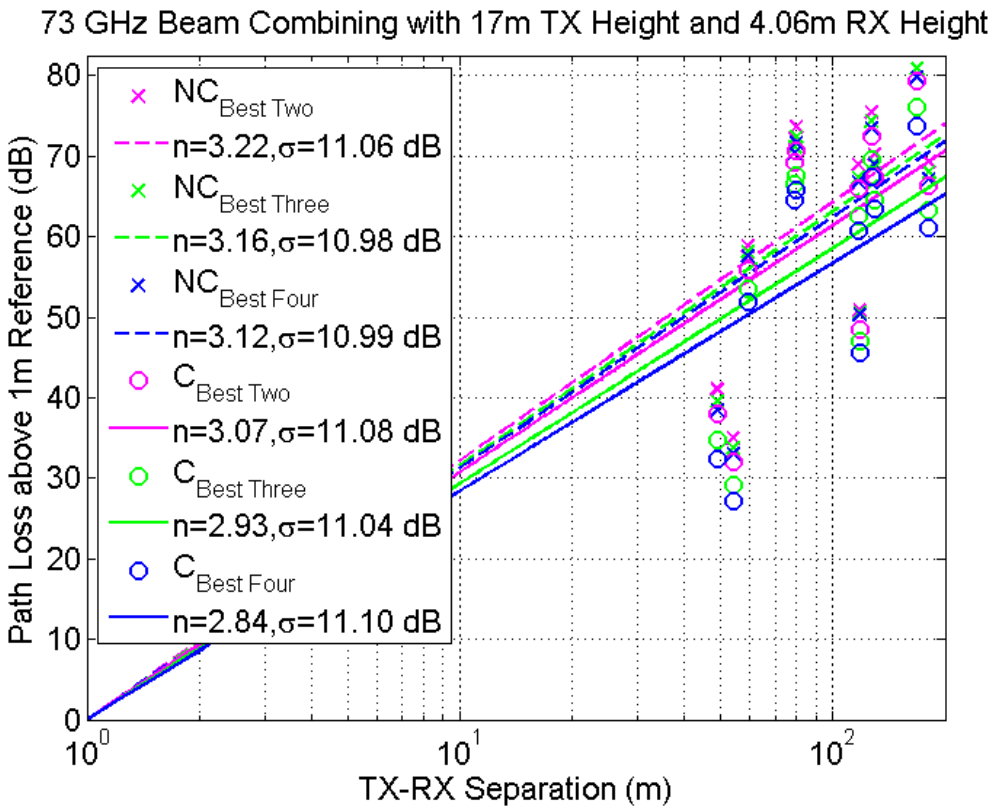

Fig. 93. Path loss versus TX-RX separation at 73 GHz in NYC for the best (i.e. strongest) two, three and four signals combined noncoherently and coherently at each RX location for 11 NLOS TX-RX location combinations with the 17m-high TX and 4.06m-high RX. The values in the legend represent the PLEs and shadowing factors for each kind of beam combination, "NC" denotes non-coherent combining, and "C" means coherent combining.

4.6 Comparison of 28 GHz and 73 GHz Beam Combining Results

The contrast of the PLEs and shadowing factors in different scenarios between 28 GHz and 73 GHz carrier frequencies is also manifested by Table **10**. Without beam combining, comparing the PLEs in base station-to-mobile scenarios at both frequencies, where the RX antenna height is 1.5 m at 28 GHz and 2 m at 73 GHz, it can be obtained that the overall PLEs in NLOS situations are smaller at 28 GHz than at 73 GHz. While the PLEs at both 28 GHz and 73 GHz are around 4 or 5 for the overall received beams, and around 3.5 on average for the best single beam, indicating that the path loss values are comparable for same TX heights and similar RX heights. These observations suggest that there is no definite relationship between path loss and the carrier frequency in the

mmWave range in a densely populated urban environment like New York City. It is evident from the 8th column in Table 1 that the PLE for a certain propagation condition exhibits the same trend at both 28 GHz and 73 GHz, i.e. it drops considerably after multi-beam combining is performed, and decreases monotonically as the number of combined signals increases. For instance, the PLE corresponding to four coherently combined signals in a NLOS environment with 7 m TX height and 2 m RX height at 73 GHz declined by 1.65 and 0.55 compared to that before beam combining and that of using the single best beam, respectively. Considering the TX-RX separation of 100 m, when the PLE decreases from 4.91 to 3.26, the equivalent path loss drops by about 33 dB, and 11 dB for the PLE descending from 3.81 (corresponding to the best single beam) to 3.26, which is a remarkable improvement in link budget and quite significant to carriers. Similarly, path loss can be reduced by up to 26.4 dB for 100 m T-R separation at 28 GHz contrasting the result of combining four beams and that without beam combining. These improvements can be easily found based on Eq. (4) by using d_0 = 1 m, and d = 100 m, and comparing the path loss values for the two different PLEs.

Table 10 Path loss exponents (PLEs) with respect to 1 m free space references and standard deviations (or shadowing factors) at both 28 GHz and 73 GHz for various transmitter and receiver heights and different propagation scenarios. The beam combining results are obtained using the coherent combining scheme. At each TX-RX location combination, at least four unique beams are obtained and all beams are assumed to be aligned in time for coherent power combining.

Frequency (GHz)	TX, RX Antenna Gains (dBi)	TX-RX Separation Range (m)	TX Height (m)	RX Height (m)	Path Loss Scenarios (Using Coherent Beam Combining)		Path Loss Exponent (PLE)	σ_{SF} (dB)
28 GHz New York City	+24.5, +24.5 both vertically polarized	30 ~ 200	7	1.5	Non-line-of-sight (NLOS)	Overall	4.47	10.20
						Best One	3.68	8.76
						Best Two	3.41	9.03
						Best Three	3.26	9.25
						Best Four	3.15	9.39
			17	1.5	Non-line-of-sight (NLOS)	Overall	4.39	9.00
						Best One	3.79	8.46
						Best Two	3.52	8.75
						Best Three	3.36	8.95
						Best Four	3.25	9.11
73 GHz New York City	+27, +27 both vertically polarized	30 ~ 200	7	4.06	Line-of-sight (LOS)		2.43	6.56
					Non-line-of-sight (NLOS)	Overall	4.77	12.34
						Best One	3.90	10.09
						Best Two	3.62	10.08
						Best Three	3.48	10.09
						Best Four	3.38	10.08
				2	Line-of-sight (LOS)		2.49	5.17
					Non-line-of-sight (NLOS)	Overall	4.91	11.81
						Best One	3.81	8.85
						Best Two	3.52	9.22
						Best Three	3.36	9.35
						Best Four	3.26	9.51
			17	4.06	Line-of-sight (LOS)		2.34	3.96
					Non-line-of-sight (NLOS)	Overall	4.54	12.76
						Best One	3.32	11.14
						Best Two	3.07	11.08
						Best Three	2.93	11.04
						Best Four	2.84	11.10
				2	Line-of-sight (LOS)		2.21	2.69
					Non-line-of-sight (NLOS)	Overall	4.42	11.88
						Best One	3.22	9.23
						Best Two	2.96	9.26
						Best Three	2.82	9.21
						Best Four	2.73	9.19

The striking effect of coherent multi-beam combining at the mobile receiver antenna on PLEs and link quality at both 28 GHz and 73 GHz carrier frequencies has been demonstrated. The results show that beam combining can significantly reduce PLEs (e.g. from 4.91 to 3.26) and shadowing factors (e.g. from 11.81 to 9.51), thus improving received signal quality and extending link coverage. In particular, combining the four strongest signals yields 33 dB of link enhancement over arbitrarily pointed beams, and more 11 dB of improvement when compared to a single optimum beam over a 100 m TX-RX separation at 73 GHz. And the maximum possible improvement on received power at 28 GHz reaches 26.4 dB. Besides, path loss exhibit similar values at both frequencies. This work reveals the potential of using smart antennas to exploit the spatial degrees of freedom in the

propagation channel and ameliorate link margin in future cellular communication systems.

4.7 Beam Combining Results Using Measured Data Defined in A Omni Model

In the previous section, NLOS consists of both strict NLOS and LOS_NB. In this section, in order to keep consistent with the definition used in omni-directional models, NLOS only refers to strict NLOS excluding LOS_NB. The corresponding path loss scatter plots and beam combining results at 28 GHz and 73 GHz are shown in Fig. **94** to Fig. **105**. Although the NLOS environment is defined differently from that in the previous section, the path loss values, PLEs, and beam combining results exhibit similar behavior.

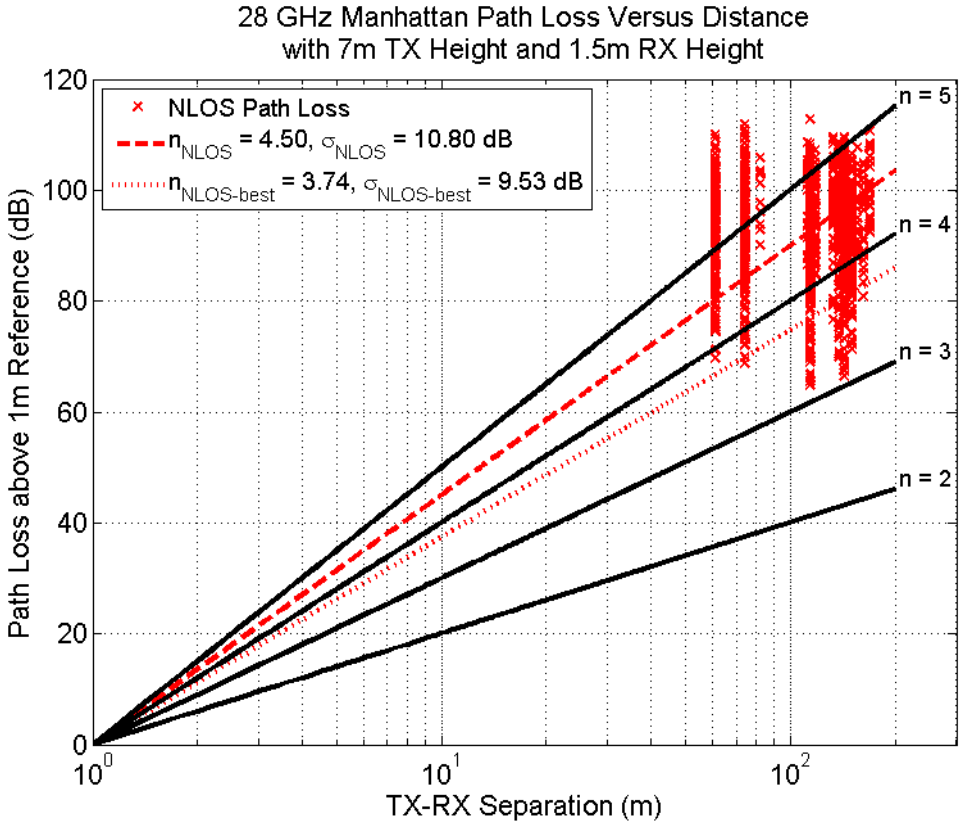

Fig. 94. Measured path loss values relative to 1 m free space path loss for 28 GHz outdoor cellular channels. These path loss values were measured using the 24.5 dBi narrow beam antennas with 7m TX height and 1.5m RX height. The values in the legend represent the PLEs and shadowing factors.

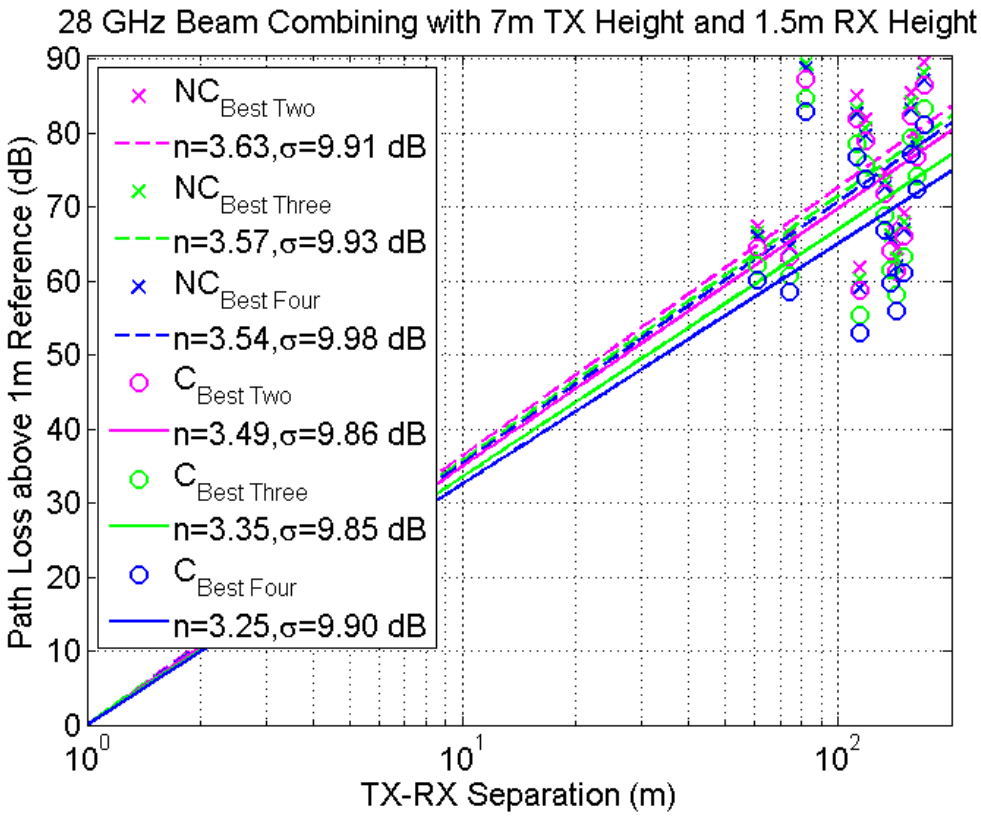

Fig. 95. Path loss versus TX-RX separation at 28 GHz in NYC for the best (i.e. strongest) two, three and four signals combined coherently at each RX location with the 7m-high TX and 1.5m-high RX. The values in the legend represent the PLEs and shadowing factors for each kind of beam combination.

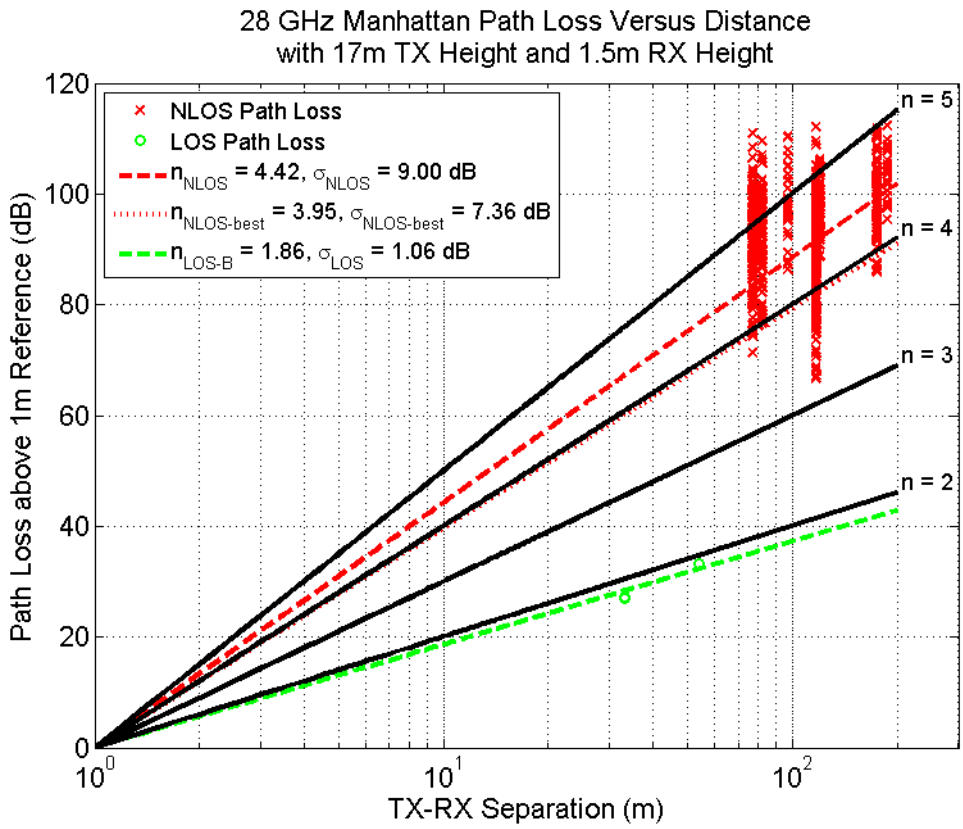

Fig. 96. Measured path loss values relative to 1 m free space path loss for 28 GHz outdoor cellular channels. These path loss values were measured using the 24.5 dBi narrow beam antennas with 17m TX height and 1.5m RX height. The values in the legend represent the PLEs and shadowing factors. The values in the legend represent the PLEs and shadowing factors.

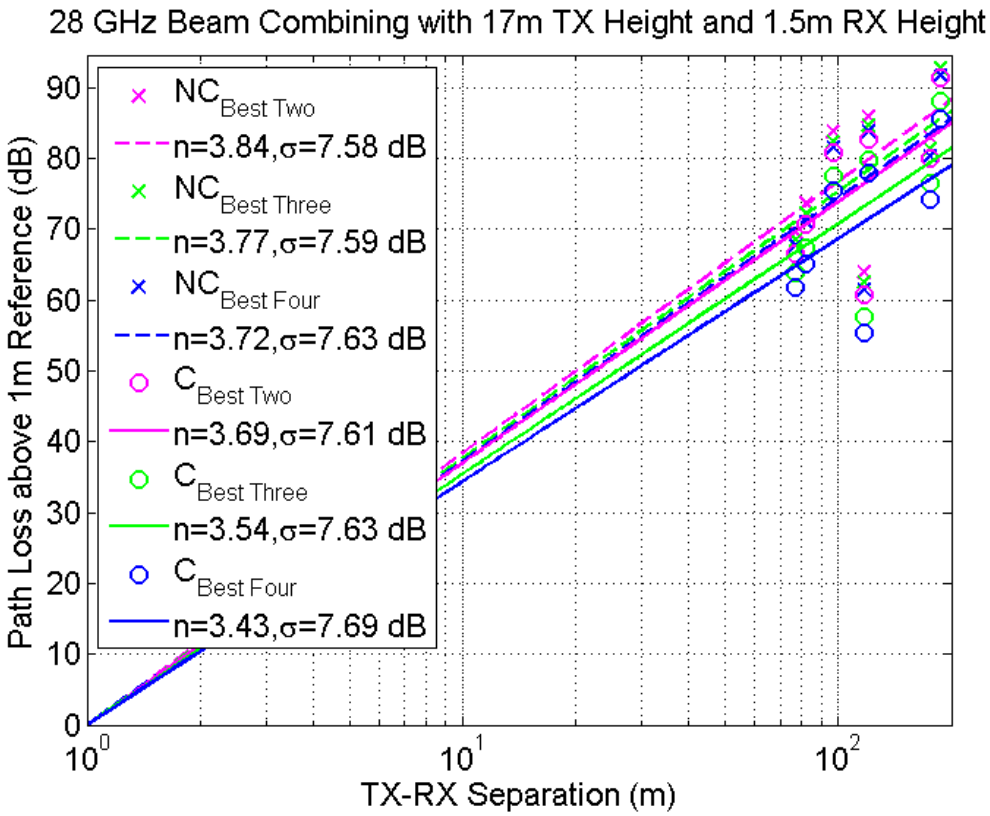

Fig. 97. Path loss versus TX-RX separation at 28 GHz in NYC for the best (i.e. strongest) two, three and four signals combined coherently at each RX location with the 17m-high TX and 1.5m-high RX. The values in the legend represent the PLEs and shadowing factors for each kind of beam combination.

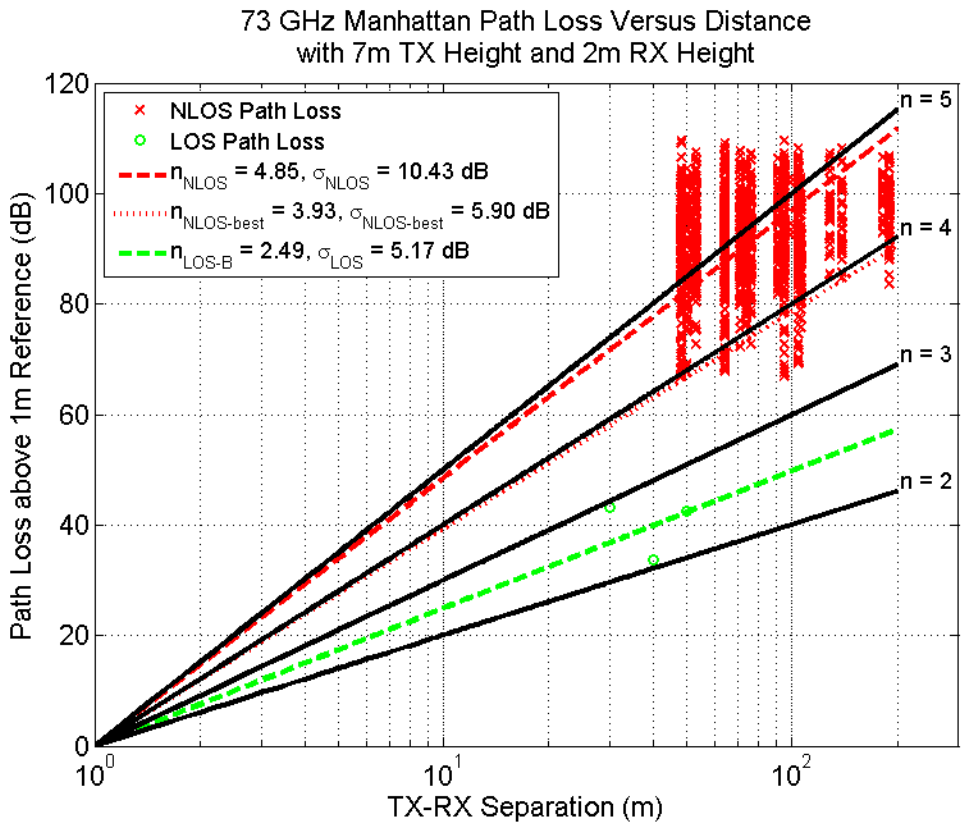

Fig. 98. Measured path loss values relative to 1 m free space path loss for 73 GHz outdoor cellular channels. These path loss values were measured using the 27 dBi narrow beam antennas for 19 TX-RX location combinations with 7m TX height and 2m RX height. The values in the legend represent the PLEs and shadowing factors.

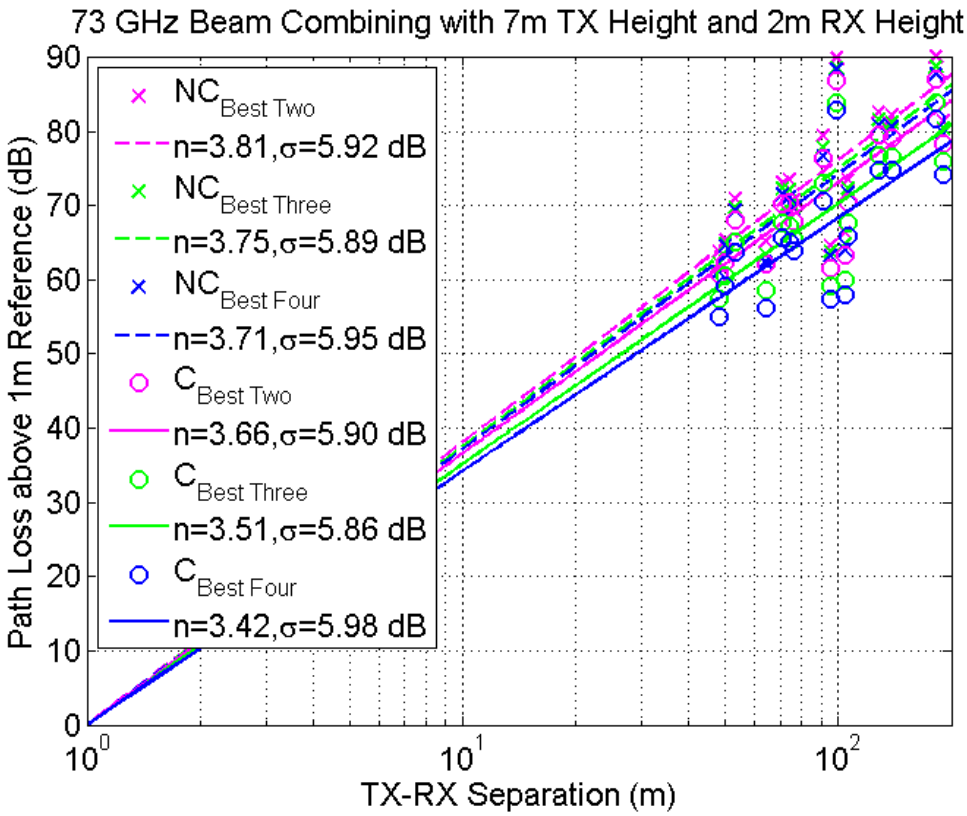

Fig. 99. Path loss versus TX-RX separation at 73 GHz in NYC for the best (i.e. strongest) two, three and four signals combined noncoherently and coherently at each RX location for 19 NLOS TX-RX location combinations with the 7m-high TX and 2m-high RX. The values in the legend represent the PLEs and shadowing factors for each kind of beam combination, "NC" denotes non-coherent combining, and "C" means coherent combining.

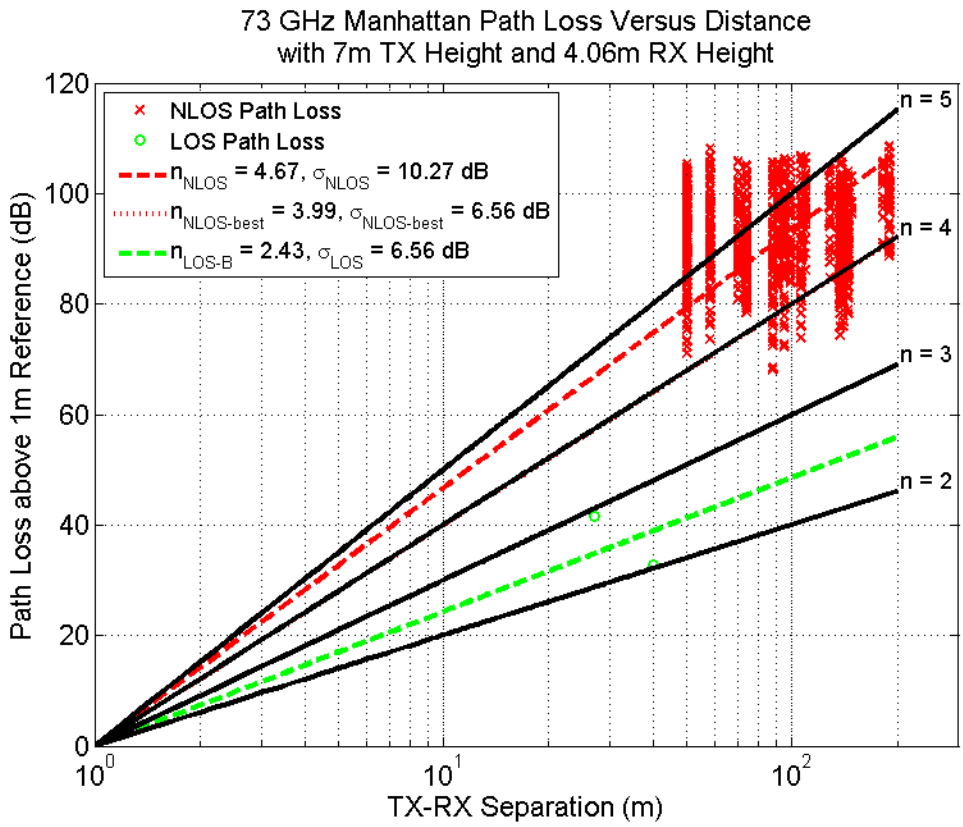

Fig. 100. Measured path loss values relative to 1 m free space path loss for 73 GHz outdoor cellular channels. These path loss values were measured using the 27 dBi narrow beam antennas for 21 TX-RX location combinations with 7m TX height and 4.06m RX height. The values in the legend represent the PLEs and shadowing factors.

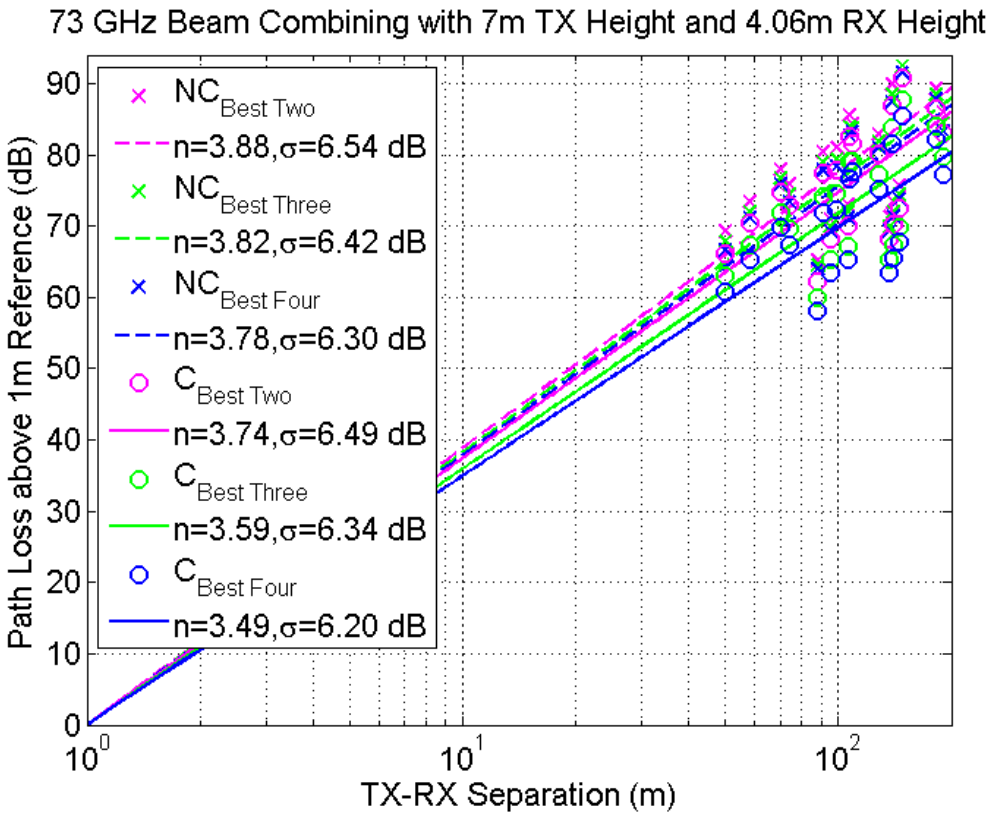

Fig. 101. Path loss versus TX-RX separation at 73 GHz in NYC for the best (i.e. strongest) two, three and four signals combined noncoherently and coherently at each RX location for 21 NLOS TX-RX location combinations with the 7m-high TX and 4.06m-high RX. The values in the legend represent the PLEs and shadowing factors for each kind of beam combination, "NC" denotes non-coherent combining, and "C" means coherent combining.

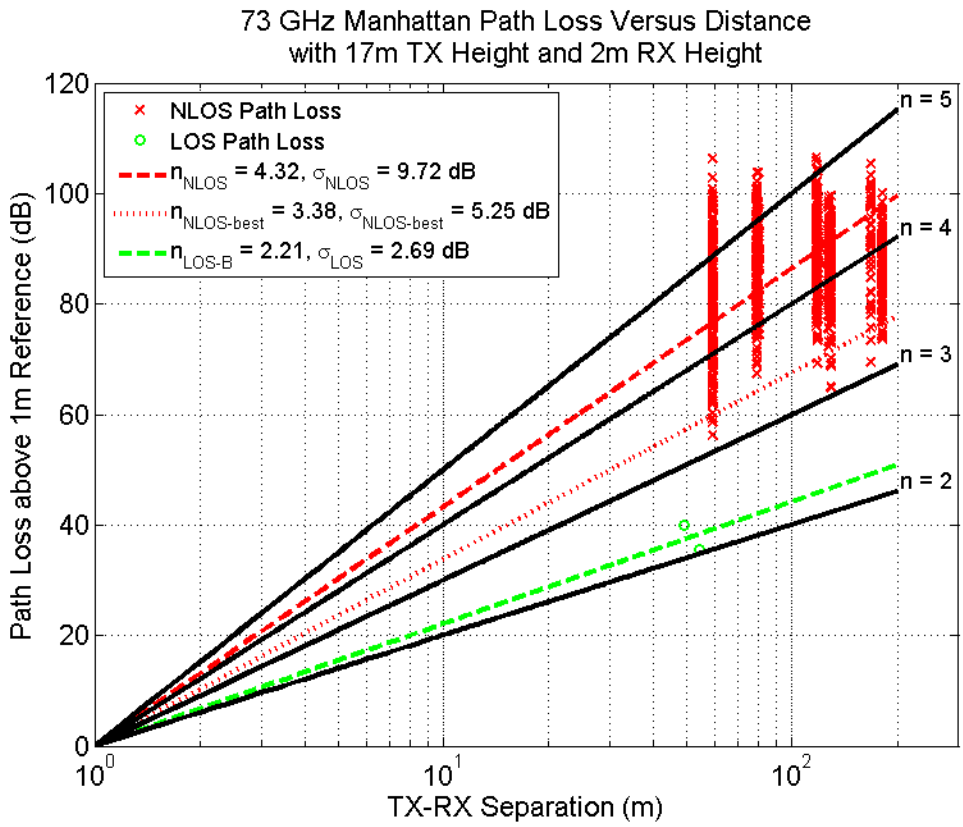

Fig. 102. Measured path loss values relative to 1 m free space path loss for 73 GHz outdoor cellular channels. These path loss values were measured using the 27 dBi narrow beam antennas for 11 TX-RX location combinations with 17m TX height and 2m RX height. The values in the legend represent the PLEs and shadowing factors.

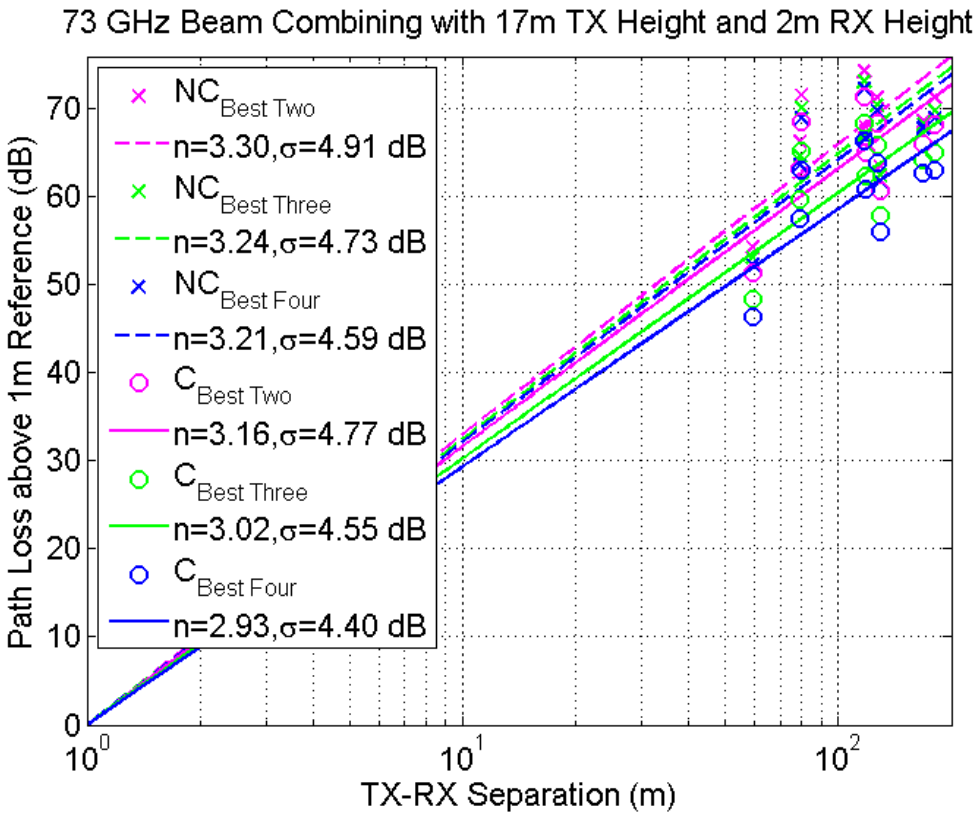

Fig. 103. Path loss versus TX-RX separation at 73 GHz in NYC for the best (i.e. strongest) two, three and four signals combined noncoherently and coherently at each RX location for 11 NLOS TX-RX location combinations with the 17m-high TX and 2m-high RX. The values in the legend represent the PLEs and shadowing factors for each kind of beam combination, "NC" denotes non-coherent combining, and "C" means coherent combining.

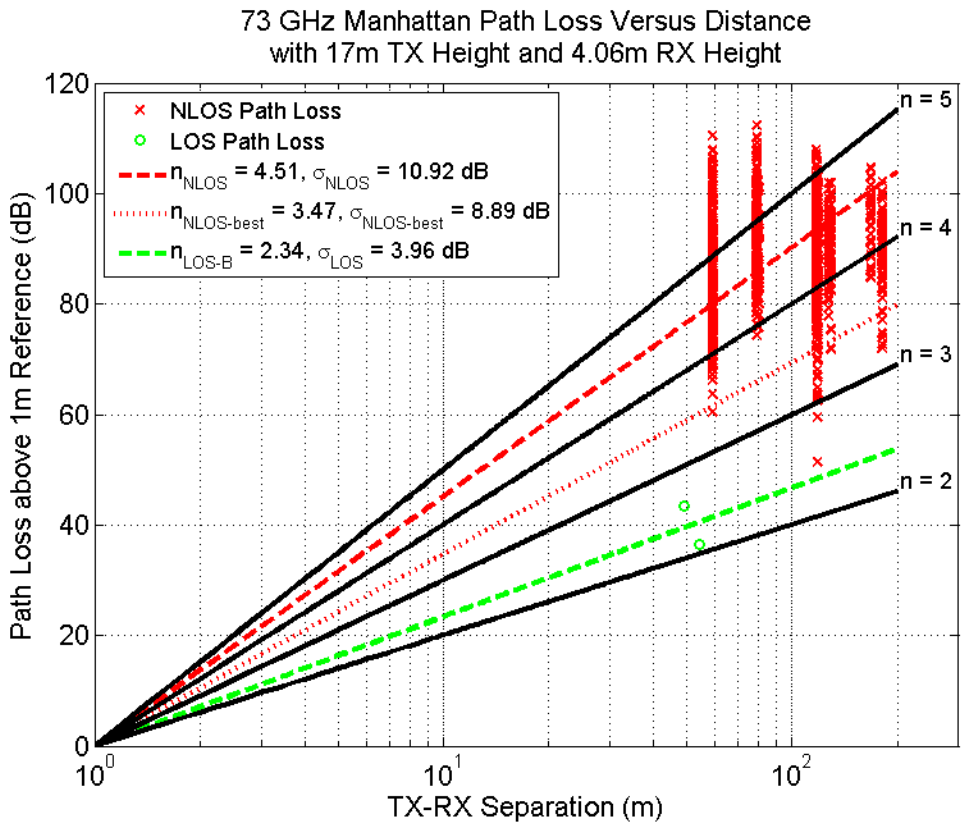

Fig. 104. Measured path loss values relative to 1 m free space path loss for 73 GHz outdoor cellular channels. These path loss values were measured using the 27 dBi narrow beam antennas for 11 TX-RX location combinations with 17m TX height and 4.06m RX height. The values in the legend represent the PLEs and shadowing factors.

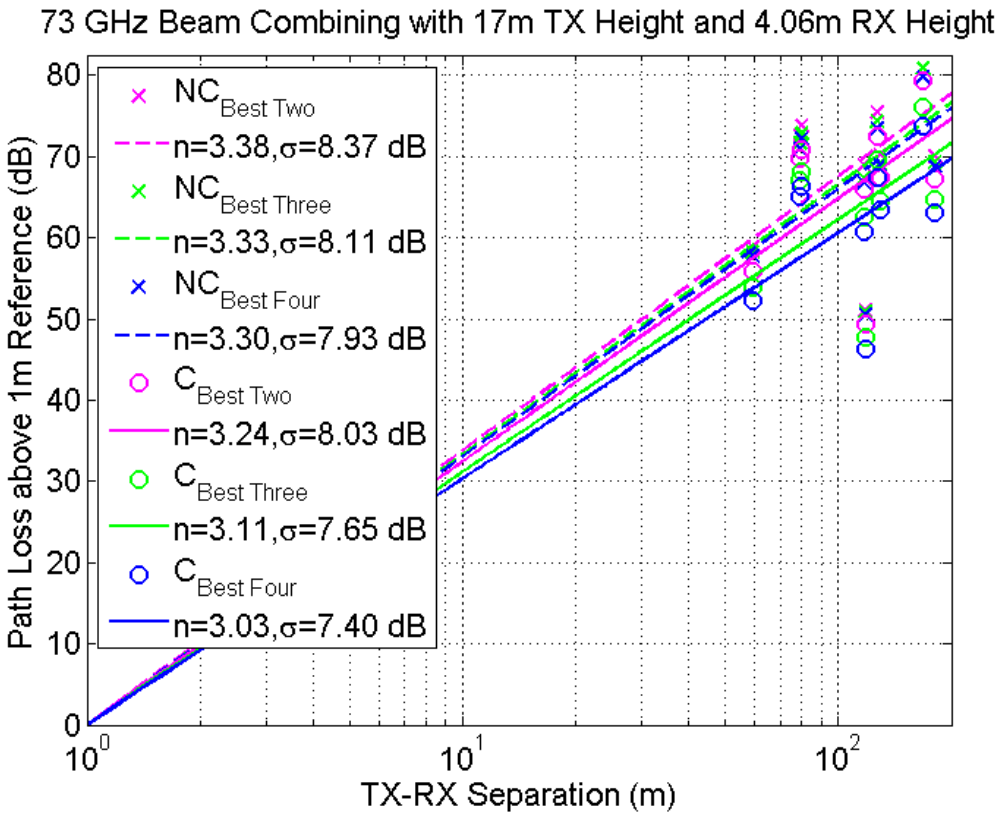

Fig. 105. Path loss versus TX-RX separation at 73 GHz in NYC for the best (i.e. strongest) two, three and four signals combined noncoherently and coherently at each RX location for 11 NLOS TX-RX location combinations with the 17m-high TX and 4.06m-high RX. The values in the legend represent the PLEs and shadowing factors for each kind of beam combination, "NC" denotes non-coherent combining, and "C" means coherent combining.

CHAPTER 5 MIMO SYSTEMS AND BEAMFORMING

5.1 Antenna Array

Antenna arrays are usually utilized to steer radiated power towards a desired direction. The basic block of an antenna array is a single antenna, which can be a dipole antenna, a patch antenna, etc. Fig. **106** illustrates a 3D schematic of a single rectangular patch antenna and its radiation pattern at 2.4 GHz simulated using ADS (Advanced Design System, Agilent Technologies).

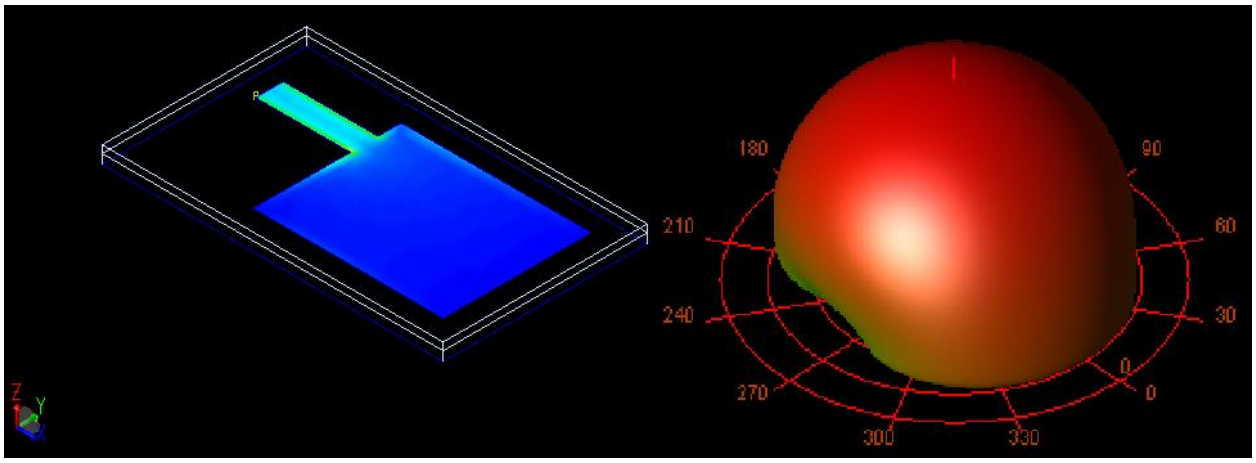

Fig. 106. 3D layout of a single rectangular patch antenna (left) and its radiation pattern at 2.4 GHz (right) (simulated by ADS).

The most fundamental feature of an array is that the relative displacements of the antenna elements with respect to each other introduce relative phase shifts in the radiation vectors, which can then add constructively in some directions or destructively in others [71]. This is a direct consequence of the translational phase-shift property of Fourier transforms: a translation in space or time becomes a phase shift in the Fourier domain. There are many forms of antenna arrays, such as the uniform linear array (ULA), uniform rectangular array (URA), and circular array, etc. ULA and URA are the most common forms of antenna arrays.

5.1.1 Uniform Linear Array

A uniform linear array (ULA) is a one-dimensional array, where the antennas are uniformly distributed in a line with equal spacing between adjacent antenna elements. The azimuth angle and elevation angle are represented as ϕ and θ, respectively. Note that φ denotes the azimuth incident angle between the incident direction and the normal direction of the ULA. Define $\psi = kdsin(\varphi)$, where $k = 2\pi/\lambda$ is the wavenumber, and d is the spacing between adjacent array elements. Considering the simplest case where the array elements have equal weights. For an array of N isotropic elements at locations $x_n = nd$, n = 0, 1,…, N-1, the array factor is defined as

$$A(\psi) = \frac{1}{N}\left[1 + e^{j\psi} + e^{2j\psi} + \cdots + e^{(N-1)j\psi}\right] = \frac{1}{N}\frac{e^{jN\psi} - 1}{e^{j\psi} - 1} = \frac{\sin\left(\frac{N\psi}{2}\right)}{N\sin\left(\frac{\psi}{2}\right)} e^{j(N-1)\psi/2}$$

where the array is along the x-axis and the look direction is on the xy-plane. The array factor has been normalized to have unity gain at dc, that is, at $\psi = 0$, or at the broadside azimuthal angle $\varphi = 0^0$. The normalized power gain of the array is:

$$g(\varphi) = |A(\psi)|^2 = \left|\frac{\sin\left(\frac{N\psi}{2}\right)}{N\sin\left(\frac{\psi}{2}\right)}\right|^2 = \left|\frac{\sin\left(\frac{Nkdsin(\phi)}{2}\right)}{N\sin\left(\frac{kdsin(\phi)}{2}\right)}\right|^2$$

The main beam direction if the ULA described by the above equation is at the broadside ($\phi = 0^0$). Table 11 lists the simulated half power beamwidth (HPBW) as a function of the number of array elements N. As expected from the Fourier transform relationship, the larger the N is, the narrower the HPBW.

Table 11 Simulated relationship between the number of ULA elements and half power beamwidth (HPBW) of the main beam. The elements spacing is half the carrier wavelength.

Number of Array Elements N	4	8	16	32
HPBW (^{0})	26.34	12.80	6.36	3.20

A ULA is typically designed to have maximum directive gain at broadside (for an array along the x-axis.). It is often necessary to "electronically" rotate, or steer, the array pattern towards some other direction, e.g. ϕ_0, without physically rotating it. The corresponding wavenumber at the desired look-direction is:

$$\psi_0 = kdsin(\phi_0)$$

Such steering operation can be achieved by wavenumber translation in ψ-space, that is, replacing the broadside pattern $A(\psi)$ by the translated pattern $A(\psi - \psi_0)$. Thus, we define:

$$A(\psi') = A(\psi - \psi_0)$$

and the translated wavenumber variable

$$\psi' = \psi - \psi_0 = kd(\sin\phi - \sin\phi_0)$$

Fig. **107** illustrates the change in the amplitude of the array factor $A(\phi)$ when the mainlobe direction is altered from the broadside to 30^0. The variation of the corresponding power gain pattern $g(\phi)$ is shown in Fig. **108.** The number of array elements N = 8, and the element spacing is half the carrier wavelength.

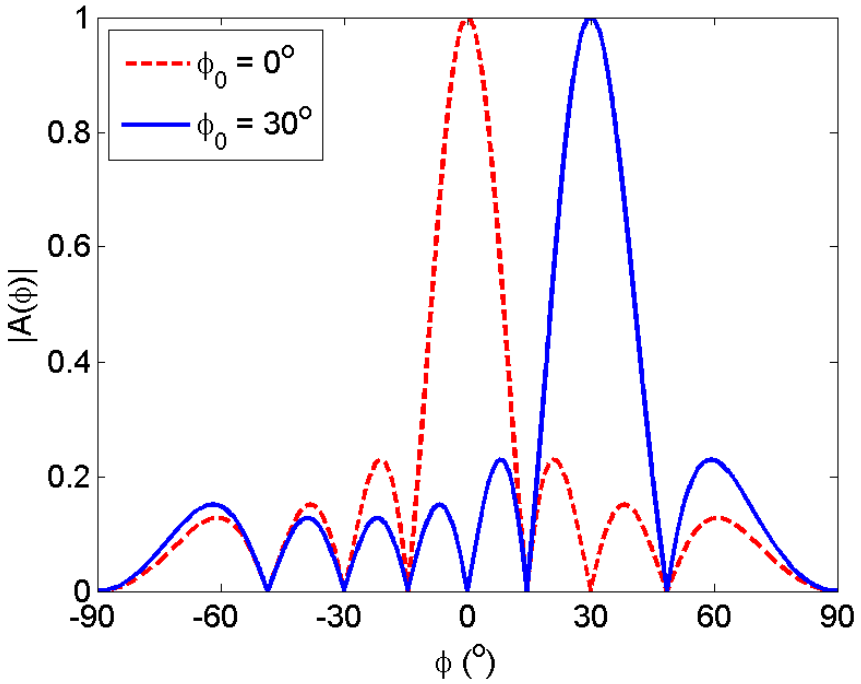

Fig. 107. Change in the amplitude of the array factor $\mathbf{A}(\boldsymbol{\phi})$ when the mainlobe direction $\boldsymbol{\phi}$ varies from the broadside to 30^0.

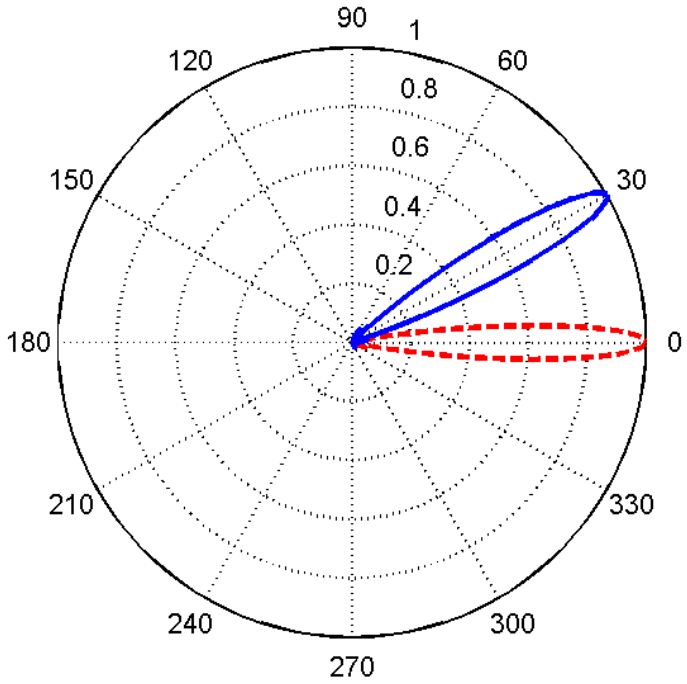

Fig. 108. Change in the power gain pattern $\mathbf{g}(\boldsymbol{\phi})$ when the mainlobe direction $\boldsymbol{\phi}$ varies from the broadside to 30^0. The dashed red curve denote the case of the broadside, and the solid blue curve denote the case of 30^0.

Table **12** shows the simulated relationship between the half power beamwidth (HPBW) of the main lobe and steering direction ϕ_0 for N = 8 and N = 16, respectively. As can be observed, a larger value of N renders a narrower HPBW at the same look direction, and supports a wider scanning range. For example, when N = 8, the steerable angle region is -60^0 to 60^0; while the region is extended to -70^0 to 70^0 when N = 16.

Table 12 Simulated relationship between the half power beamwidth (HPBW) of the main lobe and steering direction $\boldsymbol{\phi_0}$ for N = 8 and N = 16, respectively. The elements spacing is half the carrier wavelength.

	ϕ_0 (^{0})	0	±10	±20	±30	±40	±50	±60	±70
N = 8	HPBW (^{0})	12.80	13.01	13.65	14.84	16.88	20.48	28.88	N/A
N = 16		6.36	6.53	6.77	7.35	8.32	9.96	13.00	22.25

Fig. 109 ~ Fig. 111 show the power pattern of an 8 by 8 uniform rectangular array (URA) for various target azimuth angles ϕ_0 and elevation angels θ_0. As can be observed from Fig. 111, when the desired looking angle reaches 60^0, the 8 by 8 URA forms a beam at another direction besides the target direction. While when the array size increases to 12 by 12, as shown by Fig. 112, the power pattern improves significantly with regard to the desired direction. Thus a large number of array elements is necessary in order to form a descent pattern at a large angle off the broadside.

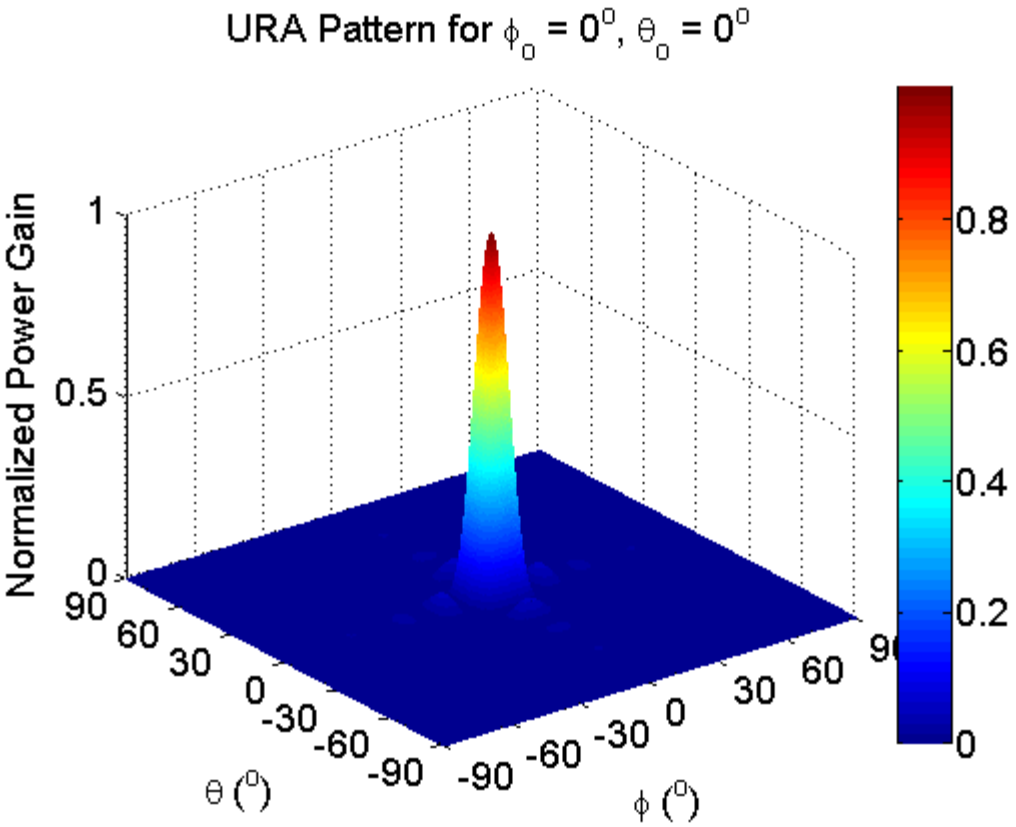

Fig. 109. Power pattern of an 8 by 8 URA for $\boldsymbol{\phi_0 = 0^0, \theta_0 = 0^0}$.

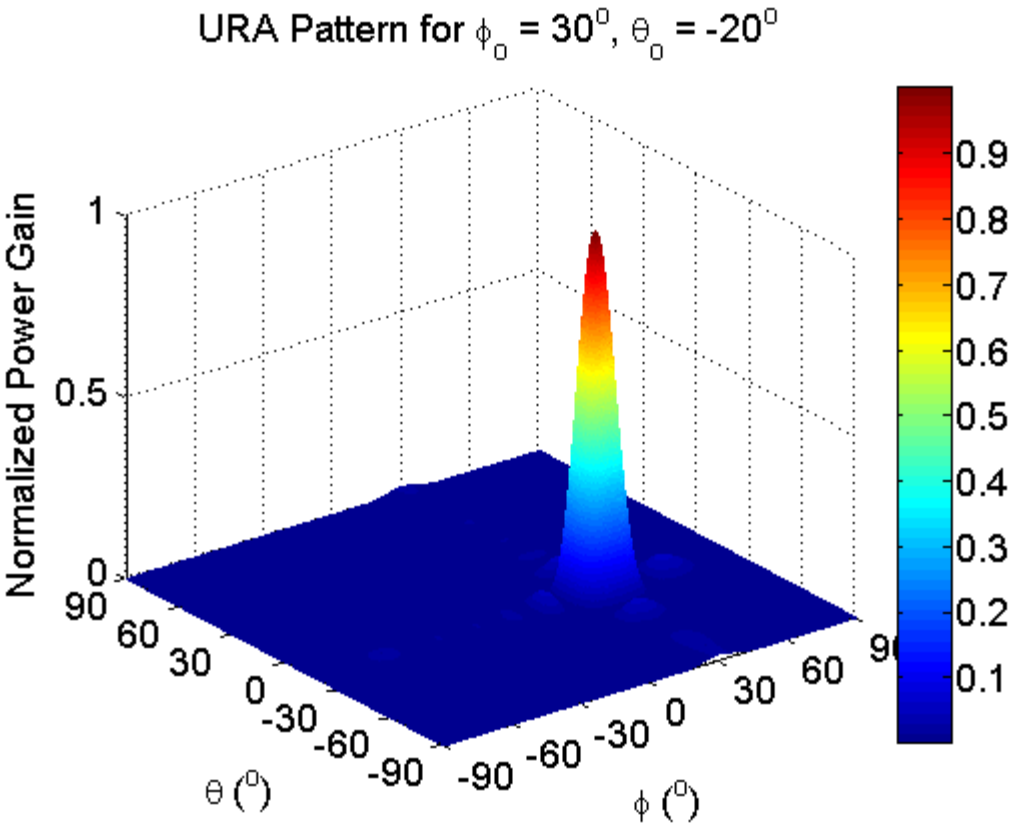

Fig. 110. Power pattern of an 8 by 8 URA for $\boldsymbol{\phi_0 = 30^0, \theta_0 = -20^0}$.

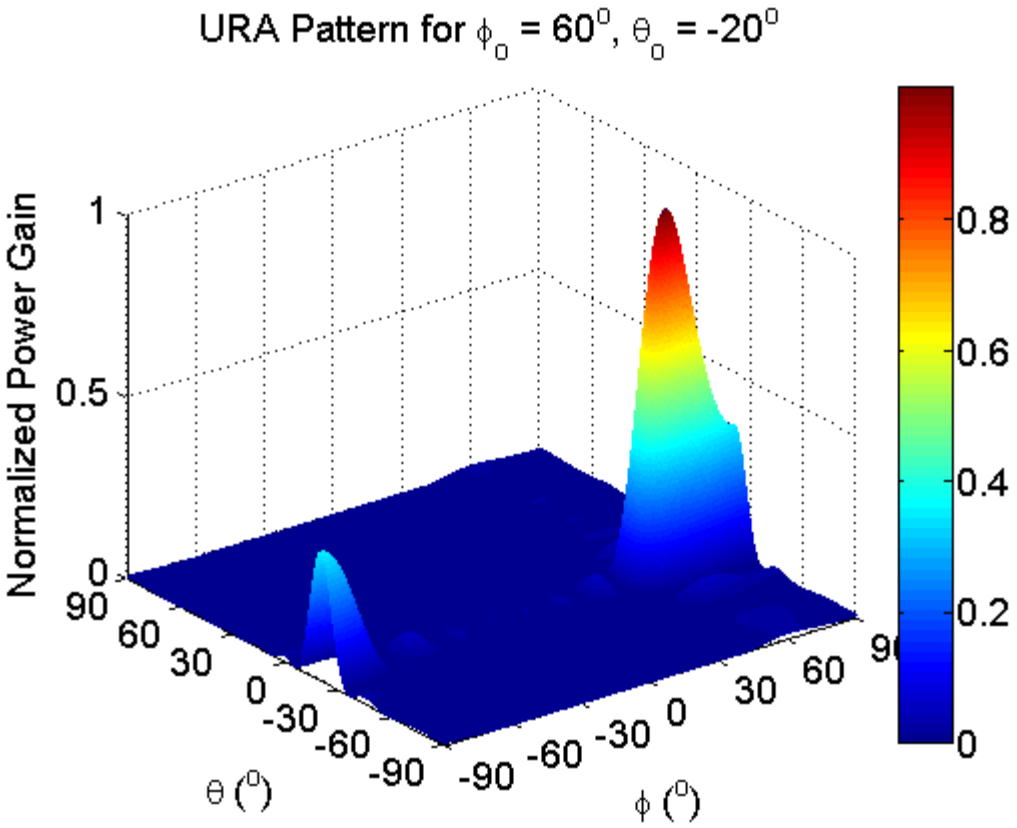

Fig. 111. Power pattern of an 8 by 8 URA for $\boldsymbol{\phi_0 = 60^0, \theta_0 = -20^0}$.

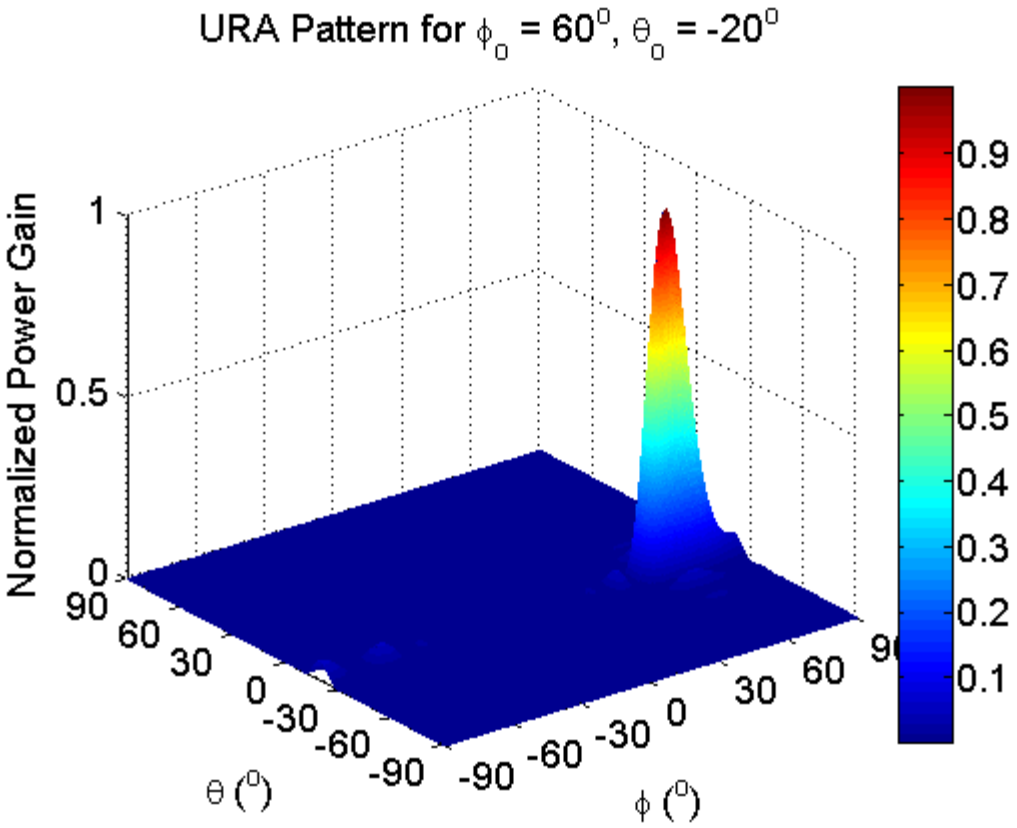

Fig. 112. Power pattern of an 12 by 12 URA for $\boldsymbol{\phi_0 = 60^0, \theta_0 = -20^0}$.

5.2 MIMO Systems

5.2.1 MIMO Channel Matrix

A narrowband time-invariant wireless channel with N_t transmit antennas and N_r receive antennas is described by an N_r by N_t deterministic matrix H. The received signal at the receiver is given by [72]

$$y = Hx + n$$

where y, x, and n denote the received signal, transmitted signal, and zero-mean white Gaussian noise respectively at the receiver. In the channel matrix H, h_{ij} represents the channel gain from transmit antenna j to receive antenna i. The signals from the transmit antennas are subject to the total power constraint P. This is a vector Gaussian channel, and the capacity can be calculated by

decomposing the vector channel into a set of parallel, independent scalar Gaussian sub-channels. From basic linear algebra, every linear transformation can be represented as a composition of three operations: a rotation operation, a scaling operation, and another rotation operation. In the notation of matrices, the matrix H has a singular value decomposition (SVD):

$$H = U\Lambda V^H$$

where U and V are unitary matrices, and Λ is a rectangular matrix whose diagonal elements are non-negative real numbers and whose off-diagonal elements are zero. The diagonal elements $\lambda_1 \geq \lambda_2 \geq \cdots \geq \lambda_N$ are the ordered singular values of the matrix H with $N = min(N_t, N_r)$. Each λ_i corresponds to an eigenmode of the channel (also called an eigenchannel), and each non-zero eigenchannel can support a data stream; thereby the MIMO channel can support the spatial multiplexing of multiple streams. Since

$$HH^H = U\Lambda\Lambda^T U^H$$

the squared singular values λ_i^2 are the eigenvalues of the matrix HH^H and also of $H^H H$. Note that there are *N* singular values of *H*, the SVD can be rewritten as

$$H = \sum_{i=1}^{N} \lambda_i u_i v_i^*$$

Namely, H can be expressed as the sum of the rank-one matrices $\lambda_i u_i v_i^*$. Thus the rank of H is actually the number of non-zero singular values.

Assume

$$\tilde{x} = V^H x, \tilde{y} = U^H y, \tilde{n} = U^H n$$

then the equivalent received signal can be rewritten as:

$$\tilde{y} = \Lambda\tilde{x} + \tilde{n}$$

where $\tilde{n}$ has the same distribution as *n*, and $\|\tilde{x}\|^2 = \|x\|^2$ since V^H is a unitary matrix.

Therefore, the energy is preserved and we have an equivalent expression as parallel Gaussian channels:

$$\tilde{y}_i = \lambda_i \tilde{x}_i + \tilde{n}_i, i = 1, 2, \dots, N.$$

The capacity of this MIMO channel is given by:

$$C = \sum_{i=1}^{N} log_2 \left(1 + \frac{P_i \lambda_i^2}{N_0}\right) \ bits/s/Hz$$

where $P_1, \dots, P_N$ are the transmit powers allocated using the water filling principle:

$$P_i = (\mu - \frac{N_0}{\lambda_i^2})$$

in which μ is can be determined by the total power constraint $\sum_i P_i = P$.

With respect to the relationship between the average power for MIMO channels and the eigenvalues for MIMO channels, it has been shown that the widely used WINNER channel model [73] is not suitable for large antenna arrays [74], and its elevation characteristics are insufficient [75]. Fig. 113 shows the MIMO channel power distribution as a function of MIMO eigenvalues at 2 GHz obtained from WINNER model (solid dots) and measurement (hollow dots) for different antenna array sizes in a NLOS environment. The power on the vertical axis denotes the normalized average power for all channels, and the abscissa represents the index number of sorted eigenvalues for the MIMO channel, which are taken from the average of 100 random channels. As can be observed, when the antenna array size is 0.3 × 0.3 m, the power distribution from WINNER model agrees relatively well with that from the measurement. When the array size increases to 4 × 4 m, however, the result from WINNER model is substantially different than that from the measurement. In the WINNER model, the exact size of antenna array for which unrealistic results start to exhibit depend on the angular spread and frequency.

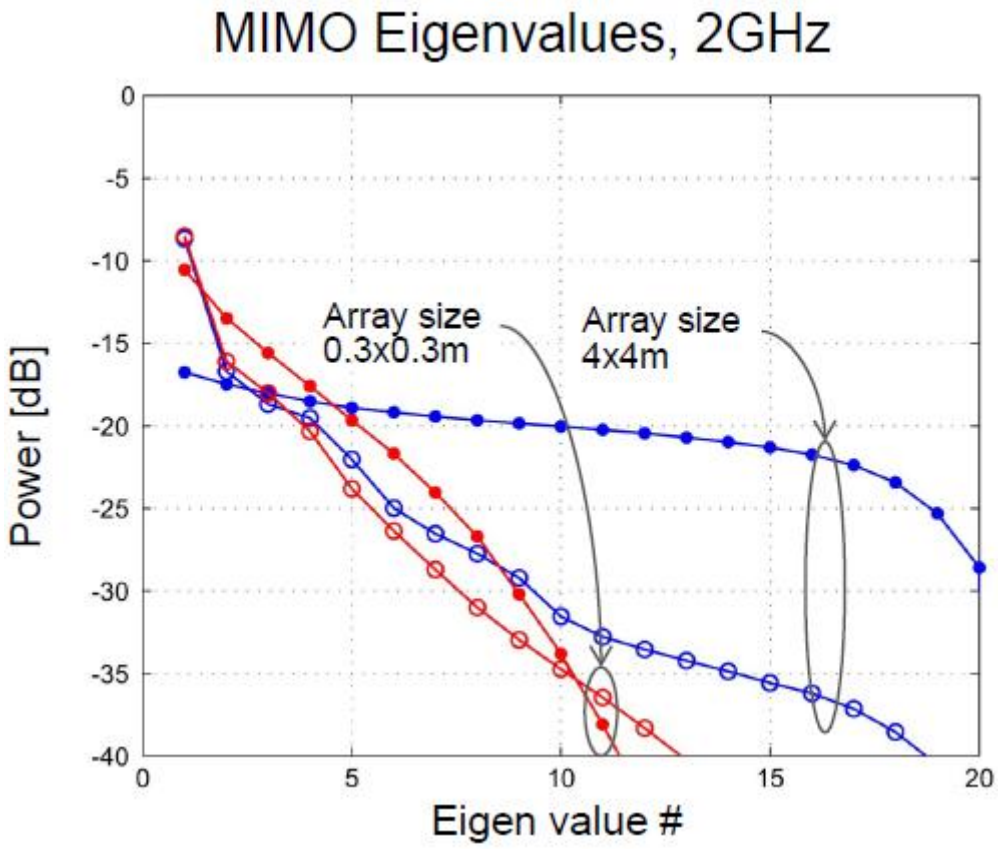

Fig. 113. Power distribution as a function of MIMO eigenvalues at 2 GHz obtained from WINNER model (solid dots) and measurement (hollow dots) for different antenna array sizes in a NLOS environment [74].

5.2.2 Functions of MIMO Systems

MIMO technique has been adopted by IEEE 802.11n. 802.11n defines many "Nt x Nr" antenna configurations, ranging from “1 x 1” to “4 x 4”. This refers to the number of transmit (Nt) and receive (Nr) antennas – for example, an AP with two transmit and three receive antennas is a "2 x 3" MIMO device. The more antennas an 802.11n device uses simultaneously, the higher its maximum data rate.

According to IEEE 802.11n, there are three major advanced signal processing techniques used in MIMO systems: spatial multiplexing (SM), space-time block coding (STBC), and transmit beamforming (TxBF).

5.2.2.1 Spatial Multiplexing

Spatial Multiplexing (SM) subdivides an outgoing signal stream into multiple pieces, transmitted through different antennas. Because each transmission propagates along a different path, those pieces – called spatial streams – arrive with different strengths and delays. Multiplexing two spatial streams onto a single channel effectively increases capacity and thus maximizes data rate. All 802.11n access points (Aps) must implement at least two spatial streams, up to a maximum of four. 802.11n stations can implement as few as one spatial stream [76].

If a transmitter is equipped with Nt antennas and the receiver has Nr antennas, the maximum spatial multiplexing order is Ns = min (Nt, Nr). if a linear receiver is used. This means that Ns streams can be transmitted in parallel, ideally leading to an Ns increase of the spectral efficiency (the number of bits per second and per Hz that can be transmitted over the wireless channel). The practical multiplexing gain can be limited by spatial correlation, which means that some of the parallel streams may have very weak channel gains.

5.2.2.2 Space-Time Block Coding

Space-Time Block Coding (STBC) sends an outgoing signal stream redundantly, using up to four differently-coded spatial streams, each transmitted through a different antenna. The fact that the transmitted signal must traverse a potentially difficult environment with scattering, reflection, refraction and so on and may then be further corrupted by thermal noise in the receiver means that some of the received copies of the data will be "better" than others [76]. This redundancy results in a higher chance of being able to use one or more of the received copies to correctly decode the received signal. By comparing arriving spatial streams, the receiver has a better chance of accurately determining the original signal stream in the presence of RF interference and distortion. That is, STBC improves reliability by reducing the error rate

experienced at a given SNR. This optional 802.11n feature may be combined with SM.

5.2.2.3 Transmit Beamforming

Transmit Beam-forming (TxBF) steers an outgoing signal stream towards the intended receiver by concentrating transmitted RF energy in a given direction. This technique leverage additive and destructive environmental impacts. This optional 802.11n feature is not yet widely implemented [76].

The simplified schematic of the above three advanced signal processing techniques are illustrated in Fig. **114.**

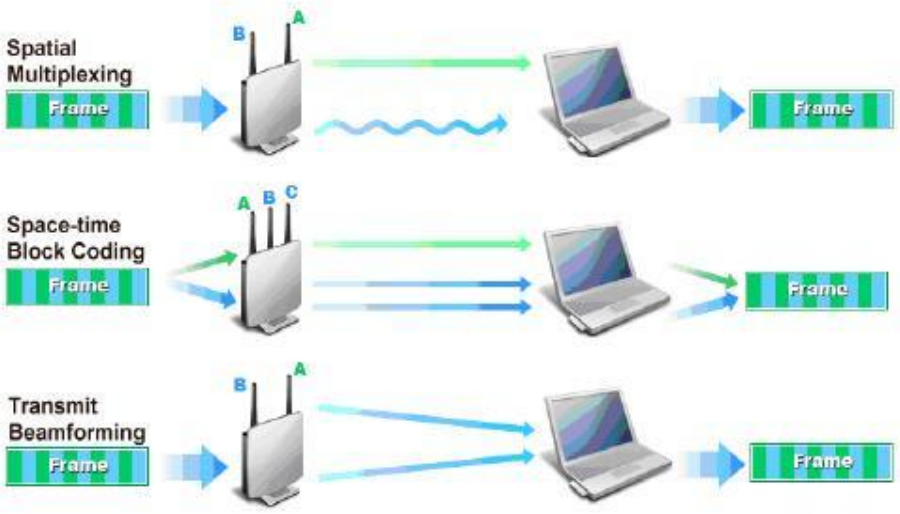

Fig. 114. Simplified schematics of spatial multiplexing (SM), space-time block coding (STBC), and transmit beamforming (TxBF) defined in IEEE 802.11n [76].

5.2.3 Spatial Multiplexing Combined with Transmit Beamforming

Spatial multiplexing (SM) and beamforming (BF) are two of the functions of MIMO systems. Spatial multiplexing requires the spacing between the antenna elements to be large enough so that the fading channels among different antenna elements are uncorrelated or low-correlated. While for BF, the antenna spacing needs to be small in order to utilize the strong spatial

correlation to process the transmitted/received signals via various BF techniques [77]. BF can provide high BF gain and mitigate the interference in highly spatially correlated MIMO sub-channels. Given the advantages provided by these techniques and the fact that they are both based on multiple antenna systems, it might be beneficial to integrate different techniques to obtain more gains.

5.2.3.1 Theoretical Analysis

The structure of a downlink transmission scheme combining SM and BF at the base station is illustrated in Fig. **115**. There are N_t antenna arrays and N_t data streams at the base station, and each array consists of N antennas.

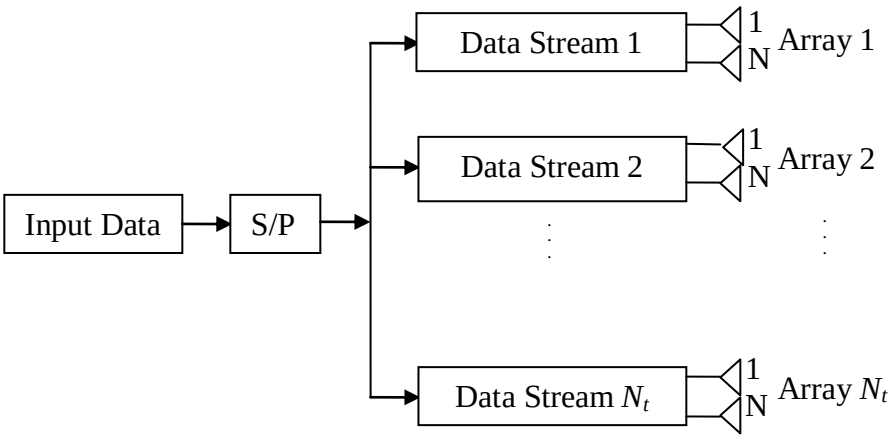

Fig. 115. Proposed scheme model combining spatial multiplexing (SM) and beamforming (BF) at the base station.

When there exist N_t antenna arrays at the base station and N_r antennas at the mobile station, and each antenna array is comprised of N antenna elements, the MIMO channel matrix can be expressed as [77]:

$$\mathrm{H} = \begin{bmatrix} \boldsymbol{h_1^1} & \boldsymbol{h_1^2} & \cdots & \boldsymbol{h_1^{N_t}} \\ \boldsymbol{h_1^1} & \boldsymbol{h_2^2} & \cdots & \boldsymbol{h_2^{N_t}} \\ \vdots & \vdots & \cdots & \vdots \\ \boldsymbol{h_{N_r}^1} & \boldsymbol{h_{N_r}^2} & \cdots & \boldsymbol{h_{N_r}^{N_t}} \end{bmatrix}$$

where

$$\boldsymbol{h_i^j} = [h_{i,1}^j, \ldots, h_{i,N}^j]$$

represents the channel fading vector between the *j*th antenna array at the base station and the *i*th antenna at the mobile station, and $h_{i,n}^j$ is the channel coefficient connecting the nth antenna element in the jth antenna array at the base station and the ith antenna at the mobile station. When considering BF, assuming the angle of departure (AOD) of the signal from the jth antenna array at the base station is θ_j, then the corresponding beamforming vector is:

$$\mathbf{a_j} = \mathrm{a}(\theta_j) = [1, e^{-\frac{j2\pi d sin(\theta_j)}{\lambda}}, \ldots, e^{-\frac{j2\pi(N-1)dsin(\theta_j)}{\lambda}}]^T$$

where d is the distance between adjacent antenna elements, λ is the carrier wavelength, the superscript T represents the matrix transposition operation. The received signal at the *i*th receive antenna element can be derived as [77]:

$$y_i = h_i^1 \mathrm{a}_1 s_1 + \cdots + h_i^{N_t} \mathrm{a}_{N_t} s_{N_t} + n_i$$

where n_i is a spatially uncorrelated complex white Gaussian noise vector. Therefore, the received signal in the matrix form is as follows:

$$\begin{bmatrix} y_1 \\ y_2 \\ \vdots \\ y_{N_r} \end{bmatrix} = \begin{bmatrix} \boldsymbol{h_1^1 a_1} & \boldsymbol{h_1^2 a_2} & \cdots & \boldsymbol{h_1^{N_t} a_{N_t}} \\ \boldsymbol{h_2^1 a_1} & \boldsymbol{h_2^2 a_2} & \cdots & \boldsymbol{h_2^{N_t} a_{N_t}} \\ \vdots & \vdots & \cdots & \vdots \\ \boldsymbol{h_{N_r}^1 a_1} & \boldsymbol{h_{N_r}^2 a_2} & \cdots & \boldsymbol{h_{N_r}^{N_t} a_{N_t}} \end{bmatrix} \begin{bmatrix} s_1 \\ s_2 \\ \vdots \\ s_{N_t} \end{bmatrix} + \begin{bmatrix} n_1 \\ n_2 \\ \vdots \\ n_{N_r} \end{bmatrix}$$

We can construct an effective $N_t \times N_r$ channel matrix $\widetilde{H}$ that includes the both the MIMO channel fading and the BF vector:

$$\widetilde{H} = \begin{bmatrix} \boldsymbol{h_1^1 a_1} & \boldsymbol{h_1^2 a_2} & \cdots & \boldsymbol{h_1^{N_t} a_{N_t}} \\ \boldsymbol{h_2^1 a_1} & \boldsymbol{h_2^2 a_2} & \cdots & \boldsymbol{h_2^{N_t} a_{N_t}} \\ \vdots & \vdots & \cdots & \vdots \\ \boldsymbol{h_{N_r}^1 a_1} & \boldsymbol{h_{N_r}^2 a_2} & \cdots & \boldsymbol{h_{N_r}^{N_t} a_{N_t}} \end{bmatrix}$$

Thus the received signals and data signals can be directly related using this effective channel matrix $\widetilde{H}$.

Assuming flat-fading Rayleigh channels, then it can be roughly obtained that [77]

$$\boldsymbol{h_i^j} = b_{i,j}\boldsymbol{a_j^H}$$

where the superscript H denotes the Hermitian (conjugate transposition) matrix operation, and $b_{i,j}$ is independent and identically Rayleigh-distributed random variable. Therefore it follows that

$$h_i^j a_j = b_{ij} a_j^H a_j = N b_{ij}$$

And the matrix $\widetilde{H}$ can be rewritten as:

$$\widetilde{H} = N * \begin{bmatrix} b_{11} & b_{12} & \cdots & b_{1N_t} \\ b_{21} & b_{22} & \cdots & b_{12} \\ \vdots & \vdots & \cdots & \vdots \\ b_{N_r 1} & b_{N_r 2} & \cdots & b_{N_r N_t} \end{bmatrix}$$

At the mobile receiver side, certain BF algorithm is performed to detect the received signal. Assuming the receive BF matrix to be F, then the detected signal is

$$\mathbf{z} = \mathrm{F}\mathbf{y} = \mathrm{F}\widetilde{H}\boldsymbol{s} + F\boldsymbol{n}$$

The most commonly used receive BF algorithms are zero forcing (ZF) BF algorithm and minimum mean squared error (MMSE) BF algorithm. The ZF BF algorithm is employed here, and the corresponding BF matrix is

$$\mathrm{F} = (\widetilde{H}^H \widetilde{H})^{-1} \widetilde{H}^H$$

5.2.3.2 Simulation Results

To simulate the performance of the SM with BF scheme at the base station, the bit error rate (BER) as a function of SNR using different modulation schemes without channel coding is investigated. The distance between adjacent base station antenna arrays is larger than 10 times the carrier wavelength, while the mobile station antenna spacing is half the carrier wavelength. ZF BF algorithm is adopted at the receiver. In the first set of simulation, there are 4 transmit antenna arrays at the base station and 4 receive antennas at the mobile station, and 16 QAM modulation scheme is employed. Simulation and comparison are performed with varying number of the antenna elements N in each array at the base station. The second simulation uses 8 transmit antenna arrays, 8 receive antennas, and 16 QAM modulation. 64 QAM modulation scheme is utilized in the last two simulations, and the transmit antenna arrays and receive antennas are 4 by 4 and 8 by 8, respectively. The simulated BER performance are shown in Fig. 116 to Fig. 119, and the simulated MIMO channel capacity is illustrated in Fig. 120. .

A common observation from the four figures is that the BER performance is enhanced when the number of antenna elements N in each transmit array increases. Specifically, when N = 2, the performance is improved by 10log10(2) = 3.0 dB compared to the pure SM, and 10log10(3) = 4.8 dB improvement is achieved when N = 3. The simulated performance improvements are clearly due to the BF gain and agree well with the theoretical analysis. For identical values of N and SNR, it is seen by comparing Fig. 116 to Fig. 119 that the BER increases as the number of antenna arrays or antennas and the modulation scheme increases. On the other hand, however, the largest achievable MIMO channel capacity also goes up with the increasing number of antenna arrays or antennas, as shown in Fig. 120. Thus it is necessary to select the appropriate number of antennas and modulation schemes according to the specific requirement on BER and channel capacity. Besides, the channel capacity increases as N increases because of the BF gain.

It is obvious from Fig. 116 to Fig. 119 that the transmit architecture integrating SM and BF is superior to the conventional SM technique.

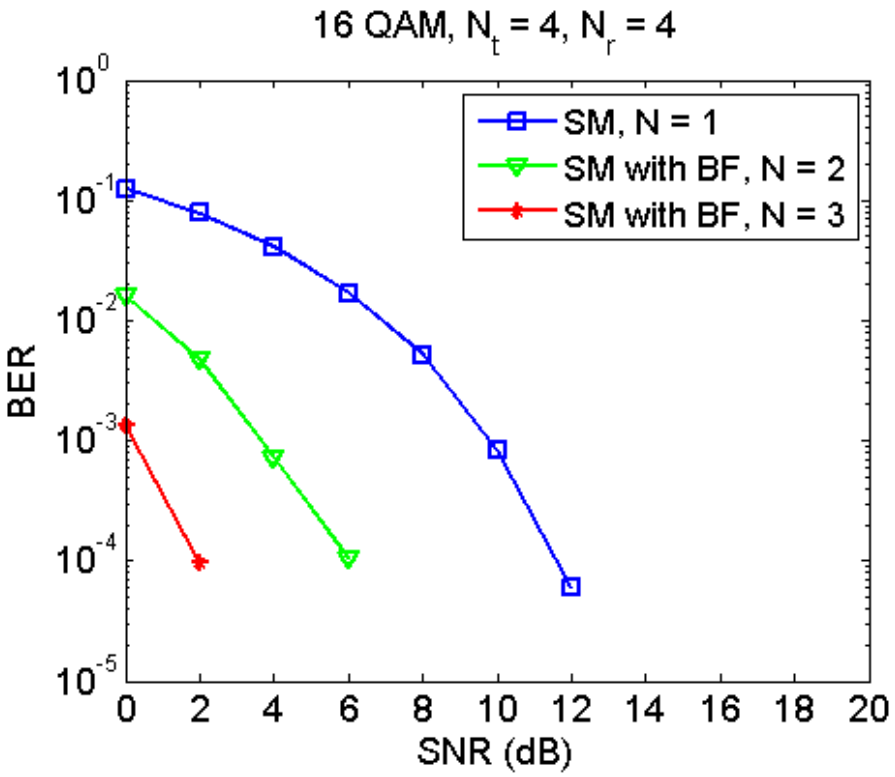

Fig. 116. Simulation results of the proposed scheme using 16 QAM modulation, Nt = 4, Nr = 4, and various values of N.

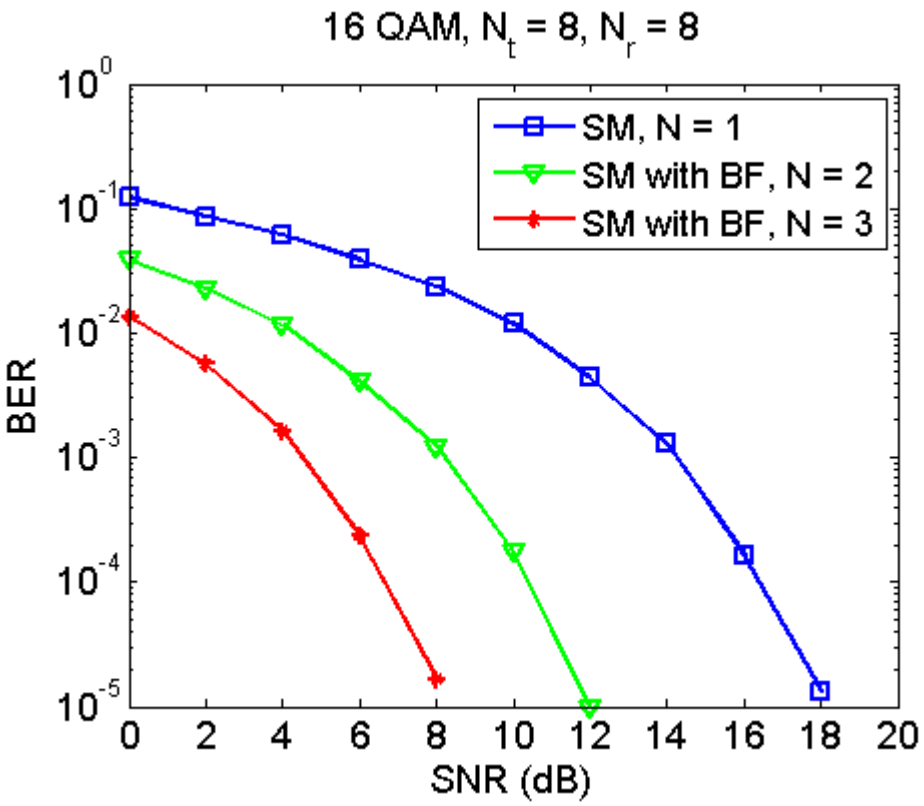

Fig. 117. Simulation results of the proposed scheme using 16 QAM modulation, Nt = 8, Nr = 8, and various values of N.

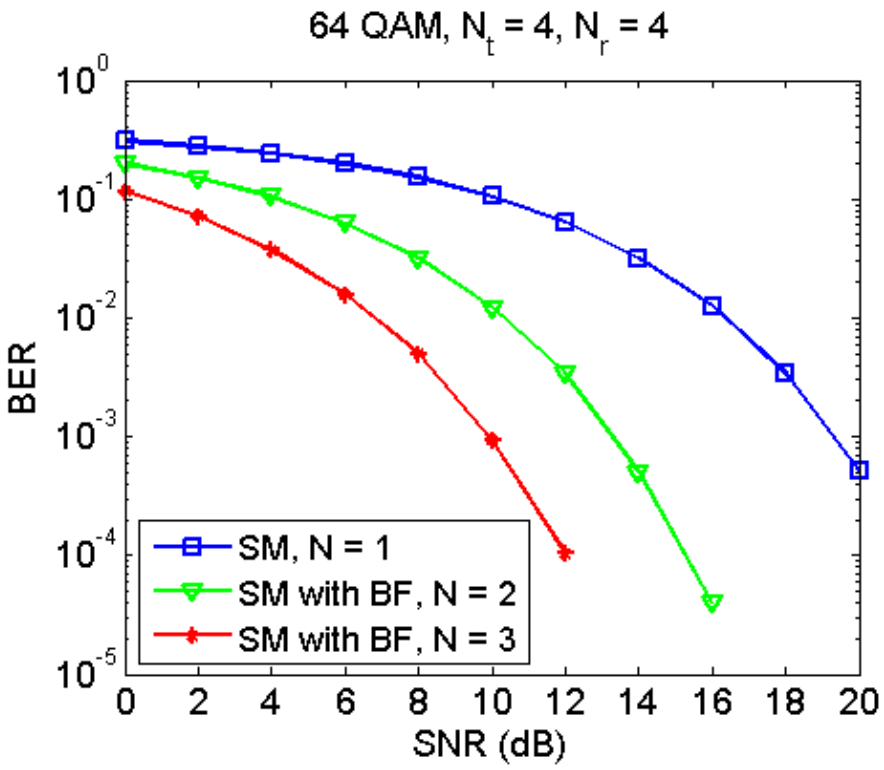

Fig. 118. Simulation results of the proposed scheme using 64 QAM modulation, Nt = 4, Nr = 4, and various values of N.

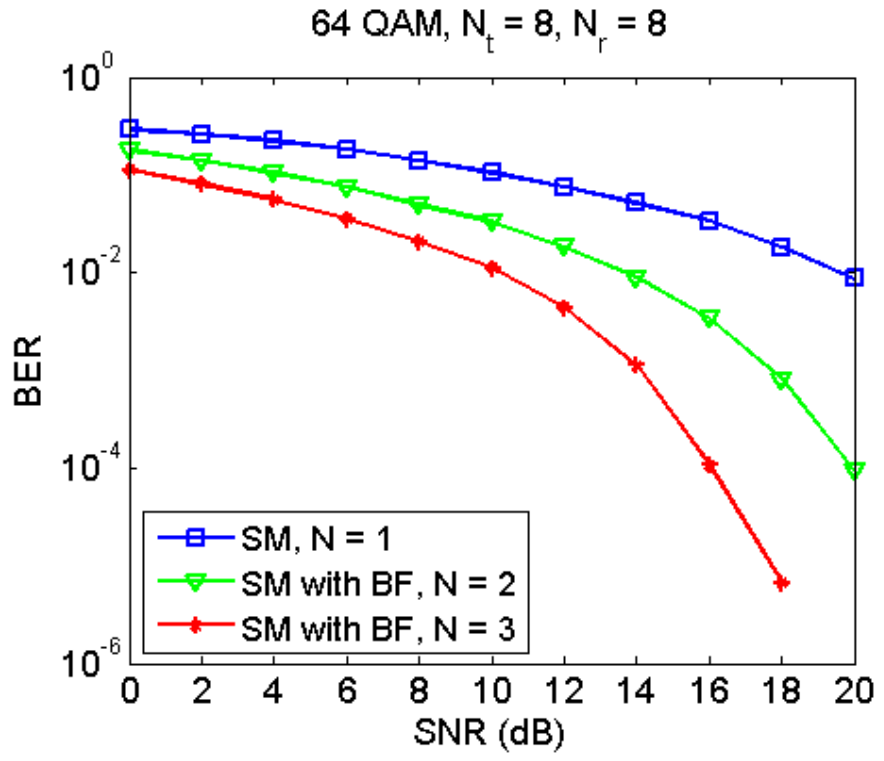

Fig. 119. Simulation results of the proposed scheme using 64 QAM modulation, Nt = 8, Nr = 8, and various values of N.

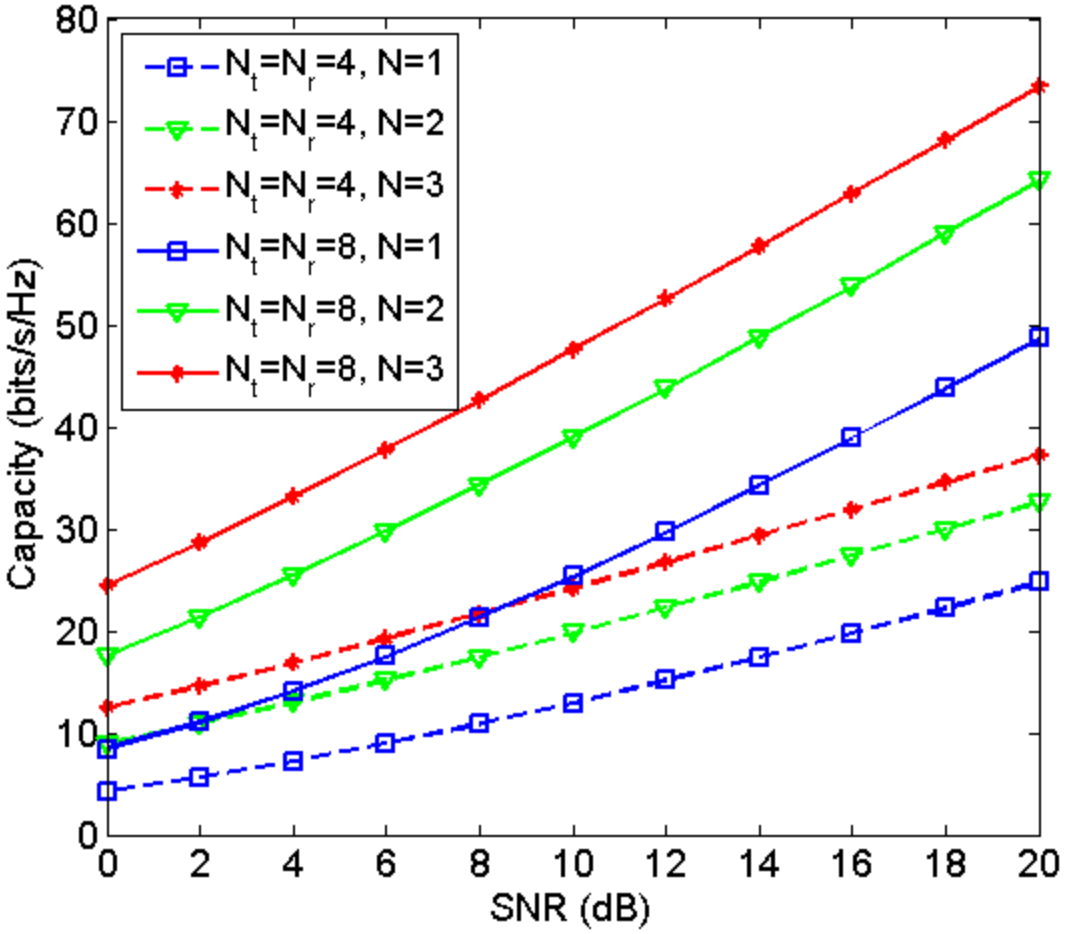

Fig. 120. Simulated channel capacity of the proposed scheme for various Nt , Nr, and N.

5.3 Massive MIMO versus Small Cell

Both massive MIMO and small cell network (SCN) are regarded as promising approaches to provide high spectral efficiency (SE). Massive MIMO consists of a large number of antennas to serve a small number of users and thus has a high array gain. SCN deploys densely distributed low-cost, low-power base stations (BSs), and enjoys the cell-splitting gain with the decrease of the cell size. Liu *et al* investigated and compared the energy efficiency (EE) of massive MIMO and SCN [78]. For a fair comparison, they considered identical number of users and identical number of antennas in the same area of a multi-cell network, and the cell-edge SNR is equal, and

perfect channel state information was assumed available at the BSs. Three BS sleep strategies were considered: a BS will turn into a sleep mode when there are no users, one user, and two users in its coverage, respectively, corresponding to increasing values of the sleep threshold. Through simulation, they found that the EE of SCN increases with the cell size shrinking, and the achievable SE of SCN and massive MIMO increase with the cell-edge SNR. When the number of cells is large, the EE of SCN is always higher than massive MIMO. When the number of cells is small, however, massive MIMO achieves higher EE than SCN if the circuit power consumptions of massive MIMO are much lower than SCN.

5.4 Beamforming Categories

5.4.1 Transmit Beamforming

Transmit beamforming (TxBF) is a technique implemented in digital signal processing (DSP) logic to improve range and data rate for a given client, or device. In a basic system (single stream), Tx BF works on the principle that signals sent on separate antennas can be coordinated to combine constructively at the receive antenna. Specifically, the phases of the transmit signals are manipulated to improve directivity. Tx BF is specified in the IEEE 802.11n specification and takes advantage of the multiple transmit antennas available in a multiple input, multiple output (MIMO) system. Efficient steering of individual streams in such a system provides overall gain. This can be achieved through knowledge of the channel between the transmitter and receiver. Thus, it can be viewed as a form of transmit diversity with a known channel.

In a typical 802.11 system, an AP beamforms to the client and provides increased gain at the client. This leads to higher data rates and reduced number of retries, which in turn can increase the overall capacity of the system and lead to more efficient use of the spectrum. The gain improvement can be up to 12dB, and range improvement can be up to twice that of a system

without beamforming—in the case of a 4 transmit antenna system beamforming to a 1 receive antenna system. Also, TxBF provides maximum benefit in an asymmetrical system, where the number of transmit antennas is different from the number of receive antennas. TxBF algorithms include zero-forcing TxBF (ZF-TxBF) and singular value decomposition TxBF (SVD-TxBF).

5.4.1.1 ZF-TxBF

ZF-TxBF allows a transmitter to send data to desired users together with nulling out the directions to undesired users and for uplink, ZF-BF receives from the desired users together with nulling out the directions from the interference users. ZF-TxBF can achieve close to the optimal capacity especially when the number of users is sufficient. With limited channel status information at the transmitter, ZF-BF requires the amount of feedback overhead proportional to the average signal-to-noise-ratio (SNR) to achieve the full gain. Therefore, inaccurate channel state information at the transmitter may suffer the significant performance loss of the system throughput because of the interference among transmit streams is remained.

Suppose the data streams to be sent to the receiver are expressed by the vector s, the TxBF matrix is T, and the channel matrix is H, the noise at the receiver is n, then the actually transmitted signal from the multiple transmit antennas can be expressed as:

$$x = Ts$$

And the received signal at the receiver is

$$y = Hx + n = HTs + n$$

If ignoring the noise at the receiver, in order to recover the original data s, we need y = s, i.e. HTs = s, hence we can obtain:

$$HT = 1, i.e., T = H^H(HH^H)^{-1}$$

The advantage of ZF-TxBF is that no noise enhancement would be introduced, but it suffers

the problem of power constraint, because the magnitude of the entries in the diagonal of the matrix T may differ very much, which indicates that the transmitted power allocated to each data stream may be quite different and some data streams may have a very low transmitted power.

5.4.1.2 SVD-TxBF

SVD is a factorization of a real or complex matrix, with many useful applications in signal processing and statistics. Formally, the singular value decomposition of an m×n real or complex matrix H is a factorization of the form:

$$H = U\Sigma V^H$$

where U is a m×m real or complex unitary matrix, Σ is an m×n rectangular diagonal matrix with nonnegative real numbers on the diagonal, and V^H (the conjugate transpose of V, or simply the transpose of V (if V is real) is an n×n real or complex unitary matrix. The diagonal entries $\Sigma_{i,j}$ of Σ are known as the singular values of H. The m columns of U and the n columns of V are called the left-singular vectors and right-singular vectors of H, respectively. The singular value decomposition and the eigen decomposition are closely related. namely: (1) The left-singular vectors of H are eigenvectors of HH^H. (2) The right-singular vectors of H are eigenvectors of H^HH. (3) The non-zero singular values of H (found on the diagonal entries of Σ are the square roots of the non-zero eigenvaluesof both H^HH and HH^H.

In SVD-TxBF, T = V (and usually the receive beamforming matrix R = U^H), so that the received signal is

$$z = Ry = RHTx = U^HUDV^HVx = Dx$$

In this way, the channel matrix H of a MIMO system is conversed into the channel matrix D of a SISO system, which significantly simplifies the computation process.

Fig. 121 illustrates the antenna patterns for both transmit and receive beamforming using

SVD in various MIMO systems.

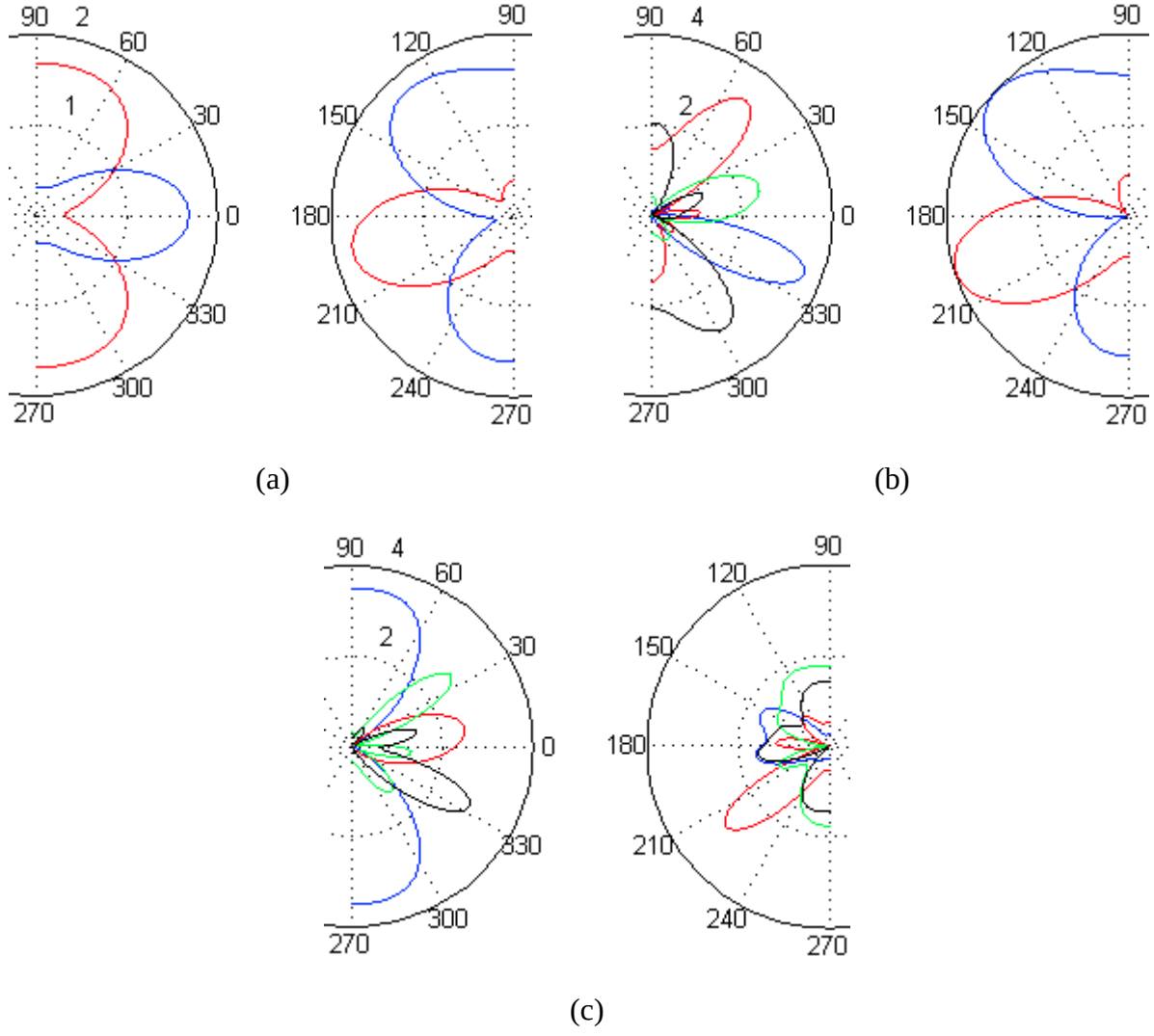

Fig. 121. Transmit (left) and receive (right) antenna patterns using SVD beamforming for (a) a 2 by 2 MIMO system, (b) a 4 by 2 MIMO system, and (c) a 4 by 4 MIMO system. I n the left pictures of (a)(b)(c), 0 denotes the broadside direction, 90 represents counterclockwise 90^0 from the broadside, and 270 indicates clockwise 90^0 from the broadside; i n the right pictures of (a)(b)(c), 180 denotes the broadside direction, 270 represents counterclockwise 90^0 from the broadside, and 90 indicates clockwise 90^0 from the broadside.

5.4.2 Receive Beamforming

Receive Beamforming (RxBF) methods include ZF, MMSE, SVD, least squares (LS), least mean squares (LMS), steepest descent (SD), etc, as introduced in the first chapter.

5.5 DOA Estimation Algorithms

The purpose of DOA estimation is to use the data received by the array to estimate the direction of arrival of the signal. The results of DOA estimation are then used by the array to design the adaptive beam former in such way as to maximize the power radiated towards the users and to suppress the interference. In short the successful design of adaptive array smart antenna depends highly on the performance of DOA estimation algorithm. In the design of adaptive array smart antenna for mobile communication the performance of DOA estimation algorithm depends on many parameters such as number of mobile users and their space distribution , the number of array elements and their spacing, the number of signal samples and SNR. DOA estimation algorithms can be implemented by FPGA or DSP platforms, and the simulation using MATLAB is a good way to investigate the performance of different algorithms.

5.5.1 MUSIC Algorithm

The term MUSIC stands for Multiple Signal Classification. It is high resolution technique based on exploiting the eigen structure of input covariance matrix [71][79]. MUSIC makes assumption that the noise in each channel is uncorrelated making correlation matrix diagonal. The incident signals are somewhat correlated creating non-diagonal signal correlation matrix.

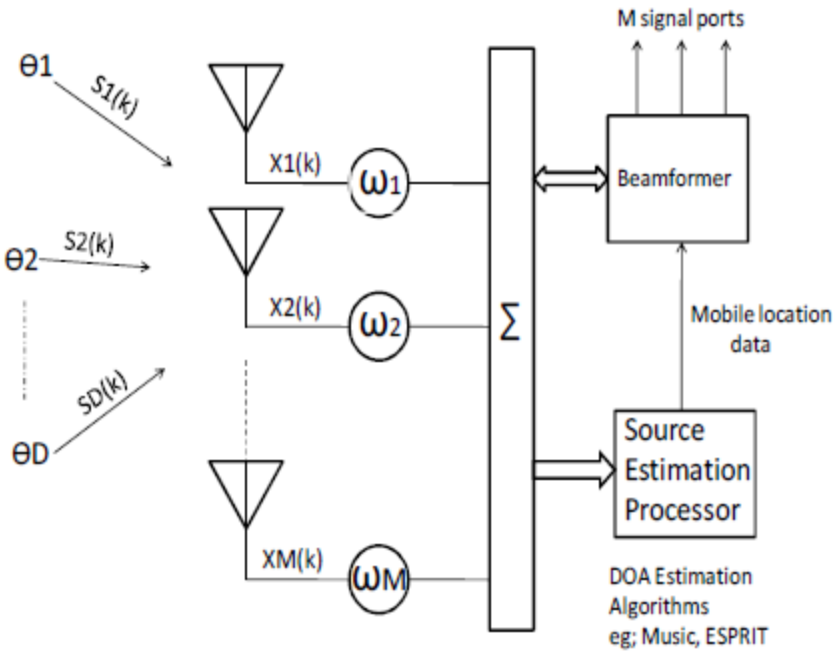

Fig. 122. M element array with D arriving signals.

Assume there are M antennas at the receiver antenna array, where the array is a uniform linear array (ULA), as shown in Fig. **122.** K samples of signals are acquired at each of the M antennas. If there are L signal sources received by the array, the signal model is as follows:

$$x(t) = As(t) + n(t)$$

where x(t) is the M by 1 received signal vector, s(t) is the L by 1 source signal vector, n(t) is the M by 1 noise vector [71].

$$x(t) = \begin{bmatrix} x_1(t) \\ x_2(t) \\ \vdots \\ x_M(t) \end{bmatrix} = \begin{bmatrix} 1 \\ e^{-\frac{j2\pi d sin\theta}{\lambda}} \\ \vdots \\ e^{-\frac{j2\pi(M-1)dsin\theta}{\lambda}} \end{bmatrix} s(t) + n(t) = a(\theta)s(t) + n(t)$$

where $a(\theta)$ is called the steering vector.

The M by M correlation matrix of the received data x(t) is calculated as follows:

$$R_x = E\{x(t)x^H(t)\} = AR_sA^H + \sigma_0^2 I$$

in which

$$R_s = E\{s(t)s^H(t)\}$$

If the source signals are somewhat correlated such that R_s is not diagonal, it will still work if R_s has full rank. If the source signals are correlated such that R_s is rank deficient, then it is a problem. A common solution is spatial smoothing. The rank of R_s is very important because it defines the dimension of the signal subspace.

For M > L, the matrix AR_sA^H is singular, i.e.

$$\det[AR_sA^H] = \det[R_x - \sigma_0^2 I] = 0$$

This implies that σ_0^2 is an eigenvalue of R_x. Since the dimension of the null space of AR_sA^H is M-L, there are M-L such eigenvalues σ_0^2 of R_x. Since both R_x and AR_sA^H are non-negative definite, there are L other eigenvalues σ_i^2.

Let u_i be the *i*th eigenvector of R_x corresponding to σ_i^2:

$$R_x u_i = [\, AR_sA^H + \sigma_0^2 I]u_i = \sigma_i^2 u_i, \qquad i = 1,2,\dots,M$$

Partition the M-dimensional vector space into the signal subspace U_s and noise subspace U_n:

$$[U_s\ U_n] = [u_1 \dots u_L, u_{L+1} \dots u_M]$$

The steering vector $a(\theta_i)$ is in the signal subspace. The signal subspace is orthogonal to the noise subspace:

$$AR_sA^H u_i = \begin{cases} (\sigma_i^2 - \sigma_0^2)u_i; & i = 1,2,\dots,L \\ 0; & i = L+1,\dots,M \end{cases}$$

This implies that $a^H(\theta_i)U_n = 0$. Thus the MUSIC algorithm searches through all incident angles θ, and plots the spatial spectrum:

$$P(\theta) = \frac{1}{a^H(\theta_i)U_n {U_n}^H a(\theta_i)}$$

Wherever $\theta = \theta_i$, $P(\theta)$ exhibits a peak. Peak detection will give spatial angles of all incident sources.

Fig. **123** illustrates the MUSIC spectrum for a ULA with 4 array elements and K = 100, SND = 20 dB for direction of arrivals (DOAs) of -5, 10, and 25 degrees. The spacing between adjacent array elements is assumed to be $\lambda/2$, where λ is the wavelength of the incident signal. The sampling rate is twice the carrier frequency of the incident signal.

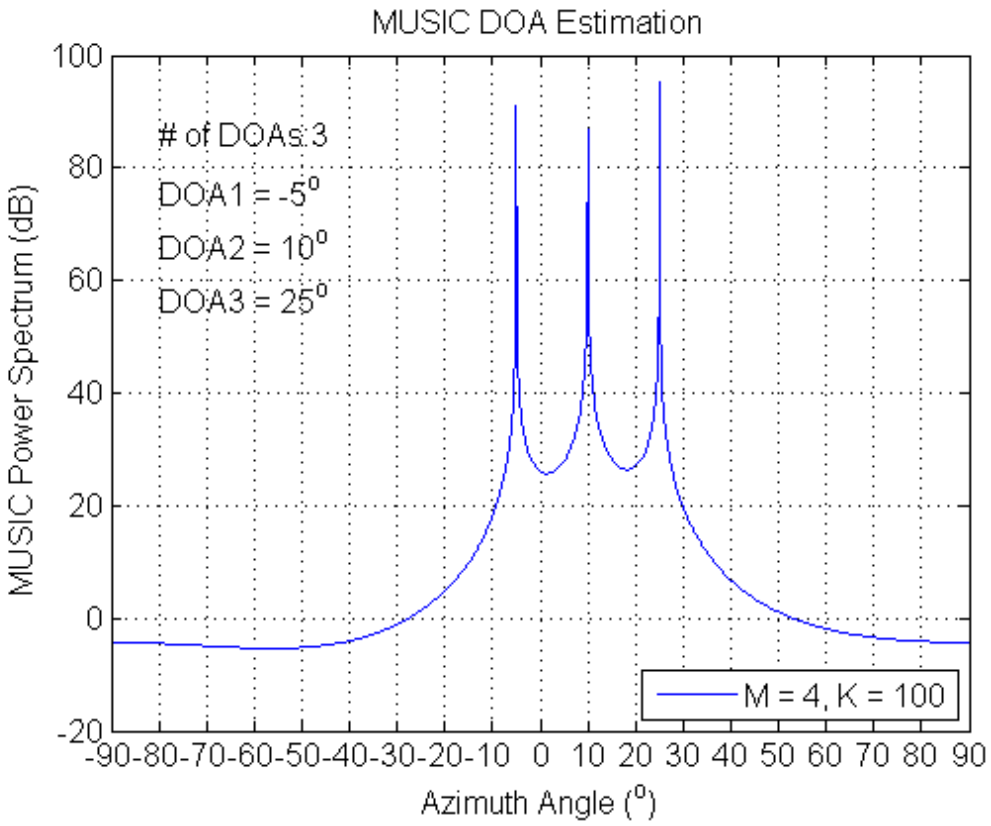

Fig. 123. MUSIC spectrum for M = 4, K = 100, and SNR = 20 dB.

Fig. **124** shows the MUSIC spectrum for the same DOAs stated above but with two different numbers of array elements, 4 and 10. As can be observed, the peaks become significantly sharper when the number of array elements M increases from 4 to 10, indicating that angular resolution can be improved by increasing M. However, a larger M means more phase shifters, larger size

and more cost, thus a balance needs to be achieved between these factors. As shown in Fig. 124, M = 4 can already provide an acceptable angular resolution, hence when the number of signal sources is less than 4, using 4 array elements is sufficient.

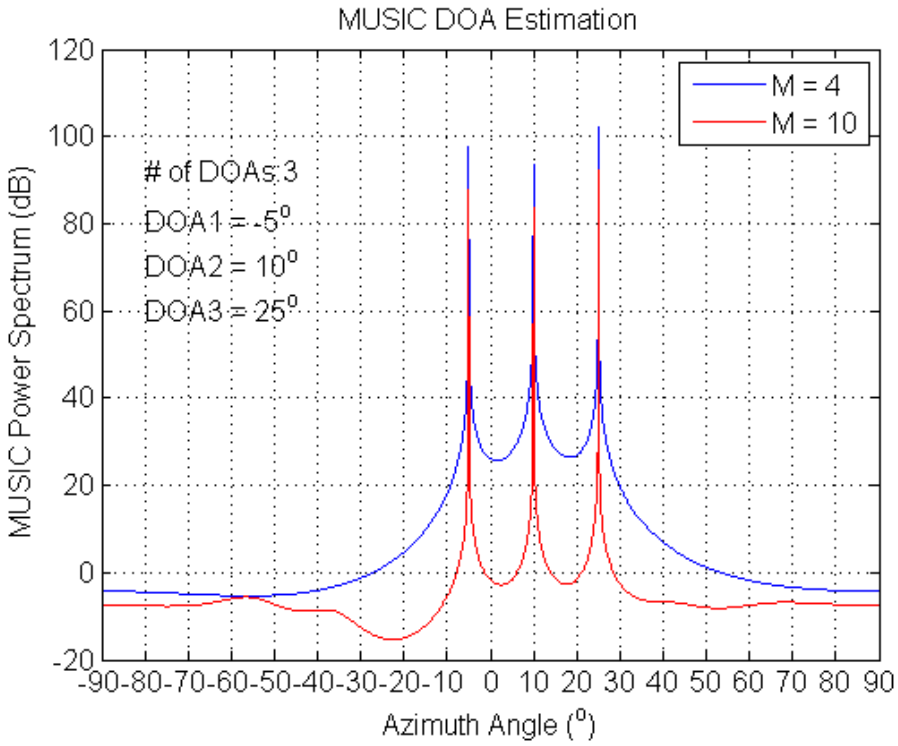

Fig. 124. MUSIC spectrum for varying number of array elements with K = 100, and SNR = 20 dB.

The influence of the number of data samples K on the angular resolution of the MUSIC algorithm is given in Fig. **125**. When K increases from 10 to 1000 for M = 10 and SNR = 20 dB, the peaks are only sharpened by a small amount, which implies that K does not exert a significant effect on the angular resolution using the MUSIC algorithm. The simulation results for M = 4 and SNR = 20 dB with different numbers of data samples are displayed in Fig. **126**, where there is no distinguishable difference in the spectrum with K = 10 and K = 1000, hence the effect of varying K is negligible for small values of M.

Fig. **127** shows the MUSIC spectrum obtained for SNR equal to -30 dB, 0 dB, and 30 dB,

respectively, for the DOAs of -5^0, 10^0, and 25^0. The spectrum almost remains the same as long as the SNR is not extremely low (e.g. to -30 dB). As a comparison, when the DOAs are much closer to each other, e.g., at -5^0, 0^0, and 5^0, the performance of the MUSIC algorithm is highly dependent on the SNR. As shown in Fig. **128**, when the SNR is 20 dB, high angle resolution is achieved; when the SNR decreases to 0 dB, the resolution also decreases; when the SNR drops to -20 dB, the three DOAs cannot even be determined correctly.

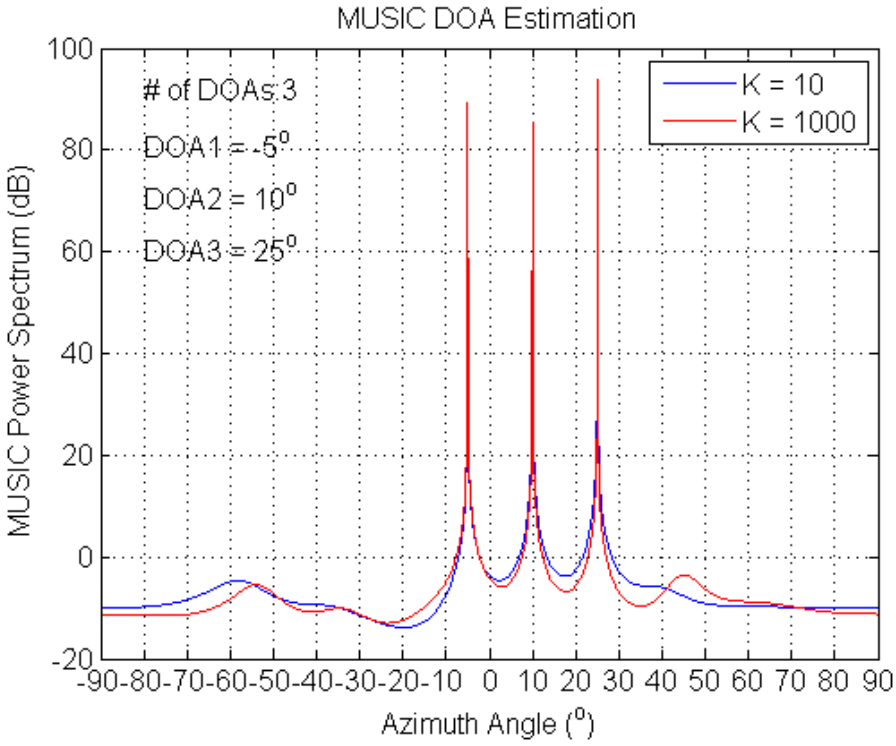

Fig. 125. MUSIC spectrum for varying number of data samples with M = 10, and SNR = 20 dB.

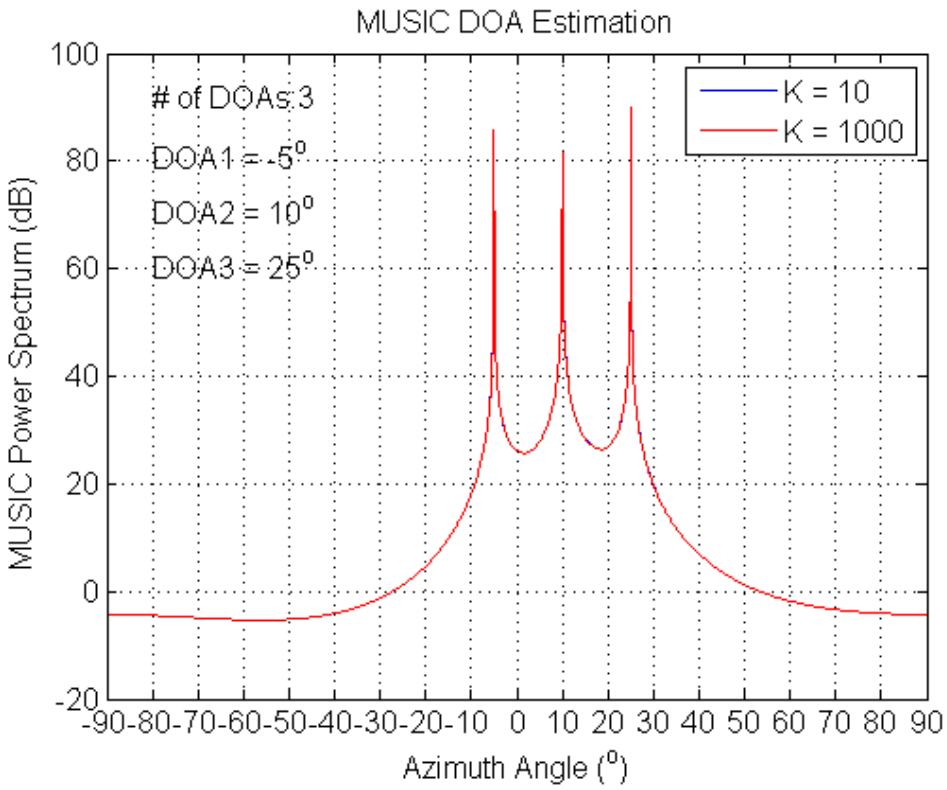

Fig. 126. MUSIC spectrum for varying number of data samples with M = 4, and SNR = 20 dB.

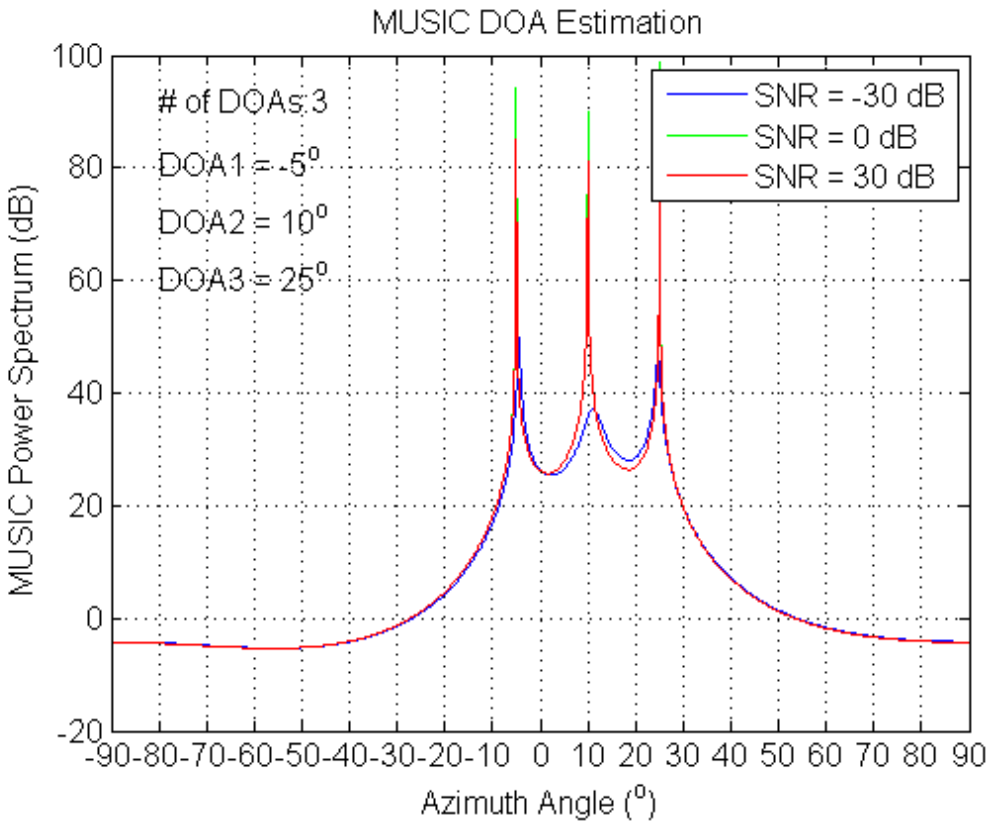

Fig. 127. MUSIC spectrum for varying number of data samples with M = 4, and K = 100, and DOAs of -5^0, 10^0, and 25^0.

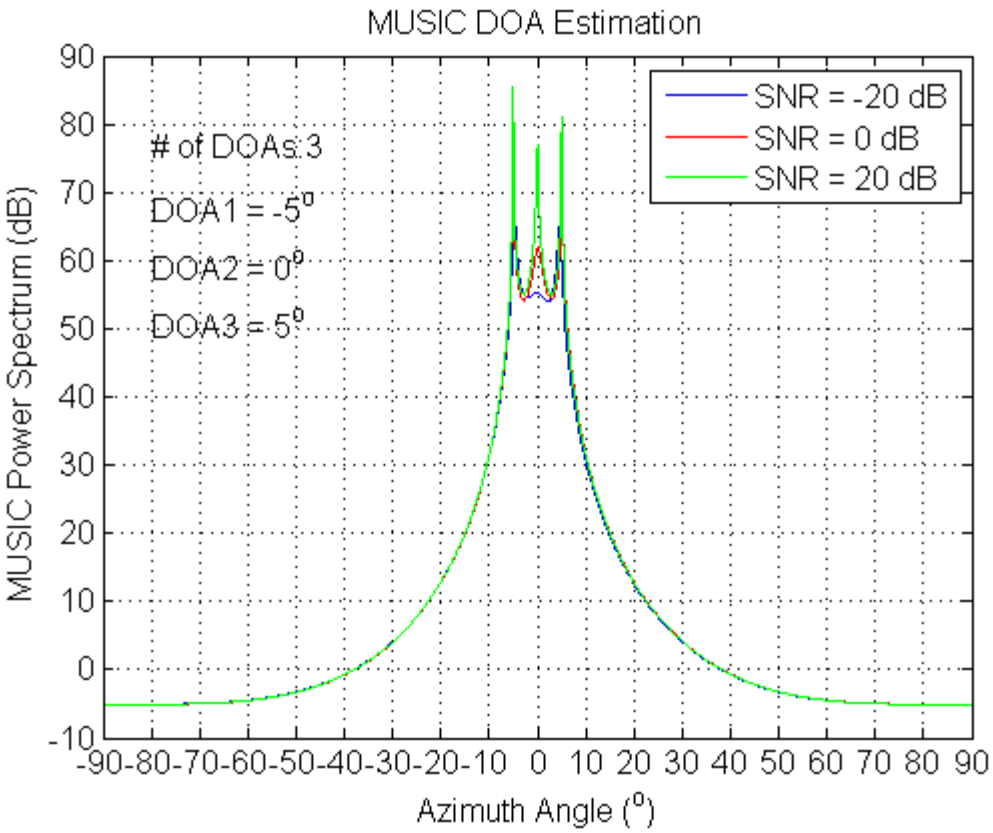

Fig. 128. MUSIC spectrum for varying number of data samples with M = 4, and K = 100, and DOAs of -5^0, 0^0, and 5^0.

5.5.2 ESPRIT Algorithm

Another high-resolution DOA estimation algorithm is ESPRIT, i.e., Estimation of Signal Parameters via Rotational Invariance Technique [71][79]. The ESPRIT algorithm is based on "doublets" of sensors (antennas), i.e., in each pair of sensors the two should be identical, and all doublets should line up completely in the same direction with a displacement vector Δ having magnitude Δ. The amount of delay between two sensors in each doublet for a given incident signal is the same for all doublets, which is $\Delta \sin(\theta)/c$. There are no restrictions other than the alignment of the doublets; the sensor patterns could be quite different from one pair to another, the positions of the doublets are also arbitrary, which makes calibration a little easier.

Fig. **129** shows two examples of doublets arrangement. In Fig. **129**(a), there are three doublets whose patterns are different from each other, and their positions are also random. While in Fig. **129**(b), there are also three doublets, yet their patterns are the same and some array elements are common in different doublets.

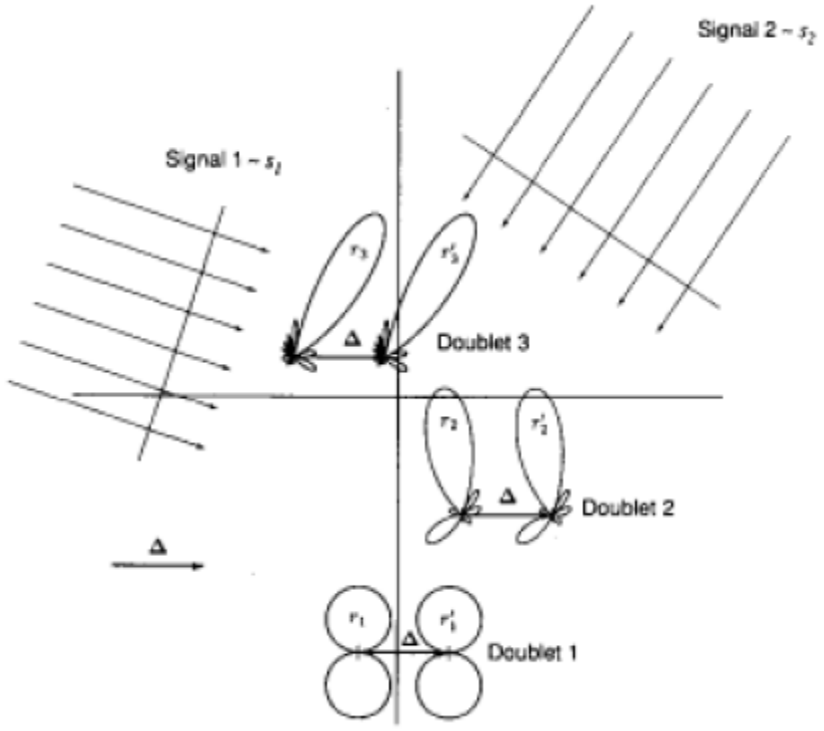

(a)

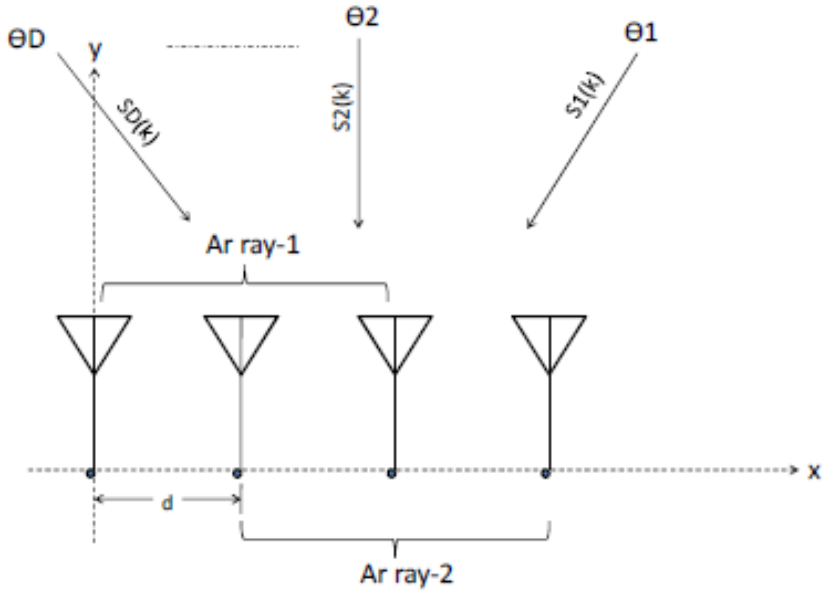

(b)

Fig. 129. (a) An example sensor array of doublets with different array patterns. (b) An example sensor array of doublets with the same array pattern and overlapped array elements.

Define

$$z(t) = \begin{bmatrix} x(t) \\ y(t) \end{bmatrix} = \begin{bmatrix} A \\ A\Phi \end{bmatrix} s(t) + \begin{bmatrix} n_x(t) \\ n_y(t) \end{bmatrix} = \bar{A}s(t) + n_y(t)$$

where $\Phi = diag.\{e^{j\gamma_1}, e^{j\gamma_2}, \ldots, e^{j\gamma_L}\}$, and $\gamma_i = \omega_0 \Delta \sin(\theta_i)/c$.

Compute the 2M by 2M correlation matrix:

$$R_z = E\{z(t)z^H(t)\} = \bar{A}R_s\bar{A}^H + \sigma_0^2 I$$

Since there are L signal sources, the L eigenvectors of R_z corresponding to the L largest eigenvalues form the signal subspace U_s, and the remaining 2M-L eigenvectors form the noise subspace U_n. The size of U_s is 2M by L, and its span is the same as the span of $\bar{A}$, hence there exists a unique nonsingular L by L matrix T such that

$$U_s = \bar{A}T$$

Partition U_s into two M by L submatrices:

$$U_s = \begin{bmatrix} U_x \\ U_y \end{bmatrix} = \begin{bmatrix} AT \\ A\Phi\mathrm{T} \end{bmatrix}$$

The columns of both U_x and U_y are linear combinations of A, so each of them has a column rank L. Since the arrays are translationally related, the subspaces of eigenvectors are related by a unique nonsingular transformation matrix B such that

$$ATB = A\Phi\mathrm{T}$$

Finally we can get

$$\Phi = TBT^{-1}$$

Thus the eigenvalues of B must be equal to the diagonal elements of Φ. Therefore, once the eigenvalues of B, $\lambda_1, \lambda_2, \ldots, \lambda_L$, are calculated, the DOAs can be estimated as

$$\theta_i = sin^{-1}(\frac{\arg(\lambda_i)}{\Delta d})$$

Obviously, the ESPRIT algorithm eliminates the search procedure and produces the DOA estimation directly in terms of the eigenvalues without much computational and storage requirements. This eigenstructure method has shown excellent accuracy and resolution in many experimental and theoretical studies.

Simulation of ESPRIT algorithm using MATLAB for a ULA with four pairs of doublets (five array elements) is carried out by varying different parameters of the ULA. Table **13** displays the influence of the angular separation between arriving signals on the accuracy of the estimated DOAs. In the first set of simulation, two input DOAs, which are respectively 0 degree and 1 degree, are selected, and in the second set of simulation, the actual DOAs are 0 degree and 20 degrees. The simulated DOAs using the ESPRIT algorithm are shown in the third column of Table **13**. It can be observed that the percentage error in DOA estimation decreases as the angular separation increases. The effect of the number of sampled data using the ESPRIT algorithm is illustrated in Table **14**. The input DOAs are -10 degrees and 10 degrees, and the number of samples data K are set to 10 and 1000 respectively. As is seen, the percentage errors are the same for these two K values. Table **15** shows the largest number of DOAs the ESPRIT algorithm can detect using a ULA with four pairs of doublets, clearly it can successfully estimate up to four DOAs.

The advantages and disadvantages of the MUSIC and ESPRIT DOA estimation algorithms are summarized and compared in Table **16**.

Table 13 DOA estimation using the ESPRIT algorithm for varying angular separation (M = 4, K = 100, SNR = 0 dB).

Simulation Set	Input DOA (degrees)	ESPRIT DOA (degrees)
1	0	-0.000000000000040
	1	1.000000000000048
2	0	-0.000000000000001
	20	20.000000000000000

Table 14 DOA estimation using the ESPRIT algorithm for varying number of data samples (M = 4, SNR = 0 dB).

Input DOA (degrees)	ESPRIT DOA (degrees)
K = 10	
-10	-10.000000000000002
10	10.000000000000002
K = 1000	
-10	-10.000000000000002
10	10.000000000000002

Table 15 DOA estimation using the ESPRIT algorithm for varying number of signals (M = 4, K = 100, SNR = 0 dB).

Number of signals	Input DOA (degrees)	ESPRIT DOA (degrees)
4	-40	-39.999999999999979
	-20	-20.000000000000000
	20	20.000000000000000
	40	39.999999999999979
5	-40	-36.488289656005740
	-20	3.236682809209635
	0	32.361948003036900
	20	-68.080087149594448
	40	-44.341656756587476

Table 16 Comparison of the MUSIC and ESPRIT DOA estimation algorithms.

	MUSIC	ESPEIT
Advantages	High spatial resolution	Works for any doublet shape Takes much less computation; Relaxed calibration requirement
Disadvantages	Sensitive to sensor position, gain, and phase errors, need careful calibration to make it work	More array elements

	well; High computation load	

5.6 Optical Beamforming Hardware Architecture

5.6.1 Brief Literature Review

As introduced in Chapter 1, adaptive array antenna beamforming (BF) architectures can be classified into five main categories: digital BF, LO BF, IF BF, Aerial BF, and optical BF. Conventional RF phase shifters are based on switched-line, ferrite materials, or monolithic microwave integrated circuit technologies. These purely electrical components, however, encounter limitations in terms of bandwidth and phase-shift range. Since optically fed phased arrays have many inherent advantages brought by the photonic technologies over conventional electronically controlled phased arrays, such as broad bandwidth, small size, weight, and power (SWaP), immunity to electromagnetic interference (EMI), and extreme frequency agility, they are highly promising as a substitution of traditional adaptive array BF architectures and can find practical applications in various related fields such as radar, ultra-fast communication, RF sensing, and imaging systems [80].

5.6.1.1 Optically controlled phased array antenna using multiple single mode optical fibers (SMFs)

Fig. **130** shows the schematic diagram of the optically addressed phased array antenna using the single SMF [81]. Thick and thin line represents the lightwave and microwave signal, respectively. Phase control for each antenna element is carried out using dispersion of the SMF and adjustment of each laser diode (LD) wavelength. Optical carriers with different LD wavelengths, λ_1 –λ_n are combined by optical multiplexer (MUX), and modulated with the

microwave signal by optical modulator (MOD).When the modulated optical carrier waves pass through the single SMF, different delay due to each wavelength is caused by the dispersion of the SMF. After the delay, the modulated optical carrier waves are demuxed into each wavelength by optical demultiplexer (DEMUX), and they are detected by photodiode (PD). In the end, suitable microwave phase for each antenna element for the BF can be obtained by the delay caused by the single SMF.

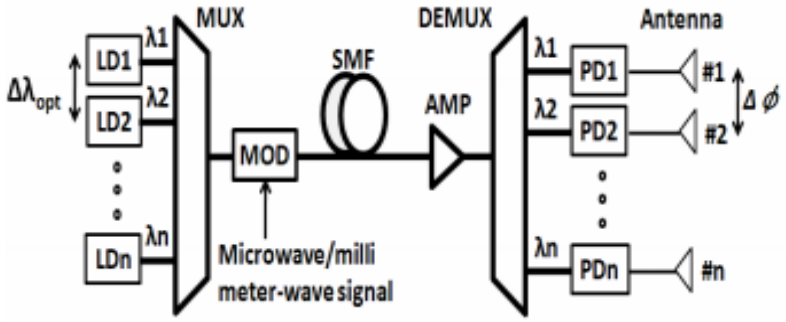

Fig. 130. Schematic diagram of optically addressed phased array antenna using a single SMF [81].

For the architecture in Fig. **130**, the microwave/mmW beam can be steered by adjusting the wavelength of each LD [81]. The same wavelength, however, cannot be assigned to different LDs due to the constraint of the DEMUX. In order to control the microwave/mmW phase freely, it is necessary to be able to assign the same wavelength to different antenna elements. As a consequence, a novel optically addressed phased array antenna has been proposed using multiple SMFs, whose schematic diagram is shown in Fig. **131**. The array antenna using multiple SMFs has the advantage of increase in design freedom especially. Furthermore, microwave loss of the signal can be suppressed because the DEMUX is not used to assign the optical carrier to antenna element differently.

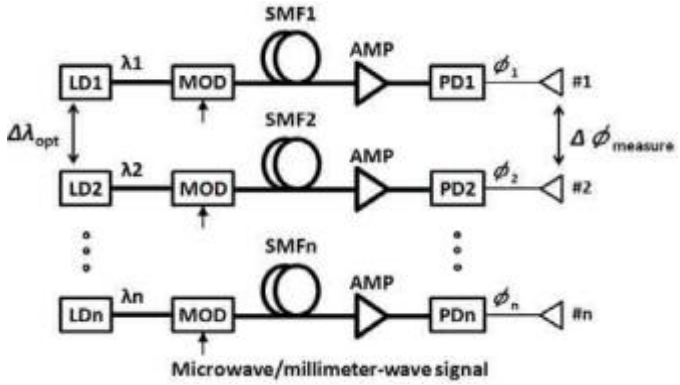

Fig. 131. Schematic diagram of optically addressed phased array antenna using multiple SMFs [81].

5.6.1.2 Ultra-wideband (UWB) optically addressed transmitting phased array

In optically controlled UWB phased antenna arrays, the laser outputs are fed into an optical interleaving and feeding network, consisting of two 1-to-N beam splitters, N electro-optic phase modulators, N 2-to-1 beam combiners and fiber couplers [82][83]. The beam splitting, phasing, and recombining can be achieved through typical fiber-based components. The proposed approach, however, imposes some technical difficulties in the practical implementation. Due to thermal and mechanical stresses in each channel, the relative phase between channels will drift over time, thereby resulting into significant distortion in the RF BF.

In order to mitigate the time-varied phase fluctuation due to environmental impact, a new phase feed network for phased array antennas is proposed, as shown in Fig. **132** [82][83]. Two coherent optical sources, labeled as ω1 and ω2, are combined with a polarization combiner into the fast and slow axes of a polarization maintaining (PM) fiber, respectively. The signals can be amplified simultaneously with polarization independent power amplifier, then split into N channels with beam splitters, and eventually delivered to antenna heads for RF generation and transmission. In doing so, two key advantages can be recognized. First, the phase fluctuation occurring before the polarization combiner at two optical tones will be equally distributed to each channel. Therefore, the produced RF signal after photo-mixing will be independent on these

phase noise. Second, due to the copropagation of both optical signals in the same fiber after the polarization combiner, they will experience the same phase fluctuation. In doing so, the overall phase noise in each channel can be significantly reduced. Each channel will be fed into an electro-optic (EO) phase modulator to tune the phase for beam scanning. The Z-cut $LiNbO_3$ modulator is used particularly, in which the TM mode (E field is aligned in z direction) is phase modulated and the TE mode has a negligible modulation due to the odd distribution of electric field refers to the optical mode. After the phase modulation of ω2, both signals will be projected to the fast and slow axes by applying a 45^0 rotational key. The two sets of orthogonal signals will be filtered by a linear polarizer before being delivered to the photodetectors.

Photo detectors are used primarily as an optical receiver to convert light into electricity. The principle that applies to photo detectors is the photoelectric effect, which is the effect on a circuit due to light. A photo detector operates by converting light signals that hit the junction to a voltage or current. The junction uses an illumination window with an anti-reflect coating to absorb the light photons. The result of the absorption of photons is the creation of electron-hole pairs in the depletion region.

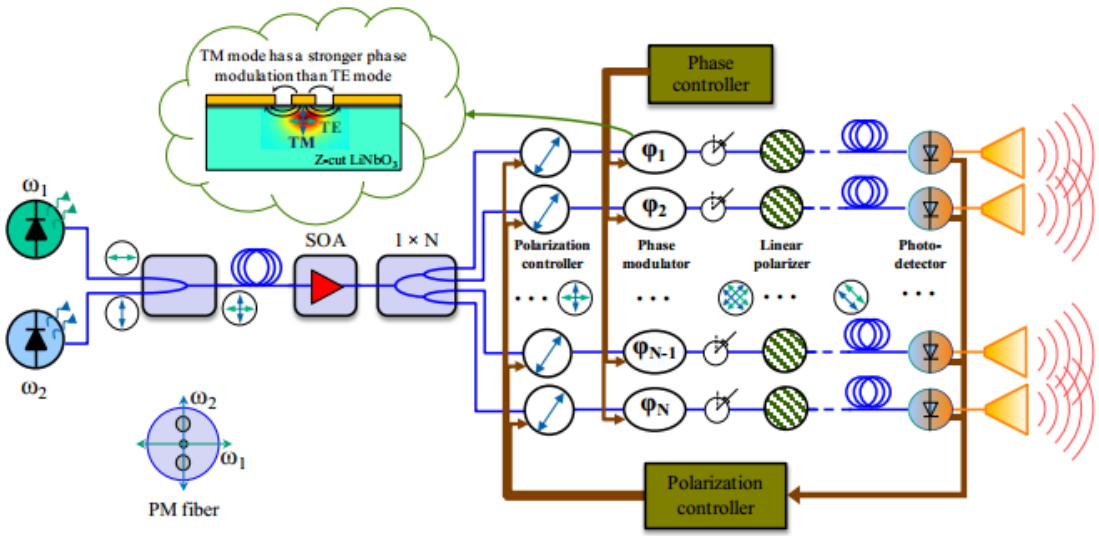

Fig. 132. Optically controlled ultra-wideband phased array [82][83].

Fig. **133** displays the implemented a 1x4 optically addressed phased array [82]. After a 1-to-4 beam splitter, four voltage controlled polarization controllers are used to adjust the state of polarization (SoP) before being fed into the LiNbO3 phase modulator. All channels of optical signals are mixed at 40GHz high-speed photodetectors (from u^2t) to produce the transmitting RF signals. And a various set of array antennas are used as transmitting antennas. The electronic control system, including the voltage driver of EO phase modulators, and DC current acquisition from bias ports of high-speed photodetectors, is realized by utilizing LabVIEW DAQ chassis.

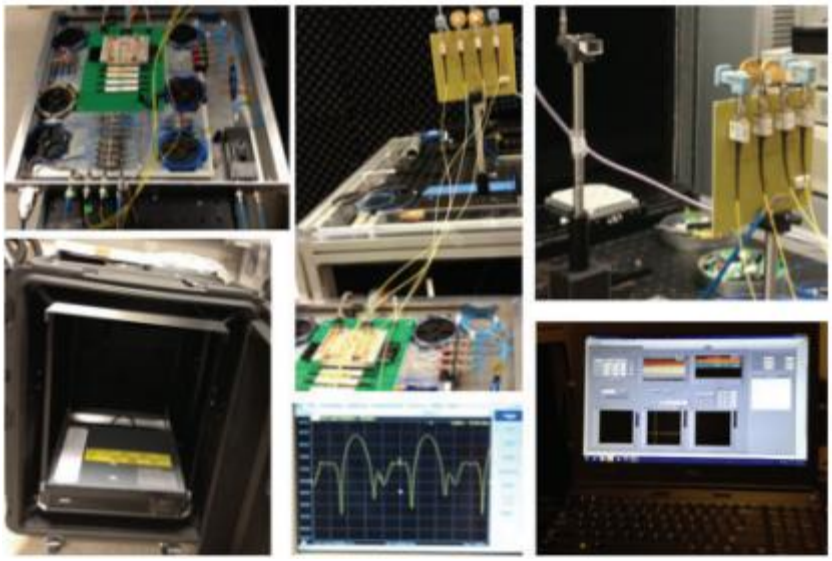

Fig. 133. Practical implementation of a 1x4 phased array antenna, consisting of optical generated RF source, feed network, and a variety of antenna array [82].

Conformal optically addressed transmitting phased patch array and photonic RF receiver are developed and consolidated into rack mount cart for system demonstration of an all-optical mmW transceiver system, which is shown in Fig. **134** [82]. The 4×4 patch antenna array is designed at Ka-band on liquid crystal polymer (LCP) substrate, owning to its low dielectric constant and low dielectric loss at high frequencies. Slot coupled microstrip patch is used to broaden the impedance bandwidth up to 25%. The array consists of four 1×4 subarrays to demonstrate the beam steering capability. Each subarray is evenly fed by a 1×4 microstrip power divider, and arranged in the E-plane. Improved gain of the array leads to smaller radiation beamwidth in the E-plane of 30^0. Four subarrays make up a 4×4 array, as shown in Fig. **134.** The winding microstrip lines are designed to have equal electric length to maintain the equal phase at the feed head of the each antenna. In the case of in-phase optical feed of the array, the 4×4 array attains a gain of 15.6 dB and a beamwidth of 15° in both the E- and H- planes. The adjustment of the array phase is realized via controlling the DC bias of each phase modulator in the embedded controller system.

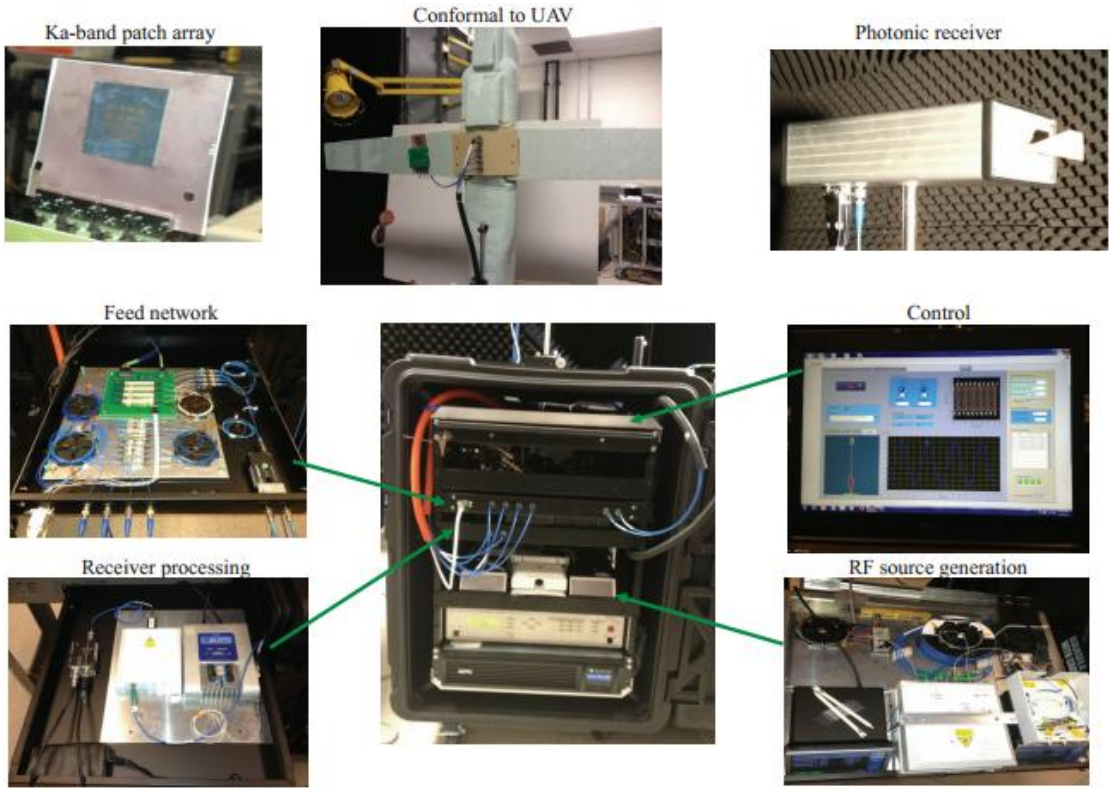

Fig. 134. Pictorial details of the optically enabled Ka-band phased array transmitter showing details of the optical generation and processing box (lower left), the emitting patch array mounted to a mock UAV and the photonic receiver used to capture array emissions (upper), and the details of the RF generated emission as swept across the receiver and the frequency spectrum of the generated tone (lower right) [82].

To further confirm the far field beam scan capability, the transmitting phased array is mounted on the rotation stage and photonic RF receiver is set in the far field region to measure the radiation pattern [82]. With in-phase feed at each antenna element, over -90^0 to 90^0 angular range is measured, a polar plot of radiation pattern is shown in Fig. **135**. The measured maximum sidelobe is more than 15 dB lower than the main beam. The 3dB beam width is about ±15°, which is consistent with the measured pattern with the electric feed. Asymmetric radiation pattern observed from the pattern is likely due to the complicated measuring environment.

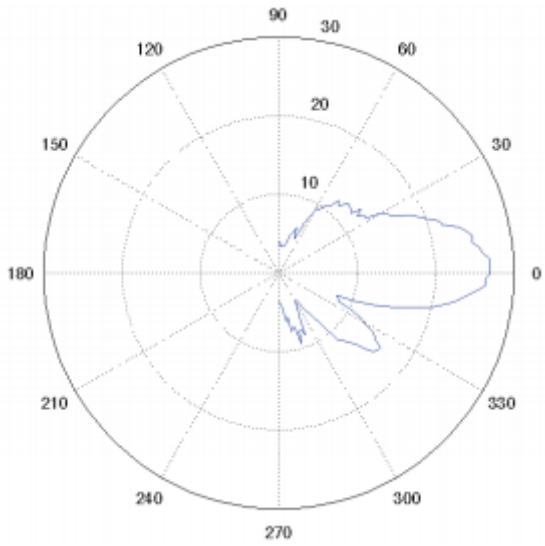

Fig. 135. Rotational scanning of far field of the 4×4 phased array antenna with fixed phase assignment at each channels [82].

5.6.1.3 On-Chip Ultra-Wideband Microwave Photonic Phase Shifter

Time-delay-line (TDD) units are basic processing units for a diversity of high-frequency, broadband RF signal processing applications; particularly, they comprise fundamental building blocks for the implementation of BF networks for antenna arrays, ultra-wideband pulse shapers, and reconfigurable microwave photonic filters (MPFs) [84].

A compact and ultra-wideband phase-shifted waveguide Bragg grating (PS-WBG) that could act as both a phase shifter and a true time delay (TTD) unit was designed and integrated in an SOI (silicon on insulator) waveguide [84]. The gratings with a period of 325 nm were constituted with 100 nm sidewall corrugations. The device was fabricated on a 200 mm SOI wafer by the use of a CMOS-compatible process with deep ultraviolet (UV) lithography. The theoretical bandwidth of the PS is in the order of 0.9 THz, and the operable bandwidth as TDD could reach 8 GHz.

A fiber Bragg grating (FBG) is a type of distributed Bragg reflector constructed in a short segment of optical fiber that reflects particular wavelengths of light and transmits all others [88].

This is achieved by creating a periodic variation in the refractive index of the fiber core, which generates a wavelength specific dielectric mirror. A fiber Bragg grating can therefore be used as an inline optical filter to block certain wavelengths, or as a wavelength-specific reflector. The basic principle of a FBG is illustrated in Fig. **136**. The fundamental principle behind the operation of a FBG is Fresnel reflection, where light traveling between media of different refractive indices may both reflect and refract at the interface. The refractive index will typically alternate over a defined length. The reflected wavelength λ_B, called the Bragg wavelength, is defined by the relationship [88]

$$\lambda_B = 2n_e\Lambda$$

where $n_e$is the effective refractive index of the grating in the fiber core and Λ is the grating period. The bandwidth of the reflected light is

$$\Delta\lambda = \lambda_B \frac{2\delta\eta}{\pi}$$

where δ is the variation in the refractive index (n3-n2), and η is the fraction of power in the core. Note that this approximation does not apply to weak gratings where the grating length, Lg, is not large compared to λ_B/δ.

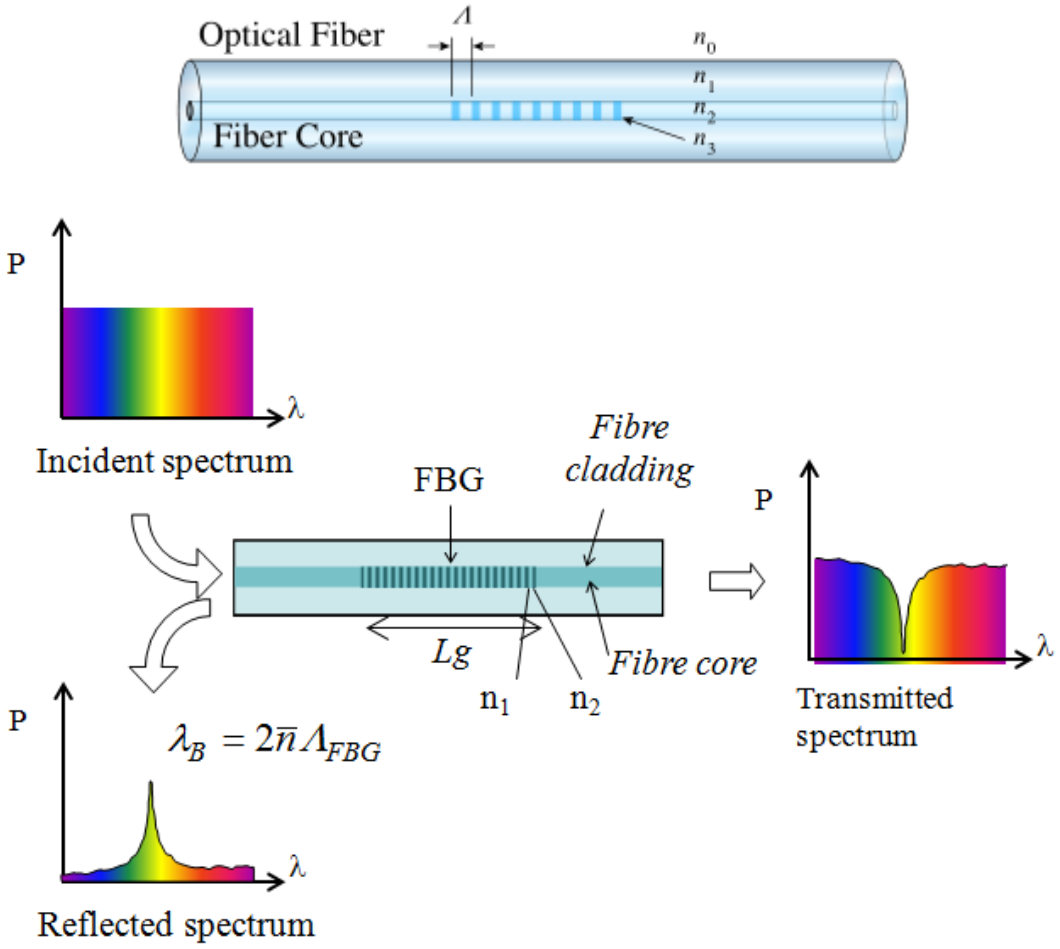

Fig. 136. Schematic of the functional principle of a fiber Bragg grating (FBG) [88][89].

The schematic of the PS-WBG is shown in Fig. **137**(a) [84]. The measured reflection spectral response of the proposed PS-WBG is shown in Fig. **137**(b) [84]. shows a nearly flat response (ripple < 2.5 dB) over a band of more than 1.7 THz, with a shallow notch (approx. 2.3 dB) around the center of the reflection band (194.496 THz). The notch corresponds to a sharp transition in the phase response (approx. 300 degrees over 80 GHz) that can be used to implement the desired RF photonic signal processing functionalities. Using an optical single sideband modulation with full carrier (OSSB+C). When RF signal frequency is 80 GHz or higher, it is possible to provide the desired amount of phase shift to the optical carrier from 0 to 300

degrees without affecting the sideband phase, by adjusting the optical carrier wavelength with respect to the resonance frequency. Fig. **138** depicts the measurement setup for the characterization of the PS-WBG [84].

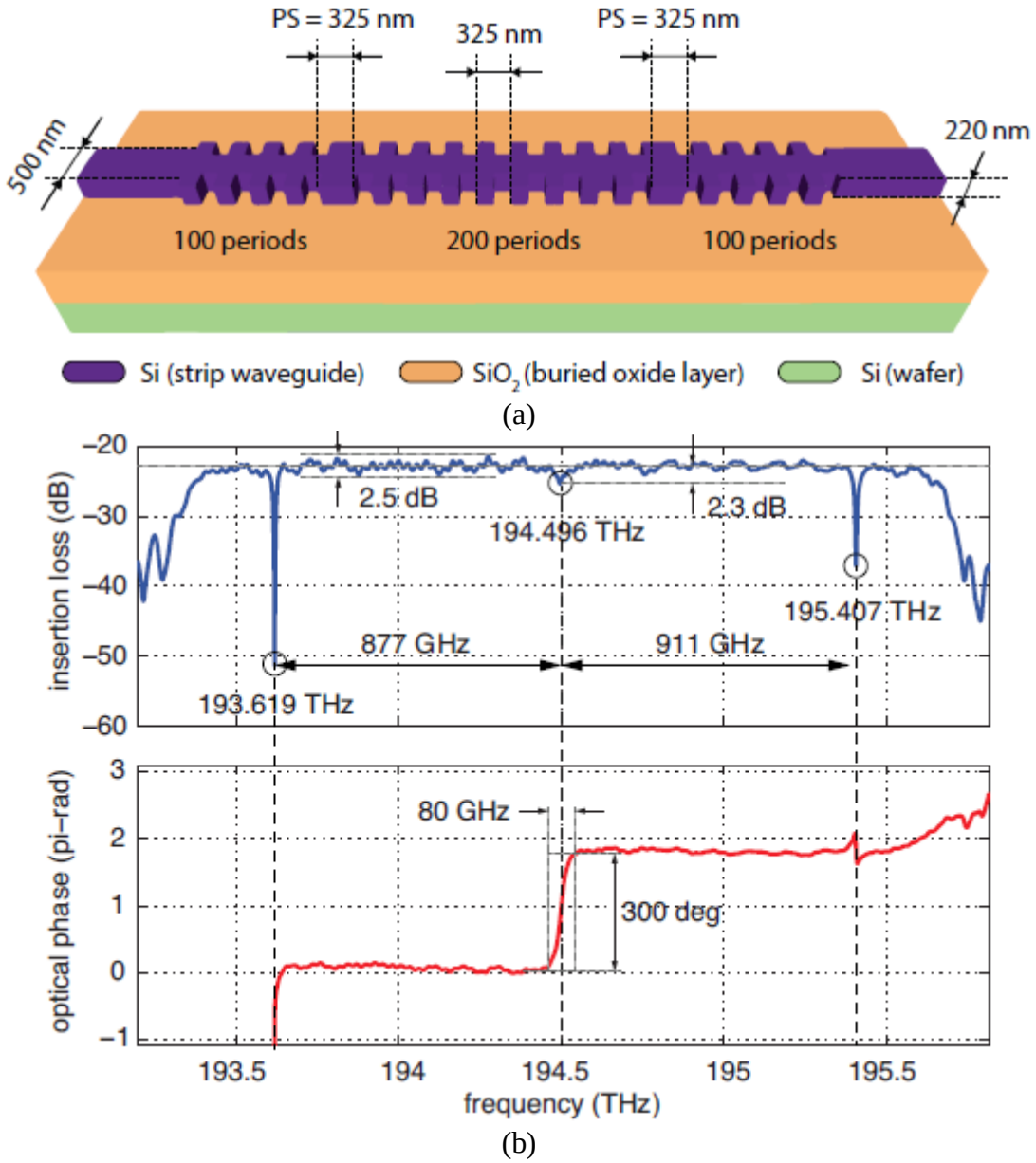

Fig. 137. (a) Simplified schematic of the phase-shifted waveguide Bragg grating (PS-WBG) used in the experiments. (b) Measured reflection spectral responses of the PS-WBG [84].

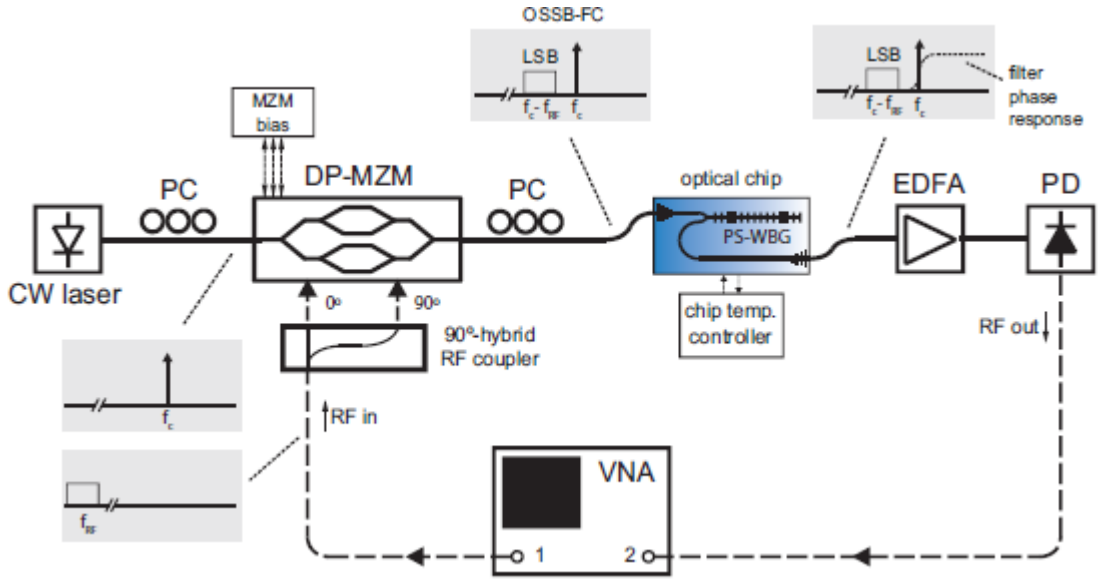

Fig. 138. Setup for the implementation and characterization of the broadband RF photonic true time delay (TTD) and phase shift (PS) [84].

5.6.2 Preliminary Hardware Architecture Design

One of the preliminary designs of the hardware architectures using optically controlled phased array antennas is shown in Fig. 139. Assuming N antennas are needed at the front end, then the whole BF system is mainly comprised of a laser diode (LD), a polarization modulator (PolM) [85], an optical bandpass filter (OBPF), an 1× N optical coupler, N polarizers (Pols) and N photodetectors (PDs). The PolM is a special phase modulator that supports phase modulation with complementary modulation indices along the two principal axes, $\hat{x}$ and $\hat{y}$ [86]. By adjusting polarization controller (PC) to make the polarization direction of the incident light wave at an angle of 45° relative to one principal axis of the PolM, the light wave is projected equally to the two principal axes. At the output of the PolM, two phase-modulated light waves with identical amplitude but complementary phase modulation that are orthogonally polarized are generated. the complementarily phase-modulated signals at the output of the PolM can be expressed as [85][87]:

$$\begin{bmatrix} E_x \\ E_y \end{bmatrix} \propto \begin{bmatrix} \exp(j\varphi)\left[\sum_{n=-\infty}^{\infty} j^n J_n(\beta) e^{jn\omega_e t}\right] \\ \sum_{n=-\infty}^{\infty} j^n J_n(-\beta) e^{jn\omega_e t} \end{bmatrix} = \begin{bmatrix} \exp(j\varphi)\left[J_0(\beta) + jJ_1(\beta)e^{j\omega_e t} - jJ_{-1}(\beta)e^{-j\omega_e t}\right] \\ J_0(\beta) - j(\beta)e^{j\omega_e t} + jJ_{-1}(\beta)e^{-j\omega_e t} \end{bmatrix}$$

where φ is the phase difference between E_x and E_y, which is introduced by the DC bias of the PolM and is given by $2\pi V_{bias}/V_{\pi b}$, where V_{bias} is the bias voltage and $V_{\pi b}$ is the half-wave voltage of the PolM for a modulation signal applied via the bias port. ω_e is frequency of the RF modulating signal, J_n is the first-kind Bessel function of order n, β is the phase modulation index, given by $\pi V/V_{\pi m}$, where V is the amplitude of the microwave signal and $V_{\pi m}$ is the half-wave voltage of the PolM for a modulation signal applied via the microwave port. Note that small-signal modulation is assumed so that the higher order sidebands are small and ignored.

After passing through the OBPF, the signal become single sideband (SSB) and can be represented as [85]:

$$\begin{bmatrix} E_x \\ E_y \end{bmatrix} \propto \begin{bmatrix} \exp(j\varphi)\left[J_0(\beta) + J_{-1}(\beta)\exp\left(-j\left(\omega_e t + \frac{\pi}{2}\right)\right)\right] \\ J_0(\beta) + J_{-1}(\beta)\exp\left(-j\left(\omega_e t - \frac{\pi}{2}\right)\right) \end{bmatrix}$$

By adjusting the PC to align the polarization direction of the polarizer to have an angle of α to one of the principle axes of the PolM, the two orthogonally polarized SSB signals are combined:

$$E(t) = E_x cos\alpha + E_y sin\alpha$$

The output current of the PD can be expressed as:

$$I(t) = E(t)E^*(t)$$

$$\propto (1 + sin2\alpha cos\varphi)J_0^2(\beta) + (1 - sin2\alpha cos\varphi)J_{-1}^2(\beta) - 2(\cos(2\alpha)\sin(\omega_e t)$$

$$+ \sin(2\alpha)\cos(\omega_e t)\, sin\varphi)J_0(\beta)J_{-1}(\beta)$$

Suppose $\varphi = \pi/2$, then we obtain:

$$I(t) \propto \cos(\omega_e t + 2\alpha + \frac{\pi}{2})J_0(\beta)J_{-1}(\beta)$$

It can be seen from the above equation that the phase shift of the RF signal is 2α, thus when 360^0 phase shift can be achieved by adjusting α from 0^0 to 180^0. The PCs can be electronically controlled so that the phase shift at each antenna element can be implemented electronically at a fast speed.

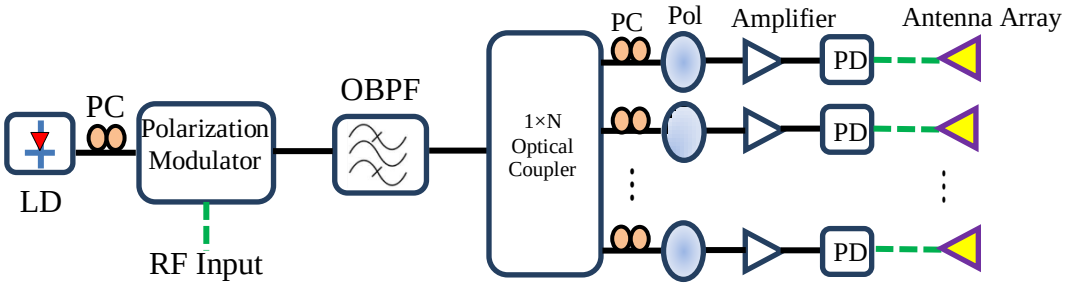

Fig. 139. An optically controlled phased array antenna architecture design using a Mach–Zehnder modulator (MZM), polarization controllers (PCs) and polarization beam splitters (PBSs). The optical source is a laser diode (LD). The solid black lines denote the optical paths, while the dashed green lines denote the electrical paths.

Fig. 140 illustrates the schematic diagram of another proposed optically addressed phase array antenna system. N tunable laser diodes (LDs) are used to generate N optical carrier sources, which are combined by the optical combiner. All the optical carrier wavelengths are modulated by the same RF signal in the Mach–Zehnder modulator (MZM) to obtain optical single sideband (OSSB) signals. Then the modulated light waves travel through an optical circulator to a

phase-shifted fiber Bragg grating (PS-FBG). All the emitted wavelengths of the tunable LDs are selected to fall into the reflection resonance bandwidth of the PS-FBG (e.g., 194.5 THz ± 40 GHz for the case shown in Fig. 137), and further adjusted according to the phase shift requirement of the BF operation. The N phase-shifted optical carriers are separated by an optical coupler into N streams, and then propagate to the array antennas after the amplifier and photo detector (PD).

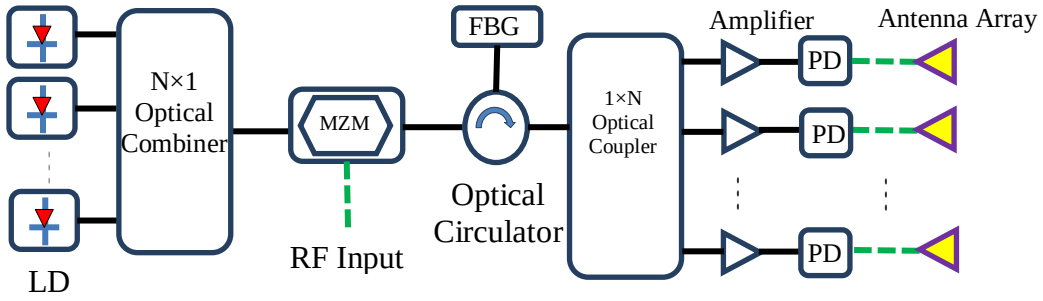

Fig. 140. An optically controlled phased array antenna architecture design using a Mach–Zehnder modulator (MZM) and a fiber Bragg grating (FBG). The solid black lines denote the optical paths, while the dashed green lines denote the electrical paths.

CHAPTER 6 CONCLUSION AND FUTURE WORK

6.1 Conclusion

This thesis has focused on 28 GHz and 73 GHz outdoor propagation measurements, data processing, propagation parameter analysis, beam combining using the measured data, and beamforming. The measurement results at these two mmWave frequencies show that the path loss values are comparable at 28 GHz and 73 GHz, and are only slightly higher than current cellular systems, but the higher path loss can be totally compensated for by directional transmission using phased array antennas. Thus the mmWave spectrum is promising for use in next generation wireless communications to deliver higher data rates and capacity. This thesis provides new technical knowledge in the following ways: 1) understanding how 28 GHz and 73 GHz mmWaves propagate in dense urban environments for future wireless communications , 2) analyzing how beam combining improves received signal quality and extend base station coverage range, 3) reviewing various beamforming (BF) algorithms and hardware architectures and how they can be used for broadband mmWave communication systems, 4) analyzed how spatial multiplexing and BF can be combined to improve MIMO system performance, and 5) investigated MUSIC and ESPRIT DOA estimation algorithms.

6.2 Future Work

While the extensive measurement campaigns at 28 GHz and 73 GHz generated significant insight and data, additional measurements may be desired to further characterize the channel, such as how antenna polarizations influence the propagation. Different beam combining schemes like maximal ratio combining (MRC) and hybrid selection MRC can be explored to further improve the SNR and link budget. Furthermore, how to actually build phased antenna array and implement appropriate BF

algorithms for broadband mmWave communications needs to be addressed. Finally, BF performance at mmWave frequencies and system level protocols need to be investigated.

Bibliography

[1] J.H. Winters, “On the capacity of radio communications systems with diversity in Rayleigh fading environments,” IEEE J. Selected Areas Comm., vol. 5, pp. 871–878, June 1987.

[2] D. Gesbert, M. Shafi, D.S. Shiu, P.J. Smith, and A. Naguib, “From theory to practice: An overview of MIMO space-time coded wireless systems,” IEEE J. Select. Areas Commun., vol. 21, pp. 281–302, Apr. 2003.

[3] A. F. Molisch, Wireless Communications, 2nd Edition, New York: Wiley-IEEE press, 2010.

[4] J. B. Andersen, “Antenna arrays in mobile communications: Gain, diversity, and channel capacity,” IEEE Antennas Propagat. Mag.,vol. 42, pp. 12–16, April 2000.

[5] D.G. Brennan, "Linear diversity combining techniques," Proc. IRE, vol.47, no.1, pp.1075–1102, June 1959.

[6] T. S. Rappaport, Wireless Communications: Principles and Practice, 2nd Edition, New Jersey: Prentice Hall, 2002.

[7] L. Kahn, “Ratio Squarer,” *Proceedings of IRE (Correspondence)*, Vol. 42, pp. 1074, November 1954.

[8] A. Annamalai, C. Tellambura and Vijay and K. Bhargava “Equal gain diversity receiver performance in wireless channels”, IEEE Trans. on Comm., vol. 48, no. 10, 2000.

[9] D. A. Zogas, G. K. Karagiannidis, and S. A. Kotsopoulos, “Equal gain combining over Nakagami-n (Rice) and Nakagami-q (Hoyt) generalized fading channels,” IEEE Trans. Wireless Commun., vol. 4, no. 2, pp. 374–379, Mar. 2005.

[10] G. K. Karagiannidis, N. C. Sagias, and D. A. Zogas, “Error analysis of M-QAM with equal-gain diversity over generalized fading channels,” IEE Proc. Commun, vol. 152, no. 1, pp. 69–74, Feb. 2005.

[11] I. Develi, A. Akdagli, "Approximate expression of bit error rate in uplink MC-CDMA systems with equal gain combining," Communications and Networks, Journal of , vol.15, no.1, pp.25,30, Feb. 2013.

[12] A. F. Molisch, M. Z. Win “MIMO systems with Antenna Selection,” IEEE Microwave Mag., Vol. 5, No. 1, pp. 46–56, Mar. 2004.

[13] M.Z. Win and J.H. Winters, "Virtual branch analysis of symbol error probability for hybrid selection/maximal-ratio combining in Rayleigh fading," IEEE Trans. Commun., vol. 49, pp. 1926–1934, Nov. 2001.

[14] A. F. Molisch, M. Z. Win, and J. H. Winters, "Capacity of MIMO systems with antenna selection," in Proc. IEEE Int. Conf. on Communications, Helsinki, 2001, pp. 570–574.

[15] M. Z. Win and J. H. Winters, "Analysis of hybrid selection/maximalratio combining in Rayleigh fading," IEEE Trans. Commun., vol. 47, pp. 1773–1776, Dec. 1999.

[16] T.K.Y. Lo, "Maximum ratio transmission," in Proc. IEEE Int. Conf. Commun. pp. 1310–1314, 1999.

[17] A.F. Molisch, M.Z. Win, and J.H. Winters, "Capacity of MIMO systems with antenna selection," in Proc. IEEE Int. Conf. on Communications, Helsinki, pp. 570–574, 2001.

[18] G.J. Foschini and M.J. Gans, "On limits of wireless communications in a fading environment when using multiple antennas," Wireless Personal Commun., vol. 6, pp. 311–335, Feb. 1998.

[19] Y. S. Choi, A. F. Molisch, M. Z. Win, and J. H. Winters, "Fast antenna selection algorithms for MIMO systems," in Proc. Veh. Technol. Conf., Orlando, FL, Oct. 2003.

[20] M. Vavrda,"Digital beamforming in wireless communications", Brno University of Technology, 2011.

[21] W. Roh, "Performances and Feasibility of mmWave Beamforming Prototype for 5G Cellular Communications," 2013 IEEE International Conference on Communications (ICC), June 9-13, 2013.

[22] Z. Rong, "Simulation of Adaptive Array Algorithms for CDMA Systems," Master's thesis, Virginia Polytechnic Institute and State University, Blacksburg, VA, September 1996.

[23] R. T. Compton, Jr., Adaptive Antennas, Concept and Performance, Prentice Hall, Englewood Cliffs, New Jersey, 1988.

[24] R. S. Adve, "Switched and Sectored Beamforming," [online] Available: http://www.comm.utoronto.ca/~rsadve/Notes/SwitchedBeam.pdf.

[25] J. Butler, and R. Lowe, "Beam forming matrix simplifies design of electronically scanned antennas," Electronic Design, Vol. 9, pp. 170-173, Apr. 1962.

[26] K. Wu, Y. J. Cheng, T. Djerafi, X. P. Chen, N. Fonseca, and W. Hong, "Millimeter-wave integrated waveguide antenna arrays and beamforming networks for low-cost satellite and

mobile systems," presented at the Eur. Conf. on Antennas and Propagation, Barcelona, Apr. 2010, (Invited paper).

[27] T. Djerafi, M. Daigle, H. Boutayeb, X. P. Zhang, K. Wu, "Substrate integrated waveguide six-port broadband front-end circuit for millimeter-wave radio and radar systems," 39th Europ. Microwave Conf. Proc. (EuMC 2009), Rome. pp.77-80.

[28] Y. Cassivi, D. Deslandes, K. Wu, "Substrate integrated waveguide directional couplers," 2002 Asia-Pacific Microwave Conf. Proc. (APMC'02), Vol. 3, pp. 1409-1412, Nov. 19-22, Kyoto, Japan.

[29] W. Rotman and R.F. Turner, "Wide-angle microwave lens for line source applications," IEEE Trans. Antennas Propag., vol. AP-11, pp. 623–632, Nov. 1963.

[30] D. Nußler, H. H. Fuchs, and R. Brauns, "Rotman lens for the millimeter wave frequency range," in Proc. Eur. Microw. Conf., Oct. 2007, pp.696–699.

[31] J. Hall, H. Hansen, and D. Abbot, "Rotman lens for mm-wavelengths," Proc. Smart Structures, Devices, and Systems, SPIE, vol. 4935, pp. 215–221, 2002.

[32] M. Weiss, "Digital antennas," educational notes RTOEN- SET 133, 2009, pp. 5.1 - 5.29, Multistatic Surveillance and Reconnaissance: Sensor, Signals and Data Fusion.

[33] Nüßler, Dirk, and Hans-Hellmuth Fuchs. "A Rotman Lens at W-Band."Frequenz 56.11-12 (2002): 244-248.

[34] Lee, Woosung, et al. "Multi-layer beamforming lens antenna array with a new line design for millimeter-wave system-in-package applications." IEEE Proceedings of the 5th European Conference on Antennas and Propagation (EUCAP), 2011.

[35] A. R. Lopez, "Performance predictions for cellular switched-beam intelligent antenna systems," Communications Magazine, IEEE, vol.34, no.10, pp.152-154, Oct 1996.

[36] Preston, S.L., Thiel, D.V., Lu, J.W., O'Keefe, S.G., and Bird, T.S., "Electronic beam steering using switched parasitic patch elements ," Electronics Letters , vol.33, no.1, pp.7-8, 2 Jan 1997.

[37] T. Ohira, "Adaptive array antenna beamforming architectures as viewed by a microwave circuit designer", *Proc. IEEE Asia-Pacific Microwave Conf.*, pp.828 -833, 2000.

[38] T. Ohira , Y. Suzuki , H. Ogawa and H. Kamitsuna "Megalithic microwave signal processing for phased-array beamforming and steering", IEEE Trans. Microwave Theory Tech., vol. MTT-45, no. 12, pp.2324 -2332 1997.

[39] Y. Ji , K. Inagaki , O. Shibata and Y. Karasawa "Receive mode of optical signal processing multibeam array antennas", IEEE Microwave Guided Wave Lett., vol. 8, no. 7, pp.251 -253 1998.

[40] S. Obayashi , H. Shoki , O. Shibata , H. Kasami , S. Otaka , H. Tsurumi and Y. Suzuki "An adaptive array for high speed wireless local loop steered by local signal phase shifters", Proc. IEEE Antennas and Propagation Society Int. Symp. Digest, vol. 2, pp.1436 -1439, 1999.

[41] T. Ohira et al, "Electronically steerable passive array radiator antennas for low-cost analog adaptive beamforming", IEEE International Conference Phased Array Systems Tech., pp.lOl-104, Dana Point, CA, May 2000.

[42] A. F. Molisch, "Ultrawideband propagation channels and their impact on system design," in Proc. Int. Symp. on Microwave, Antenna, Propag. and EMC Technol. for Wireless Commun., 2007, pp. K4–1–K4–5.

[43] A. Saleh and R. A. Valenzuela, "A statistical model for indoor multipath propagation," IEEE J. Selected Areas Comm., vol. 5, pp. 128-137, Feb. 1987.

[44] A. Goulianos and S. Stavrou, "Uwb path arrival times in body area networks," Antennas and Wireless Propagation Letters, vol. 6, pp. 223-226, 2007.

[45] L. Frost, III, "An algorithm for linearly constrained adaptive array processing," Proc. IEEE, vol. 60, no. 8, pp. 926–935, Aug. 1972.

[46] H. Duan , B. P. Ng , Ch. M. See , J. Fang , "Broadband Beamforming Using TDL-Form IIR Filters." IEEE Transactions on Signal Processing, vol. 55, no.3, pp. 990-1002, March 2007.

[47] Piper, J.E., "Broadband beamforming," OCEANS 2011 , pp.1-4, 19-22 Sept. 2011.

[48] W. Liu, S. Weiss, "Off-broadside main beam design and subband implementation for a class of frequency invariant beamformers," Signal Processing, vol. 89, pp. 913-920, May 2009.

[49] Y. Zhao,W. Liu, R. Langely , "A least squares approach to design of frequency invariant beamformers," 17th European Signal Processing Conference , Glasgow, Scotland, pp. 844-848, August 2009.

[50] I. D. Doltic, "Minimax frequency invariant beamforming ," Electronics Letters , vol 40, no. 19, 16th Septembr 2004.

[51] L. C. Godara, "Application of the fast Fourier transform to broadband beamforming," Journal of the Acoustic Society of America , vol. 98, no.1, July 1995.

[52]T. Do-Hong, P. Russer, "Spatial Signal Processing for Wideband Beamforming," Proceedings of XII International symosium on theoretical electrical engineering (ISTET) , pp. 73-76,July 2003.

[53]Habibifar, Hossein, and Saeid Reza Seydnejad. “A Broadband Beamforming Method Based on Frequency Band Decomposition,” International Conference on Communications Engineering (ICCE), Dec. 22-24, 2010.

[54]Seshadrinathan, Kalpana. “Broadband Beamforming,” Spring, 2003.

[55]T. S. Rappaport, Wireless Communications: Principles and Practice, 2nd ed. Englewood Cliffs, NJ, USA: Prentice-Hall, 2002.

[56]Ben-Dor, Eshar, “Cellular and Peer-to-Peer Millimeter Wave Channel Sounding in Outdoor Urban Environments,” M. S. Thesis, December 2011.

[57]R.J. Pirkl, G.D. Durgin, “Optimal Sliding Correlator Channel Sounder Design,” IEEE Trans. on Wireless Comm., Vol. 7, No. 9, Sept. 2008.

[58]J. Talvitie and T. Poutanen, "Self-noise as a factor limiting the dynamic range in impulse response measurements using sliding correlation," in IEEE International Symposium on Spread Spectrum Techniques and Applications (ISSSTA), vol. 2, Jul. 1994, pp. 619-623.

[59]R. C. Dixon, Spread Spectrum Systems. New York, NY: Wiley, 1976.

[60]Y. Azar, G. N. Wong, K. Wang, R. Mayzus, J. K. Schulz, H. Zhao, F. Gutierrez, D. Hwang, and T. S. Rappaport, ``28 GHz propagation measurements for outdoor cellular communications using steerable beam antennas in New York City," in Proc. IEEE Int. Conf. Commun., Jun. 2013, pp. 1-6.

[61]H. Zhao, R. Mayzus, S. Sun, M. Samimi, J. K. Schulz, Y. Azar, K. Wang, G. N. Wong, F. Gutierrez, Jr., and S. T. Rappaport, ``28 GHz millimeter wave cellular communication measurements for re_ection and penetration loss in and around buildings in New York City," in Proc. IEEE Int. Conf. Commun., Jun. 2013, pp. 1-6.

[62]T. S. Rappaport, S. Sun, R. Mayzus, H. Zhao, Y. Azar, K. Wang, G. N. Wong, J. K. Schulz, M. K. Samimi, F. Gutierrez, "Millimeter wave mobile communications for 5G cellular: It will work!" IEEE Access, vol. 1, 2013.

[63]M. Samimi, K. Wang, Y. Azar, G. N. Wong, R. Mayzus, H. Zhao, J. K. Schulz, S. Sun, F. Gutierrez, and T. S. Rappaport, ‘‘28 GHz angle of arrival and angle of departure analysis for

outdoor cellular communications using steerable beam antennas in New York City,'' in Proc. IEEE Veh. Technol. Conf., 2013, DOI: 10.1109/VTCSpring.2013. 6691812.

[64] S. Sun, T. S. Rappaport, "Wideband mmWave channels: Implications for design and implementation of adaptive beam antennas," to appear in *2014 IEEE International Microwave Symposium (IMS)*, Orlando, FL, USA, June 1-6, 2014.

[65] T. S. Rappaport, F. Gutierrez, E. Ben-Dor, J. N. Murdock, Y. Qiao; J. I. Tamir, "Broadband millimeter-wave propagation measurements and models using adaptive-beam antennas for outdoor urban cellular communications," IEEE Transactions on Antennas and Propagation, vol.61, no.4, pp.1850-1859, April 2013.

[66] S. Nie, "Millimeter Wave Indoor Propagation Channel Measurements and Characterization at 73 GHz and Coverage Studies in Dense Urban Environments", M.S. Thesis, May 2014.

[67] M. K. Samimi, "Characterization of the 28 GHz Millimeter-Wave Dense Urban Channel for Future 5G Mobile Cellular," M. S. Thesis, May 2014.

[68] G. R. MacCartney, Jr., J. Zhang, S. Nie, and T. S. Rappaport, ''Path loss models for 5G millimeter wave propagation channels in urban microcells,'' in *Proc. IEEE Global Telecommun. Conf.*, Dec. 2013.

[69] S. Sun and T. S. Rappaport, "Multi-beam antenna combining for 28 GHz cellular link improvement in urban environments," in *Proc. IEEE Global Telecommun. Conf.*, Dec. 2013.

[70] S. Sun, G. R. MacCartney, M. K. Samimi, S. Nie, and T. S. Rappaport, "Millimeter Wave Multi-beam Antenna Combining for 5G Cellular Link Improvement in New York City," to appear in *2014 IEEE International Conference on Communications (ICC)*, Sydney, Australia, June 10-14, 2014.

[71] T. K. Sarkar, Michael C. Wicks, M. Salazar-Palma, Robert J. Bonneau, Smart Antennas. Wiley-IEEE Press, May 2003.

[72] A. Goldsmith, Wireless Communications. Cambridge, U.K.: Cambridge Univ. Press, 2004.

[73] P. Kyösti et al., "WINNER II Channel Models," IST-4-027756 WINNER II Deliverable D1.1.2 v.1.2.4.2.2008 (http://www.ist-winner.org/deliverables.html).

[74] J. Medbo, "5G channel modeling challenges," the Brooklyn 5G Summit, April 23-25, 2014.

[75] J. Medbo, H. Asplund, J. E. Berg, and N. Jalden, "Directional channel characteristics in elevation and azimuth at an urban macrocell base station," in Proc. 6th European Conference on Antennas and Propagation (EUCAP), pp. 428-432.

[76] Wi-Fi every where [online]. Available: http://ilovewifi.blogspot.com/2012/08/80211n-features.html.

[77] S. Fang, L. Li, X. Tao, and P. Zhang, "A spatial multiplexing mimo scheme with beamforming for downlink transmission," in Vehicular Technology Conference, 2007. VTC-2007 Fall. 2007 IEEE 66th, 2007, pp. 700–704.

[78] W. Liu; S. Han; C. Yang; C. Sun, "Massive MIMO or small cell network: Who is more energy efficient?," Wireless Communications and Networking Conference Workshops (WCNCW), 2013 IEEE , pp.24-29, April 2013.

[79] T. Lavate, V. Kokate, and A. Sapkal, "Performance analysis of music and esprit doa estimation algorithms for adaptive array smart antenna in mobile communication," in Computer and Network Technology (ICCNT), 2010 Second International Conference on, pp. 308–311, April 2010.

[80] J. Yao, "A tutorial on microwave photonics," *IEEE Photonics Society Newsletter,* April 2012.

[81] D. Tkeuchi, W. Chujo, S. Yamamoto, and Y. Koyamada, "Phase control and calibration characteristics of optically controlled phased array antenna feed using multiple SMFs" IEICE Trans. Electronics, vol. E94C, No. 10, pp: 1634-1640, 2011.

[82] S. Shi, J. Bai, G. Schneider, Y. Zhang, R. Nelson, J. Wilson, C. Schuetz, D. Prather, "Conformal ultra-wideband optically addressed transmitting phased array and photonic receiver systems," *2013 International Topical Meeting on Microwave Photonics (MWP)*, pp.221-224, Oct. 2013.

[83] S. Shi, J. Bai, G. J. Schneider, and D. W. Prather, "Optical phase feed network and ultra-wideband phased array", *IEEE Photonics Conference*, San Francisco, Sep. 2012.

[84] M. Burla, L. Cortes, M. Li, X. Wang, L. Chrostowski, J. Azana, "On-chip ultra-wideband microwave photonic phase shifter and true time delay line based on a single phase-shifted waveguide Bragg grating," *2013 International Topical Meeting on Microwave Photonics (MWP)*, pp.92-95, Oct. 2013.

[85] S. Pan and Y. Zhang, "Tunable and wideband microwave photonic phase shifter based on a single-sideband polarization modulator and a polarizer," *Opt. Lett.* 37(21), 4483–4485 (2012).

[86] J. D. Bull, N. A. F. Jaeger, H. Kato, M. Fairburn, A. Reid, and P. Ghanipour, "40 GHz electro-optic polarization modulator for fiber optic communications systems," Proc. SPIE 5577, pp. 133–143, 2004.
[87] W. Li, W. Zhang, and J. Yao, "A wideband 360° photonic-assisted microwave phase shifter using a polarization modulator and a polarization-maintaining fiber Bragg grating," Opt. Express 20,pp. 29838–29843, 2012.
[88] Fiber Bragg grating [online]. Available: http://en.wikipedia.org/wiki/Fiber_Bragg_grating.
[89] Com&Sens, Sensor technology [online]. Available: http://www.com-sens.eu/sensor-technology.